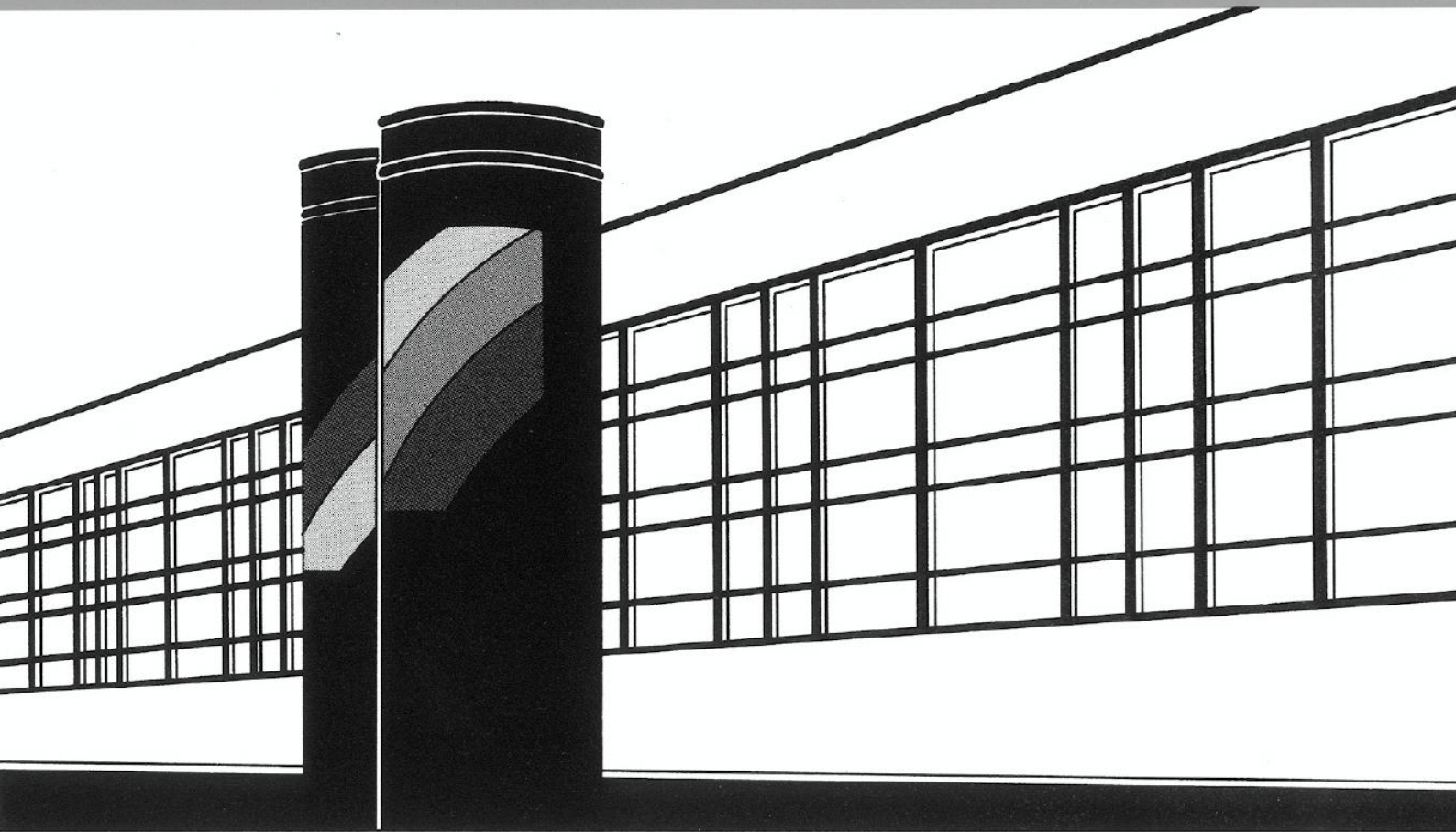


Universität Stuttgart



Institut für Wasser- und Umweltsystemmodellierung

Mitteilungen



Heft 223 Klaus Mosthaf

Modeling and Analysis of Coupled
Porous-Medium and Free Flow with
Application to Evaporation Processes

Modeling and Analysis of Coupled Porous-Medium and Free Flow with Application to Evaporation Processes

Von der Fakultät Bau- und Umweltingenieurwissenschaften und dem
Stuttgart Research Centre for Simulation Technology
der Universität Stuttgart zur Erlangung der Würde eines
Doktor-Ingenieurs (Dr.-Ing.) genehmigte Abhandlung

Vorgelegt von
Klaus Mosthaf
aus Stein am Kocher

Hauptberichter:	Prof. Dr.-Ing. Rainer Helmig
Mitberichter:	Prof. Dr. rer. nat. Insa Neuweiler
Mitberichter:	Prof. Dr. Dani Or

Tag der mündlichen Prüfung: 10. Oktober 2013

Institut für Wasser- und Umweltsystemmodellierung
der Universität Stuttgart
2014

Heft 223 Modeling and Analysis of
Coupled Porous-Medium and
Free Flow with Application to
Evaporation Processes

von
Dr.-Ing.
Klaus Mosthaf

Eigenverlag des Instituts für Wasser- und Umweltsystemmodellierung
der Universität Stuttgart

D93 Modeling and Analysis of Coupled Porous-Medium and Free Flow with Application to Evaporation Processes

Bibliografische Information der Deutschen Nationalbibliothek

Die Deutsche Nationalbibliothek verzeichnet diese Publikation in der Deutschen Nationalbibliografie; detaillierte bibliografische Daten sind im Internet über <http://www.d-nb.de> abrufbar

Mosthaf, Klaus:

Modeling and Analysis of Coupled Porous-Medium and Free Flow with Application to Evaporation Processes von Klaus Mosthaf. Institut für Wasser- und Umweltsystemmodellierung, Universität Stuttgart. - Stuttgart: Institut für Wasser- und Umweltsystemmodellierung, 2014

(Mitteilungen Institut für Wasser- und Umweltsystemmodellierung, Universität Stuttgart: H. 223)

Zugl.: Stuttgart, Univ., Diss., 2014

ISBN 978-3-942036-27-6

NE: Institut für Wasser- und Umweltsystemmodellierung <Stuttgart>: Mitteilungen

Gegen Vervielfältigung und Übersetzung bestehen keine Einwände, es wird lediglich um Quellenangabe gebeten.

Herausgegeben 2014 vom Eigenverlag des Instituts für Wasser- und Umweltsystemmodellierung

Druck: Document Center S. Kästl, Ostfildern

Danksagung

Ich möchte mich an dieser Stelle bei allen Personen bedanken, die bei der Entstehung dieses Werks direkt oder indirekt mitgewirkt haben. Zunächst möchte ich der DFG danken, die die Graduiertenschule SimTech sowie die internationale Forschergruppe MUSIS (FOR 1083), in deren Rahmen diese Arbeit entstanden ist, finanziert hat. In diesem Zusammenhang möchte ich auch allen Kolleginnen und Kollegen der Forschergruppe MUSIS danken. Die Treffen, Workshops und Kooperationen waren alle sehr spannend, fruchtbar und positiv. Vielen Dank geht auch an Insa Neuweiler und Dani Or für die Übernahme der Mitberichte. Letzterer ermöglichte mir zwei Aufenthalte in seiner Arbeitsgruppe an der ETH Zürich. Dort wurde ich bestens aufgenommen und durfte selbst Experimente durchführen oder daran mitwirken, wobei ich viele Eindrücke bekommen und viel gelernt habe. Außerdem möchte ich allen weiteren Personen, mit denen ich während meiner Promotion zusammen gearbeitet oder inspirierende Diskussionen geführt habe, danken. Hierzu zählen neben anderen Barbara Wohlmuth, Iryna Rybak, Toon Leijnse, Kathleen Smits, Ebrahim Shahraeeni und Steffen Müthing.

Des Weiteren möchte ich mich bei all meinen Kolleginnen und Kollegen für die angenehme Atmosphäre, die gemeinsamen Aktivitäten und die gute Zusammenarbeit und Unterstützung in der Gruppe bedanken. Dazu zählen natürlich auch Maria Costa Jornet und Prudence Lawday, die stets für einen reibungslosen Ablauf der Organisation und Verwaltung in unserem Lehrstuhl sorgen, sowie David Werner und Michelle Hartnick, die sich um die Hard- und Software an unserem Lehrstuhl kümmern. Vielen Dank auch an Holger Class und Bernd Flemisch, die immer ein offenes Ohr für Fragen hatten und mir stets geholfen haben. Dank geht auch an meine Diplomanden, Bachelor- und Masterstudenten bei deren Betreuung auch ich viel gelernt habe und deren Betreuung eine willkommene Abwechslung im Arbeitsalltag darstellte. Außerdem möchte ich mich bei meinen Hiwis bedanken, die mir freundlich helfend zur Seite gestanden haben. Großer Dank geht auch an meine Freunde und Familie, die immer an mich geglaubt und mich bei meinem Tun stets unterstützt haben.

Zu guter Letzt möchte ich mich bei meinem Betreuer Rainer Helmig bedanken, der mir stets mit Rat und Tat zur Seite gestanden hat und zu einem großen Teil für das außergewöhnlich gute Arbeitsklima in der Arbeitsgruppe verantwortlich ist. Mit seinem großen Ideenreichtum, Diskussions- und Motivationsbereitschaft, Weitblick und Engagement hat er maßgeblich zum Gelingen meiner Arbeit beigetragen und mir viel Fachliches sowie Nicht-Fachliches beigebracht.

Contents

List of Figures	V
List of Tables	XI
Nomenclature	XIII
Abstract	i
Zusammenfassung	v
1 Introduction	1
1.1 Challenge and motivation	1
1.2 Structure of the thesis	3
2 Fundamentals	5
2.1 Terms and definitions	5
2.1.1 Scales	5
2.1.2 Phase	7
2.1.3 Component	7
2.1.4 Interface	8
2.1.5 Quantities arising from volume-averaging	8
2.2 Material properties	13
2.2.1 Liquid phase: water	13
2.2.2 Gaseous phase: air	13
2.3 General conservation equations	17
2.3.1 Mass conservation	18
2.3.2 Momentum conservation	18
2.3.3 Energy conservation	19
2.4 Relevant processes	19
2.4.1 Transport phenomena	19
2.4.2 Evaporation from porous media	20
2.4.3 Flow conditions and boundary layers	22

2.4.4	Radiation	25
2.5	Summary of this chapter	26
3	Evaporation experiments	27
3.1	Experimental setup	27
3.1.1	Drying rates	29
3.1.2	Heat exchange and thermal boundary layer	30
3.2	Possible error sources and uncertainties	32
3.3	Summary of this chapter	33
4	Conceptual model	35
4.1	Review of prior research and overview of coupling approaches	35
4.1.1	Single-domain approach	36
4.1.2	Two-domain approach	38
4.1.3	Evaporation models	40
4.2	Model concepts in the subdomains	40
4.2.1	Model concept in the porous-medium domain	41
4.2.2	Model concept in the free-flow domain	47
4.3	Interface conditions and coupled model	49
4.3.1	Mechanical equilibrium	51
4.3.2	Thermal equilibrium	55
4.3.3	Chemical equilibrium	57
4.3.4	Extension to turbulent flow conditions	59
4.3.5	Coupling conditions with turbulent free flow	62
4.4	Summary of this chapter	63
5	Numerical model concept	65
5.1	Discretization scheme	65
5.2	Primary variables	69
5.3	Boundary and coupling conditions	70
5.4	Computational algorithm	73
5.5	Summary of this chapter	75
6	Process analysis and parameter study	77
6.1	Description of the reference case	78
6.2	Influence of the porous-medium system	85
6.2.1	Porosity	86
6.2.2	Intrinsic permeability	86
6.2.3	Capillary pressure and relative permeability	87

6.2.4	Vertically textured porous medium	91
6.2.5	Statistical distribution of the soil parameters	95
6.2.6	Temperature	95
6.2.7	Thermal conductivity	96
6.2.8	Thermal non-equilibrium in the porous medium	98
6.2.9	Summary of the influence of the porous-medium system	99
6.3	Conditions and processes in the free-flow compartment	99
6.3.1	Inflow vapor concentration	101
6.3.2	Atmospheric pressure variation	101
6.3.3	Free-flow velocity	103
6.3.4	Temperature	103
6.3.5	Summary of the influence of the free-flow system	105
6.4	Influence of interface processes	105
6.4.1	Beavers-Joseph coefficient - slip velocity	105
6.4.2	Surface water content / saturation	106
6.4.3	Surface roughness	111
6.4.4	Radiation	112
6.4.5	Summary of the influence of the interface processes	113
6.5	Summary of this chapter and discussion	115
7	Summary and outlook	117
7.1	Summary	117
7.2	Outlook and suggestions for future work	119
7.2.1	Concept development	119
7.2.2	Numerical developments	120
7.2.3	Experiments	121
	Bibliography	123

List of Figures

1.1	Complex interactions of evaporation processes from porous media.	2
2.1	Different scales: Molecular scale, pore scale, REV scale and field scale.	5
2.2	Schematics of the considered fluid phases and components with exchange processes.	7
2.3	Capillary pressure on the pore and REV scale.	11
2.4	Density and viscosity of water in dependency on temperature.	14
2.5	Density and viscosity of air in dependency on temperature.	14
2.6	Saturated vapor pressure and saturated pressure lowering according to the Kelvin equation.	16
2.7	Specific enthalpies of liquid and gaseous water and of air.	17
2.8	Qualitative evolution of the drying rate from a porous medium	21
2.9	Qualitative evolution of a boundary layer above a flat plate with a different boundary layer thicknesses for velocity, concentration and temperature.	23
2.10	Approximation of the typical distribution of the global solar radiation when reaching the surface after Jury and Horton (2004).	25
3.1	Overview of the experimental setup. Figures (a) and (b) show the wind tunnel with the insulated sample mounted on a digital balance, the infrared camera above the sample and two flow anemometers and a heat and moisture sensor in the center of the transparent section of the wind tunnel. Figure (c) shows the two arrays of stacked thermocouples at the end of the sand sample.	28
3.2	Schematic overview of the experimental setup with approximate position of flow anemometers, thermocouple elements and heat and moisture sensor.	28
3.3	(a) Measured drying rates for the coarse material. (b) Measured drying rates for the fine material.	29

3.4	(a) Temperature evolution at different positions above and below the surface during an evaporation process from the fine sand sample for a flow velocity of 3.5 m/s . The temperatures were determined with the thermocouples. (b) Measured temperature profiles for an evaporation process from the fine material with different free-flow velocities. The differences of the temperature above and below the surface are more pronounced for higher flow velocities and amount to more than 4 K	30
3.5	(a) Evaporation rate and temperature evolution with a vertically textured media. (b) Comparison of the same experimental setup with the coarse material 3.5 m/s measured twice.	31
3.6	Infrared images (top view) of an evaporation experiment with a vertically textured media.	31
3.7	Surface temperature showing a cooler region in the interior of the evaporating surface and warmer zones towards the vessel walls (sides of the figure).	33
4.1	Interface descriptions: (a) REV scale, (b) micro/pore scale,(c) interface description.	36
4.2	Single-domain approach using the Brinkman equation with one set of equations vs. two-domain approach with a sharp interface and coupling conditions.	37
4.3	(a) Effective diffusion coefficient for vapor in the gas phase in the porous medium. (b) Effective thermal conductivity after Johansen and Somerton.	43
4.4	Transition from a pore-scale to a volume-averaged description.	50
4.5	Mechanical equilibrium on the pore scale and on the REV scale (normal component).	52
4.6	For a fully water-saturated porous medium ($S_l = 1$) the capillary pressure inside the porous medium is zero, while it equals the entry pressure at the interface to the gaseous free-flow region.	53
4.7	Mechanical equilibrium at the pore scale and at the REV scale (tangential component). The coupling conditions on the REV scale have to account for the traction between the gas phase in the free-flow region and the gas, solid and water phase in the porous medium.	55
4.8	Thermal equilibrium on the pore scale and on the REV scale.	56
4.9	Chemical equilibrium at the pore scale and at the REV scale.	57
5.1	Schematic description of the spatial discretization (box scheme). b) shows a control volume (box) assigned to node i, c) depicts an element.	66
5.2	Treatment of the nodes where the coupling interface meets the boundaries of the subdomains.	68

5.3	Illustration of the spatial discretization (box scheme) at the interface.	71
5.4	Schematic overview of the coupling conditions.	72
5.5	Depiction of the global matrix for the coupled system.	74
6.1	(a) Porous-medium model coupled to a laminar free flow, (b) porous-medium model coupled to a laminar free flow with a solution-dependent boundary condition for the diffusive vapor fluxes to account for the boundary layer, (c) porous-medium model coupled to a turbulent free-flow model.	78
6.2	(a) Setup of wind tunnel, insulated sand sample and measurement devices. (b) Model setup with grid and boundary conditions.	79
6.3	(a) Successive grid refinement using the laminar free-flow model coupled to the porous medium, starting with 10×62 cells. (b) Comparison of a measured drying curve from a wind tunnel experiment with computed drying curves employing a laminar free-flow model, a laminar free flow in combination with a boundary layer approximation (constant boundary layer thickness and Blasius solution) and a turbulent free-flow model.	80
6.4	Evolution of the mass fraction of vapor in the free-flow domain (upper part of the figure) and of the water saturation in the porous medium (lower part). . .	81
6.5	Evolution of the temperature in the free-flow domain (upper part of the figure) and in the porous medium (lower part).	81
6.6	Influence of the porosity on the computed drying rates. The transition from stage-1 to stage-2 happens later for a higher porosity because more water is in place and can evaporate.	86
6.7	Influence of the intrinsic permeability on the computed drying rates. A lower permeability shortens the duration of stage-1 due to a higher resistance to flow.	87
6.8	(a) Capillary-pressure curves for different <i>van-Genuchten</i> parameters α_{vGN} . (b) Influence of the <i>van-Genuchten</i> parameter α_{vGN} on the computed drying rates.	88
6.9	(a) Capillary-pressure curves for different <i>van-Genuchten</i> parameters n [-]. (b) Influence of the <i>van-Genuchten</i> shape parameter n [-] on the computed drying rates.	88
6.10	Computed drying rates with the <i>van-Genuchten</i> and the <i>Brooks-Corey</i> model with the respective capillary-pressure curves.	89
6.11	(a) Capillary-pressure curves with and without linear regularization and according drying rates. (b) This figure demonstrates the earlier onset of stage-2, when the capillary-pressure curve is linearized in the dry region at different effective water saturations.	90

6.12	(a) The capillary-pressure curve of the reference case scaled with the Leverett-J function using different intrinsic permeabilities with a linearized capillary pressure at an effective water saturation of 0.3. (b) Computed drying rates with no contrast and with a lower permeability in the right half of the domain. Three stages can be observed.	91
6.13	The mass fractions of vapor in the free flow (top) and the evolution of the water saturation (bottom) are shown after 0, 0.5, 2 and 10 days.	92
6.14	(a) Model setup and boundary conditions. (b) Evolution of temperature in the free flow and the porous medium. Only the upper part of the porous medium is shown.	92
6.15	Upper part of the simulated porous-medium domain. The arrows indicate the flow field of the water phase after 0.3 days. Water flows due to capillary forces from the coarse (right) into the fine material (left). Thus, the water saturation in the coarse material decreases faster. The highest velocities can be found at the top of the domain at the interface between the two materials.	93
6.16	(a) Evolution of mass fractions of vapor (top) and water saturation (bottom). (b) Heterogeneous distribution of the van-Genuchten α	94
6.17	Comparison of a measured drying curve with a simulation with a heterogeneous distribution of the <i>van-Genuchten</i> parameter α	94
6.18	Influence of the temperature in the porous medium on the computed drying rates.	96
6.19	Influence of different values for the thermal conductivity of the solid phase on the computed drying rates. A higher thermal conductivity provides a better energy supply due to heat conduction within the porous medium. This counteracts the cooling effect of evaporation and leads to higher vapor concentrations at the surface during stage-1 evaporation.	97
6.20	Semi-logarithmic velocity profile, scaled by the wall friction velocity for a fully developed pipe flow.	100
6.21	Foto of the experimental setup and two-dimensional model domain for the turbulent simulation.	102
6.22	Evaporation rate for different eddy thermal conductivity models.	102
6.23	(a) Influence of the relative humidity at the inflow on the computed drying rates. (b) Influence of a sinusoidal variation of atmospheric pressure with ± 3000 Pa	103
6.24	(a) Influence of the free air stream velocity on the computed drying rates. (b) Measured drying curves from a wind tunnel experiment.	104
6.25	Influence of the inflow air temperature on the computed drying rates.	104
6.26	(6.26a) Comparison of the computed drying rates for different <i>Beavers-Joseph</i> coefficients. (6.26b) Zoom to stage-1 of the evaporation process.	106

6.27	Pore-scale consideration of evaporation in the boundary layer with orderly flow parallel to the interface.	107
6.28	The relative evaporation rate k_m according to the Schlünder model with a constant boundary-layer thickness of 1.6 mm is depicted for different characteristic pore sizes.	108
6.29	(a) Comparison of the measured evaporation rate with computed drying curves using the Schlünder concept. b) Comparison of the measured evaporation rate and the computed drying curves using capillary-pressure curves which are linearized roughly at an effective saturation of 0.3.	110
6.30	Comparison of a drying curve from a wind tunnel experiment (Shahraeeni et al., 2012) with a computed drying with a lower free air stream velocity of 1.5 m/s leading to a lower atmospheric demand. Compared to the curve with 3.5 m/s, the decrease in stage-1 is less.	111
6.31	(a) Net radiation and latent heat flux (b) according to Novak (2010). (c) Computed net radiation and latent heat flux using the coupled model.	114

List of Tables

- 3.1 Soil parameters of the two quartz sands 28

- 5.1 Summary of the balance equations describing the different sub-models and listing of the according primary variables. 70
- 5.2 Interpretation of coupling conditions as boundary conditions in the perspective of the submodels. 72

- 6.1 Values of the reference case and considered parameter ranges. 84

Nomenclature

Greek		ϕ	porosity of the porous medium	[-]	
α_{BJ}	Beavers-Joseph coefficient	[-]	ψ	chemical potential	[-]
α_s	surface albedo	[-]	ϱ	density	[kg/m ³]
α_{stab}	stabilization parameter	[-]	ϱ_b	dry bulk density	[kg/m ³]
α	contact angle	[°]	ϱ_s	average density of the solid material	[kg/m ³]
ε_a	atmospheric emissivity	[-]	σ	surface tension	[N/m ²]
ε_s	surface emissivity	[-]	$\boldsymbol{\sigma}$	traction tensor	[N/m ²]
η_E	nodes of element E		σ_B	Boltzmann constant	[W/m ² K ⁴]
Γ	boundary of the model domain		τ	tortuosity	[-]
κ	Karman constant	[-]	$\boldsymbol{\tau}$	shear stress tensor	[N/m ²]
λ_α	thermal conductivity	[W/m K]	θ	volumetric moisture content	[-]
λ_{BC}	Brooks-Corey parameter	[-]	Latin		
λ_{dry}	effective thermal conductivity of dry soil	[W/m K]	A_g	contact area between free gas phase and the gas phase in the porous medium	[m ²]
λ_{sat}	effective thermal conductivity of water-saturated soil	[W/m K]	A_l	contact area between water filled pores and the gaseous free-flow region	[m ²]
λ_{pm}	effective thermal conductivity	[W/m K]	B_i	box	
μ	dynamic fluid viscosity	[kg m/s ²]	c	concentration	[kg/m ³]
$\tilde{\mu}$	apparent (Brinkman) viscosity	[kg m/s ²]	D	diffusion coefficient	[m ² /s]
Ω	model domain				

d	pore diameter	[m]	\mathbf{n}_f	unit outward normal of the respective subcontrol-volume face in direction of the neighboring node	[-]
E	element				
\mathbf{F}_m	mass flux	[kg/m ² s]	n	Reynolds number	[-]
\mathbf{F}_h	heat flux vector	[J/m s ²]	p	pressure	[Pa]
\mathbf{F}_v	matrix-valued momentum flux	[N/m ² s]	p_0	reference pressure	[Pa]
\mathbf{g}	gravity vector	[m/s ²]	p_c	capillary pressure	[Pa]
H	Henry coefficient	[Pa]	p_d	entry pressure	[Pa]
h	specific enthalpy	[J/kg]	$p_{\text{sat,Kelvin}}$	lowered saturated vapor pressure (Kelvin equation)	[Pa]
h_f	mesh width	[m]	Pr	Prandtl number	[-]
\mathbf{I}	identity tensor	[-]	p_{sat}	saturated vapor pressure	[Pa]
\mathbf{J}	Jacobi matrix	[-]	q	source or sink term	[kg/m ³ s]
\mathbf{K}	intrinsic permeability tensor	[m ²]	q_h	heat source	[J/m ³ s]
k	corresponding component of the porous-medium permeability	[-]	q_m	mass source or sink	[kg/m ³ s]
K_{ij}	harmonic mean of the intrinsic permeabilities of nodes i and j	[m ²]	\mathbf{R}	Residuum	[-]
k_m	saturation-dependent mass transfer coefficient	[-]	\mathbb{R}	universal gas constant	[J/mol K]
k_r	relative permeability	[-]	r_{char}	characteristic pore radius	[m]
M	molar mass	[kg/mol]	Re	Reynolds number	[-]
m	Reynolds number	[-]	R_l	individual gas constant of water vapor	[J/kg K]
Re	Reynolds number	[-]	R_n	net radiation	[W/m ²]
\mathbf{n}	normal vector	[-]	S	saturation	[-]
			Sc	Schmidt number	[-]

$s(i)$	subcontrol-volume face i of a box	N	Neumann
S_{irr}	solar irradiance	$[\text{W}/\text{m}^2]$	r residual
T	temperature	$[\text{K}]$	s solid phase
t	time	$[\text{s}]$	ups upstream node depending on the direction of the velocity
$\boldsymbol{\tau}$	shear stress tensor	$[\text{N}/\text{m}^2]$	
Superscripts			
\mathbf{t}_i	basis of the tangent plane of the interface Γ	$[-]$	a component air
u	specific internal energy	$[\text{J}/\text{kg}]$	ff free-flow subdomain
\hat{u}_i	solution at node i	$[-]$	κ component
\mathbf{v}	velocity vector	$[\text{m}/\text{s}]$	pm porous-medium subdomain
\mathbf{v}_i^k	subcontrol volume		w component water
V	volume	$[\text{m}^3]$	
X	mass fraction	$[-]$	
x	mole fraction	$[-]$	
x_f	integration points	$[-]$	

Subscripts

α	phase
D	Dirichlet
eff	effective
g	gas phase
i	node i
j	node j
l	liquid phase

Abstract

Exchange processes between fluid-filled porous media and an adjacent free flow occur in a wide range of natural and technical systems. In the course of these processes, the flow dynamics in the porous domain and in the free flow exhibit a strong interdependency, which is often controlled by mechanisms at the common interface. Understanding and modeling these interactions is decisive for diverse technical, medical and environmental applications. Prominent technical examples are the drying of products such as food, concrete or clothes. Further technical examples comprise landmine detection, industrial filtration processes, and the flow and transport processes in proton exchange membrane fuel cells (PEM-FC). A possible medical application is the exchange and transport of substances like therapeutic agents between blood vessels and tissue in the human body.

Evaporation from natural soils as an environmental example is an extremely important process, since it constitutes a dominant part of the terrestrial water and energy balance and is actively involved in a variety of climatic processes. On the one hand, evaporation processes are decisively influenced by the prevailing ambient conditions, such as flow velocity, temperature and air humidity, and, on the other hand, by the porous-medium system with its fluid and solid properties and flow dynamics. A good understanding of the ongoing processes and elaborate modeling tools are crucial for climate modeling and water resources management, particularly in arid regions. The main focus of this thesis is on this environmental application: the modeling and analysis of evaporation processes from porous media like bare soils or sands which are exposed to an adjacent free flow.

The objectives of this study are on one hand the development of a detailed coupled model which allows the simulation of a two-phase porous-medium system in conjunction with a single-phase free flow, and on the other hand to conduct a comprehensive analysis of the relevant processes for the mass, momentum and energy transfer of the two flow compartments. A major goal is to advance the development of an elaborate model for evaporation processes from porous media on the REV scale. This model has to take the mutual influence of the two flow compartments and the processes occurring at the common interface into account to allow for a detailed analysis of the influencing quantities. Theoretical and experimental evidence suggests that the interface between free flow and porous medium plays a crucial role for modeling evaporation processes on the REV scale.

Evaporation experiments in which a water-saturated porous medium (sand) was exposed to the air stream of a wind tunnel, were performed in cooperation with the Soil and Terrestrial

Environmental Physics (STEP) research group of Professor Dani Or at the ETH Zürich. The experimental data are presented and used as a basis and anchor in reality for the model development, giving important insights into the dynamics of drying processes, with the aim of capturing relevant processes and characteristics with the developed model concept. The physical basics and their representation in the REV-scale model are explained. Then, a coupling concept for two-phase porous-medium flow exposed to an adjacent free flow under non-isothermal conditions allowing for compositional effects is developed. It considers two composite subdomains with different sets of equations which are coupled by appropriate coupling conditions at the lower-dimensional interface. The coupling conditions ensure flux continuity across the common interface and are based on local mechanical, thermal, and chemical equilibria. The numerical implementation of the sub-models and the coupling concept into the modeling framework *DuMu^x* is elaborated and the employed discretization scheme described. For this purpose, one large matrix is assembled, which contains entries from both subdomains and the coupling conditions.

In a first step, the coupling concept is developed for laminar flow conditions in the free flow. Phenomenological explanations and model examples lend support to the developed concept, but also show its limitations and issues requiring suitable extensions and adaptations. When air flow above a porous medium is considered, turbulent conditions are likely to develop. This has a crucial impact on the flow field and the boundary layers for mass, momentum and energy, which critically influence the exchange fluxes between porous medium and free flow. Comparisons of simulated data with experimental drying curves with high atmospheric demand demonstrate, that a laminar free-flow model leads to an overestimation of the relevant boundary-layer thickness and thus to drying rates below the ones observed in the experiments. For this reason, a simple boundary-layer approximation is integrated, which approximates the diffusive vapor fluxes across the boundary layer according to the measured evaporation rates. In a further step, the coupled model is extended to turbulent flow conditions and an algebraic turbulence model is included. Both approaches, boundary layer approximation and turbulence model, lead to an improved quality of the model computations. The observed drying rates at the beginning of the evaporation process could be met.

An extensive parameter and process analysis with the coupled model sheds light on the influence of several processes and properties of the porous medium, the fluids, the flow field and the common interface. It shows that evaporation processes are affected by a multitude of influencing quantities in a complex manner. The influence of soil hydraulic properties, such as porosity and permeability, and parameters which quantify fluid-solid interactions, like the effective thermal conductivity and capillary pressure, on the evaporation dynamics is demonstrated. To this end, a reference case based on the wind-tunnel experiment is defined and single parameters are varied over a wide range. The capillary-pressure gradient close

to residual saturation is identified as having a crucial influence on the transition from the high drying rate in the externally-controlled and relatively high evaporation rate in stage-1 to the diffusion-dominated and considerably lower rate in stage-2 of an evaporation process. Further, the numerical investigations indicate that common parametrizations of the capillary-pressure / saturation relation, like the *Brooks-Corey* or the *van-Genuchten* model, overestimate the capillary pressure and relative permeability of water in the dry regime, resulting in a delayed transition from stage-1 to a lower rate in stage-2. Thus, the capillary-pressure curve is linearized and limited in the dry range. This adjustment results in an improved capture of the transition from stage-1 to stage-2. The significance of the capillary pressure and relative permeability for the drying dynamics is emphasized.

Drying experiments with relatively high evaporative demand have exhibited decreasing evaporation rates during stage-1, which is also often termed as “constant rate period”. These are caused by the complex interplay of evaporating pores or pore clusters and the boundary layer. However, geometrical information about evaporating pores is not readily available on the REV scale, and this effect can only be integrated in an averaged fashion in dependency of the surface water content. The simulation runs demonstrate that the use of a homogeneous distribution of the soil parameters without a further modification of the coupling conditions in the numerical simulations leads to relatively constant drying rates in stage-1. To include a representation of the surface-water dependency on the exchange fluxes, the model is extended by a mass-transfer coefficient obtained from pore-scale considerations. This coefficient scales the diffusive vapor fluxes across the boundary layer in dependency on surface moisture content and boundary-layer thickness based on the work presented in Haghghi et al. (2013) and Schlünder (1988). It is integrated and tested for its applicability in the REV-scale framework. Incorporation of this coefficient to scale the diffusive vapor fluxes at the interface improved the agreement between computed and experimentally measured evaporation rates during the transition from stage-1 to stage-2. Furthermore, solar radiation is integrated in the model concept and sample calculations are shown.

Zusammenfassung

Austauschprozesse zwischen fluidgefüllten porösen Medien und einer angrenzenden freien Fluidströmung treten in einer Vielzahl von natürlichen und technischen Systemen auf. Dabei weisen die Strömungs- und Transportprozesse im porösen Gebiet und in der freien Strömung eine starke Abhängigkeit voneinander auf, welche oft maßgeblich durch Mechanismen am gemeinsamen Interface gesteuert wird. Das Verständnis und die Modellierbarkeit der Interaktionen dieser zwei Fließkompartimente ist für verschiedene technische, medizinische und ökologische Anwendungen von großer Bedeutung. Beispiele hierfür finden sich unter anderem im industriellen Bereich, beispielsweise bei der Trocknung von Produkten wie Lebensmittel, Beton oder Kleidung, bei der Detektion von Landminen, bei industriellen Filtrationsprozessen und bei den Strömungs- und Transportvorgängen in einer Protonenaustauschmembran-Brennstoffzelle. Ein Beispiel aus dem medizinischen Bereich ist der Austausch und Transport von Substanzen zwischen Blutbahn und Gewebe.

Die Verdunstung aus natürlichen Böden als ökologisches Beispiel ist ein überaus wichtiger Prozess, weil er einen großen Teil des terrestrischen Wasser- und Energiekreislaufs ausmacht und aktiv an einer Vielzahl von klimatischen Prozessen beteiligt ist. Verdunstungsprozesse sind einerseits durch die vorherrschenden Umgebungsbedingungen wie Windgeschwindigkeit, Temperatur und Luftfeuchtigkeit beeinflusst, und andererseits durch das poröse Medium mit seinen Fluid- und Feststoffeigenschaften und der Fließdynamik innerhalb des porösen Mediums und am Interface zur Umgebung. Ein gutes Verständnis der ablaufenden Prozesse und geeignete Modellierungswerkzeuge sind wichtig für die Klimamodellierung und für das Wassermanagement, speziell in ariden Gebieten. Der Hauptfokus dieser Arbeit liegt auf einer Anwendung aus dem Umweltbereich, nämlich der Modellierung und Analyse von Verdunstungsprozessen aus porösen Medien wie zum Beispiel kahle Böden oder Sande, welche einer angrenzenden freien Strömung ausgesetzt sind. Verdunstungsprozesse weisen eine Vielzahl von komplexen Transportmechanismen und physikalischen und thermodynamischen Wechselwirkungen auf. Trotz der Bedeutung dieser Prozesse für zahlreiche natürliche und technische Anwendungen bleibt die Quantifizierung der Austauschflüsse von Masse, Impuls und Energie über das Interface zwischen dem porösen Medium und der freien Strömung eine Herausforderung.

Ziele dieser Doktorarbeit sind die Entwicklung eines detaillierten, gekoppelten Modells welches es ermöglicht, ein Gesamtsystem bestehend aus einem porösen Medium mit zwei Fluidphasen in Verbindung mit einer einphasigen freien Strömung zu simulieren, und eine umfangreiche Analyse der relevanten Prozesse für den Massen-, Impuls- und Energieaustausch der beiden

Kompartimente. Dabei ist ein Hauptaugenmerk auf der Entwicklung eines komplexen Modells für die detaillierte Beschreibung von Verdunstungsprozessen aus porösen Medien auf der REV Skala. Dieses Modell soll die wechselseitigen Einflüsse der beiden Fließkompartimente und die Prozesse, die am gemeinsamen Interface auftreten, berücksichtigen und wird für eine umfangreiche Analyse der Einflussgrößen verwendet. Theoretische und experimentelle Erkenntnisse deuten darauf hin, dass das Interface zwischen freier Strömung und porösem Medium eine entscheidende Rolle bei der Modellierung von Verdunstungsprozessen auf der REV Skala spielt.

Im Rahmen der Doktorarbeit wurden Verdunstungsexperimente, bei denen ein wassergesättigtes poröses Medium (Sand) einer Luftströmung ausgesetzt waren, in Zusammenarbeit mit der Soil and Terrestrial Environmental Physics (STEP) Forschungsgruppe von Professor Dani Or an der ETH Zürich durchgeführt. Die experimentellen Daten werden präsentiert und als Grundlage und als Realitätsanker für die Modellentwicklung verwendet. Sie geben wichtige Einblicke in die Dynamik von Trocknungsprozessen und dienen dazu, relevante Prozesse und Charakteristiken mit dem entwickelten Modellkonzept zu erfassen. Zuerst werden die physikalischen Grundlagen in den zwei Teilbereichen und ihre Darstellung auf der REV Skala (konzeptionelles Modell) erläutert. Dann wird ein Kopplungskonzept für eine Zweiphasenströmung im porösen Medium und einer anliegenden einphasigen freien Strömung entwickelt, welches auch die Zusammensetzung und Austauschprozesse der Fluide sowie nichtisotherme Effekte berücksichtigt. Es werden zwei zusammengesetzte Teilgebiete betrachtet, in denen unterschiedliche Gleichungssätze verwendet werden. Diese sind durch geeignete Kopplungsbedingungen an einem niederdimensionalen Interface gekoppelt. Die Kopplungsbedingungen stellen die Flusskontinuität über das gemeinsame Interface sicher und beruhen auf einem lokalen mechanischen, thermischen und chemischen Gleichgewicht. Die numerische Umsetzung der Teilmodelle und die Integration des Kopplungskonzepts am Interface in die Modellierungsumgebung *DuMu^x* wird beschrieben. Dabei wird eine große Matrix assembliert, die beide Gebiete sowie die Kopplungsbedingungen umfasst.

Zunächst wird das Kopplungsmodell für laminare Verhältnisse in der freien Strömung entwickelt und diskutiert. Phänomenologische Erklärungen und Modellbeispiele stützen das entwickelte Konzept, zeigen aber auch seine Grenzen und Probleme auf, die passende Erweiterungen und Anpassungen erfordern. Bei der Strömung von Luft über ein poröses Medium ist es wahrscheinlich, dass sich turbulente Fließbedingungen einstellen. Dies hat entscheidende Auswirkungen auf das Strömungsfeld und die Grenzschichten für Masse, Geschwindigkeit und Temperatur, welche einen großen Einfluss auf die Austauschprozesse zwischen porösem Medium und freier Strömung haben. Vergleiche simulierter Daten mit experimentellen Trocknungskurven zeigen, dass eine laminares Freiströmungsmodell zu einer Überschätzung der Grenzschichtdicken und dadurch zu Trocknungsraten weit unter den in den Experimenten gemessenen führt. Daher

wird zunächst eine einfache Grenzschichtapproximation eingebaut, welche die diffusiven Flüsse über die Grenzschicht entsprechend den gemessenen Verdunstungsraten approximiert. In einem weiteren Schritt wird das Kopplungsmodell auf turbulente Fließbedingungen in der freien Strömung erweitert. Für die Modellierung von turbulenten Fließbedingungen kommt ein einfaches algebraisches Turbulenzmodell zum Einsatz. Beide Ansätze, Grenzschichtapproximation und Turbulenzmodell, verbessern die Qualität der Modellberechnungen deutlich. Die beobachteten Trocknungsraten zu Beginn des Trocknungsprozesses können damit besser getroffen werden.

Eine umfangreiche Parameter- und Prozessstudie mit dem gekoppelten Modell gibt Aufschluss über den Einfluss verschiedener Prozesse und Eigenschaften des porösen Mediums, der Fluide, des Strömungsfeldes und des Interfaces auf die Verdunstungsdynamik. Sie belegt, dass Verdunstungsprozesse von einer Vielzahl an Einflussgrößen in komplexer Weise beeinflusst werden. Der Einfluss hydraulischer Bodeneigenschaften wie Porosität und Permeabilität, und von Parametern, welche die Interaktionen zwischen den Fluiden und dem Feststoff quantifizieren, wie die effektive thermische Leitfähigkeit und der Kapillardruck, auf die Verdunstungsrate wird gezeigt. Dafür wird ein Referenzfall auf Grundlage der Windkanal-Experimente definiert und einzelne Parameter über einen großen Wertebereich variiert. In der Studie wurde ein großer Einfluss des Kapillardruckgradienten in der Nähe der Residualsättigung auf den Übergang von der extern-kontrollierten und relativ hohen Verdunstungsphase 1 (Stage-1), in der die flüssige Phase am Interface vorhanden ist, zur Phase 2 (Stage-2) eines Verdunstungsprozesses, in der der Transport durch Dampfdiffusion durch den Porenraum dominiert, festgestellt. Darüber hinaus deuten die numerischen Untersuchungen darauf hin, dass gängige Parametrisierungen der Kapillardrucks-Sättigungsbeziehung, wie das van-Genuchten oder Brooks-Corey Modell, den Kapillardruck und die relative Permeabilität der flüssigen Phase im trockenen Bereich der Kurve überschätzen, was zu einem verzögerten Übergang von der hohen Verdunstungsrate in Stage-1 zu einer niedrigeren Rate in Stage-2 führen. Deshalb wurde die Kapillardruckkurve linearisiert und im trockenen Bereich beschränkt. Mit dieser Anpassung kann der Übergang von Stage-1 zu Stage-2 besser getroffen werden. Dies betont auch die Bedeutung des Kapillardrucks und der relativen Permeabilität für die Trocknungsdynamik.

Manche Trocknungsexperimente mit relativ hohem Verdunstungsbedarf weisen fallende Verdunstungsraten bereits während der ersten Verdunstungsphase auf, welche oft auch als “constant rate period”, also Phase der konstanten Verdunstungsrate bezeichnet wird. Diese fallenden Verdunstungsraten werden durch das komplexe Zusammenspiel von verdunstenden Poren oder Porenclustern und der Grenzschicht verursacht. Die geometrische Information über aktiv verdunstende Poren ist auf der REV Skala nicht ohne Weiteres verfügbar. Der zuvor beschriebene Effekt kann nur in einer gemittelten Weise in Abhängigkeit des Wassergehalts an der Oberfläche im REV-skaligen Modell berücksichtigt werden. Die durchgeführten Simulationen zeigen, dass eine homogene Verteilung der Bodenparameter ohne weitere Anpassung der Kopplungsbe-

dingungen in den numerischen Simulationen immer zu relativ konstanten Trocknungsraten während der ersten Verdunstungsphase und einem relativ abrupten Übergang zur zweiten Verdunstungsphase führt. Um eine Repräsentation der Abhängigkeit der Oberflächenfeuchte auf die Austauschflüsse einzubeziehen wird das Modell um einen Massentransferkoeffizienten erweitert, welcher von porenskaligen Betrachtungen herrührt. Dieser Koeffizient skaliert die diffusiven Dampf Flüsse in Abhängigkeit des Oberflächenwassergehalts und der Grenzschichtdicke, basierend auf den Arbeiten von Haghghi et al. (2013) und Schlünder (1988). Er wird in das Kopplungskonzept integriert und auf seine Anwendbarkeit auf der REV Skala hin geprüft. Die Einarbeitung dieses Koeffizienten für die Skalierung der diffusiven Dampf Flüsse am Interface verbessert die Übereinstimmung von simulierten und experimentell gemessenen Verdunstungsraten während des Übergangs von Stage-1 zu Stage-2. Des Weiteren wird die Berücksichtigung solarer Einstrahlung behandelt sowie ein Konzept für die Integration in das gekoppelte Modell und Beispielrechnungen vorgestellt.

1 Introduction

Exchange processes between porous media and free flow occur in a wide range of natural and technical systems. In the course of these processes, the flow dynamics in the porous domain and in the free flow exhibit a strong interdependency, which is often controlled by mechanisms at the common interface. Modeling and understanding these interactions is decisive for diverse technical, medical and environmental applications. Prominent technical examples are the drying of products such as food (Maroulis et al., 1995), concrete (Defraeye et al., 2012b) or clothes. Further technical examples comprise landmine detection (Smits et al., 2013), industrial filtration processes, and the flow processes between the gas distributor and membrane (Gurau and Mann, 2009) of proton exchange membrane fuel cells (PEM-FC). A possible medical application is the exchange and transport of substances like therapeutic agents between blood vessels and tissue in the human body (Erbertseder et al., 2012).

Evaporation from soils is an extremely important process, since it constitutes a dominant part of the terrestrial water and energy balance and is actively involved in a variety of climatic processes. On the one hand, evaporation processes are decisively influenced by the prevailing ambient conditions, such as flow velocity, temperature and air humidity, and, on the other hand, by the porous-medium system with its fluid and solid properties and flow dynamics. A good understanding of the ongoing processes and elaborate modeling tools are crucial for climate modeling and water resources management, particularly in arid regions. The main focus of this thesis is on this environmental application: the modeling and analysis of evaporation processes from porous media like bare soils or sands which are exposed to an adjacent free flow.

1.1 Challenge and motivation

Evaporation from porous media into an adjacent free flow involves a multitude of complex transport mechanisms and physical and thermodynamic interactions, as illustrated in Figure 1.1. Despite the significance of this process for many natural and technical applications, the quantification and prediction of the exchange fluxes of mass, momentum and energy between a porous medium and the adjacent free flow remains a challenge. This is due to the complexity

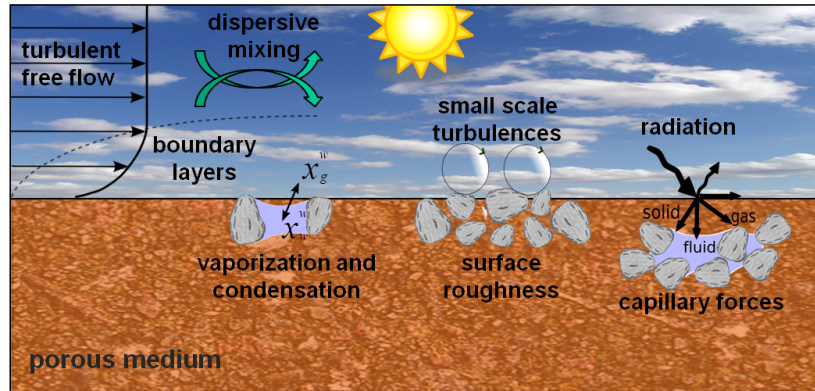


Figure 1.1: Complex interactions of evaporation processes from porous media.

of the interactions between the porous-medium system where the internal exchange and transport mechanisms reveal rich dynamics and the soil properties are usually uncertain and heterogeneous, and the free-flow system with its variable ambient conditions of, for example, air humidity, pressure, temperature and possibly turbulent flow behavior, and which may involve external processes like radiation.

For the modeling of free flow and the porous-medium flow, elaborate model concepts have been developed. Most state-of-the-art evaporation models consider either the free flow (climate modeling) or the porous-medium flow (soil physics, hydromechanics) in a decoupled fashion, requiring the specification of exchange fluxes as boundary conditions. The models employed in the subdomains are usually simplified, and often several processes are lumped together to empirical fitting parameters. This makes it difficult to analyze the mutual influence of the two domains and may lead to false predictions. The processes in both flow compartments and particularly those occurring at the interface between free flow and porous medium may form a bottleneck for the exchange fluxes. Moreover, the interface between the two domains reveals a complex coupling; thus, a coupled model is a highly beneficial tool for the consideration of such systems.

One major objective of this thesis is to develop a detailed, physically based model concept on the scale of representative elementary volumes (REV) that allows the detailed description of a two-phase multi-component porous-medium system coupled to a multi-component single-phase free flow under non-isothermal conditions. A special focus is on the applicability to evaporation processes from soils influenced by atmospheric processes like wind and radiation. The coupling concept aims at describing the processes at the transition of free flow and porous medium with a simple and solvable model that is based on phenomenological explanations and existing modeling approaches.

For the analysis and interpretation of the influencing quantities and processes and for a

comparison of the developed models with measured data, a series of drying experiments in a wind tunnel was conducted at the research facilities of the ETH Zürich in cooperation with Professor Dani Or. The experimental setup with measured parameter values serves as the reference case for a broad parameter study and allows the discussion of the model output in the context of realistic data. Furthermore, model extensions and special conditions accounting for complex processes at the interface, like the dependency of the evaporative fluxes on the surface water content, are integrated and tested for their capabilities. The developed model concept is employed to shed a light on the variety of influencing quantities and to interpret their impact on the evaporation process. Moreover, the detailed model is a valuable tool for gaining a better understanding of the validity limits of current state-of-the-art models and their simplifications, and to bridge the gap in cases where state-of-the-art models fail.

1.2 Structure of the thesis

The thesis is structured as follows: Chapter 2 provides the relevant definitions and the physical foundation of coupled porous-medium and free-flow systems. The physical properties of porous media and of the fluids considered, namely water and air, are introduced. Then, Chapter 3 describes the setup and realization of laboratory drying experiments in a wind tunnel at the research facilities at the ETH Zürich. Subsequently, Chapter 4 presents the conceptual model for coupled single-phase free flow and two-phase porous-medium flow with a detailed description of the models in the free flow and in the porous medium. In Chapter 5, the integration of the coupling concept into the numerical modeling framework *DuMu^x* including the description of the numerical scheme is explained. Then, in Chapter 6, three model combinations for evaporation processes are introduced and employed to study the effects of various quantities and processes: a porous-medium model coupled to a laminar free-flow model, to a simple boundary-layer model, and finally to a Reynolds-averaged turbulence model which uses algebraic expressions to account for the turbulent flow behavior. These model combinations are employed to evaluate the influence of different parameters and processes on the computed drying rates. Furthermore, the dependency of the exchange fluxes on various parameters and processes, such as radiation or the surface moisture content, is examined and the possible impact of small-scale heterogeneities is discussed. The analysis stresses the importance of the interface properties, boundary layers and the flow conditions on the transfer fluxes. Finally, Chapter 7 summarizes the thesis and gives an outlook on issues which could not be covered here and should be the subject of future work.

2 Fundamentals

This chapter deals with fundamental physical processes and material properties, which appear in the context of the concepts and the analysis of evaporation processes from porous media exposed to free flow presented in this work. First, the spatial scales, on which the occurring processes are considered, are and some expressions are made (Section 2.1). Quantities arising from volume averaging of the balance equations, like saturation and permeability, are briefly explained. These are prerequisites for the development and explanation of the conceptual model and the description of processes in a later part of the document. In Section 2.2, the physical properties of water and air and of porous media are explained. Section 2.3 provides the general conservation laws for mass, momentum and energy which form the basic framework for the model concepts in the porous-medium and the free-flow domain. The last section (Section 2.4) introduces several physical processes relevant in the context of this study.

2.1 Terms and definitions

2.1.1 Scales

Flow phenomena in porous media and in free flows can be considered on different *scales*. Examples thereof are the molecular scale, the pore scale, the REV scale (Bear, 1988) and the

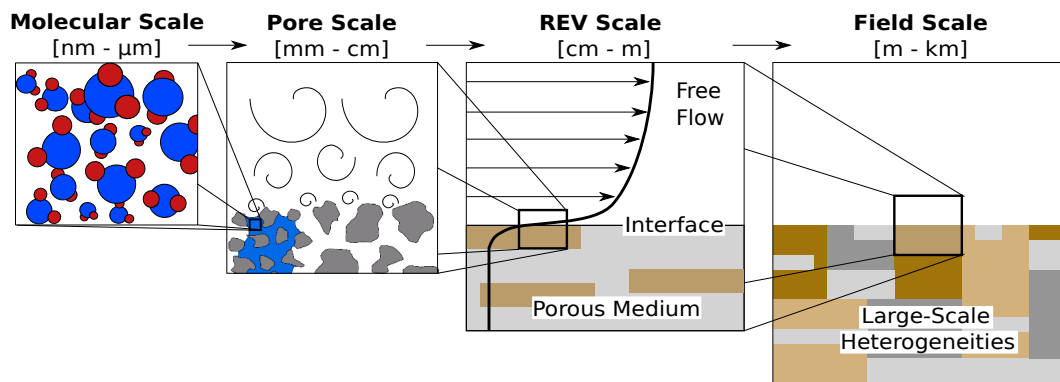


Figure 2.1: Different scales: Molecular scale, pore scale, REV scale and field scale.

field scale (or plot scale), as depicted in Figure 2.1. The *molecular scale* has its focus on the intermolecular processes, namely the motion and collisions of molecules in the fluid phases. This scale is particularly useful for the determination of chemical and physical fluid properties. An averaging of the molecular scale over a certain volume results in new quantities like density, pressure or temperature. These parameters are used on the *continuum scale* where they are continuously defined in space.

On the *pore scale*, the phase interfaces and the phase distribution spatially resolved with measurement technology like x-ray or neutron tomography (Shokri et al., 2008; Shahraeeni and Or, 2012). The technology for this has been advancing fast in the last decades. This allows more and more detailed scans with a higher spatial and temporal resolution (Wildenschild and Sheppard, 2013), which provide important insights. Besides artificially generated geometries, the scans can be used as input for pore-scale models which compute, for example, the flow field and transport phenomena in the pore space.

However, many practical applications with a larger extent require models with quantities averaged over so-called *representative elementary volumes* (REV). The respective scale, on which this work focuses, is called *REV scale*. The size of an REV cannot be chosen arbitrarily but has to be in a range where an increase or decrease of the averaging volume would lead to the same value for the averaged quantity (Bear, 1988). The lower bound is given by the microscopic variability, which leads to strong fluctuations of the averaged quantities, if the averaging volume is chosen too small. The upper bound is usually relevant for inhomogeneous porous media where an enlargement of the REV would lead to a too low resolution of the considered structures and, thus, the macroscopic heterogeneities would strongly influence the resulting averaged quantities.

The REV scale can be subdivided into the laboratory scale of single meters or less, whereas larger applications happen on a scale in the order of tens of meters to kilometers, which is referred to as *field scale*. The scale of the model concept is usually chosen in dependency on the spatial extend of the considered application and on the problem at hand. Naturally, processes from smaller scales have to be properly accounted for in larger-scale models. For this purpose, averaged or effective quantities are employed, which come usually along with an information loss about the distribution within the averaging volume. REV-scale models with different complexity are widely used for practical applications in porous-medium modeling, such as the simulation of CO₂ sequestration (Class et al., 2009), oil production, subsurface remediation (Ochs et al., 2010), for groundwater modeling or product optimization.

2.1.2 Phase

Since fluid flow in porous-medium and free-flow systems is considered, the terms fluid phase and component are introduced first. A *phase* α is a pure substance or a mixture of substances in the same physical state (solid, liquid or gaseous) with relatively uniform properties and composition. On the continuum scale, the physical state of a phase is characterized by its thermodynamic state variables, such as pressure, density or temperature. The number of coexisting phases is limited: several liquid and solid phases may coexist, but only a single gaseous phase is possible. Multiple phases are separated from each other by distinct interfaces. For evaporation processes, two fluid phases are usually considered: a gaseous air phase and a liquid water phase, hereinafter marked with the subscripts l (liquid water) and g (gaseous air).

2.1.3 Component

A *component* κ is a chemical substance, which is a chemical constituent of a phase. The components which are considered here are water (superscript w), which may exist in the liquid state or gaseous state as vapor (the solid state is not considered here), and the pseudo-component air (superscript a), which is not a pure substance but a mixture of different components. However, except for the vapor content, the composition of this pseudo-component is assumed to remain constant in the considered system, thus it is treated as being one component. Phases may exchange their components by processes like vaporization, condensation, dissolution or degassing, as schematically shown in Figure 2.2.

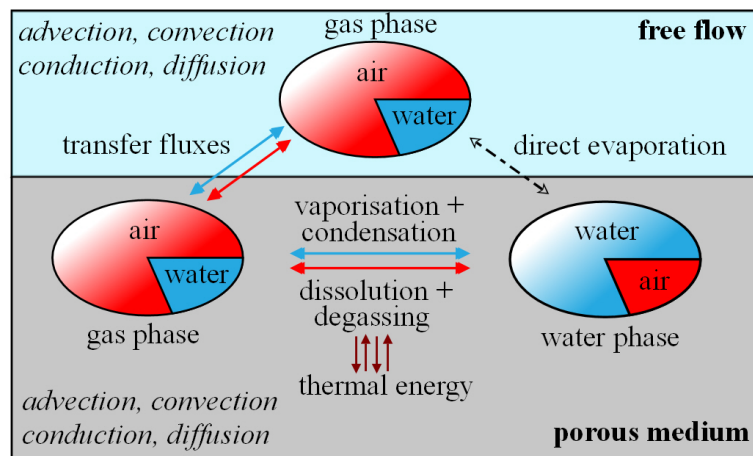


Figure 2.2: Schematics of the considered fluid phases and components with exchange processes.

2.1.4 Interface

Interfaces on different scales are involved in the context of evaporation processes from porous media. In this thesis, three different kinds of interfaces occur, namely

- the fluid-fluid and fluid-solid interfaces between different phases,
- the interfaces between porous media with different properties (heterogeneities),
- the interfaces between free flow and interface.

The term *interface* refers usually to the interface between porous medium and free flow throughout this thesis, if not stated differently. Physically, this interface is a thin transition zone.

2.1.5 Quantities arising from volume-averaging

Flow processes on the REV scale are described involving volume-averaged quantities. The equations used on the REV scale are often empirically determined or derived using the method of volume averaging (Whitaker, 1986a,b; Hassanizadeh and Gray, 1990; Gray et al., 1993; Gray and Miller, 2005; Jackson et al., 2009) or the homogenization methodology (Szymkiewicz et al., 2012). On this scale, phase interfaces and detailed geometric information are not resolved anymore, but their influence is accounted for by using quantities originating from the volume-averaging. Some of these averaged quantities will be described in the following lines.

Porosity

When the detailed pore structure of a porous medium is not resolved anymore, the *porosity* quantifies the volume fraction of the pore space that can be occupied by fluids (Bear, 1988; Nield and Bejan, 2006):

$$\phi = \frac{V_{\text{void space}}}{V_{\text{REV}}}. \quad (2.1)$$

Saturation

The pore space can be filled with different fluid phases α . Then, the phase *saturation* S_α gives the volume fraction occupied by a phase in the void space of an REV:

$$S_\alpha = \frac{V_\alpha}{V_{\text{void space}}}. \quad (2.2)$$

The sum of all fluid saturations has to equal unity:

$$\sum_{\alpha} S_\alpha = 1. \quad (2.3)$$

For unsaturated flow in soils, the volumetric moisture content θ_α is often used instead of the saturation (Bear, 1988):

$$\theta_l = \phi S_l. \quad (2.4)$$

It quantifies the volume fraction of the entire REV which is occupied by the water phase and is linked to the water saturation via the porosity.

Mass fraction, mole fraction and concentration

The composition of a phase is usually described by *mass fractions* X_α^κ , *mole fractions* x_α^κ or *concentrations* c_α^κ , which quantify the share of a component in a phase. These three quantities can be easily converted into each other with the help of the fluid density and the molar masses. The mass fraction can be computed from the mole fraction as

$$X_\alpha^\kappa = \frac{x_\alpha^\kappa M^\kappa}{\sum_{\kappa} x_\alpha^\kappa M^\kappa} = \frac{x_\alpha^\kappa M^\kappa}{\bar{M}_\alpha} \quad (2.5)$$

where M^κ is the molar mass of the component and $\bar{M}_\alpha = \sum_{\kappa} x_\alpha^\kappa M^\kappa$ is the average molar mass of the phase. Furthermore, the sum of mass or mole fractions of all components in one phase is always one:

$$\sum_{\kappa} X_\alpha^\kappa = \sum_{\kappa} x_\alpha^\kappa = 1. \quad (2.6)$$

The mass concentration can be seen as partial density (mass of the component per volume):

$$c_\alpha^\kappa = \rho_\alpha X_\alpha^\kappa. \quad (2.7)$$

Darcy velocity

A prominent equation widely used for the modeling of flow in porous media on the REV scale is *Darcy's law*, which gives a relation between gradient of the piezometric height and the average flow velocity. Instead of solving the momentum balance, Darcy's law can be inserted in the mass balance equation. In its original form, it was obtained empirically for a single-phase system (Darcy, 1856):

$$\mathbf{v} = -\mathbf{K}_0 \nabla h \quad (2.8)$$

where the piezometric height is defined as $h = \frac{p}{\rho g} + z$ and \mathbf{K}_0 is the hydraulic conductivity tensor, defined as a combined parameter of the intrinsic permeability, fluid properties and the gravity vector:

$$\mathbf{K}_0 = \mathbf{K} \frac{\rho \mathbf{g}}{\mu}. \quad (2.9)$$

Darcy's law has been generalized for multiple fluid phases (Scheidegger, 1974; Helmig, 1997) by introducing saturation-dependent relative permeabilities $k_{r\alpha}$, which take the nonlinear viscous resistance of one phase onto the other into account. Darcy's law is based on the potential theory and expresses the average phase velocity \mathbf{v}_α as function of the potential gradient. It reads:

$$\mathbf{v}_\alpha = -\frac{k_{r\alpha}}{\mu_\alpha} \mathbf{K} (\nabla p_\alpha - \rho_\alpha \mathbf{g}) \quad (2.10)$$

where μ_α are the dynamic phase viscosities, \mathbf{g} is the gravity vector, \mathbf{K} is the intrinsic permeability tensor of the porous medium, and p_α are the phase pressures.

For the validity of Darcy's law, the pore Reynolds number ($Re_p = \frac{\mathbf{v}d}{\nu_\alpha}$) with the pore diameter d should not exceed unity, or a nonlinear drag may become important (Nield and Bejan, 2006). In such cases the Forchheimer equation is an option, which includes an additional nonlinear term in the balance equation. For further details about Darcy's law be referred to standard textbooks about porous-medium flow, such as Jury and Horton (2004); Helmig (1997); Bear (1988). The derivation of Darcy's law with the method of volume-averaging is presented for single-phase flow in Whitaker (1986a), and for two-phase flow in Whitaker (1986b) and Hassanizadeh (1986).

Capillary pressure

On the pore scale, the capillary pressure p_c quantifies the pressure difference between two fluid phases across the usually curved phase interface, as illustrated in Figure 2.3. Capillarity is related to the surface tension and the curvature of the phase interface and is caused by adhesive and cohesive forces on the molecular scale. On the pore scale it can be quantified with the Young-Laplace equation as

$$p_c = \sigma \left(\frac{1}{r_x} + \frac{1}{r_y} \right) \approx \frac{4\sigma \cos \alpha}{d}, \quad (2.11)$$

with the surface tension σ , the pore radius r and diameter d . The contact angle α distinguishes the wetting ($\alpha < 90^\circ$) and the non-wetting fluid ($\alpha > 90^\circ$). In this thesis, the liquid water phase is considered as the wetting fluid and the gaseous air phase as non-wetting fluid within a hydrophilic porous medium. For hydrophobic porous media, this is reversed.

On the REV scale, a volume-averaged capillary pressure is considered, which is also defined as difference between the pressure of the wetting phase (water) and the non-wetting phase (air):

$$p_c = p_g - p_l. \quad (2.12)$$

It is usually parametrized as nonlinear function of the phase saturation. Examples of such parametrizations are the *Brooks-Corey* and the *van-Genuchten* model. The Brooks-Corey law (Brooks and Corey, 1964) is defined as

$$S_{\text{eff}}(p_c) = S_{\text{eff}} = \frac{S_l - S_{lr}}{1 - S_{lr}} = \left(\frac{p_d}{p_c} \right)^\lambda \quad (2.13)$$

where p_d designates the entry pressure, S_{eff} the effective saturation, S_{lr} the residual liquid phase saturation and λ the Brooks-Corey parameter. The *van-Genuchten* model (van Genuchten,

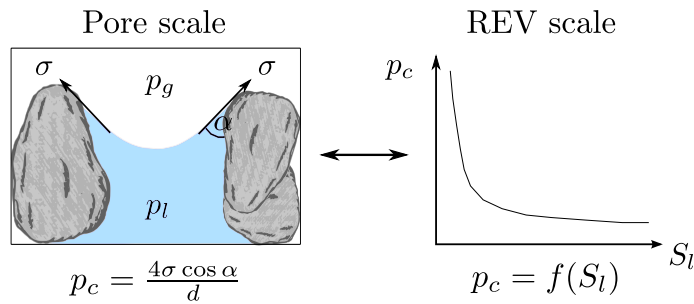


Figure 2.3: Capillary pressure on the pore and REV scale.

1980) approximates the capillary pressure as follows:

$$S_{\text{eff}}(p_c) = (1 + (\alpha_{\text{VgN}} p_c)^n)^m, \quad (2.14)$$

with the dimensionless *van-Genuchten* parameters m and n and the parameter α_{VgN} , which is related to the entry pressure.

Intrinsic permeability and relative permeability

Originating from Darcy's law, the *intrinsic permeability* tensor \mathbf{K} is a measure for the effective resistance of the porous medium against the flow of a fluid phase. It is usually empirically determined and a pure soil property.

The influence of the viscous resistance of one phase onto the flow of a different fluid phase in a porous medium is commonly accounted for by the *relative permeability* $k_{r\alpha}$. It is usually parametrized as nonlinear function of the water saturation and is in the range of zero to one. Therefore, parametrizations like *van Genuchten* or *Brooks-Corey* are employed in conjunction with the models proposed in Burdine (1953) and Mualem (1976).

In the *Brooks-Corey* model, the relative permeability is obtained using the *Burdine* approach:

$$k_{rw} = S_{\text{eff}}^{\left(\frac{2+3\lambda}{\lambda}\right)}, \quad (2.15a)$$

$$k_{rn} = (1 - S_{\text{eff}})^2 + 1 - S_{\text{eff}}^{\left(\frac{2+\lambda}{\lambda}\right)} \quad (2.15b)$$

where λ_{BC} is the *Brooks-Corey* parameter that has to be determined experimentally.

The *van Genuchten* model can be used in combination with the *Mualem* model to obtain the relative permeability as follows:

$$k_{rw} = S_{\text{eff}}^\epsilon \left(1 - \left(1 - S_{\text{eff}}^{1/m}\right)^m\right)^2, \quad (2.16a)$$

$$k_{rn} = (1 - S_{\text{eff}})^\gamma \left(1 - S_{\text{eff}}^{1/m}\right)^{2m} \quad (2.16b)$$

where m is a *van-Genuchten* parameter that has to be determined experimentally. The two parameters γ and ϵ which appear only in the relative permeability and not in the capillary-pressure function according to *van Genuchten* are related to the connectivity of the pores. They allow to change the shape of the relative-permeability curve independently of the capillary-pressure curve.

Both, the capillary pressure and the relative permeability may show a hysteretic behavior, meaning that their value does not only depend on the saturation but also on the history of

previous displacement process in the considered system. However, in this study, hysteresis is not considered. The porous-medium systems are assumed to be initially water-saturated. Then, the evaporation process can be seen as a primary drainage of the system.

2.2 Material properties

In the scope of this thesis, the focus is on a liquid water phase and a gaseous air phase in a porous medium, such as a sand. After clarifying the meaning of some physical and thermodynamic quantities occurring in this context, the properties of the water phase and the air phase are presented.

2.2.1 Liquid phase: water

Water is a fluid with unique properties. Some of these properties will be explained in the following. Depending on the ambient conditions like pressure and temperature, water can exist in different aggregation states: solid (ice), liquid (water) or gaseous (vapor). At standard ambient temperature and pressure conditions ($T = 298.15 \text{ K}$, $p = 10^5 \text{ Pa}$), water is liquid and has a density of approximately 1000 kg/m^3 with a low compressibility. The highest density occurs at 4°C and below 0°C solid ice is formed. The viscosity μ_α of a fluid describes the internal resistance towards motion. The liquid density and viscosity of pure liquid water in dependency on temperature for a constant pressure of 10^5 Pa are depicted in Figure 2.4. Dissolved substances like salt may change the fluid properties of water like its density or viscosity. However, only little amounts of air dissolve in the water phase, having a negligible influence. Thus, the dissolved air is not described further, but accounted for in the model concept (Chapter 4).

2.2.2 Gaseous phase: air

The air phase, which is the considered gaseous phase, is a composition of several substances. Its main components are nitrogen ($\approx 78 \text{ Vol.-%}$), oxygen ($\approx 21 \text{ Vol.-%}$), argon ($\approx 1 \text{ Vol.-%}$), carbon dioxide ($\approx 0.04 \text{ Vol.-%}$), vapor and several other trace gases. All components except vapor are considered as one pseudo-component, as mentioned above. Except vapor, the individual constituents of air are not distinguished because the main focus is on vapor transport; it is further assumed that the composition remains relatively constant.

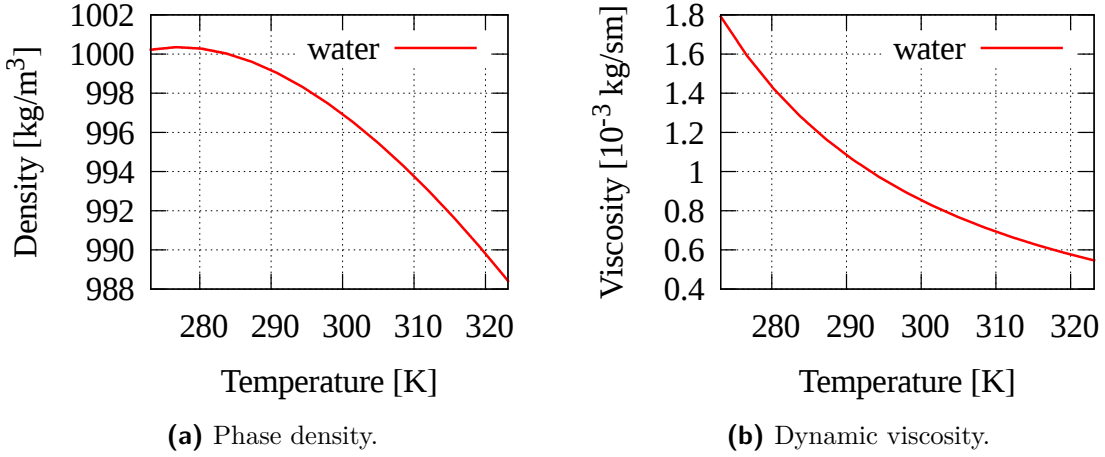


Figure 2.4: Density and viscosity of water in dependency on temperature (0 °C to 50 °C).

The gas phase is assumed to be an ideal gas throughout this thesis. Thus, the ideal gas law can be applied, which gives a relationship between density, pressure and temperature:

$$\rho = \frac{p\bar{M}}{\mathbb{R}T}. \quad (2.17)$$

with $\bar{M} = \sum_{\kappa} (x^{\kappa} M^{\kappa})$. At standard ambient pressure and temperature conditions, the viscosity of air is roughly two orders of magnitude smaller than the viscosity of water. The phase density is considerably smaller as the water phase density. The temperature-dependency of density and viscosity is depicted for a temperature range between 0 °C to 50 °C in Figure 2.5. Only a narrow pressure range is considered in this thesis, subsequently the pressure-dependency of the parameters is not depicted.

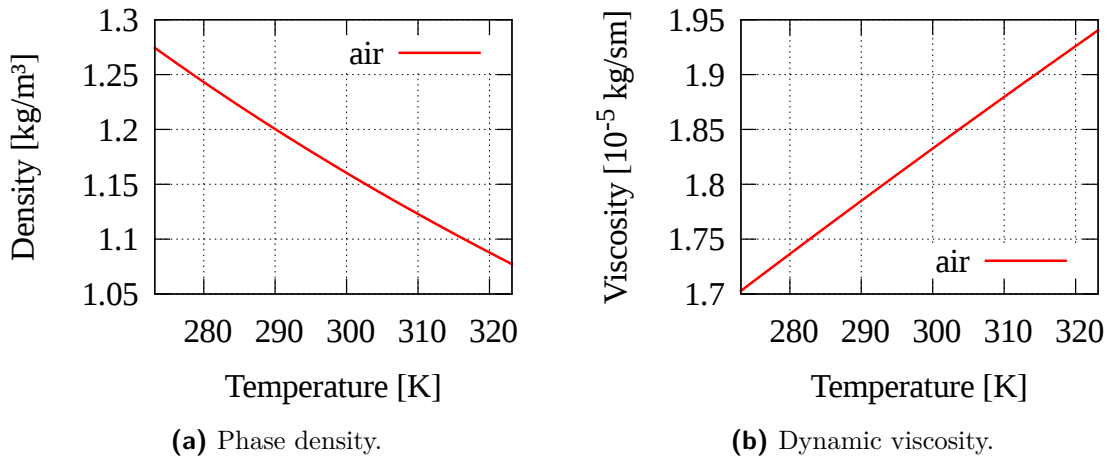


Figure 2.5: Density and viscosity of air in dependency on temperature (0 °C to 50 °C) with a mass fraction of vapor of 10^{-3} and a constant pressure of 10^5 Pa.

Partial pressure and Dalton's laws

The pressure is exerted by a component in the gas phase is expressed by its partial pressure p_g^κ . The partial pressure is proportional to the mole fraction of the component:

$$p_g^w = x_g^w p_g. \quad (2.18)$$

This can be exploited to calculate the mole fraction of each component, if one partial pressure (like in case of chemical equilibrium the saturated vapor pressure) is known. Dalton's law states, that the sum of the partial pressures of all components is equal to the gas phase pressure:

$$\sum_{\kappa} p_g^\kappa = p_g. \quad (2.19)$$

Saturated vapor pressure

When a liquid and a gaseous phase coexist, the two phases may be in a chemical equilibrium. Then, the saturated vapor pressure, also called equilibrium vapor pressure (Ho, 2006), quantifies the partial pressure that the vapor of the main liquid component exerts in the gaseous phase. The saturated vapor pressure of water increases considerably with temperature. Figure 2.6a shows the saturated vapor pressure curve of water for a temperature range between 0 °C and 50 °C. Moreover, high capillary pressures lead to a change of the saturated vapor pressure. This influence can be captured with the Kelvin equation (Class, 2009):

$$p_{\text{sat,Kelvin}}^w = p_{\text{sat}}^w \exp\left(-\frac{p_c}{\rho_l R_l T}\right), \quad (2.20)$$

with the individual gas constant $R_l = \mathbb{R}/\overline{M}_l$ Graph 2.6b demonstrates, that the effect of the vapor pressure lowering due to capillary pressure is less than 4 Pa in a capillary-pressure range of 2×10^5 Pa. Thus, it is not considered further. When the saturated vapor pressure is exceeded, vapor is transformed to liquid water. This mechanism is also responsible for the development of fog.

When a gaseous phase and a liquid phase are in equilibrium, the equilibrium mole fraction can be calculated as

$$x_g^w = p_{\text{sat}}^w / p_g. \quad (2.21)$$

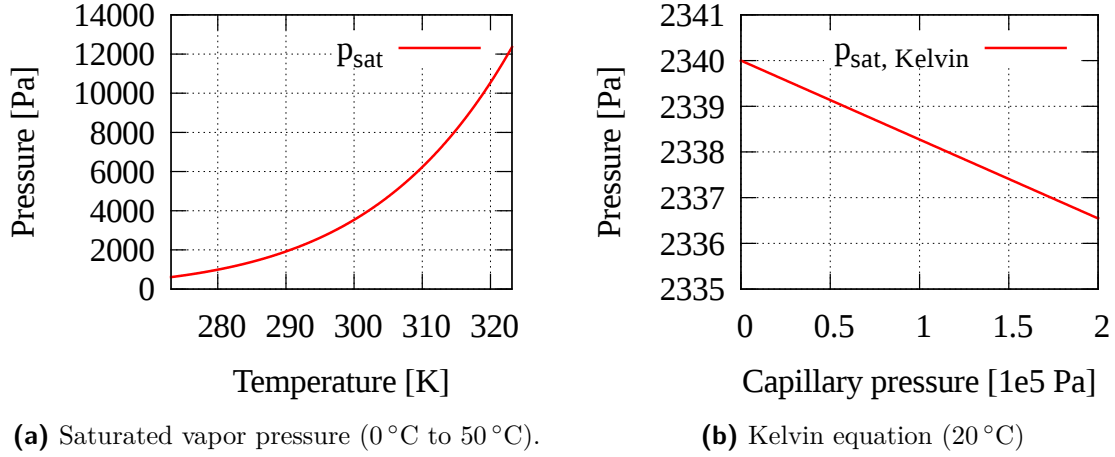


Figure 2.6: Saturated vapor pressure as function of temperature (0 °C to 50 °C). Saturated pressure lowering according to the Kelvin equation at a temperature of 20 °C.

Relative humidity

The relative humidity RH is defined as the ratio between the vapor pressure in the gas phase and the saturated vapor pressure at the prevailing temperature:

$$RH = \frac{p_g^w}{p_{\text{sat}}^w(T)}.$$

Internal energy and enthalpy

The internal energy U quantifies the total intrinsic energy of a thermodynamic system and is an extensive system property, which depends on the extend of the considered system. Its constituents are the internal kinetic energy of particle motion (also called thermal energy) and the potential energy which includes other forms of energy like chemical and nuclear energy (Incropera et al., 2007b). Thermal energy can be further subdivided in sensible heat, which can be quantified with the temperature, and latent heat, which is associated with phase changes like vaporization.

For practical purposes, the specific internal energy is mostly used, which is an intensive quantity independent of the considered system size. It is defined as $u = U/m$. If additionally the volume changing work is considered, the total energy of the system is called enthalpy $H = U + pV$. This is again an extensive quantity which can be converted to an intensive one by dividing by the mass: $h = H/m = u + p/\rho$. In the context of this work, the specific quantities are used and the fluid phases are considered as thermodynamic systems. The internal energy and the enthalpy are then formulated as functions of pressure, temperature and composition.

For the water phase, the volume changing work is relatively small due to its low compressibility. Thus, the internal energy and the phase enthalpy are almost identical. The enthalpy of the gaseous phase is composed of contributions of the components. For such a multi-component system, the phase enthalpy can be computed as mass-weighted average of the component enthalpies:

$$h_\alpha = \sum_{\kappa} (X_\alpha^\kappa h_\alpha^\kappa). \quad (2.22)$$

The specific enthalpy of vapor is considerably higher as for liquid water, as depicted in Figure 2.7a. The difference between the specific liquid and vapor enthalpy is the vaporization enthalpy, which quantifies the amount of energy required to completely vaporize one kilogram of liquid water isothermally. It is also called latent heat of vaporization. Considering pure water, the vaporization enthalpy is roughly 2.5×10^6 J/kg; it is the reason for the cooling effect of evaporation. The enthalpy of dry air (Figure 2.7b) is less influenced by the temperature as water.

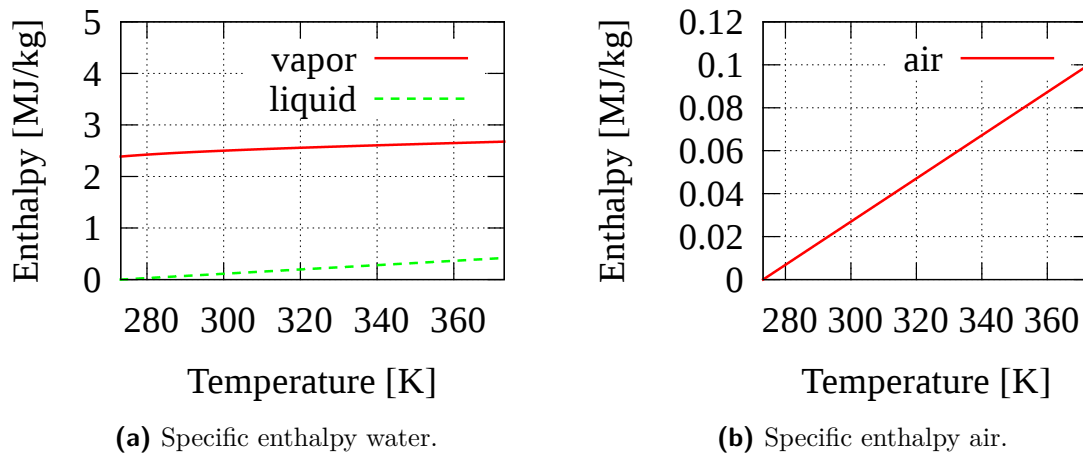


Figure 2.7: (a) Specific enthalpies of liquid and gaseous water, with the vaporization enthalpy as difference between the two curves. (b) Specific enthalpy of dry air (0 °C to 100 °C).

2.3 General conservation equations

In general, mass, momentum and energy are conserved quantities, which can not be created or destroyed. However, they can be converted into one another. Here, the fundamental conservation laws for mass, momentum and energy are presented. They are based on a general conservation equation a conserved intensive quantity e (Helmig, 1997; Truckenbrodt, 2008a).

This conservation equation gives the temporal change of an extensive property E with the intensive property $e = E/m$, and is composed of a time-dependent storage term and a flux term for a control volume Ω , with sources and sinks denoted as q :

$$\begin{aligned}\dot{E} &= \frac{d}{dt} \int_{\Omega} (\rho e) d\Omega = \int_{\Omega} \left(\frac{\partial(\rho e)}{\partial t} + \nabla \cdot (\rho e \mathbf{v}) \right) d\Omega \\ &= \int_{\Omega} \frac{\partial(\rho e)}{\partial t} d\Omega + \int_{\Gamma} (\rho e) (\mathbf{v} \cdot \mathbf{n}) d\Gamma = q.\end{aligned}\tag{2.23}$$

For reasons of brevity, the following balance equations are written in differential form. For an infinitesimally small control volume, the general conservation equation can be written as:

$$\frac{\partial(\rho e)}{\partial t} + \nabla \cdot (\rho e \mathbf{v}) = q.\tag{2.24}$$

2.3.1 Mass conservation

The continuity equation is a fundamental law, which states the continuity of mass fluxes and ensures that mass is not created or destroyed. It reads as follows:

$$\frac{\partial \rho_{\alpha}}{\partial t} + \nabla \cdot (\rho_{\alpha} \mathbf{v}_{\alpha}) = q_m,\tag{2.25}$$

with the density of fluid phase α ρ , the phase velocity \mathbf{v} and the external mass sources or sinks q_m .

2.3.2 Momentum conservation

A similar conservation law as for mass can be formulated for the momentum. The fundamental law of conservation of momentum is based on Newton's laws of motion and states that the total momentum within a closed system is constant. For fluid motion, it is termed Navier-Stokes equation and can be defined as

$$\underbrace{\frac{\partial(\rho_{\alpha} \mathbf{v}_{\alpha})}{\partial t} + \nabla \cdot \rho_{\alpha} \mathbf{v}_{\alpha} \mathbf{v}_{\alpha}}_{\text{acceleration}} + \underbrace{\nabla \cdot \mathbf{F}_{\mathbf{v}} - \rho_{\alpha} \mathbf{g}}_{\text{gravity force}} = 0.\tag{2.26}$$

This involves gravity as body force. The matrix-valued momentum flux accounts for the surface forces. Here, the pressure forces and the viscous forces are considered:

$$\mathbf{F}_{\mathbf{v}} = \underbrace{p_{\alpha} \mathbf{I}}_{\text{pressure force}} - \underbrace{\boldsymbol{\tau}}_{\text{viscous forces}}\tag{2.27}$$

with the $d \times d$ identity tensor \mathbf{I} and the viscous stress tensor $\boldsymbol{\tau}$.

2.3.3 Energy conservation

Different formulations of the energy balance equation are possible. Here, the formulation based on the phase enthalpy and internal energy is shown. It reads

$$\frac{\partial (\varrho_\alpha u_\alpha)}{\partial t} + \nabla \cdot \mathbf{F}_h - q_h = 0, \quad (2.28)$$

with the internal energy of the phase u_α and the heat flux defined as

$$\mathbf{F}_h = \underbrace{\varrho_\alpha h_\alpha \mathbf{v}_\alpha}_{\text{convection}} - \underbrace{\lambda_\alpha \nabla T}_{\text{conduction}} - \underbrace{\sum_\kappa D_\alpha^\kappa \varrho_\alpha \nabla x_\alpha^\kappa \frac{M^\kappa}{M} h_\alpha^\kappa}_{\text{heat transfer due to diffusion}}, \quad (2.29)$$

where λ_α is the thermal conductivity, h_α is the phase enthalpy and q_h are heat sources/sinks. The heat transfer due to mass diffusion occurs in multi-component systems. Model specific adaptations and simplifications of the general balance equations are explained in the chapter of the respective sub-model in Chapter 4.

2.4 Relevant processes

Figure 1.1 shows an overview of several processes, which may influence the exchange of mass, momentum and energy between the free flow and the porous-medium domain. In the following lines, some of these processes are explained in more detail.

2.4.1 Transport phenomena

Considering the transport of a physical quantity, it is distinguished between advective and diffusive transport. Advective transport happens due to a velocity field, whereas diffusion is driven by gradients of the transported quantity, like concentration or temperature. Furthermore, physical quantities can be transferred across phase boundaries. These phase transfer processes include evaporation (vaporization), condensation in the gaseous phase, dissolution and degassing in a liquid phase.

2.4.2 Evaporation from porous media

The term *evaporation* denotes the transition of water across the phase interface from the liquid to the gaseous phase. When a substance evaporates, the most energetic molecules pass over from the liquid to the gaseous phase. The vaporization enthalpy is absorbed and the water phase cools down as consequence of the evaporation. Evaporation is driven by a vapor pressure gradient and is usually considered as a diffusion-dominated process (Brutsaert, 1982). For low flow velocities parallel to the surface of an open water (lake), the air at the liquid-gas interface is in chemical equilibrium with the water phase and thus fully vapor saturated (saturated vapor pressure). If drier air passes across the lake, the vertical gradient of the partial pressure within the air layer next to the water surface causes a diffusive upwards transport of evaporated water, which is superimposed by the advective transport due to the air motion. Evaporation from lakes is mainly affected by the saturated vapor pressure based on the prevailing temperature and on the physical conditions in the adjacent flow. Fully water-saturated porous media behave similar to free water surfaces. In the context of this thesis, the term *evaporation rate* (or drying rate) quantifies the net water flux across the interface between free flow and porous medium.

Different stages of a drying process

The drying rates from porous media like quartz sand are typically subdivided into three different stages of the evaporation process (Lehmann et al., 2008; Yiotis et al., 2007; Hillel, 2004; van Brakel, 1980), as schematically shown in Figure 2.8:

1. externally controlled period or stage-1 with sufficient water supply at the surface of the porous medium, which is in the case of a relatively constant drying rate also termed constant-rate period,
2. profile-controlled stage or stage-2, which is controlled by a combination of transport processes within the porous medium and at the surface; opposed to the constant-rate period it is often termed falling rate period,
3. a slow-rate period or vapor-diffusion stage with a vaporization plane below the surface without direct evaporation at the porous surface.

The evaporation rate from an initially saturated porous medium tends to be high and often remains relatively constant. This phase, at which the primary vaporization plane is at the porous-medium surface, is known as stage-1 or constant-rate evaporation period (van Brakel, 1980; Yiotis et al., 2007; Lehmann et al., 2008). It is characterized by water flow in connected liquid pathways, which provide a great deal of the water supply to the evaporating pores at

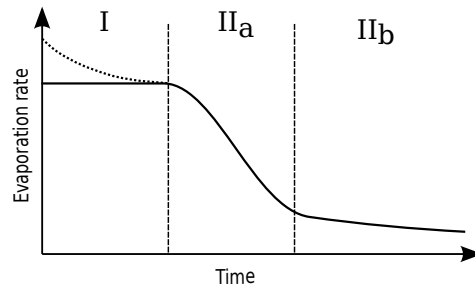


Figure 2.8: Qualitative evolution of the drying rate from a porous medium showing different characteristic stages. For thin boundary layers and a large distance between evaporating pores, the drying rate may decrease already from the beginning on, as indicated by the dashed line.

the surface of the porous medium (Shokri et al., 2009). The similarity of evaporative drying to drainage processes (Shahraeeni et al., 2012) is exhibited by the sequential pore invasion at the porous-medium surface according to the prevailing capillary forces, which means that the largest pores empty first. In stage-1, the evaporative demand at the porous surface is often relatively constant and the drying rate does not change much for a certain time period. For conditions where the internal capillary flow to the evaporation front is not limiting (stage-1), details of vapor exchange from the surface across the boundary layer exert a large influence on the drying rate. As long as many pores at the interface are water-filled, the adjacent air immediately above remains fully vapor saturated (saturated vapor pressure can be assumed) and an almost one-dimensional vertical vapor diffusion through the boundary layer with a relatively constant concentration gradient controls the evaporation rate. Note, however, that experimental evidence suggests that this may not always be the case, and the evaporation rate may drop from the onset of the drying process on, as indicated by the dashed line in Figure 2.8. This drop in the evaporation rate is often associated with high wind velocities with relatively thin boundary layers and large pores (Shahraeeni et al., 2012). An overview of the variety of possible shapes of drying curves is given in van Brakel (1980).

The transition from the externally controlled stage-1 to the falling rate in stage-2 is defined here by the following criteria:

- the water saturation at the surface drops to zero and the porous-medium surface dries out,
- the temperature at the surface increases in response to the dry interface without direct evaporation and without the cooling effect of the vaporization enthalpy.

When the liquid connections supplying the interface cannot meet the evaporative demand at the surface anymore, the porous surface dries and the vaporization plane migrates below the surface forming a secondary drying front as described in Shokri and Or (2011). This transition from stage-1 to stage-2 of the evaporation process is indicated as IIa in Figure 2.8 and also

called profile-controlled stage (Hillel, 2004). It is determined by a combination of transport processes happening within the porous medium and at the surface. The surface area that contributes to the direct evaporation from the water phase decreases. This may be partly or even completely compensated by a stronger evaporation per water-filled pore, as discussed in Shahraeeni et al. (2012), leading to a relatively constant drying rate.

However, for a high atmospheric demand associated with a thin boundary layer, the evaporation rate may gradually decrease from the onset of evaporation, even during stage-1, when the vaporization plane remains anchored at the surface. This gradual decrease of the evaporation rate may reflect a significant viscous resistance within the porous medium that could limit liquid supply to the evaporating surface, or, more likely, limitations to the flux compensation at the drying surface such as large pores and spacings relative to the boundary layer thickness (see Shahraeeni et al., 2012). In summary, as the surface gradually dries and the distance between remaining evaporating pores or pore clusters increases, the quasi one-dimensional diffusion through the boundary layer may change its character and become three-dimensional (Shahraeeni et al., 2012). This effect is considered in a later part of this work (Section 6.4.2).

When the surface water saturation decreases further, the rate of vapor transport in the air phase through the tortuous porous medium becomes the limiting process. The secondary evaporation front recedes into the porous medium and the diffusion distance to the surface gradually increases, resulting in a decrease of the evaporative flux during stage-2 evaporation. Hence, during this stage which is indicated as IIb in Figure 2.8, the restrictions for the drying rate are usually within the porous medium and the boundary layer is less important for the vapor exchange to the free flow. The external flow may increase the mixing in the top layers of the porous medium due to pressure fluctuations at the surface.

2.4.3 Flow conditions and boundary layers

The flow regime and the accompanying boundary layers may have a crucial effect on the transfer fluxes of mass, momentum and heat and on the mixing of these quantities in the free flow. An critical quantity in this context is the thickness of the boundary layer. The flow regime can either be laminar (including creeping flow) or turbulent. The Reynolds number Re is commonly used as a indicator for the underlying regime. It is based on the flow velocity \mathbf{v} , on the kinematic fluid viscosity ν , and on a characteristic length l and it compares viscous and inertial forces:

$$Re = \frac{\mathbf{v}l}{\nu}. \quad (2.30)$$

When the viscous forces dominate, the flow is orderly with mainly parallel and smooth streamlines. A domination of inertial forces leads to the formation of chaotic flow with eddies and crossing streamlines. Fluids with a low viscosity, like gases, tend already at low flow velocities to a turbulent flow behavior, whereas the high viscosity of e.g. honey dampens the formation of eddies. In the scope of this thesis, Newtonian fluids are considered, which have a linear relationship between shear stress and velocity gradient.

For relatively simple configurations, analytical solutions of the flow field are available. Two of such configurations are presented here to introduce the physics of boundary layers: The flow above a flat plate where an analytical solution is provided by Blasius (1908), and pipe flows.

Flow above a flat plate

The evolution of a flow field along a flat plate, as schematically depicted in Figure 2.9, illustrates the key features of boundary layers. The boundary layer thickness of the velocity field δ_v is usually defined as the vertical distance from the surface, at which the velocity has reached 99% of the undisturbed flow velocity v_∞ (see, for example, Schlichting and Gersten,

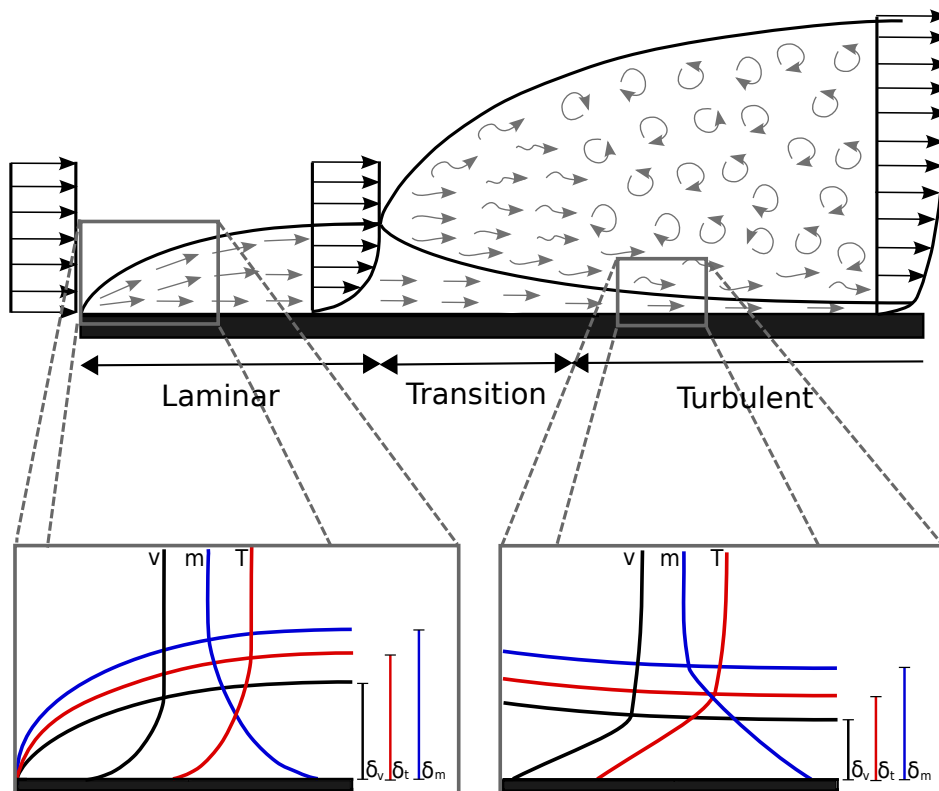


Figure 2.9: Qualitative evolution of a boundary layer above a flat plate with a different boundary layer thicknesses for velocity, concentration and temperature.

2006; Incropera et al., 2007a). For the temperature and the concentration, the definition is accordingly, but their extent may differ from the velocity boundary layer. The extent of the thermal and the concentration boundary layer is often related to the velocity boundary layer using the dimensionless Schmidt and Prandtl numbers (Bird et al., 2007): $\delta_t \approx \frac{\delta_v}{Pr^{1/3}}$ and $\delta_c \approx \frac{\delta_v}{Sc^{1/3}}$. The Prandtl number Pr is the ratio of kinematic viscosity and thermal diffusivity a . It is computed as $Pr = \frac{\nu}{a} = \frac{c_p \mu}{\lambda}$ with the heat capacity c_p and the heat conductivity λ . For air at atmospheric pressure and a temperature of 298 K, the Prandtl number is approximately 0.71. Furthermore, the Schmidt number relates the kinematic viscosity to the binary diffusion coefficient: $Sc = \frac{\nu}{D}$. Under the ambient conditions mentioned above, the Schmidt number is roughly 0.78. With these values, both, the temperature and the concentration boundary layer are thicker than the velocity boundary layer.

When a turbulent flow field evolves over a flat plate, the boundary layer remains for a certain distance laminar, as indicated in Figure 2.9. At the beginning of the flow field, viscosity plays a dominating role and laminar conditions prevail within the boundary layer. The transition from laminar to turbulent flow happens usually at a critical Reynolds number, $Re_{crit} \equiv \frac{\rho v_\infty x_c}{\mu} \approx 5e5$. The critical Reynolds number is not a fixed value, but may vary from 10^5 to 3×10^6 in dependency on the surface roughness and the conditions in the free flow, see Incropera et al. (2007a); Baehr and Stephan (2010) or Schlichting and Gersten (2006).

Moreover, the transition from laminar to turbulent conditions does not happen abruptly. With increasing Reynolds number, more and more turbulent eddies penetrate into the laminar boundary layer resulting in an alternation of laminar and turbulent states in the boundary layer. This state of the boundary layer is termed *intermittent*.

In contrast to laminar ones, turbulent boundary layers may be subdivided into two sub-layers: the viscous sublayer where viscosity has an influence and flow is rather laminar and parallel to the interface, and the turbulent part of the boundary layer with fluctuating motion. Vertical transport of scalar quantities, such as energy or concentration, are mainly driven by diffusive processes through this thin sublayer (see e.g. Oke, 1978). Thus, the viscous sublayer may be seen as resistance for mass and energy exchange. The exterior flow has usually chaotic flow conditions with turbulent eddies, which lead to a strong mixing of transported quantities.

Pipe flows

Flow in channels or pipes behave similar to flow above a plate, but the growth of their boundary layer is limited by the pipe geometry. The boundary layers grows along the pipe until the boundary layers from different sides merge. Then, the flow is fully developed and does not change much further. For laminar flows, this leads to a parabolic velocity profile.

The flow regime in pipes is characterized by the critical Reynolds number for pipe flows, $Re_{\text{crit}} \equiv \frac{u_{\infty} d}{\nu}$. If a critical value of 2300 is exceeded, the flow is usually turbulent (White, 2000). Here, the characteristic length appearing in the Reynolds number is the pipe diameter d . Again, this value is not a fixed number but is usually in the range between 2000 and 20000 depending on the smoothness of the pipe and existing disturbances of the flow field. If air flow in pipes is considered, turbulent flow conditions can usually be expected due to the small value of the kinematic viscosity.

2.4.4 Radiation

Radiation is a main driving force for evaporation from soils. It is an important part of the surface energy balance and provides energy input for the vaporization of water. Radiation emitted by a body is usually quantified with the Stefan-Boltzmann law:

$$q_{\text{rad}} = \sigma_B \epsilon_s (T_2^4 - T_1^4), \quad (2.31)$$

with the Stefan-Boltzmann constant $\sigma_B = 5.67 \times 10^{-8} \text{ W/m}^2\text{K}^4$ and the dimensionless surface emissivity ϵ_s .

The sun emits high-energetic short wave radiation, which reaches partly the atmosphere of the earth. There, a great portion of the radiation is dissipated, reflected, scattered or absorbed. The part that passes the atmosphere and reaches the soil surface is again split into different parts as shown in Figure 2.10. The combination of soil evaporation and plant transpiration is called evapotranspiration. Globally, the largest contribution to terrestrial evapotranspiration is from plant transpiration. Approximately thirty percent of the global evapotranspiration

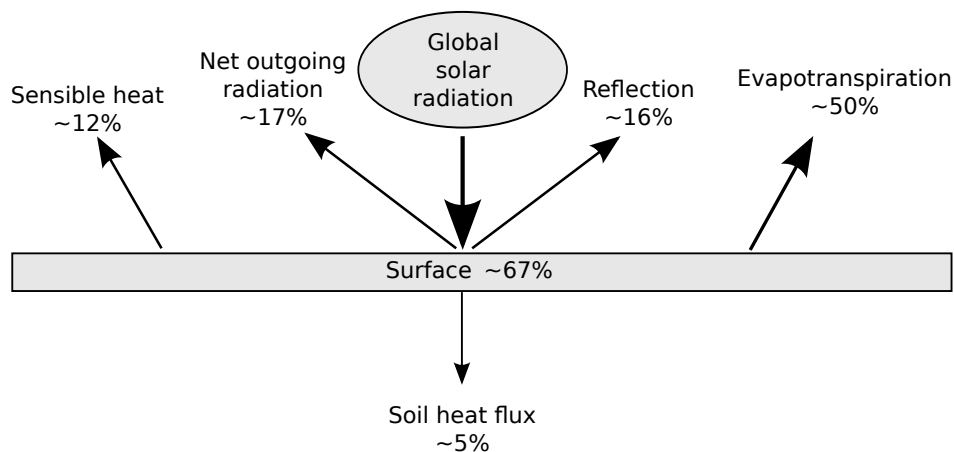


Figure 2.10: Approximation of the typical distribution of the global solar radiation when reaching the surface after Jury and Horton (2004).

is contributed from bare soil evaporation according to Choudhury and DiGirolamo (1998). However, this ratio depends strongly on the considered location. The focus here is completely on bare-soil evaporation and plant transpiration is not considered.

The general surface energy balance can be formulated as

$$R_n = L_e E + H + G, \tag{2.32}$$

with the net radiation R_n , the latent heat of vaporization $L_e E$, the sensible heat flux into the atmosphere H , and the ground heat flux G (Brutsaert, 1982).

2.5 Summary of this chapter

This chapter has introduced physical processes and quantities, which are relevant for the modeling of evaporation processes from porous media. The general balance equations were presented and important transport phenomena explained. With this as basis, the physical experiments will be introduced in the following chapter.

3 Evaporation experiments

In the previous chapter the context was established and basic definitions and processes were introduced. This chapter delves into the heart of the problem starting with experimental work on evaporation. In order to study the different influencing quantities on evaporation processes from porous media and to allow a first comparison of measured data with the results of the numerical simulations, a series of drying experiments in a wind tunnel has been conducted. This was done in collaboration with the Soil and Terrestrial Environmental Physics (STEP) research group of Professor Dani Or at the ETH Zürich in their laboratory in the framework of the DFG (German Research Foundation) funded research group MUSIS (Multi-scale interfaces in unsaturated soil, www.musis.uni-hannover.de). The experiments serve also as basis for the definition of a reference case for the simulations and analysis, which will be presented in Chapter 6. This chapter starts with a description of the experimental setup. Then, the observations and measured data are presented. The chapter concludes with some remarks considering uncertainties in the measured data and possible error sources.

3.1 Experimental setup

A thermally insulated glass vessel ($0.25\text{ m} \times 0.25\text{ m} \times 0.08\text{ m}$) was filled with quartz sand and saturated with water from the bottom of the vessel. Then, the surface was exposed to the air flow of a wind tunnel ($d=0.5\text{ m}$), as shown in Figures 3.1 and schematically depicted in Figure 3.2. The experimental setup is the same as used in Shahraeeni et al. (2012).

Two different sand have been applied as porous material: a medium (also called coarse hereinafter) and a fine sand. The sands have been analyzed and used in several experiments from the DFG research unit MUSIS and in the drying experiments presented in Lehmann et al. (2008) and Shokri et al. (2008). The key parameters for the two sands are listed in Table 3.1.

The mass loss from the vessel has been recorded at predefined intervals with a balance below the sample with an accuracy of 0.1 g. The maximum flow velocity within the wind tunnel has been measured with two hot-wire anemometers, which were placed on the center line of the tunnel. The flow velocity can be varied in the range of 0.5 to 4.0 m/s. Furthermore, the air

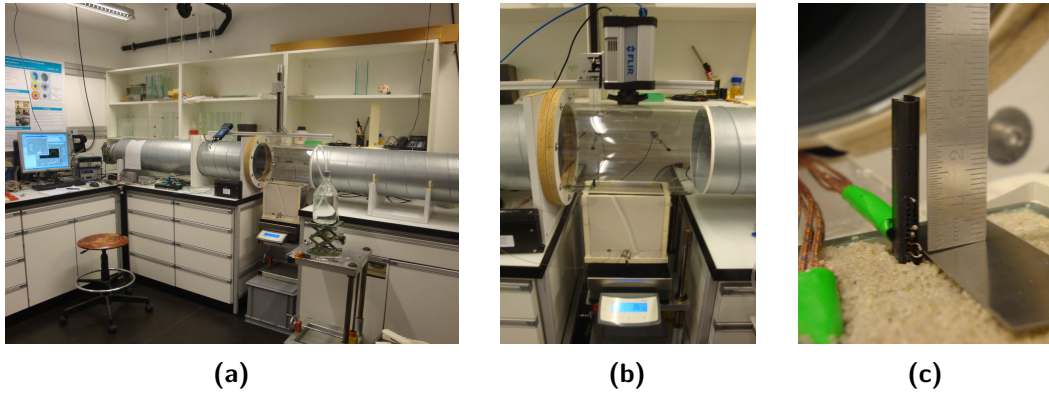


Figure 3.1: Overview of the experimental setup. Figures (a) and (b) show the wind tunnel with the insulated sample mounted on a digital balance, the infrared camera above the sample and two flow anemometers and a heat and moisture sensor in the center of the transparent section of the wind tunnel. Figure (c) shows the two arrays of stacked thermocouples at the end of the sand sample.

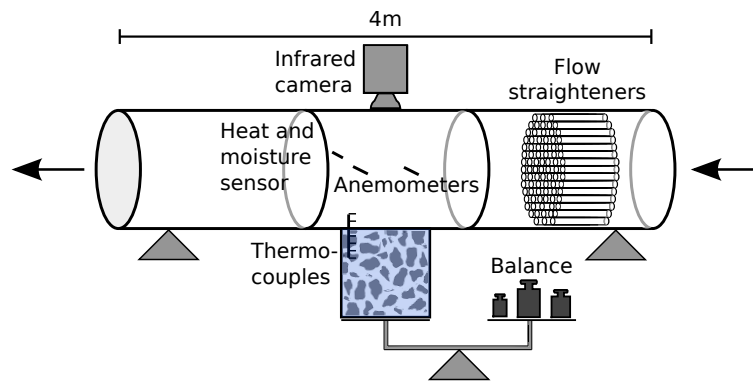


Figure 3.2: Schematic overview of the experimental setup with approximate position of flow anemometers, thermocouple elements and heat and moisture sensor.

Table 3.1: Soil parameters of the two quartz sands

	d [mm]	K [m^2]	ϕ [-]	α_{vGN} [$1/Pa$]	n [-]
fine sand	0.3-0.9	$2.65e-10$	0.41	$6.37e-4$	8.0
medium sand	0.7-1.2	$5.0e-10$	0.44	$8.74e-4$	3.35

humidity and temperature in the free flow were determined at two points above the porous sample at the center of the wind tunnel. An infrared camera was installed above the sample, focusing on the surface of the porous medium. It records the surface temperature evolution (thermal signature of the evaporation process). The measured temperature data can be used as further indicator for the transition from stage-1 to stage-2 and gives information about local heat fluxes.

3.1.1 Drying rates

Experiments with a mean flow velocity of 1.0 m/s and 3.5 m/s at the center of the wind tunnel have been conducted in order to obtain data for evaporation under high and lower atmospheric demand. The respective drying rates for the two materials and at the two velocities are shown in Figure 3.3. The experiments have been conducted at least until the transition to stage-2 evaporation could be recognized, which was roughly after 2 to 4 days. For the free stream velocity of 3.5 m/s , a constant drying rate could not be observed; instead the evaporation rate dropped continuously from the onset of the experiment on. This initial decrease of the drying rate was smaller for a lower velocity of 1 m/s . Due to turbulent velocity fluctuations, non-uniform drying behavior, breakdown of measurements, and other disturbances, the evaporation curves are relatively noisy and a moving average was applied to obtain the curves presented in Figure 3.3. However, the principal behavior and the transition from stage-1 to stage-2 can still be identified. The first stage of the evaporation process and the transition to the second stage can still be identified, supported by the temperature data from the infrared camera and the thermocouple elements in the surroundings of the interface, as described in the following lines.

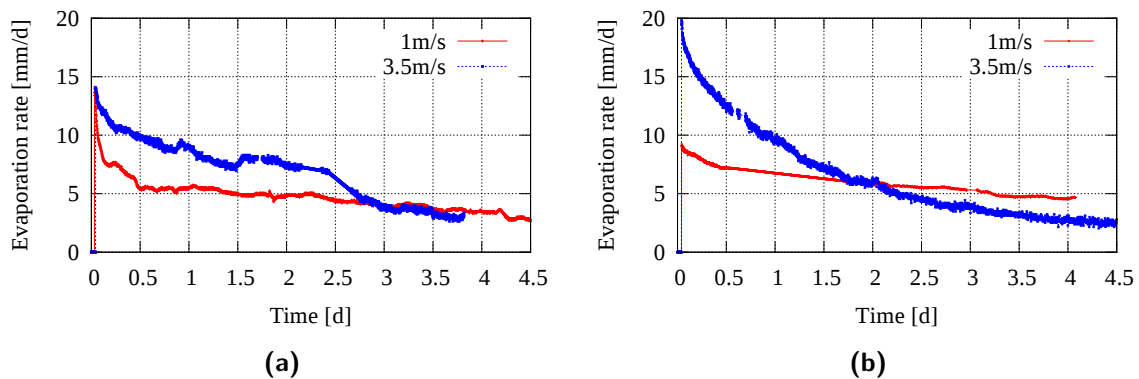


Figure 3.3: (a) Measured drying rates for the coarse material. (b) Measured drying rates for the fine material.

3.1.2 Heat exchange and thermal boundary layer

The heat transfer was monitored with an array of stacked thermocouples above and below the surface. The measurement points were at 1, 2, 4, 5 and 11 mm above and 1, 3, 5, 10 and 20 mm below the surface of the porous medium. The thermocouples were placed in the last part of the sample to reduce their influence on the flow field and boundary layer. As can be seen in Figure 3.4b, the thermocouples below the sand surface show clear temperature gradients within the sand towards the surface. This reflects the effect of evaporative cooling and heat conduction, as long as the evaporation process remained in stage-1 and with the vaporization plane at the surface of the sample. The thermocouples above the sample show also a vertical gradient as long as water is evaporating, indicating the thermal boundary layer. This gradient becomes considerably smaller, when the surface dries out. An infrared camera was placed above the porous surface to give detailed information about the surface temperature evolution during the drying experiments. The temperature data can be used as further indicator for the transition from stage-1 to stage-2 and to obtain information about heat fluxes and the local evaporation. The maximum decrease of temperature at the surface was about 3.5 K. This is also displayed in Figure 3.4a as difference between the thermocouple above and below the porous-medium surface.

Additionally to the homogeneous setups, a vertically textured media has been setup and

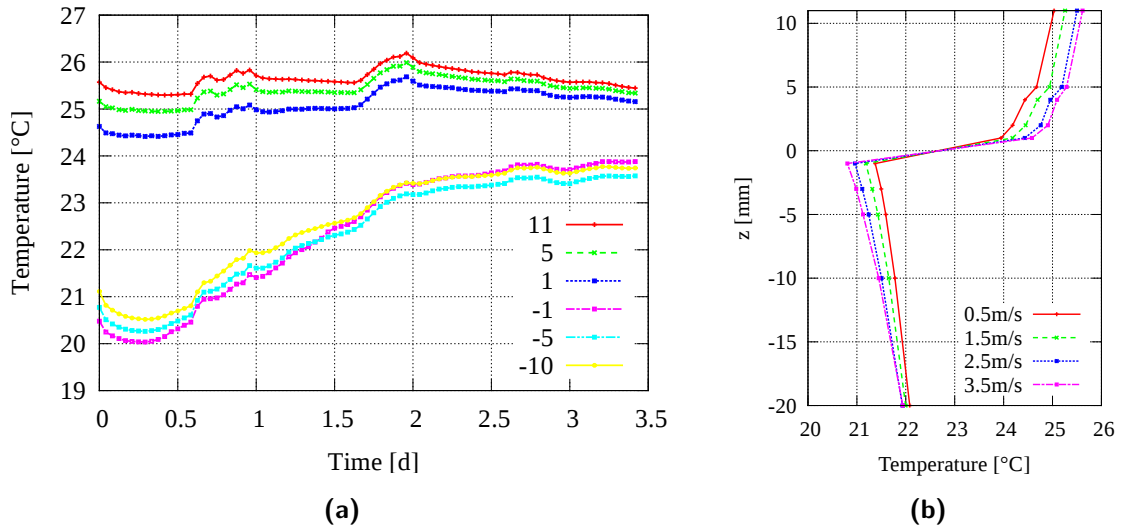


Figure 3.4: (a) Temperature evolution at different positions above and below the surface during an evaporation process from the fine sand sample for a flow velocity of 3.5 m/s . The temperatures were determined with the thermocouples. (b) Measured temperature profiles for an evaporation process from the fine material with different free-flow velocities. The differences of the temperature above and below the surface are more pronounced for higher flow velocities and amount to more than 4 K.

measured. The first half of the vessel was filled with fine sand and the other half with medium sand. Then, the vessel was water-saturated and exposed to the flow of the wind tunnel. The respective evaporation rate and the temperature in the center of the wind tunnel are shown in 3.5a. After approximately 2.5 days, the drying curve increases considerably. This is because an interval heating fan was placed at the inflow of the wind tunnel to accelerate the drying process. Due to the heating device, the temperature in the wind tunnel increased from 25 °C to 33 °C, thereby raising the evaporation rate. Figure 3.6 depicts the evolution of the temperature distribution at the surface. The focus of the infrared camera was on the interface of the two different sands.

Despite that kink in the curve, the overall trend can be summarized as follows: The drying rate shows a short stage where both soils contribute similarly to the evaporation rate. The coarse material dries out, leading to a first drop of the evaporation rate and a subsequent plateau, when only the fine material is directly evaporating. Water flows from the coarse to the fine material due to capillary pressure gradients, but only little water is transported as vapor from the coarse porous medium across the interface into the free flow. Then, after approximately 7 days, the fine material dries also out, resulting in a low evaporation rate dominated by diffusion through the void space of the porous medium.

The measured drying rates allow some general statements:

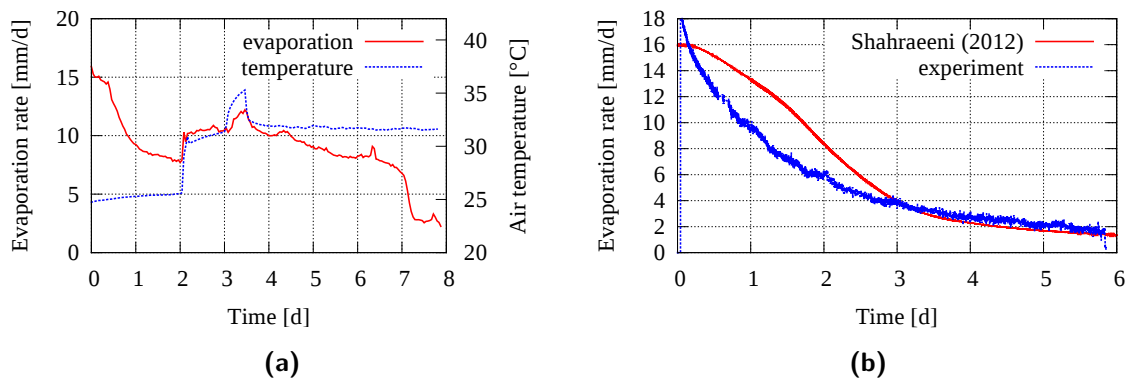


Figure 3.5: (a) Evaporation rate and temperature evolution with a vertically textured media. (b) Comparison of the same experimental setup with the coarse material 3.5 m/s measured twice.

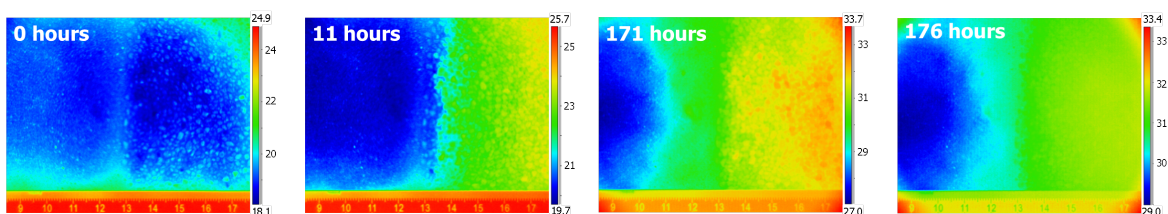


Figure 3.6: Infrared images (top view) of an evaporation experiment with a vertically textured media.

- A higher free stream velocity leads to a higher evaporation rate. This may be explained by a faster transport in the free flow, a thinner concentration boundary layer, which has to be transcended to get to the turbulent free flow with a strong mixing.
- The fine sand leads to higher evaporation rates than the coarse sand. A possible explanation is that the coarse sand has a higher surface roughness, leading to a thicker boundary layer. Thus, the concentration gradient across the mass boundary layer above the coarse sand is lower and the resulting evaporative fluxes are smaller. This is supported by a less steep decrease of the evaporation rate within stage-1. The water supply within capillaries towards the surface and also the pore structure at the surface are different for the two sands leading to different evaporation patterns.
- A vertically textured media with a fine and a medium sand shows several transitions. The coarse sand dries out first and water flows due to capillary forces into the finer material where it evaporates. The direct evaporation from the fine sand is sustained longer. When it dries out, a second drop of the evaporation rate can be observed.

3.2 Possible error sources and uncertainties

So far, the experiments are considered and simulated as 2D processes. However, there are clear 3D phenomena, which are then omitted. The sample has a thickness of 8 cm. Thus, an influence of the walls on the ongoing processes can not be excluded. Moreover, it is likely that the soil density varies spatially and that local heterogeneities exist due to the packing of the sample. The infrared images from the homogeneous runs show a slightly lower temperature at the center of the porous surface as towards the glass walls, as illustrated in Figure 3.7. This indicates that also more water evaporates at the center of the sample surface and may be due to wall effects and the packing of the sample. The pores at the glass wall are larger compared to the ones in the interior, leading to capillary pressure gradients and may evoke a water transport towards the center of the vessel.

Further, it has to be noted that the run-up distance for the flow was probably too short to obtain a fully developed turbulent boundary layer and flow field. The Reynolds number of the wind tunnel Re_d is larger than the critical Reynolds number of 2300 for the considered flow velocities, hence turbulent flow conditions can be expected to develop. However, a critical Reynolds number $Re_x > 10^5$, which signalizes the transition of the boundary layer from laminar to turbulent is not guaranteed due to the restricted length of the wind tunnel of 4 m. For a flow velocity of 3.5 m/s at the given conditions, the critical Reynolds number would be reached roughly after 2 m. For the lower velocity of 1.0 m/s the calculated position for the

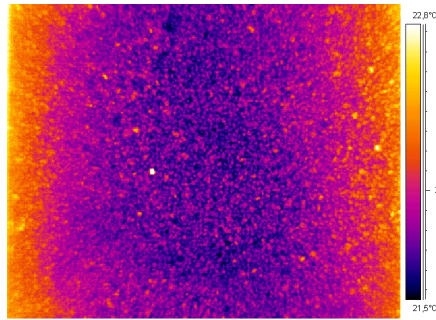


Figure 3.7: Surface temperature showing a cooler region in the interior of the evaporating surface and warmer zones towards the vessel walls (sides of the figure).

transition is outside the wind tunnel, thus a rather intermittent (laminar boundary layer with turbulent perturbations) behavior may prevail.

The measured soil parameter values contain uncertainties, especially with respect to their values at the surface of the sample, and the values in the experiments may deviate due to the packing of sand into the vessel. A uniform filling is not possible with a sand where all grains have different shapes, and local heterogeneities are created depending on shape and positioning of the grains. As shown in Figure 3.5b, the same experiment conducted by different persons may lead to a difference in the drying curves. Due to these uncertainties, the experimental data allows only rough comparisons to the simulated cases. For better comparisons with experimental data and a better transferability to field scale systems, more detailed drying experiments on a larger scale are required. Special care should be attributed to the measurement of the soil parameters and to a standardized filling procedure, which has a strong influence on the transition from state-1 to stage-2. An option to improve the reliability of the experimental data is to do repeated drying experiments with a larger sample (surface) size to minimize the influence of the vessel walls and of small-scale heterogeneities.

3.3 Summary of this chapter

The experimental setup of the wind tunnel experiment is described. This was used to perform experiments with different wind velocities while measuring the mass loss and the conditions in the wind tunnel (flow velocity, vapor concentration, temperature). Furthermore, temperature evolution on the porous-medium surface was recorded with an infrared camera and in the vicinity of the interface with thermocouple elements. The measured data is presented and briefly discussed, also considering possible measurement errors and uncertainties in the data.

4 Conceptual model

This chapter¹ presents a model concept for the coupled simulation of compositional free flow and compositional two-phase porous-medium flow on the REV scale under non-isothermal conditions. It starts with a review of the work that has already been done in the field of coupling free flow and flow in porous media on the REV scale. Then, the model concepts employed in the free flow and in the porous medium with adaptations of the general balance equations presented in Section 2.3) to each domain are introduced. The coupling concept, which has been developed in Mosthaf et al. (2011) and which couples the two domains at the common interface, is worked out. Parts of this chapter have been published in Mosthaf et al. (2011) and are excerpts from the paper.

4.1 Review of prior research and overview of coupling approaches

Due to its prominence for a variety of applications, the modeling of coupled porous-medium and free-flow systems has been subject to vital research over the past years. This is also reflected by a rapidly growing number of publications in this field. When the pore space is resolved, models and methods like direct numerical simulation (DNS), lattice-Boltzmann (LB), or volume-of-fluids (VoF) can be applied on the pore-scale (Pan et al., 2006; Tölke et al., 2006; Ahrenholz et al., 2011). Then, the same set of equations can usually be employed to model the free flow and the flow in the pore space without the need of a special coupling concept at the interface of the two domains. A modeling on the pore scale requires usually much computational power and is restricted to a relatively small spatial extent. It is a valuable tool for the determination of effective quantities and for a detailed analysis of processes.

On the averaged scale of representative elementary volumes, however, the potential theory and Darcy's law are usually applied in the porous medium, whereas Stokes flow or Navier-Stokes flow has to be considered in the free flow. Thus, the two model domains are not directly compatible and a suitable concept for the coupled treatment of the two domains is required. Models which couple both domains, a porous-medium domain and a free flow, are rare,

¹The development of the coupling concept was published in Mosthaf et al. (2011) and parts of the following are repetitions thereof.

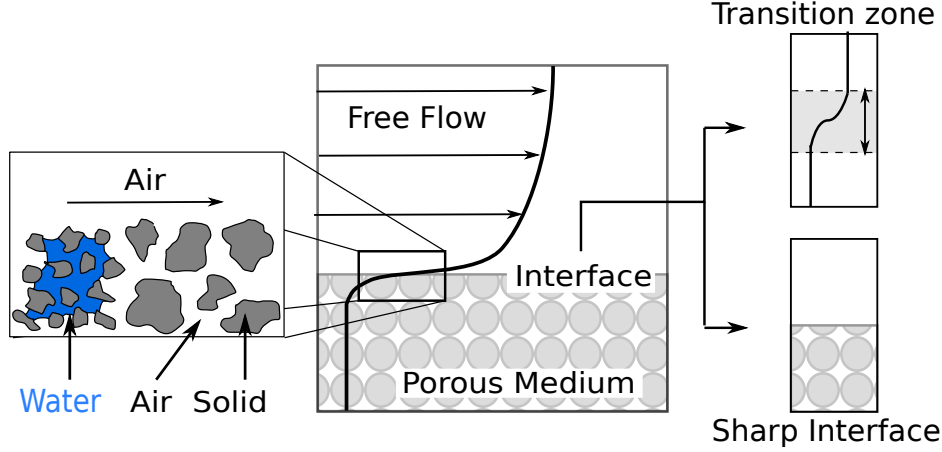


Figure 4.1: Interface descriptions: (a) REV scale: velocity profile for coupled free flow (single-phase Stokes equations) and porous-medium flow (multiphase Darcy's law), (b) micro/pore scale: the distribution of all phases and pore sizes is resolved, (c) interface description either as a transition zone with continuously varying parameters or as a sharp interface (partly after Chandesris and Jamet, 2009).

especially models that consider two fluid phases in the porous medium, as it is required for evaporation processes from soils (water and air). For the tackling of such coupled systems on the REV scale two basic strategies are commonly distinguished: the *single-domain* and the *two-domain approach* (Jamet et al., 2009; Shavit, 2009), as illustrated in Figure 4.2.

4.1.1 Single-domain approach

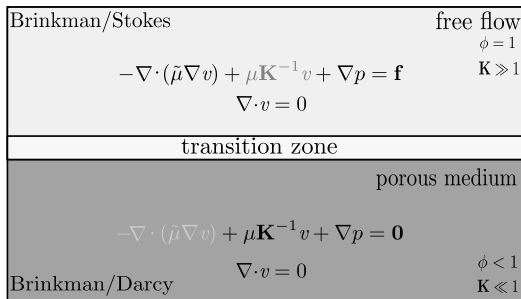
The *single-domain approach* assumes one set of equations to be valid throughout the entire domain, as schematically shown in Figure 4.2a. Therefore, the Brinkman equation (Brinkman, 1947), which is essentially a superposition of Darcy's law and the Stokes equation, or an extension of the Brinkman concept (Shavit et al., 2002), is usually applied in the entire domain. It has also been derived in a later study using the method of volume-averaging (Ochoa-Tapia and Whitaker, 1995) and reads

$$-\nabla \cdot (\tilde{\mu} \nabla \mathbf{v}) + \frac{\mu}{\mathbf{K}} \mathbf{v} + \nabla p = \mathbf{f}. \quad (4.1)$$

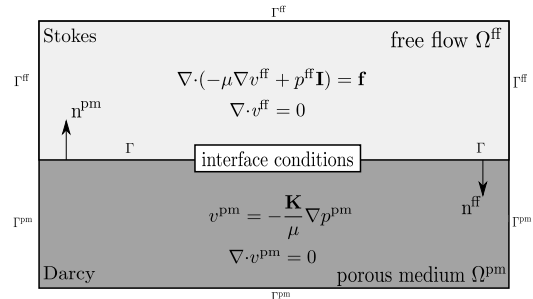
The transition from one domain to the other one is either achieved by a thin equidimensional transition zone at the porous-medium side of the interface where soil properties like permeability

and porosity are continuously varied, or by allowing a discontinuous jump of the property values across a lower-dimensional interface. The continuous parameter variation within this thin region leads to strong changes and gradients of quantities like velocity, concentration and temperature. Due to the use of the same set of equations in both subdomains, the flux and stress continuity is automatically satisfied and a special coupling concept at the interface is not required. However, an effective viscosity $\tilde{\mu}$ is introduced, which has to account for the momentum exchange in the transition region. In the free flow, the fluid viscosity is used, whereas no clear methodology for the choice for the apparent viscosity in the porous medium exists. Depending on the geometric properties of the porous medium and the flow direction and conditions, the apparent viscosity may be smaller or larger than the fluid viscosity (Rosenzweig and Shavit, 2007).

The single-domain approach has been analyzed and applied by many authors for single-phase systems (Durlinsky and Brady, 1987; Gupte and Advani, 1997; Angot, 1999; Shavit et al., 2004) and for heat exchange problems (Somerton and Catton, 1982). The difficulties of the approach involving the Brinkman equation are the correct quantification of the transition-zone thickness, which is usually only a few grain diameters (Jamet et al., 2009), and the meaningful choice of parameter values in the transition region, like the apparent viscosity (Martys et al., 1994; Goyeau et al., 2003; Rosenzweig and Shavit, 2007), which is a prerequisite for a correct description of the momentum exchange. The Brinkman concept is restricted to media with a relatively high porosity (Martys et al., 1994). According to Lundgren (1972) the Brinkman equation is applicable to porosities larger than 60%, which is rarely the case for natural porous media (Nield and Bejan, 2006). Further studies have successfully employed the Brinkman concept to a porous medium with a porosity of 50%. Considering applicable extensions to two fluid phases in the porous medium, there is only little work available at present.



(a) Single-domain coupling concept.



(b) Two-domain coupling concept.

Figure 4.2: Single-domain approach using the Brinkman equation with one set of equations vs. two-domain approach with a sharp interface and coupling conditions.

4.1.2 Two-domain approach

In contrast to the single-domain approach, the *two-domain approach* (Figure 4.2b) considers two distinct domains, which are modeled with different sets of equations and which are separated by a sharp interface: The porous-medium flow is usually modeled using the potential theory and Darcy's law for the flow velocity, whereas in the free-flow domain, the Navier-Stokes equations are solved, which can be simplified to the Stokes equations for laminar flow conditions ($Re < 2300$) by neglecting the nonlinear inertia term. In addition to the models in the subdomains, appropriate coupling conditions, which link both domains properly and which integrate relevant processes within the transition zone into the REV-scale modeling framework, have to be specified.

The physical transition zone can either be approximated as simple interface devoid of thermodynamic properties, or as an interface that can store and transport mass and other thermodynamic quantities (Hassanizadeh and Gray, 1989). The simple interface corresponds to continuity of thermodynamic properties at the interface, whereas an interface with thermodynamic properties leads to discontinuities which are characterized by conditions involving jump coefficients (Ochoa-Tapia and Whitaker, 1995; Chandesris and Jamet, 2009). One way to derive the coupling conditions is to apply the volume-averaging technique (Gray et al., 1993; Whitaker, 1999; Jackson et al., 2012). The resulting conditions include either complex closure relations or excess surface terms to account for the transition between the free-flow and the porous-medium region (Ochoa-Tapia and Whitaker, 1995; Chandesris and Jamet, 2009). Based on these excess terms, the jump coefficients can be derived (Valdés-Parada et al., 2009a,b). However, the coupling conditions are often simplified by neglecting the contribution of these terms and assuming continuity, since the characteristics of these surface excess terms are hard to determine (Valdés-Parada et al., 2007). The decision of continuity or discontinuity has to be made for mass, momentum and energy respectively. One approach is to employ a stress-jump condition obtained by volume averaging (Ochoa-Tapia and Whitaker, 1995). Chandesris and Jamet (2006, 2007) present a two-step upscaling approach and the method of matched asymptotic expansions for the derivation of a velocity-jump and a stress-jump condition at the interface. An alternative approach, which is followed in the sequel, is to guarantee mass conservation and the continuity of normal forces across the interface (Layton et al., 2002).

Moreover, the Beavers-Joseph velocity-jump condition (Beavers and Joseph, 1967) is often used to provide a connection between the tangential free-flow velocity, shear stress at the interface and the seepage velocity in the porous medium. It is required as an additional boundary condition for the Stokes domain, because the equations in the two domains are of different order. The relation between velocity jump at the interface and shear stress is given

in terms of an additional proportionality factor: the Beavers-Joseph coefficient α_{BJ} . This parameter depends mainly on the geometry and the properties of the permeable material, such as the roughness of the interface, and can be determined experimentally or by numerical simulation. Saffman (1971) showed that the filtration velocity in the porous medium is very small compared to the free-flow velocity appearing in the Beavers-Joseph condition and can thus be neglected. Then, the Beaver-Joseph condition becomes a Robin boundary condition for the tangential free-flow velocity as it contains the derivative of the velocity as well as the velocity itself. The Beavers-Joseph-Saffman condition has been mathematically justified by Jäger and Mikelić (2000, 2009) by means of homogenization. There exist several alternatives to the Beavers-Joseph condition (Levy and Sanchez-Palencia, 1975; Alazmi and Vafai, 2001; Goyeau et al., 2003).

Summing up, the challenge of the one-domain approach is the meaningful description of the spatial variation of parameter values in the transition zone, whereas in case of the two-domain approach, the definition of well-fundeed coupling conditions that represent the transfer processes at the interface is the challenging task, especially, since a correct description should account for the surface excess terms. Valdés-Parada et al. (2007) analyzed the one- and the two-domain approach and pointed out that both can be derived by volume-averaging. In this thesis, the two-domain approach considering a simple interface is applied, as described in detail in Section 4.3.

The concepts presented above have been developed for single-phase single-component systems describing the coupling for mass and momentum. However, in many applications compositional multi-phase flow occurs, and there was an urgent need for a more general model. Work considering the coupling with two fluid phases in the porous medium is scarce. For the modeling of a non-isothermal system, coupling conditions for the energy balance have to be found additionally. Prat (1990) used the method of volume-averaging to analyze the one- and two-domain approach for conductive heat transfer between free-flow and porous medium. Jamet et al. (2009) showed the equivalence of the discontinuous one- and two-domain approach for a heat conduction problem, provided that the one-domain approach is mathematically interpreted in the sense of distributions. Alazmi and Vafai (2001) reviewed coupling conditions for conductive and convective heat transfer and found that both continuity and discontinuity of temperature and heat flux have been applied in various combinations, showing only minor differences.

For the description of transport processes in compositional single-phase flow, it is again possible to use either the one- or the two-domain approach. Valdés-Parada et al. (2006, 2007), for example, show the coupling of diffusive mass flux across the interface using both approaches. In Valdés-Parada et al. (2006), the diffusive mass transport between micro- and macro pores in

packed-bed reactors is described and a jump condition for the two-domain approach is derived by volume-averaging. Neglecting surface accumulation and surface transport excess, the jump in diffusive flux is determined by a jump coefficient that accounts for the reaction rate at the fluid-porous interface. This jump condition is supplemented by a continuity assumption for the concentrations at the interface. In case of a non-reactive medium, this leads to continuity of diffusive mass flux and concentration. Valdes-Parada et al. (2009a) extended the concept to convective transport, along with adsorption and reaction in the porous medium.

4.1.3 Evaporation models

The modeling of evaporation on the REV scale is often done with decoupled models, which have their focus either on the free flow (Aydin et al., 2005) or the porous medium (Liu et al., 2005; Bittelli et al., 2008; Smits et al., 2011; Zeng et al., 2011; Smits et al., 2012). Furthermore, the porous medium is often simplified by neglecting the advective air flow in the porous medium, usually involving the Richards equation in an extended form (van Dam and Feddes, 2000; Bechtold et al., 2011). Recently, a coupled model with similar coupling conditions as the ones which will be presented in the sequel was employed in (Defraeye et al., 2012a) to extensively study the heat and mass transfer processes at building surfaces (Saneinejad et al., 2012) and during the drying of gypsum boards (Defraeye et al., 2012b), which is considered as evaporation process from a porous medium. There, a focus is on the free-flow processes and on the determination of local heat and mass transfer coefficients.

In summary, model concepts for the coupled description of compositional single-phase systems under non-isothermal conditions are available. For the modeling of evaporation processes from porous media, an extension to multi-phase systems in the porous medium was required. In the following two sections, the sub-models which are used in each domain are explained, beginning with the porous-medium model. Then, Section 4.3 introduces and explains the coupling concept based on the two-domain approach. The concept was developed for two phases in the porous medium and aims at simulating evaporation processes with water and air as fluids, but is also adaptable for a wide range of further applications.

4.2 Model concepts in the subdomains

Two fluid phases, a gaseous phase and a liquid phase, can be present in the porous medium and interact with a single gas phase (air) in the free flow, as illustrated in Figure 2.2. In the context of evaporation processes, the fluids are typically water (liquid phase) and air (gaseous phase). A compositional (miscible) model is chosen to allow for the description of the

component exchange between the two fluid phases, each of which consists of two components, namely water and the pseudo-component air (see Section 2.2). The gaseous phase contains water in the form of vapor, whereas small amounts of air are dissolved in the liquid phase.

The free-flow domain Ω^{ff} and the porous-medium domain Ω^{pm} are bounded and separated by the common interface $\Gamma = \partial\Omega^{\text{ff}} \cap \partial\Omega^{\text{pm}}$ with the constant outward unit normal vectors \mathbf{n}^{ff} and \mathbf{n}^{pm} (see Figure 4.2b). For simplicity of notation, the superscripts (ff) and (pm) are only applied on quantities at the interface, with (ff) referring to the values in the free-flow subdomain and (pm) to the properties on the porous-medium side.

4.2.1 Model concept in the porous-medium domain

In the porous-medium domain Ω^{pm} a mass-balance equation for a component, the total mass balance and an energy balance are used, see for example Class et al. (2002). The momentum balance is not solved explicitly, but Darcy's law (Equation (2.10)) is employed and inserted into the mass balance equation. The porous-medium system is simplified based on the following assumptions:

1. local thermodynamic (mechanical, thermal and chemical) equilibrium is assumed,
2. the porous medium is rigid (the porosity does not change), isotropic and the solid phase (subscript s) inert,
3. two-phase flow is considered, consisting of a liquid phase (subscript l) and an ideal gas phase (subscript g), both of them are assumed to be Newtonian fluids,
4. each fluid phase is composed of two components: water (superscript w) and air (superscript a),
5. a compositional model is employed, facilitating a phase transition of components,
6. a non-isothermal model is employed that comprises an energy balance and two mass-balance equations, one for the water component and one for the total mass,
7. creeping flow ($\text{Re} \ll 1$) is assumed, allowing the application of Darcy's law for multiple phases,
8. a static capillary-pressure / saturation relationship without hysteresis is considered,
9. the influence of dispersion is neglected.

Hydrodynamic dispersion is linked to heterogeneities of flow velocities caused by differences in the pore sizes and the flow path lengths. It is neglected in the presented numerical studies due to the assumption of slow flow velocities and comparatively high diffusion coefficients in the gas phase.

Mass balance

The mass conservation in Ω^{pm} is expressed by two mass-balance equations, one for each component $\kappa \in \{w, a\}$,

$$\sum_{\alpha \in \{l, g\}} \phi \frac{\partial (\varrho_{\alpha} X_{\alpha}^{\kappa} S_{\alpha})}{\partial t} + \nabla \cdot \mathbf{F}_m^{\kappa} - \sum_{\alpha \in \{l, g\}} q_{\alpha}^{\kappa} = 0 \quad (4.2)$$

where the mass fluxes of the components are given by

$$\mathbf{F}_m^{\kappa} = \sum_{\alpha \in \{l, g\}} \left(\varrho_{\alpha} \mathbf{v}_{\alpha} X_{\alpha}^{\kappa} - D_{\alpha, \text{pm}}^{\kappa} \varrho_{\alpha} \nabla x_{\alpha}^{\kappa} \frac{M^{\kappa}}{M} \right). \quad (4.3)$$

This involves the Darcy velocity \mathbf{v}_{α} of the fluid phase α , and the given source or sink terms q_{α}^{κ} . Since compressible fluids are considered, the phase densities ϱ_{α} depend on pressure, temperature and fluid composition.

The gas phase is assumed to be an ideal gas and the formulations proposed in IAPWS (2009) and Reid et al. (1987) are used for the properties of the air-vapor mixture. Fickian diffusion (Fick, 1855) is assumed and a binary system with equimolar diffusion is considered where the diffusion coefficients of both components within one phase are equal, $D_{\alpha}^w = D_{\alpha}^a = D_{\alpha}$, and where $\nabla x_{\alpha}^w = -\nabla x_{\alpha}^a$. However, due to the tortuous pathways in the porous material, a component cannot diffuse freely but is constrained by the geometry of the pore space. Hence, effective diffusion coefficients $D_{\alpha, \text{pm}}$ are used, which are based on the properties of the porous material (porosity, tortuosity) and of the fluids (saturation, binary diffusion coefficients). For this purpose, different approaches can be employed.

Here, the effective diffusion coefficient for phase α in the porous medium $D_{\alpha, \text{pm}}$ is approximated as

$$D_{\alpha, \text{pm}} = \tau \phi S_{\alpha} D_{\alpha}. \quad (4.4)$$

The dimensionless tortuosity τ can be estimated as proposed in Millington and Quirk (1961):

$$\tau = \phi^{1/3} S_{\alpha}^{7/3}.$$

Thus, the effective diffusion coefficient $D_{\alpha,\text{pm}}$ depends in a nonlinear manner on the unknown saturation S_α , see Figure 4.3a.

By summing up the mass-balance equations (4.2) of the two components with $X_\alpha^w + X_\alpha^a = 1$ and the assumption of binary diffusion, the total mass-balance equation is obtained,

$$\sum_{\alpha \in \{l,g\}} \phi \frac{\partial (\rho_\alpha S_\alpha)}{\partial t} + \nabla \cdot \sum_{\alpha \in \{l,g\}} (\rho_\alpha \mathbf{v}_\alpha) - \sum_{\alpha \in \{l,g\}} q_\alpha = 0 \quad (4.5)$$

where the source/sink term is composed of the component sources, $q_\alpha = q_\alpha^w + q_\alpha^a$. It is possible to choose equivalently two of the three equations (4.2) for $\kappa \in \{w, a\}$ and (4.5) for a complete model description. The choice of the total mass balance and a mass-balance equation of one of the components leads to a simpler system and reduces nonlinearity.

Energy balance

Subject to the requirement of slow flow velocities, local thermal equilibrium ($T_l = T_g = T_s = T$) is assumed throughout the porous medium. Hence, only a single energy-balance equation has to be solved (Class et al., 2002). It considers the storage of heat in the fluid phases and in the porous material, convective heat fluxes in the two fluid phases, an effective heat conduction within all phases, and the heat sources q_h within the domain:

$$\sum_{\alpha \in \{l,g\}} \underbrace{\phi \frac{\partial (\rho_\alpha u_\alpha S_\alpha)}{\partial t}}_{\text{storage in fluids}} + \underbrace{(1 - \phi) \frac{\partial (\rho_s c_s T)}{\partial t}}_{\text{storage in solid phase}} + \nabla \cdot \mathbf{F}_T - q_h = 0, \quad (4.6)$$

with the internal energy $u_\alpha = h_\alpha - p_\alpha / \rho_\alpha$, the soil density ρ_s , the heat capacity c_s of the solid porous material and the external heat source or sink term q_h .

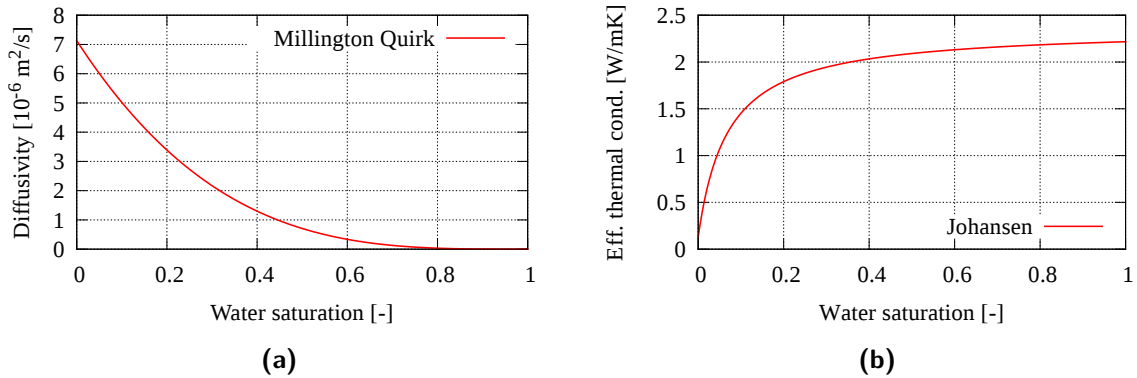


Figure 4.3: (a) Effective diffusion coefficient for vapor in the gas phase in the porous medium. (b) Effective thermal conductivity after Johansen and Somerton.

The heat flux is composed of convective heat fluxes in the fluid phases and the effective heat conduction within all phases and is defined as

$$\mathbf{F}_T = \sum_{\alpha \in \{l, g\}} \varrho_\alpha h_\alpha \mathbf{v}_\alpha - \underbrace{\lambda_{\text{pm}} \nabla T}_{\text{eff. heat conduction}}, \quad (4.7)$$

with the specific phase enthalpy h_α , which is a given function of temperature T and phase pressure p_α . For the component air, the simple relationship $h^a(T) = 1005(T - 273.15 \text{ K})$ is employed, while for the component water, the accurate thermodynamic formulation of the International Association for the Properties of Water and Steam (IAPWS, 2009) is used. The enthalpy of the composite gas phase h_g is evaluated as sum of the component enthalpies weighted by their mass fractions:

$$h_g = X_g^w h^w + X_g^a h^a. \quad (4.8)$$

This inherently accounts for the energy of vaporization in case of a phase change. Only little amounts of air dissolve in the liquid phase under the conditions which are of interest, having only negligible influence on the water phase properties. Thus, the water phase enthalpy is simply approximated as the enthalpy of pure water, $h_l = h^w$.

The main modification to the general energy balance (Equation (2.3.3)) is the introduction of effective quantities for the thermal conductivity and molecular diffusivity. Similar to the effective diffusivity in the component mass balance, the thermal conductivity λ_{pm} is described as effective quantity accounting for heat conduction within all phases. Due to the wetting behavior of water, the thermal conductivity is usually a nonlinear function of the water saturation. It can be computed according to Johansen (1977) as

$$\lambda_{\text{pm}} = \lambda_{\text{dry}} + K_e(\lambda_{\text{sat}} - \lambda_{\text{dry}}). \quad (4.9)$$

λ_{dry} and λ_{sat} are the effective thermal conductivity of a completely dry and an entirely wet porous medium, K_e is usually a nonlinear function of the water saturation and can be approximated according to Côté and Konrad (2005) and Smits et al. (2010) as

$$K_e = \kappa S_l / (1 + (\kappa - 1) S_l) \quad (4.10)$$

where κ is an empirical fitting parameter accounting for the influence of the grain size distribution and S_l is the water saturation (liquid). In this analysis, $\kappa = 15.6$ is chosen, a value which was fitted to a similar sand as used in the drying experiments in Zürich, (30/40 loose) in Smits et al. (2010).

For the description of the saturated thermal conductivities, different averaging techniques

and semi-empirical relations may be used (Smits et al., 2010). One option is to estimate the water-saturated thermal conductivity as geometric mean of the thermal conductivity of the solid and the liquid phase as

$$\lambda_{\text{eff},l} = \lambda_s^{1-\phi} \lambda_w^\phi.$$

For very dry conditions a more accurate approximation has been developed in Johansen (1977):

$$\lambda_{\text{eff},g} = \frac{0.135 \varrho_b + 64.7}{\varrho_s - 0.947 \varrho_b},$$

with the dry bulk density ϱ_b and the mean density of the solid material ϱ_s .

The local thermodynamic equilibrium, which is assumed in the porous-medium domain, is composed of mechanical, thermal and chemical equilibrium. First analyses regarding the local thermal non-equilibrium within the porous medium have been made in the scope of a Diploma thesis (Geiges, 2009). Based on the findings, the local thermal equilibrium is regarded as a valid assumption in the porous medium for the considered system. However, this assumption may not hold at the interface to the free flow, especially if the free stream velocity is high. As temperature significantly influences the evaporation process, an ill-founded assumption of local thermal equilibrium can lead to a wrong estimation of the evaporation rate. This remains subject to further research.

Supplementary equations and constitutive relations

The balance equations and the equations of state for the porous-medium region have been presented. So far, this system of equations contains more unknowns than equations and hence, supplementary equations and constitutive relations have to be stated. To close the system, the following supplementary equations and constitutive relationships are useful:

1. phase saturations: $S_g = 1 - S_l$,
2. capillary pressure: $p_c(S_l) = p_g - p_l$ with a given capillary-pressure / saturation-relationship where the *van-Genuchten* (2.14) or *Brooks-Corey* (2.13) parametrization may be employed.
3. relative permeabilities: $k_{r\alpha}(S_l)$ with a given relationship between relative permeabilities and liquid saturation, where the *Brooks-Corey* law is often used in conjunction with the *Burdine* model (2.15), whereas the *van-Genuchten* parametrization is usually combined with the *Mualem* model (2.16), as described in Section 2.1.5,
4. mass and mole fractions: $X_\alpha^w + X_\alpha^a = x_\alpha^w + x_\alpha^a = 1$ where $\alpha \in \{l, g\}$,

5. mass and mole fractions can be converted with the help of the molar masses M^κ according to

$$X_\alpha^\kappa = x_\alpha^\kappa M^\kappa / (x_\alpha^w M^w + x_\alpha^a M^a) \quad (4.11)$$

where $\alpha \in \{l, g\}$, $\kappa \in \{w, a\}$,

6. Dalton's law: $p_g = p_g^w + p_g^a$, introducing the partial pressures p_g^κ .

Then, primary variables are selected and the secondary variables have to be expressed in dependency on the chosen primary variables. If both fluid phases are present, one possible choice of primary variables is the pressure of the gas phase p_g , the saturation of the liquid phase S_l and the temperature T . This selection of primary variables allows to specify conditions for the gas-phase pressure at the interface where usually atmospheric conditions prevail and is favorable for the modeling of evaporation processes from porous media. Due to the assumption of a local chemical equilibrium, the mass fractions can be calculated as secondary variables of p_g and T with the help of the following relations:

1. Henry's law can be used for the computation of the equilibrium mole fraction of air in the liquid phase x_l^a , due to a relatively small air concentration in the water phase. It reads

$$x_l^a = \frac{p_g^a}{H_{gl}^a} \quad (4.12)$$

where $H_{gl}^a(T)$ is the temperature-dependent Henry coefficient for the component air in the liquid-gas mixture.

2. The Kelvin equation accounts for the lowered saturated vapor pressure due to capillarity effects:

$$p_{\text{sat,Kelvin}}^w = p_{\text{sat}}^w \exp\left(-\frac{p_c}{\rho_l R_l T}\right) \quad (4.13)$$

where $p_{\text{sat}}^w(T)$ is the saturated vapor pressure and R_l the individual gas constant of water vapor. However, this effect has only an influence at very high capillary pressures, see Figure 2.6b and can be neglected. The saturated vapor pressure is calculated after IAPWS (2009).

3. The partial pressure p_g^w is assumed to be equal to the vapor pressure $p_{\text{sat,Kelvin}}^w$ as consequence of the chemical equilibrium, which results in the relationship

$$x_g^w = \frac{p_{\text{sat,Kelvin}}^w}{p_g}. \quad (4.14)$$

For the coupling to the free flow, the porous-medium model (4.2)-(4.6) has to be completed by appropriate interface and boundary conditions for the primary unknowns at the domain boundaries.

4.2.2 Model concept in the free-flow domain

In the free flow, the following setup is chosen:

- single-phase flow is considered (for evaporation the gas phase is selected: $\alpha = g$),
- analogous to the porous-medium domain, the gas phase is composed of the two components water (w) and air (a),
- four equations are solved: two scalar mass-balance equations (one for the water component and one for the total mass), one vector-valued momentum-balance equation and one energy-balance equation,
- binary diffusion is considered.

For the sake of consistency, the same notation and constitutive relations as in the porous medium are used wherever possible.

Balance equations for mass, momentum and energy conservation

The equations presented in the following are formulated for laminar flow conditions. An extension to turbulent condition is presented in Section 4.3.4. With the mass fractions of the components in the gas phase X_g^κ , one mass balance equation for each component $\kappa \in \{w, a\}$, can be defined:

$$\frac{\partial (\varrho_g X_g^\kappa)}{\partial t} + \nabla \cdot \mathbf{F}_m^\kappa - q_g^\kappa = 0 \quad (4.15)$$

where the mass flux of vapor is given by

$$\mathbf{F}_m^\kappa = \varrho_g \mathbf{v}_g X_g^\kappa - D_g^\kappa \varrho_g \nabla x_g^\kappa \frac{M^\kappa}{M}. \quad (4.16)$$

The source or sink term of a component is denoted as q_g^κ . A compressible and ideal gas phase is considered, as it was done in the porous medium. The phase density ϱ_g depends on pressure, temperature and the fluid composition and the ideal gas law is used as equation of state. Moreover, Fick's first law of diffusion (Fick, 1855) is used while assuming a binary system with equal molecular diffusion coefficients for the two components within one phase:

$D_g^w = D_g^a = D_g$. Based on these assumptions and conditions and with $X_g^w + X_g^a = 1$, the sum of the two component balance equations (4.15) yields the total mass-balance equation

$$\frac{\partial \varrho_g}{\partial t} + \nabla \cdot (\varrho_g \mathbf{v}_g) - q_g = 0 \quad (4.17)$$

where the source or sink term is given by $q_g = q_g^w + q_g^a$. As in the porous medium, one can choose two of the three balances (4.15) for $\kappa \in \{w, a\}$ and (4.17) for a complete model description.

The momentum balance is described by the Navier-Stokes equation considering gravity to be the only external force:

$$\frac{\partial (\varrho_g \mathbf{v}_g)}{\partial t} + \nabla \cdot \mathbf{F}_v - \varrho_g \mathbf{g} = 0. \quad (4.18)$$

The matrix-valued momentum flux is defined as

$$\mathbf{F}_v = \varrho_g \mathbf{v}_g \mathbf{v}_g + p_g \mathbf{I} - \boldsymbol{\tau}_g, \quad (4.19)$$

with the $d \times d$ identity tensor \mathbf{I} and the shear stress tensor $\boldsymbol{\tau}$. By introducing the deformation tensor $\mathbf{D} = \frac{1}{2} (\nabla \mathbf{v}_g + \nabla \mathbf{v}_g^T)$ and employing Newton's law, the stress tensor $\boldsymbol{\tau}_g$ can be written as

$$\boldsymbol{\tau}_g = 2\mu_g \mathbf{D} - \underbrace{(\lambda_d \nabla \cdot \mathbf{v}_g)}_{\text{dilatation}} \mathbf{I}. \quad (4.20)$$

Here, $\lambda_d = -\frac{2}{3}\mu_g$ can be assumed as coefficient for dilatation (Truckenbrodt, 2008a). However, the influence of dilatation is not considered in the sequel.

The combination of equations (4.18) and (4.20) and with a neglect of the nonlinear inertia term ($\varrho_g \mathbf{v}_g \mathbf{v}_g$) term and dilatation, the laminar and unsteady Stokes equation is obtained:

$$\frac{\partial (\varrho_g \mathbf{v}_g)}{\partial t} + \nabla \cdot (p_g \mathbf{I} - \mu_g (\nabla \mathbf{v}_g + \nabla \mathbf{v}_g^T)) - \varrho_g \mathbf{g} = 0. \quad (4.21)$$

In a first step the system in the free-flow region Ω^{ff} is simplified by assuming slow flow conditions, neglecting the nonlinear inertia forces expressed by the ($\varrho_g \mathbf{v}_g \mathbf{v}_g$) term and dilatation, and considering unsteady Stokes flow. Neglecting the inertia term is a simplification that is done in order to demonstrate the free flow concept on the basis of a comparatively simple model. For the analysis of the free-flow processes in Section 6.3 the inertia term is included and the algebraic turbulence model described in the subsequent section is used.

As the component mass balance equation, the energy-balance equation in the free flow is

almost identical to the general energy balance (2.3.3) and reads

$$\frac{\partial(\rho_g u_g)}{\partial t} + \nabla \cdot \mathbf{F}_T - q_h = 0, \quad (4.22)$$

with the internal energy of the gas phase u_g and the heat flux defined as

$$\mathbf{F}_T = \rho_g h_g \mathbf{v}_g - \lambda_g \nabla T - \sum_{\kappa \in \{w, g\}} D_g^\kappa \rho_g \nabla x_g^\kappa \frac{M^\kappa}{M} h_g^\kappa \quad (4.23)$$

where λ_g is the heat conductivity of the gas, h_g is the gas enthalpy and q_h are heat sources or sinks. An additional term in comparison to the heat flux in the porous medium occurs: the heat transfer due to mass diffusion (last term in Equation 4.23). Within the porous medium, this effect is assumed to be accounted for in the effective thermal conduction. Furthermore, this term is usually small and can be neglected, when the concentration gradients are relatively small. However, it may become important at the interface between porous medium and free flow where strong gradients may prevail. The gas enthalpy and internal energy are calculated in the same way as in the porous domain, see Section 4.2.1.

For the free-flow subdomain, the following supplementary relations are used:

1. mass and mole fractions: $X_g^w + X_g^a = x_g^w + x_g^a = 1$,
2. conversion between mass and mole fractions (4.11) for $\alpha = g$.

The model has to be completed by appropriate boundary and initial conditions for the primary unknowns.

4.3 Interface conditions and coupled model

A proper coupling of the two domains requires the specification of meaningful interface conditions. The challenge is to find coupling conditions in form of volume-averaged quantities, which still account for the pore-scale processes. Therefore, a coupling concept has been developed (Mosthaf et al., 2011) and is explained in the following. The concept is based on the balance equations and primary variables of the subdomain models, which have been described before. The coupling conditions will be elaborated on in the following. Some of them are based on the work presented in Layton et al. (2002).

As stated before, assumptions are made based on phenomenological explanations to simplify the description of the interface and to get as close as possible to a so-called simple interface (Hassanizadeh and Gray, 1989). Figure 4.4 illustrates the processes on the pore scale: mass, momentum and energy exchange between the three phases of the porous medium and the gas

phase in the free-flow domain. These conditions join the REV-scale models for the porous medium (Section 4.2.1) and the free-flow (Section 4.2.2).

The coupling of the single-phase two-component free-flow system and the two-phase two-component porous-medium system is based on the assumption of a local thermodynamic equilibrium on the interface of the two domains. However, due to the use of different model concepts in the two subdomains, a rigorous thermodynamic equilibrium, consisting of a mechanical, thermal and chemical equilibrium, cannot be completely achieved. Based on phenomenological explications, assumptions are made that result in conditions that are physically meaningful and as close to thermodynamic equilibrium as possible. This leads to a relatively simple and solvable model that accounts for the main physics at the interface.

Local *mechanical equilibrium* (equilibrium of forces) is given by

- the continuity of the normal stresses (4.25c) resulting in a possible jump in the gas-phase pressure,

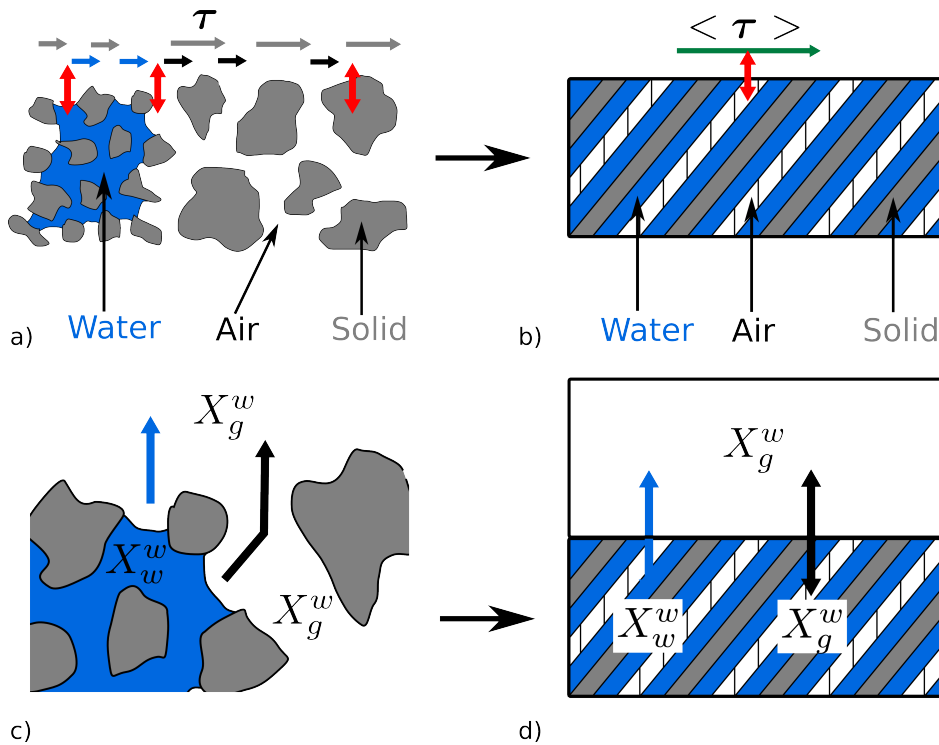


Figure 4.4: Transition from a pore-scale to a volume-averaged description: a) on the pore scale shear stresses occur due to interactions between the gas phase in the free-flow region and the gas, fluid and solid phases in the porous medium, b) a volume-averaged description has to account for all these contributions while the different phases of the porous medium are not locally resolved anymore, c) exchange processes also occur between the two mobile phases of the porous medium and the free gas phase (pore-scale description), d) on the REV scale coupling conditions account for these processes without resolving them locally.

- the continuity of the normal mass fluxes (4.27),
- a condition for the tangential component of the free-flow velocity. Here, the Beavers-Joseph-Saffman condition (4.26) is used, despite its limitations to single-phase parallel flow, its empirical character and the difficulty of determining the Beavers-Joseph coefficient.

Local *thermal equilibrium* is given by

- the continuity of temperature (4.28),
- the continuity of the normal heat fluxes (4.29).

Local *chemical equilibrium* is defined through the continuity of the chemical potential in the gas phase. In the case of a continuous pressure, this would result in the continuity of the mole fractions at the interface. However, due to the pressure jump arising from the continuity of normal stresses and the use of different concepts in the two sub-domains, continuity of chemical potential cannot be presumed. Nevertheless, continuity of the mole fractions at the interface is assumed, see coupling condition (4.32), and note that this results in a possible discontinuity of the chemical potential. Furthermore, the continuity of the component fluxes (4.33) across the interface is required.

Based on the physical equilibrium equations, the mathematical and numerical interface model is developed in Section 5. Figures 4.5 to 4.9 illustrate the conditions of thermodynamic equilibrium on the pore scale and their representation on the REV scale. The pore-scale processes are simplified and shown for illustrative reasons only. Their purpose is to help to understand the phenomenological explanations for the presented coupling conditions.

4.3.1 Mechanical equilibrium

On the pore scale, the mechanical equilibrium at the interface has to be formulated between the gas phase in the free flow and the gas, solid and water phase in the porous medium (see Figure 4.5). On the REV scale, one condition has to be found that satisfies the equilibrium between the gas phase in the free-flow region and all three phases in the porous medium, since the spatial distribution of phases within one REV is not resolved anymore.

For this purpose, the interface traction is decomposed into its normal and tangential contribution. The normal component of the traction tensor of a Newtonian fluid at the interface is given by

$$\boldsymbol{\sigma} \mathbf{n} = (\rho_g \mathbf{v}_g \mathbf{v}_g - p_g \mathbf{I} + \boldsymbol{\tau}) \mathbf{n}. \quad (4.24)$$

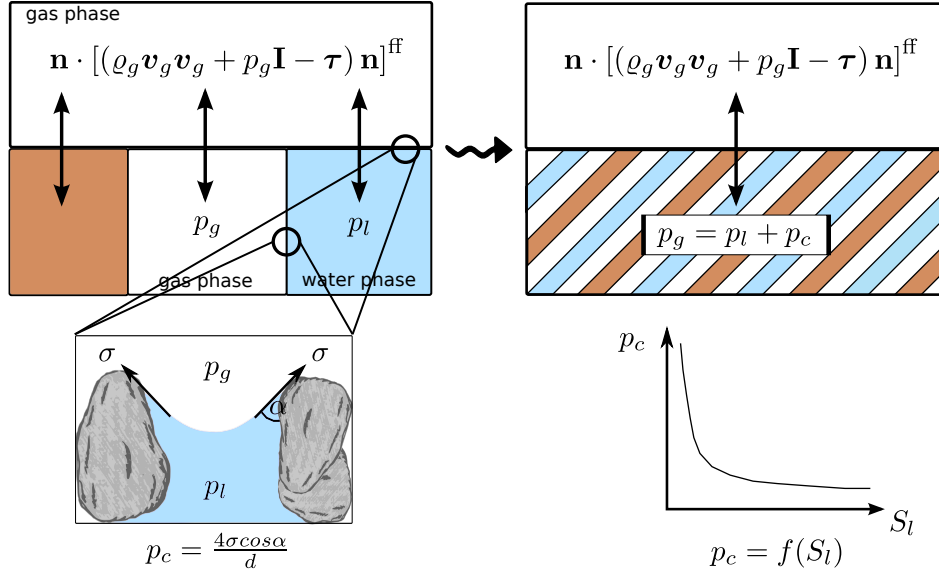


Figure 4.5: Mechanical equilibrium on the pore scale and on the REV scale (normal component). The coupling conditions on the REV scale have to account for the traction between the gas phase in the free-flow region and the gas, solid and water phase in the porous medium. Capillarity effects occur at the interface between the fluid phases in the porous medium as well as at the interface to the gaseous free-flow region. On the REV scale, capillary pressure is a function of the water saturation.

It acts as a surface load on the fluid volume inside Ω^{ff} . Thus, the force on the interface Γ is equal to $-\sigma \mathbf{n}$. At the porous-medium side of the interface, slow flow velocities are assumed and Darcy's law is used. Hence, viscous stresses τ have not to be treated explicitly since they are already accounted for in the Darcy velocity, see e.g. Whitaker (1999). Consequently, only the pressure forces acting on Γ have to be taken into account in Ω^{pm} . Under the assumption of a rigid solid phase and no-slip at the solid-phase surface, no interface condition between gas phase and solid phase needs to be formulated. Mechanical equilibrium between the gas phases in the two domains is represented by the continuity of momentum fluxes shown in equation (4.25a). Here, A_g denotes the contact area between the free gas phase and the gas phase in the porous medium. In order to identify the coupling conditions between the liquid and the gas phase across the interface, the pore scale processes must be considered.

In the porous medium, capillarity effects occur at the gas-liquid interface (see Figure 4.5) due to interfacial tension. On the pore scale, the result is a pressure discontinuity across the interface of the two fluids which is defined as capillary pressure, see Section 2.1.5. The pore-scale capillarity is transferred to the REV-scale by considering macroscopic capillarity through the capillary-pressure / saturation relation $p_c(S_l) = p_g - p_l$, which was introduced in Section 4.2.1. Note that capillarity effects occur at the interface of the gas and liquid phase in the porous medium as well as at the interface A_l of water filled pores and the gaseous free-flow

region (see Figure 4.5). Following the same reasoning as inside the porous-medium region, the gas phase at the free-flow side of the interface has to balance the sum of the water pressure and the capillary pressure (see equations (2.12) and (4.25b)). Hence, involving the normal traction (4.24), equation (4.25c) results as coupling condition representing the continuity of normal forces at the interface on the REV scale.

$$\mathbf{n} \cdot [A_g((\rho_g \mathbf{v}_g \mathbf{v}_g + p_g \mathbf{I} - \boldsymbol{\tau}) \mathbf{n})]^{ff} = [p_g A_g]^{pm} \quad (4.25a)$$

$$\mathbf{n} \cdot [A_l((\rho_g \mathbf{v}_g \mathbf{v}_g + p_g \mathbf{I} - \boldsymbol{\tau}) \mathbf{n})]^{ff} = \underbrace{[(p_l + p_c) A_l]^{pm}}_{p_g} \quad (4.25b)$$

$$(4.25a) + (4.25b) \quad \mathbf{n} \cdot [(\rho_g \mathbf{v}_g \mathbf{v}_g + p_g \mathbf{I} - \boldsymbol{\tau}) \mathbf{n}]^{ff} = [p_g]^{pm} \quad (4.25c)$$

In the perspective of the free-flow model, coupling condition (4.25c) can be seen as Neumann-like boundary condition for the normal component of the free-flow velocity (4.18), combined with the condition for the tangential component (4.26) as Robin-like boundary condition. Alternatively, (4.25c) can be employed in (4.5) as Dirichlet-like boundary condition for the pressure in the porous medium.

The capillary pressure at the interface in (4.25b) might be different from the capillary pressure inside the porous medium. This difference in the capillary pressure is assumed to be negligible and the same capillary-pressure / saturation relation as inside the first layer of the porous medium is applied. However, note that in case of a fully water-saturated porous medium, the capillary pressure p_c at the interface to the gaseous free flow is equal to the entry pressure p_c^d , while the capillary pressure within the porous medium is not defined (see Figure 4.6) due to the absence of the gas phase. Hence, the gas-phase pressure in the porous medium in equation (4.25c) is equal to $p_g = p_w + p_c^d$. Due to condition (4.25c), the pressure is possibly discontinuous at the interface, and thus, a jump in the pressure-dependent variables, such as

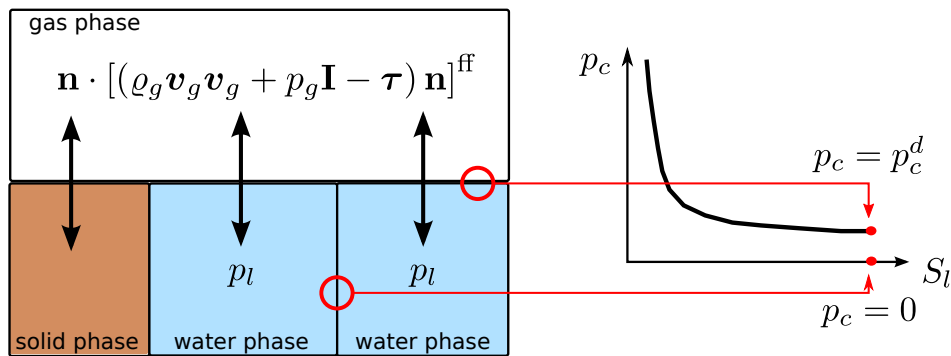


Figure 4.6: For a fully water-saturated porous medium ($S_l = 1$) the capillary pressure inside the porous medium is zero, while it equals the entry pressure at the interface to the gaseous free-flow region.

density and viscosity, can be expected. Naturally, pressure is a continuous thermodynamic property. The discontinuity arises from the use of different model concepts and causes a first perturbation of the thermodynamic equilibrium. Note that (4.25c) is exactly the pressure drop in the artificial boundary condition derived in (Heywood et al., 1996).

Additionally, a condition for the tangential component of the velocity in the free-flow domain is required. Therefore, the same lines as Beavers and Joseph (1967) are followed. They state that the slip velocity along the interface is proportional to the shear stress at the interface. With the simplification of Saffman (1971), who neglects the small tangential velocity in the porous medium at the interface, the Beavers-Joseph-Saffman condition can be written as

$$\left[\left(\mathbf{v}_g + \frac{\sqrt{k_i}}{\alpha_{\text{BJ}} \mu_g} \boldsymbol{\tau} \mathbf{n} \right) \cdot \mathbf{t}_i \right]^{\text{ff}} = 0, \quad i \in \{1, \dots, d-1\} \quad (4.26)$$

where \mathbf{t}_i , $i \in \{1, \dots, d-1\}$, denotes a basis of the tangent plane of the interface Γ . The parameter k is the corresponding component of the porous-medium permeability and equals $k_i = (\mathbf{K} \mathbf{t}_i) \cdot \mathbf{t}_i$. Equation (4.26) can be implemented as Neumann-like or Dirichlet-like condition for (4.18). The Beavers-Joseph condition is analyzed for its applicability for turbulent conditions in Hahn et al. (2002). The authors come to the conclusion, that the slip condition for laminar and turbulent flow conditions is the same, because the flow velocity at the interface is still low and laminar conditions can be expected there in many cases. Furthermore, the parameters α_{BJ} and k_i in the Beavers-Joseph condition have no dependency on the flow conditions.

The Beavers-Joseph coefficient α_{BJ} has to be determined numerically or experimentally for each specific porous medium and should be valid for a two-phase system. Figure 4.7 illustrates that the Beavers-Joseph coefficient should account for the traction between the gas phase in the free-flow region and the gas, solid and water phases in the porous medium. With a difference in viscosity between gas and water of two orders of magnitude, the no-slip condition is assumed to be valid not only for the solid phase but also for the liquid-phase surface. Thus, the Beavers-Joseph coefficient is also a function of the water saturation S_l . The correct determination of the Beavers-Joseph coefficient for two-phase systems is a demanding task, which may be tackled by pore-scale modeling and with the help of physical measurements. However, it remains to be seen whether the tangential velocity at the free-flow side of the interface has a significant influence on the evaporation process. If numerical experiments will show a significant impact of this condition, (4.26) might be replaced by a more sophisticated condition, e.g. derived from volume-averaging theory, in order to account more precisely for the influence of the multi-phase behavior, the surface roughness, the boundary layer and of the shear stresses at the interface. First numerical results with a laminar free-flow model

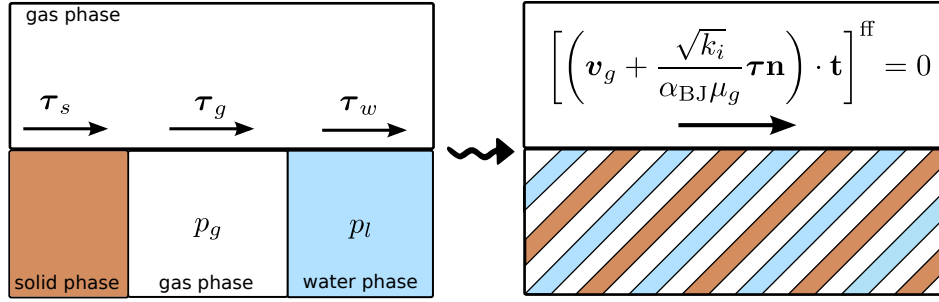


Figure 4.7: Mechanical equilibrium at the pore scale and at the REV scale (tangential component). The coupling conditions on the REV scale have to account for the traction between the gas phase in the free-flow region and the gas, solid and water phase in the porous medium.

coupled to the porous-medium system indicate, that only extremely small values of α_{BJ} have a significant impact on the transfer fluxes, as will be shown in Section 6.4.

Finally, to fulfill the mechanical equilibrium, the continuity of fluxes across the interface has to be guaranteed. Due to the use of a simple interface which cannot store mass, the mass balance requires the sum of the fluxes at the interface to be equal to zero. In the free-flow region, one phase is present, whereas in the porous medium both fluid phases have to be taken into account. In general, the flux of the liquid phase does not vanish at the interface, but it is assumed that the normal water flux evaporates directly at the transition to the free flow and releases its enthalpy of vaporization. Hence, the gas phase in the free-flow region takes up both the gas and liquid mass flux and the continuity equation for the normal phase fluxes reads

$$[\varrho_g \mathbf{v}_g \cdot \mathbf{n}]^{\text{ff}} = - [(\varrho_g \mathbf{v}_g + \varrho_l \mathbf{v}_l) \cdot \mathbf{n}]^{\text{pm}}. \quad (4.27)$$

This relationship can be used as Dirichlet-like boundary condition for the free-flow velocity in (4.18). Alternatively, if the total mass balance (4.5) is used in the porous medium, it may be used as condition for p and S .

4.3.2 Thermal equilibrium

The assumption of local thermal equilibrium at the interface provides two continuity conditions for the primary variable T and for the associated heat flux,

$$[T]^{\text{ff}} = [T]^{\text{pm}} (= [T]_{\alpha}^{\text{pm}} = [T]_s^{\text{pm}}) \quad (4.28)$$

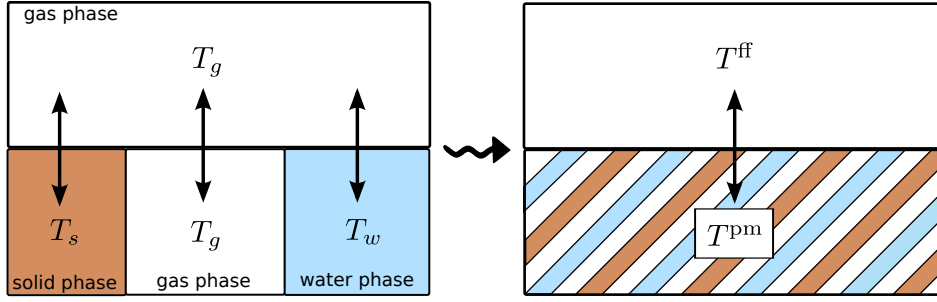


Figure 4.8: Thermal equilibrium on the pore scale and on the REV scale. On the pore scale, the gas phase in the free-flow region and the two fluid phases and the solid phase in the porous-medium may have a different temperature. On the REV scale, thermal equilibrium between the phases inside the porous medium is assumed and continuity of temperature is applied as coupling condition between the gas phase in the free flow and porous medium.

and

$$\left[\left(\varrho_g h_g \mathbf{v}_g - \lambda_g \nabla T - \sum_{\kappa} D_g^{\kappa} \varrho_g \nabla x_g^{\kappa} \frac{M^{\kappa}}{M} h_g^{\kappa} \right) \cdot \mathbf{n} \right]^{\text{ff}} = - [(\varrho_g h_g \mathbf{v}_g + \varrho_l h_l \mathbf{v}_l - \lambda_{\text{pm}} \nabla T) \cdot \mathbf{n}]^{\text{pm}}. \quad (4.29)$$

As it is assumed that the normal water flux from the porous medium evaporates completely and immediately at the interface (see equation (4.27)) the enthalpy of vaporization is included in (4.29) to account for the phase change. The energy transfer due to evaporation from the water phase and due to diffusive mass flow in the gaseous phase is accounted for due to the computation of the gas phase enthalpy as the sum of the component enthalpies, $h_g = X_g^w h^w + X_g^a h^a$. A diffusive component flux in the gas phase is manifested as a change of the phase composition and the mass fractions change, leading to an alteration of the gas phase enthalpy. The last term on the left side of Equation 4.29 is shown only for the sake of completeness. However, the heat flux due to diffusive vapor flux in the gas phase is not explicitly considered further in the energy balance at the interface.

In the perspective of the submodel, condition (4.28) can be seen as Dirichlet-like boundary condition for the temperature T in one of the equations (4.6) or (4.22), while condition (4.29) can be applied as Robin-like boundary condition for T for one of these two equations, with an additional nonlinear influence on the pressure via $\varrho_g(p_g, T, X)$ in the case of a compressible gas phase. For alternatives to the thermal equilibrium condition the reader is referred to Alazmi and Vafai (2001).

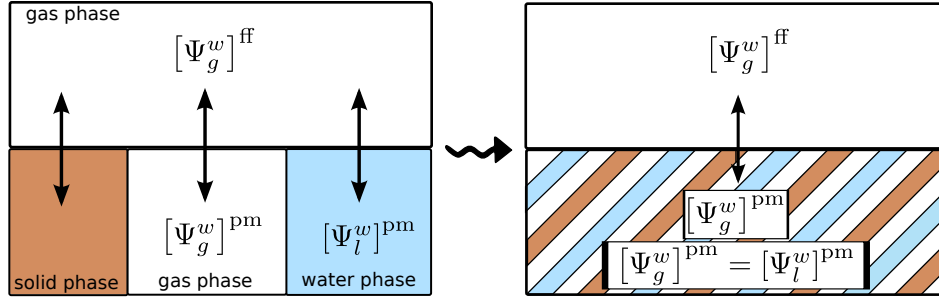


Figure 4.9: Chemical equilibrium at the pore scale and at the REV scale. On the pore scale, equilibrium conditions between the gas phase in the free-flow region and the two phases in the porous medium have to be formulated, consisting of continuity of chemical potential. On the REV scale, continuity of chemical potential between the phases inside the porous medium is assumed and continuity of mass fractions is applied as coupling condition between the gas phase in the free flow and porous medium.

4.3.3 Chemical equilibrium

The chemical equilibrium at the interface can be considered as an equilibrium between three compartments and two phases (see Figure 4.9). On the pore scale, the equilibrium for the chemical potentials of the component water ψ_α^w , $\alpha \in \{l, g\}$, can be stated from pair-wise considerations corresponding to Figure 4.9, under the assumption that the gas phase is separated by the interface,

$$[\psi_g^w]^{\text{ff}} = [\psi_l^w]^{\text{pm}}, \quad (4.30a)$$

$$[\psi_g^w]^{\text{ff}} = [\psi_g^w]^{\text{pm}}. \quad (4.30b)$$

In the subdomain model, the equilibrium between the gas and the liquid phase within the porous medium, $[\psi_l^w]^{\text{pm}} = [\psi_g^w]^{\text{pm}}$, is already satisfied (see Section 4.2.1). As a consequence, only (4.30b) has to be imposed at the interface. On the REV scale however, continuity of the chemical potential cannot be postulated since the continuity of the normal forces (4.25c) leads to a jump in the gas-phase pressure. As already stated before, this pressure difference is due to differences in the model concepts applied in the subdomains. More precisely, it is due to the application of the potential theory in the porous-medium region where shear stresses are not explicitly resolved anymore. These small differences in pressure cause discontinuities in the chemical potentials and/or discontinuous mole fractions. Assuming all components to be ideal, the difference in the chemical potential (Atkins and De Paula, 2006) can be written as

$$\psi^{\text{ff}}(p_g^{\text{ff}}) - \psi^{\text{pm}}(p_g^{\text{pm}}) = \left[\mathbb{R}T \ln \left(x_g^w \frac{p_g}{p_0} \right) \right]^{\text{ff}} - \left[\mathbb{R}T \ln \left(x_g^w \frac{p_g}{p_0} \right) \right]^{\text{pm}} = \ln \left(\frac{[x_g^w p_g]^{\text{ff}}}{[x_g^w p_g]^{\text{pm}}} \right)^{\mathbb{R}T} \quad (4.31)$$

where p_0 is the reference pressure and \mathbb{R} is the universal gas constant. However, the magnitude of the difference in chemical potential is not known and a condition for the mole fractions cannot be deduced. Therefore the continuity of the mole fractions is assumed and employed as a coupling condition:

$$[x_g^\kappa]^{\text{ff}} = [x_g^\kappa]^{\text{pm}}, \quad \kappa \in \{a, w\}. \quad (4.32)$$

By taking into account the conversion between mass and mole fractions (4.11) for $\alpha = g$, the coupling condition (4.32) can be employed as Dirichlet-like condition for X_g^w in (4.15). Alternatively, it can be used via the relationships (4.13),(4.14) as a nonlinear coupled boundary condition for p_g , S_l and T in (4.2).

Naturally, the continuity of the component fluxes across the interface is required for $\kappa \in \{w, a\}$:

$$\begin{aligned} & \left[\left(\varrho_g \mathbf{v}_g X_g^\kappa - D_g \varrho_g \nabla x_g^\kappa \frac{M^\kappa}{M} \right) \cdot \mathbf{n} \right]^{\text{ff}} = \\ & - \left[\left(\varrho_g \mathbf{v}_g X_g^\kappa - D_{g,\text{pm}} \varrho_g \nabla x_g^\kappa \frac{M^\kappa}{M} + \varrho_l \mathbf{v}_l X_l^\kappa - D_{l,\text{pm}} \varrho_l \nabla x_l^\kappa \frac{M^\kappa}{M} \right) \cdot \mathbf{n} \right]^{\text{pm}}. \end{aligned} \quad (4.33)$$

Based on the same reasoning as for the total mass fluxes, the component fluxes within both fluid phases of the porous medium that flow across the interface are added and balanced with the component fluxes in the gas phase of the free flow. Summing up equations (4.33) for $\kappa \in \{w, a\}$ results in the continuity of total mass flux (4.27). Two of the three conditions (4.27),(4.33) can be equivalently chosen according to the set of balance equations that is used in the submodels.

If applied to the free-flow domain, the conditions for the continuity of component fluxes are Robin conditions for X_g^κ in (4.15). For the porous-medium part, one can consider the constitutive relations (4.11),(4.12) for the liquid phase and (4.11),(4.13),(4.14) for the gas phase to arrive at two nonlinear coupled conditions for p , S and T in (4.2).

Note that the diffusion coefficients in both domains differ from each other. For the free-flow domain, the binary diffusion coefficient D_g (dependent on temperature and pressure) is used, whereas for the porous medium, the diffusion coefficients $D_{\alpha,\text{pm}}$ are functions of the properties of the soil and the fluids. Furthermore, if the liquid phase at the porous-medium side of the interface disappears, the coupling simplifies to a single-phase two-component system. Then, water can only be transferred by vapor diffusion and by advective transport in the gas phase across the interface between free flow and the porous-medium system.

4.3.4 Extension to turbulent flow conditions

In the context of evaporation from porous media, different flow conditions have to be considered: laminar and turbulent flow. Laminar flow can be simulated with relatively simple models. Conversely, a turbulent flow field is usually highly irregular with chaotic fluctuations of the local velocity, pressure, and transported quantities like concentrations and temperature (Bird et al., 2007). This is caused by vortices, also called turbulent eddies hereinafter, which are in general acting in all three space dimensions. Turbulent eddies occur on a wide range of length scales: the largest eddies may be in the order of the domain size, whereas the smallest eddies are related to the kinematic fluid viscosity and the rate of energy dissipation, which quantifies the conversion of the smallest eddies into heat. The large eddies carry most energy, which is transferred in a hierarchy (energy cascade) from large to smaller eddies. The *Kolmogorov microscale* (Kolmogorov, 1941) defines the spatial scale of the smallest eddies in turbulent flow. It depends on the kinematic fluid viscosity and the rate of energy dissipation.

The laminar (viscous) sublayer for turbulent flows is usually considerably thinner as for laminar flow, which has a strong effect on exchange of mass, momentum and head at the interface between porous medium and free flow, as will be shown later (Section 6.3). Modeling turbulent flow is challenging, because also the smallest eddies have to be captured to obtain physically meaningful results. A lot of work has been done in the field of turbulence modeling, and a variety of models for turbulent flow is available. An exact solution of the flow field is obtained with *direct numerical simulation* (DNS), which solves the detailed Navier-Stokes equations. However, DNS needs to resolve all possible length scales, on which eddies may occur and is usually restricted to small model domains because it has very high computational costs. For engineering and environmental applications, numerically less demanding methods are commonly employed, which do not resolve all details of the flow field. One such method is the *large eddy simulation* (LES) in which a so-called low-pass filter is employed to sort out the smallest eddies, which are then accounted for in a time- and space-averaged fashion, and only the larger eddies are resolved and simulated.

An even less-detailed but widely used model is the *Reynolds-averaged Navier-Stokes* model (RANS). For RANS models, the system is simplified by decomposing the pressure and the velocity components in a time-smoothed mean value \bar{v}_x and the fluctuations v'_x (Pope, 2000; Bird et al., 2007), as, by way of example, shown for the x-component of the velocity:

$$v_x = \bar{v}_x + v'_x. \quad (4.34)$$

This is termed *Reynolds decomposition*. Then, these mean values and fluctuations are averaged over time. The terms in which fluctuations are multiplied by the mean value disappear,

because the time-average of the temporal fluctuations is zero. However, the terms with the multiplication of two fluctuating quantities do not vanish.

Inserting the decomposed velocity in the Navier-Stokes equations leads to the *time-smoothed Navier-Stokes equations*, which contain the turbulent momentum flux due to the velocity fluctuations as additional term:

$$\frac{\partial}{\partial t} \rho \bar{\mathbf{v}} = -\nabla \bar{p} - \nabla \cdot \rho \bar{\mathbf{v}} \bar{\mathbf{v}} - \nabla \cdot \bar{\boldsymbol{\tau}} - \underbrace{\nabla \cdot \bar{\boldsymbol{\tau}}^{(t)}}_{\text{turbulent momentum flux}} + \rho \mathbf{g}. \quad (4.35)$$

The time-smoothed Navier-Stokes equations contain additional terms, which are related to the local velocity fluctuations; these terms are usually referred to as *Reynolds stresses*. These stresses are depending in a highly complex manner on the position and the turbulence intensity (Bird et al., 2007); their representation poses one of the biggest challenges for turbulence modeling. A multitude of models with different complexity has been developed for the approximation of the Reynolds-stress terms. For a closure of the system of equations, empirical or statistical methods are often employed.

It is distinguished between zero-equation, one-equation and two-equation models depending on the number of partial differential equations used for the approximation of the Reynolds stresses. The k - ϵ and k - ω models are examples for widely used two-equation approximations, which employ a partial differential equation for the turbulent kinetic energy k and for the energy dissipation ϵ . The zero-equation approximations are the simplest models and employ algebraic expressions for the Reynolds stresses. They rely on the following assumptions:

- the flow has one main direction,
- the flow field is fully developed,
- turbulence acts isotropic.

Several zero-equation models have been analyzed in the scope of a Diploma thesis (Fetzer, 2012) where different algebraic expressions for the eddy coefficients (Prandtl, 1904; van Driest, 1956; Hanna and Sandall, 1972; Schlichting and Gersten, 2006; Deissler, 1954; Baldwin and Lomax, 1978) were tested and analyzed for their applicability to reproduce a given velocity field and for their inclusion into the framework of the coupled model.

All algebraic model employ the Bussinesq assumption (Boussinesq, 1872), which treats the local velocity fluctuations in the same manner as viscous stresses and relates them to the velocity gradient:

$$\bar{\boldsymbol{\tau}}^{(t)} = -\mu^{(t)} \nabla \bar{\mathbf{v}}. \quad (4.36)$$

For this purpose, the turbulent eddy viscosity $\mu^{(t)}$ is introduced as additional proportionality factor. A widely-used and simple approach for the viscous stresses is the mixing-length approach of Prandtl (1904). He considers a mixing length l , which is in analogy to the mean free path employed in kinetic gas theory for low density gases:

$$\mu^{(t)} = \varrho l^2 \left| \frac{d\bar{v}_x}{dz} \right|. \quad (4.37)$$

The mixing length is not constant but depends on the distance z from the bounding surface (wall). It is defined with help of the *Karman* constant $\kappa = 0.41$ as $l = \kappa z$. This approach served as basis for many concepts, which were developed later on.

One of these enhancements is the model proposed in van Driest (1956) and further modified according to Hanna and Sandall (1972), which is chosen as turbulence model in Section 6.3:

$$\mu^{(t)} = \varrho \kappa^2 \frac{(1 - \exp(-z^+/A^+))^2}{1 - \exp(-B^+ z^+)} \left| \frac{\partial v_x}{\partial z} \right|. \quad (4.38)$$

In order to account for the increased transport of vapor and energy in the turbulent flow field, an eddy diffusivity $D^{(t)}$ and eddy thermal conductivity $\lambda^{(t)}$ is defined along the lines of the eddy turbulent viscosity. The following relations are employed for the products of fluctuating quantities in the sequel:

- momentum transport: $\overline{\varrho \mathbf{v}' \mathbf{v}'} \approx -\mu^{(t)} \nabla \bar{\mathbf{v}}$
- component transport: $\overline{\varrho \mathbf{v}' X^{\kappa'}} \approx -D^{(t)} \varrho \nabla \bar{x}^{\kappa} \frac{M^{\kappa}}{M}$
- energy transport: $\overline{\varrho \mathbf{v}' h'} \approx -\lambda^{(t)} \nabla \bar{T}$

In the following, the averaging sign above the time-averaged values is not employed anymore. The above listed conditions can be integrated in the balance equations for mass, momentum and energy presented before. For more details on turbulent flows, the reader is referred to the multitude of text books available in this research field, as for example Bird et al. (2007); Incropera et al. (2007a); Truckenbrodt (2008a,b); Wilcox (2006); Ferziger and Peric (2002); White (2000); Pope (2000).

Inclusion of these relations modifies the diffusive and conductive flux terms in the flux expressions of the free flow. The flux terms are then extended to

$$\mathbf{F}_m^{\kappa} = \varrho_g \mathbf{v}_g X_g^{\kappa} - \left(D_g^{\kappa} + D^{(t)} \right) \varrho_g \nabla x_g^{\kappa} \frac{M^{\kappa}}{M}, \quad (4.39)$$

and

$$\mathbf{F}_h = \varrho_g \mathbf{v}_g h_g - (\lambda_g + \lambda^{(t)}) \nabla T. \quad (4.40)$$

Again, different models can be employed for the computation of the eddy diffusivity and thermal conductivity: The simplest one is the Reynolds analogy, which assumes that eddy thermal diffusivity is directly related to the eddy viscosity. Different other options have been tested in Fetzer (2012) and the most promising one has been employed for the cases where the simulations are run using a turbulent free flow: the model proposed in Deissler (1963).

In the numerical simulations, which study the influence of porous-medium parameters in Section 6.2, laminar flow conditions are considered in the free-flow region Ω^{ff} in combination with a boundary-layer approximation, as explained later. Then, the eddy coefficients are zero and the Reynolds stress terms vanish.

4.3.5 Coupling conditions with turbulent free flow

The integration of a RANS model into the coupling framework requires small adaptations of the coupling conditions. For this purpose, the eddy coefficients (eddy kinematic viscosity, eddy diffusivity, eddy thermal conductivity) are included in the flux terms of the free flow. This inclusion modifies the normal traction at the free-flow side of the interface to:

$$\begin{aligned} \boldsymbol{\sigma} \mathbf{n} &= (\varrho_g \mathbf{v}_g \mathbf{v}_g - p_g \mathbf{I} + \boldsymbol{\tau}) \mathbf{n} \\ &= \left(\varrho_g \mathbf{v}_g \mathbf{v}_g - p_g \mathbf{I} + (\mu_g + \mu_g^{(t)}) \nabla (\mathbf{v}_g + \mathbf{v}_g^T) \right). \end{aligned} \quad (4.41)$$

It has to be noted, that the eddy coefficients directly at the interface are in general zero and these additional terms can be omitted in the coupling conditions. However, for the sake of completeness, they are shown here.

When the turbulent eddy thermal conductivity $\lambda^{(t)}$ is included, the continuity of heat fluxes reads:

$$\left[(\varrho_g h_g \mathbf{v}_g - (\lambda_g + \lambda^{(t)}) \nabla T) \cdot \mathbf{n} \right]^{\text{ff}} = - [(\varrho_g h_g \mathbf{v}_g + \varrho_l h_l \mathbf{v}_l - \lambda_{\text{pm}} \nabla T) \cdot \mathbf{n}]^{\text{pm}}. \quad (4.42)$$

An inclusion of the turbulent eddy diffusivity $D_g^{(t)}$ leads to a definition of the continuity of

component fluxes as

$$\begin{aligned} & \left[\left(\varrho_g \mathbf{v}_g X_g^\kappa - (D_g + D_g^{(t)}) \varrho_g \nabla x_g^\kappa \frac{M^\kappa}{M} \right) \cdot \mathbf{n} \right]^{\text{ff}} = \\ & - \left[\left(\varrho_g \mathbf{v}_g X_g^\kappa - D_{g,\text{pm}} \varrho_g \nabla x_g^\kappa \frac{M^\kappa}{M} + \varrho_l \mathbf{v}_l X_l^\kappa - D_{l,\text{pm}} \varrho_l \nabla x_l^\kappa \frac{M^\kappa}{M} \right) \cdot \mathbf{n} \right]^{\text{pm}}. \end{aligned} \quad (4.43)$$

4.4 Summary of this chapter

This chapter presented a detailed model concept based on flux continuity and on a local thermodynamic equilibrium for the coupled simulation of free flow and porous-medium flow. The submodels in the porous medium and in the free flow were introduced, starting with laminar flow conditions in the free flow. Then, an eddy-viscosity concept was included in the free flow to account for turbulence effects using an algebraic zero-equation turbulence model. The coupling conditions were explained in detail. In the next chapter, the integration of the coupling concept into a numerical framework is explained.

5 Numerical model concept

The objective of this chapter¹ is to provide the mathematical model and details of the numerical implementation of the coupled model, which has been elaborated in Chapter 4. We have published the numerical model in Baber et al. (2012) and parts of this chapter are repetitions thereof. At the beginning of this chapter the discretization scheme is presented (Section 5.1), supplemented by the choice of primary variables (Section 5.2) and the handling of the interface and boundary conditions (Section 5.3). At the end of this chapter details on the employed computational algorithm and the employed software framework (Section 5.4) are given.

5.1 Discretization scheme

For the discretization of the concept developed in the previous chapter, different more or less complex discretization methods as, for example, the Discontinuous Galerkin approach (Girault and Rivi re, 2009) are available. Here, the control-volume finite-element method (CV-FEM), also called *box method* (Masson et al., 1994; Huber and Helmig, 2000; Baber et al., 2012), is used in both subdomains Ω^{ff} and Ω^{pm} for the spatial discretization of the problem in combination with an implicit Euler scheme for the time discretization. The chosen method has the advantage of being relatively simple while guaranteeing local mass conservation. Especially for the free flow, however, more advanced discretization methods are available, as will be discussed later. In a first step, a simple and well-established scheme is chosen for the demonstration of the developed coupling concept and for the numerical studies presented in Chapter 6, which can be used as a benchmark for later developments. The optimization of the numerical scheme and a more efficient implementation of the coupling concept, involving for example a domain decomposition (Discacciati et al., 2007) and a different time stepping (Soares et al., 2010) in the subdomains, remains subject to future work.

In the box method, the model domain is covered by a dual mesh where a finite-element grid forms the primal mesh. The approach combines the advantages of the finite-element and finite-volume method. All primary variables are stored and computed at the vertices, which

¹The numerical model was published in Baber et al. (2012) and is partly taken from there.

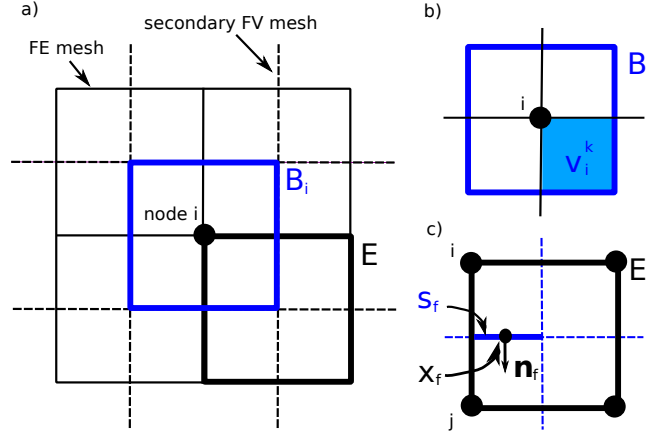


Figure 5.1: Schematic description of the spatial discretization (box scheme). b) shows a control volume (box) assigned to node i , c) depicts an element.

are situated at the corners of the elements and which represent the surrounding control volume. The secondary mesh, which describes the finite volumes is obtained by connecting the centers of gravity of each element with the associated edge midpoints. Thus, each finite volume is associated with a vertex, as schematically shown in box B_i in Figure 5.1a. The finite-element mesh divides the boxes B_i into subcontrol volumes v_i^k (see Figure 5.1b. A *control volume* is the amalgamation of all subcontrol volumes attached to a vertex.

A quadrilateral grid is considered where all primary variables are approximated with piecewise bilinear functions. These bilinear functions are mapped from the standard-reference-element basis functions. The equations are integrated over control volumes and the divergence theorem is applied. The method of weighted residuals with piecewise constant weighting functions characteristic for box B_i and mass lumping of the accumulation terms leads to the general discretized form for one box B_i :

$$|B_i| \frac{\hat{u}_i^{n+1} - \hat{u}_i^n}{\Delta t} + \sum_{f \in s(i)} \mathbf{F}_A(\tilde{u}^{n+1}(x_f)) \cdot \mathbf{n}_f |s_f| + \sum_{f \in s(i)} \mathbf{F}_D(\tilde{u}^{n+1}(x_f)) \cdot \mathbf{n}_f |s_f| - |B_i| q_i^{n+1} = 0 \quad (5.1)$$

where $|B_i|$ is the volume of box B_i , \hat{u}_i^{n+1} is the solution at node i with u standing for one of the primary variables listed in Table 5.1, $s(i)$ are the subcontrol-volume faces of the box B_i , \mathbf{n}_f is the unit outward normal of the respective subcontrol-volume face in direction of the neighboring node j , $|s_f|$ is the size of the subcontrol-volume face, and q_i^{n+1} is the source or sink term. Equation (5.1) consists of storage, flux and source/sink terms. The fluxes may be composed of an advective and a diffusive part \mathbf{F}_A , \mathbf{F}_D and are computed on the control-volume boundaries s_f at the integration points x_f , as illustrated in Figure 5.1c.

A finite-element approximation is done for each gradient and each primary variable required

for the evaluation of flux terms,

$$\tilde{u}^{n+1}(x_f) = \sum_{k \in \eta_E} N_k(x_f) \hat{u}_k^{n+1}, \quad (5.2)$$

$$\nabla \tilde{u}^{n+1}(x_f) = \sum_{k \in \eta_E} \nabla N_k(x_f) \hat{u}_k^{n+1} \quad (5.3)$$

where η_E are the nodes of the element E and $N_k(x_f)$ are the finite-element Ansatz-functions. Furthermore, a fully-upwind scheme is applied to the advective part of the equations, whereas diffusive terms are usually centrally weighted. Following the general procedure employed for finite-element methods, local operators are assembled for each element and then merged to a local stiffness matrix for the entire domain. This means, that the discretized equations are evaluated element-wise, looping over the subcontrol volumes inside an element E (see Figure 5.1c). In the following, the left-hand side of the equations is referred to as the *residuum* \mathbf{R} . The residuum corresponds to the assembled discretized equations for one node including storage term, fluxes from the neighboring vertices and source and sink terms.

For the discretized form of the mass-balance equation in the porous medium, the box method yields:

$$\begin{aligned} & \sum_{\alpha \in l, g} |B_i| \Phi_i \frac{(\varrho_{\alpha i} \hat{S}_{\alpha i})^{n+1} - (\varrho_{\alpha i} \hat{S}_{\alpha i})^n}{\Delta t} \\ & - \sum_{f \in s(i)} \sum_{\alpha \in l, g} \left(\varrho_{\alpha} \frac{k_{r\alpha}}{\mu_{\alpha}} \right)_{\text{ups}(i,j)}^{n+1} K_{ij} \left(\sum_{k \in \eta_E} (\nabla N_{\alpha k}(x_f) \hat{p}_{\alpha k}^{n+1}) + \varrho_{\alpha i}^{n+1} \mathbf{g} \right) \cdot \mathbf{n}_f |s_f| \\ & - \sum_{\alpha \in l, g} |B_i| q_{\alpha i}^{n+1} = 0. \end{aligned} \quad (5.4)$$

The nonlinear terms appearing in the balance equations, such as relative permeability, fluid viscosity or density, are upstream weighted. The subscript $\text{ups}(i, j)$ is the upstream node depending on the direction of the velocity, which is used for the determination of the upwind direction. Soil parameters are defined at the nodes (representative for one box). With this choice, the intrinsic permeabilities K_{ij} of the neighboring nodes i and j are harmonically averaged.

In the free-flow region, the *box* method employed, which is a collocated method where pressure and velocity are defined on the same spot (the vertex). This leads to possible oscillations in the pressure, resulting from the use of an equal-order approximation for pressure and velocity (Versteeg and Malalasekera, 2007). The chosen discretization does not guarantee full stability and should be exchanged by a more sophisticated discretization, such as a staggered grid (e.g. Versteeg and Malalasekera, 2007) where the pressure and the velocity are evaluated at

different locations. However, to overcome the stability problem with the employed scheme, a similar stabilization technique as the one proposed in Franca et al. is applied to the continuity equation:

$$\begin{aligned}
& |B_i| \frac{\varrho_{gi}^{n+1} - \varrho_{gi}^n}{\Delta t} + \sum_{f \in s(i)} \sum_{k \in \eta_E} \left(N_k(x_f) \hat{\mathbf{v}}_{gk}^{n+1} \right) \cdot \mathbf{n}_f |s_f| + |B_i| q_{gi}^{n+1} \\
& - \underbrace{\sum_{f \in s(i)} \alpha_{\text{stab}} h_f^2 \sum_{k \in \eta_E} \left(\nabla N_k(x_f) \hat{p}_{gk}^{n+1} \right) \cdot \mathbf{n}_f |s_f| - |B_i| \alpha_{\text{stab}} h_f^2 \nabla \cdot \left(\varrho_{gi}^{n+1} \mathbf{g} \right)}_{\text{stabilization}} = 0. \quad (5.5)
\end{aligned}$$

The stabilization terms are obtained by taking the divergence of the Stokes equation $\nabla \cdot (\nabla p_g - \mu \nabla^2 \mathbf{v} - \varrho \mathbf{g})$, multiplied by a stabilization parameter $\alpha_{\text{stab}} h_f^2$, which involves the mesh width h_f .

The Navier-Stokes equation has the following discrete form

$$\begin{aligned}
& |B_i| \frac{(\varrho_{gi} \hat{\mathbf{v}}_{gi})^{n+1} - (\varrho_{gi} \hat{\mathbf{v}}_{gi})^n}{\Delta t} \\
& + |B_i| \sum_{k \in \eta_E} \left(\nabla N_k(\mathbf{v}_i^k) \hat{p}_{gk}^{n+1} \right) \\
& - \sum_{f \in s(i)} (\varrho_g \mathbf{v}_g)_{\text{ups}(i,j)}^{n+1} \left(\tilde{\mathbf{v}}_{gk}^{n+1}(x_f) \cdot \mathbf{n}_f \right) |s_f| \\
& - \sum_{f \in s(i)} \mu_{gi}^{n+1} \sum_{k \in \eta_E} \left(\nabla \left(N_k(x_f) \hat{\mathbf{v}}_{gk}^{n+1} \right) + \nabla^T \left(N_k(x_f)^T \hat{\mathbf{v}}_{gk}^{n+1} \right) \right) \cdot \mathbf{n}_f |s_f| \\
& - |B_i| q_i^{n+1} = 0. \quad (5.6)
\end{aligned}$$

To improve stability further, the pressure term in the Navier-Stokes equation is approximated as gradient in the source/sink term of Equation (5.6) instead of including the absolute value in the flux term. As consequence, the pressure term and the viscous term are of similar order of magnitude.

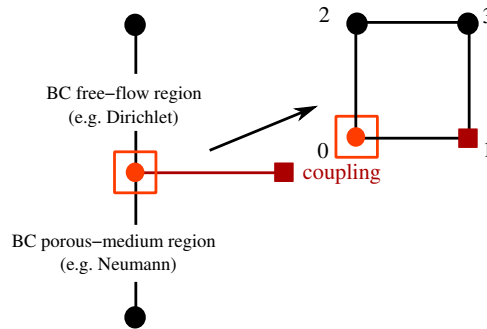


Figure 5.2: Treatment of the nodes where the coupling interface meets the boundaries of the subdomains.

Furthermore, spurious oscillations occur at the corners of the free-flow domain, both at the points where the exterior boundary meets the coupling interface ($\partial\Omega^{\text{ff}} \cap \Gamma$) and at the corners at the top of the domain. The oscillations at the interface nodes are due to the fact that the boundary conditions of the free-flow and the porous-medium domain are linked via the coupling conditions and do not necessarily match (see Figure 5.2). Since temperature and mass fractions are continuous quantities, reasonable boundary conditions can be defined. Due to the discontinuity in the gas-phase pressure origination from Equation (4.25c), oscillations occur which are avoided by replacing the residuum at the corner node by an interpolation as illustrated in Figure 5.2 and thus, depriving the corner node of its degrees of freedom. This procedure is applied only for the mass balance and must not be done if Dirichlet conditions are set for the pressure.

5.2 Primary variables

To solve the system described above, suitable primary variables have to be chosen. In the porous domain Ω^{pm} , the pressure of the gas phase p_g , the saturation of the liquid phase S_l and the temperature T are used. In the case that one phase disappears and there is only a single fluid phase present, the saturations S_l and S_g are constant ($S_l = 0$, $S_g = 1$). Hence, the model (4.2)-(4.6) plus the constitutive equations can be considerably simplified. However, in this case the saturation cannot be used as a primary variable anymore. Possible choices for the numerical algorithm are then a primary-variable switch (Class et al., 2002) or the introduction of additional primary variables and additional constraints in the form of nonlinear complementarity functions, as proposed in Lauser et al. (2011). Recently, Neumann et al. (2013) have proposed to use a phase pressure and the capillary pressure as primary variables as alternative to the variable switch.

For the concept presented here, the option involving a variable switch was selected. If the liquid phase is not present ($S_l = 0$), the liquid saturation is replaced by the mass fraction of water in the gas phase X_g^w as primary variable, which is not calculated via the local chemical equilibrium (saturated vapor pressure) anymore. The switch back to liquid saturation as primary variable is triggered when the partial pressure of vapor in the gas phase exceeds the saturated vapor pressure. Be aware that in the case of a pure gas-phase system X_l^κ is undefined ($\kappa \in \{w, g\}$) and $S_l = 0$, as X_g^κ is not defined for a pure liquid-phase system.

In the free-flow domain Ω^{ff} , the pressure of the gas phase p_g , the mass fraction of water in the gas phase X_g^w , the velocity of the gas phase \mathbf{v}_g and the temperature T are chosen as primary variables. Table 5.1 gives an overview of the primary variables used in the balance equations.

Balance equations	Primary variables
Free-flow region:	
mass balance	p_g
component mass balance	X_g^w
momentum balance	\mathbf{v}_g
energy balance	T_g
Porous medium region:	
mass balance	p_g
component mass balance	
two-phase system	S_l
one-phase system	X_g^w or X_l^a
energy balance	T

Table 5.1: Summary of the balance equations describing the different sub-models and listing of the according primary variables.

5.3 Boundary and coupling conditions

Both the porous-medium (Section 4.2.2) and the free-flow model (Section 4.2.2) have to be completed by appropriate boundary conditions. Based on the chosen set of primary variables (Table 5.1), the boundary conditions can be specified as

$$\begin{aligned}
p_g &= p_D \quad \text{on } \Gamma_D^{\text{pm}}, & \mathbf{F}_m \cdot \mathbf{n} &= \sum_{\kappa} f_N^{\kappa}, \quad \text{on } \Gamma_N^{\text{pm}}, \\
S_l &= S_D \quad \text{on } \Gamma_D^{\text{pm}}, & \mathbf{F}^w \cdot \mathbf{n} &= f_N^w, \quad \text{on } \Gamma_N^{\text{pm}}, \\
T &= T_D \quad \text{on } \Gamma_D^{\text{pm}}, & \mathbf{F}_T \cdot \mathbf{n} &= f_{N,T} \quad \text{on } \Gamma_N^{\text{pm}}
\end{aligned}$$

where $\Gamma^{\text{pm}} = \partial\Omega^{\text{pm}} \setminus \Gamma$, $\Gamma^{\text{pm}} = \Gamma_D^{\text{pm}} \cup \Gamma_N^{\text{pm}}$, $\Gamma_D^{\text{pm}} \cap \Gamma_N^{\text{pm}} = \emptyset$, in the porous medium region, and

$$\begin{aligned}
\mathbf{v}_g &= \mathbf{v}_D \quad \text{on } \Gamma_D^{\text{ff}}, & \mathbf{F}_v \cdot \mathbf{n} &= f_{N,v} \quad \text{on } \Gamma_N^{\text{ff}}, \\
X_g^w &= X_D \quad \text{on } \Gamma_D^{\text{ff}}, & \mathbf{F}^{\kappa} \cdot \mathbf{n} &= f_{N,X} \quad \text{on } \Gamma_N^{\text{ff}}, \\
T &= T_D \quad \text{on } \Gamma_D^{\text{ff}}, & \mathbf{F}_T \cdot \mathbf{n} &= f_{N,T} \quad \text{on } \Gamma_N^{\text{ff}}
\end{aligned}$$

where $\Gamma^{\text{ff}} = \partial\Omega^{\text{ff}} \setminus \Gamma$, $\Gamma^{\text{ff}} = \Gamma_D^{\text{ff}} \cup \Gamma_N^{\text{ff}}$, $\Gamma_D^{\text{ff}} \cap \Gamma_N^{\text{ff}} = \emptyset$, in the free-flow domain. For Neumann conditions, the normal flux across the boundary $\mathbf{F} \cdot \mathbf{n}$ is specified as Neumann flux f_N . Note

that the Neumann flux for the Navier-Stokes equation is defined as

$$\mathbf{f}_{N,v} = \left[\rho_g \mathbf{v}_g \mathbf{v}_g + p_g \mathbf{I} - \mu_g \left(\nabla \mathbf{v}_g + \nabla \mathbf{v}_g^T \right) \right] \mathbf{n}.$$

Since the pressure term is chosen to be discretized as a volume term (see Equation (5.6)), a correction for the pressure contribution has to be applied when a Neumann condition is set for the Stokes equation. The total mass-balance equation in the free flow requires a Dirichlet condition for the pressure in at least one point. For the coupling of the total mass balance equation, an outflow condition is set in the free-flow domain at the interface. The boundary conditions are supplemented by the coupling conditions at the common interface Γ .

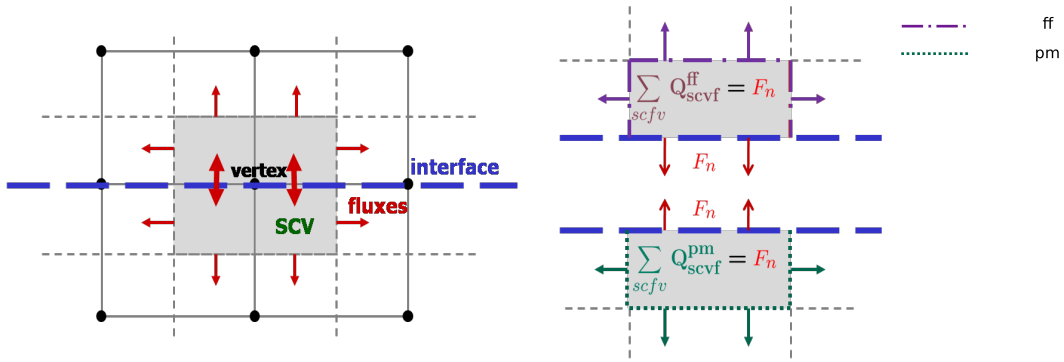


Figure 5.3: Illustration of the spatial discretization (box scheme) at the interface.

At the common boundary of two elements at the interface, a finite-volume box is composed of a free-flow part and a porous-medium part. Figure 5.3 depicts the box discretization at the coupling interface. The interface nodes belong to both domains and thus, contain two different sets of primary variables related to each other by the coupling conditions. In contrast to Neumann-type conditions which enter the weak form in a natural way as term on the right side, Dirichlet-like coupling conditions are imposed in a strong form. For the implementation of Dirichlet-like conditions at the interface, the unknown u replaces the residuum of the respective equation in the domain, for which the condition is set. The unknown of the other domain is introduced via the coupling leading to the desired condition $u^{\text{ff}} = u^{\text{pm}}$.

The implementation of the flux conditions containing gradients at the interface requires a special treatment due to the characteristics of the discretization scheme. The flux conditions (4.29) and (4.33) are third-type or so-called *Robin* conditions which are a combination of the gradient of the primary variables directly at the interface and the primary variable itself. As illustrated in Figure 5.3, these gradients have to be approximated at the interface between two elements and not, as normally done, at the subcontrol-volume faces s_f . At the edge of the elements, however, the gradient of the Ansatz functions is discontinuous causing a bad approximation of the gradients there. As a consequence, the use of gradients on the interface

should be avoided as condition for the other domain.

An alternative approach for calculating the normal fluxes across the interface is based on the fact that the sum of the temporal change in storage and all fluxes across the faces of a control volume has to be zero. Hence, the sum of the storage term and all interior fluxes across the internal subcontrol-volume faces of one control volume at the interface (see fluxes across the dotted line in Figure 5.3) is equal to the normal fluxes across the interface $\mathbf{F} \cdot \mathbf{n}$:

$$\left| \frac{B_i}{2} \right| \frac{\hat{u}_i^{n+1} - \hat{u}_i^n}{\Delta t} + \sum_{f \in s(i)_{\text{internal}}} \mathbf{F}(\tilde{u}^{n+1}(x_f)) \cdot \mathbf{n} \, d\Gamma_{\text{internal}} = \int_{\Gamma} \mathbf{F} \cdot \mathbf{n} \, d\Gamma. \quad (5.7)$$

That means that the flux directly at the interface can be expressed by balancing storage and flux contributions. The calculated normal flux is then added to the right hand side of the respective vertex in the other domain. Note that where the coupling interface touches the boundaries $\partial\Omega \cap \Gamma$, the fluxes across the external boundaries have to be considered in addition to the internal fluxes to balance the fluxes across the interface correctly. Moreover, as it was said before, the pressure has to be interpolated at these corner points.

Summarized interpretation as boundary conditions

Table 5.2 summarizes one possible implementation of the coupling conditions combined with the models describing the free-flow and porous-medium compartments. The interface

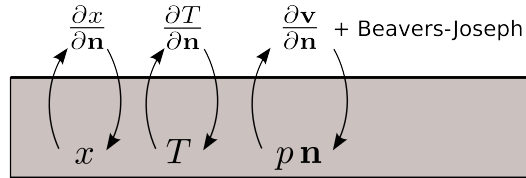


Figure 5.4: Schematic overview of the coupling conditions.

Equilibrium	Property	Porous medium	Free flow
Mechanical:	normal stress (4.25c)		Neumann for $\mathbf{v}_g \cdot \mathbf{n}$
	tangential velocity (4.26)	–	Robin for $\mathbf{v}_g \cdot \mathbf{t}$
Thermal:	temperature (4.28)		Dirichlet for T
	heat flux (4.29)	Robin for T	
Chemical:	mole fraction (4.32)		Dirichlet for X_g^w
	component flux w (4.33)	nonlinear coupled	
	mass flux (4.27)	conditions for p, S, T	

Table 5.2: Interpretation of coupling conditions as boundary conditions in the perspective of the submodels.

conditions play the role of internal boundary conditions for the coupled model, meaning that the information is exchanged simultaneously from the free-flow to the porous-medium side and vice versa.. A consistent combination of Dirichlet and Neumann or Robin conditions is chosen (see Figure 5.4). Note that in the limit case of pure advective transport, the partial differential equations are changing in type and order and so do the coupling conditions. Conditions (4.28) and (4.32) can be removed and the flux conditions (4.27), (4.29) and (4.33) have to be replaced by outflow/inflow conditions. Table 5.2 only represents one of several possible combinations, which is also employed in the numerical simulations presented later. If the solution is known within one subdomain, then the choice presented in Table 5.2 provides well-posed boundary conditions for the opposite subdomain. Setting the mass fraction of vapor in the gas phase as Dirichlet-like condition in the free flow leads to a better convergence behavior. If the mass fraction of vapor was set in the porous medium, a condition would be applied to a secondary variable in case that both fluids are present in the porous medium.

5.4 Computational algorithm

The modeling toolbox *DuMu^x* (DUNE for Multi-{Phase, Component, Scale, Physics, ...}) was chosen as framework for the implementation of the numerical scheme. *DuMu^x* is a free and open-source simulator for flow and transport processes in porous media. It is based on the Distributed and Unified Numerics Environment *DUNE* (Bastian et al., 2008), which provides grids, solvers, discretizations, etc. The main intention of *DuMu^x* is to provide a sustainable and consistent framework for the implementation and application of model concepts, constitutive relations and discretizations (Flemisch et al., 2011) with a focus on porous-medium applications.

The coupled problem (free-flow domain, porous-medium domain and interface) is written in the following operator form

$$\frac{\partial \mathbf{M}(\mathbf{u})}{\partial t} - \nabla \cdot \mathbf{F}(\mathbf{u}) = \mathbf{Q}(\mathbf{u}) \quad (5.8)$$

where $\mathbf{u} = \left(p_g^{\text{ff}}, X_g^{w,\text{ff}}, \mathbf{v}_g^{\text{ff}}, T^{\text{ff}}, p_g^{\text{pm}}, S_l^{\text{pm}} \text{ or } X_g^{w,\text{pm}}, T^{\text{pm}} \right)^T$ is the solution vector, $\mathbf{M}(\mathbf{u})$ is the storage, $\mathbf{F}(\mathbf{u})$ the flux, and $\mathbf{Q}(\mathbf{u})$ the source/sink term. The spatial discretization of the geometric domain and the designation of subdomains are based on the software package *DUNE-Multidomaingrid* (Müthing and Bastian, 2012), which allows to represent arbitrarily complex subdomain shapes with conforming interfaces. The management of the two subdomains and their associated function spaces is done with the help of *DUNE-PDELab* (Bastian et al., 2010), a general discretization framework based on *DUNE*, and its extension *DUNE-Multidomain*,

which allows a transparent definition of local operators and variables on the individual subdomains and supports the assembly of a global system matrix for the coupled problem. So far, a monolithic approach with one global matrix composed of submatrices for the two subdomains and two coupling matrices (see Figure 5.5) is employed.

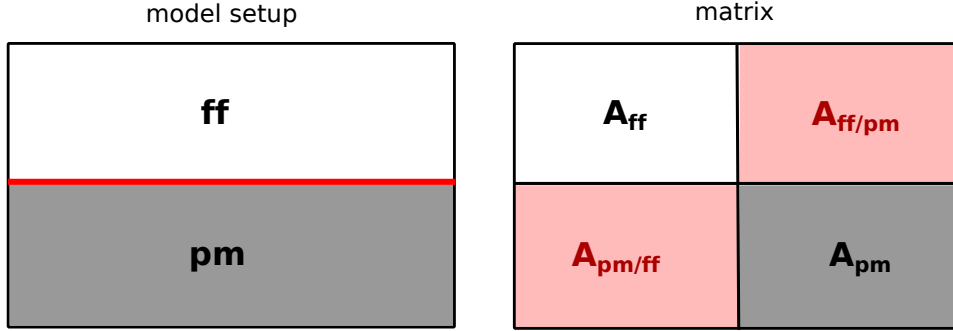


Figure 5.5: Depiction of the global matrix for the coupled system. A_{ff} and A_{pm} stand for the submatrices of the free-flow and porous-medium subproblems. $A_{ff/pm}$ and $A_{pm/ff}$ are the coupling matrices where $A_{ff/pm}$ contains the coupling conditions for the free-flow domain from the porous medium $A_{pm/ff}$ contains the coupling conditions for the porous medium.

The ability to do a full system assembly enables to solve the strongly coupled and highly nonlinear system (5.8) in a fully implicit fashion without any subdomain iteration scheme. While such an iteration scheme might become necessary and beneficial in large-scale applications to efficiently handle the different time scales in the subdomains, the strongly coupled solution is chosen. On the one hand, it eliminates the substantial task of designing, implementing and testing an iteration scheme, and on the other hand, it provides a high-fidelity benchmark solution to compare against future, weakly-coupled simulations.

A standard Newton solver is applied in order to solve the nonlinear algebraic system of equations at each time step,

$$\underbrace{\left(\frac{\partial \mathbf{R}}{\partial \mathbf{u}}\right)_{n+1,m}}_{\mathbf{J}(\mathbf{u}^{n+1,m})} \underbrace{(\mathbf{u}^{n+1,m} - \mathbf{u}^{n+1,m-1})}_{\Delta \mathbf{u}} = -\mathbf{R}(\mathbf{u}^{n+1,m}), \quad (5.9)$$

leading to a relatively stable and robust scheme. In Equation (5.9), $\mathbf{J}(\mathbf{u}^{n+1,m})$ is the Jacobi matrix calculated by numerical differentiation, $\Delta \mathbf{u}$ is the correction to the primary variables \mathbf{u} , and $\mathbf{R}(\mathbf{u}^{n+1,m})$ is the residuum at time-level $n + 1$ and iteration m . The linear problem at each Newton iteration step is solved using one of the direct linear solvers *SuperLU* (Li, 2005) or *Pardiso* (Schenk et al., 2007, 2008). Iterative solvers did not show a good convergence behavior for the given matrix structure, which is not well conditioned. A fully implicit Euler scheme with a heuristic time-step control based on the convergence rate of the Newton solver is employed for the time integration of the coupled system. Therefore, a target number of

Newton iterations N_{target} is defined. Depending on the actual number of iterations N , the new time-step size is chosen:

$$\Delta t^{n+1} = \begin{cases} \Delta t^n \left(\frac{1}{1 + \frac{N - N_{\text{target}}}{N_{\text{target}}}} \right) & N_{\text{max}} > N > N_{\text{target}}, \\ \Delta t^n \left(1 + \frac{N_{\text{target}} - N}{1.2 N_{\text{target}}} \right) & N \leq N_{\text{target}} \end{cases} \quad (5.10)$$

where Δt^n is the time-step size of time step n . The time-step size is halved if convergence is not achieved before N exceeds the maximum number of Newton iterations, N_{max} .

The time scale for the processes and the flow velocities in the two domains differs strongly, thus a multiple time-stepping scheme may drastically reduce the simulation time.

5.5 Summary of this chapter

This chapter provides the mathematical concept and explains the numerical implementation of the submodels and of the coupling concept developed in Chapter ch:ConceptualModel into the modeling environment *DuMur*^x. A monolithic approach is chosen, which uses one global matrix composed of submatrices for the two subdomains and two coupling matrices. As discretization scheme in the two subdomains, the *box* method is used in conjunction with a fully-implicit Euler scheme for the time integration. The discretized form of the balance equations was shown for the mass balance and the momentum balance. One focus of this chapter was on the handling of the coupling conditions at the interface as combination of Dirichlet and flux conditions for the respective subdomains. The numerical algorithm for the solution of the problem was explained. This is the numerical framework for the process and parameter analysis presented in the following chapter.

6 Process analysis and parameter study

This chapter¹ analyzes and discusses the influence of several parameters and processes on the evaporation rates computed with the coupled model presented in Chapter 4 and implemented as described in Chapter 5. First, a reference case with a set of realistic parameters is defined and described in Section 6.1. It is related to the setup of the drying experiments in the wind tunnel presented in Chapter 3. Then, single parameters are varied to analyze their individual effect on the drying behavior. The analysis is divided into three groups:

- parameters and conditions in the porous medium (Section 6.2),
- free-flow parameters (Section 6.3),
- processes and parameters at the coupling interface (Section 6.4).

In the simulations presented in the sequel, the porous medium is always simulated with a non-isothermal two-phase two-component porous-medium model using Darcy's law extended for multiple phases, as described in Section 4.2.1. Model combinations using a different resolution of the free-flow processes are employed for the simulation of evaporation from porous media influence by a free air stream. Naturally, it is not necessary to model all applications with the full model complexity in both flow compartments. As illustrated in Figure 6.1, the porous-medium model is combined with

- a laminar free flow model using the Stokes equations, Figure 6.1a,
- a laminar free flow in conjunction with a boundary layer model (Blasius approximation or constant boundary layer thickness) for a modified computation of the diffusive vapor fluxes across the boundary layer, Figure 6.1b,
- an algebraic turbulence model in the free flow as described in Section 4.3.4, Figure 6.1c.

¹Parts of the following are from a paper (Mosthaf et al., 2013), which has been submitted to Water Resources Research.

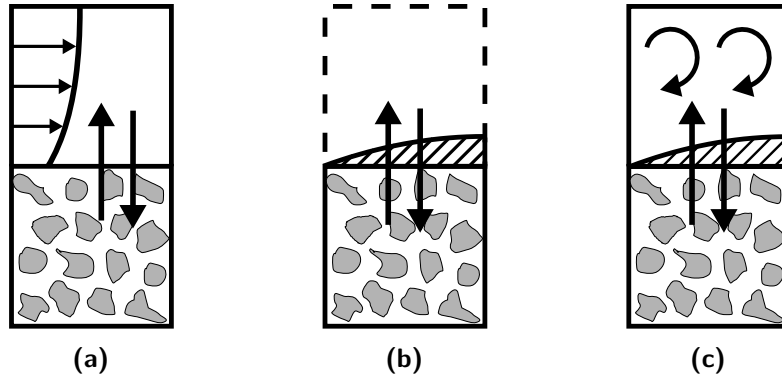


Figure 6.1: (a) Porous-medium model coupled to a laminar free flow, (b) porous-medium model coupled to a laminar free flow with a solution-dependent boundary condition for the diffusive vapor fluxes to account for the boundary layer, (c) porous-medium model coupled to a turbulent free-flow model.

6.1 Description of the reference case

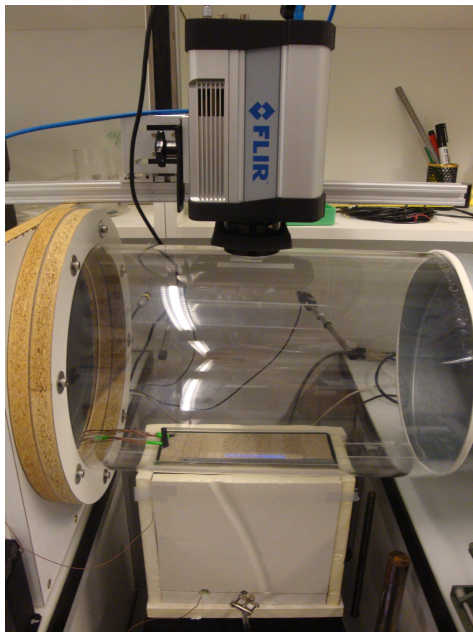
The two-dimensional porous medium (side view) has an extent of $0.25\text{ m} \times 0.25\text{ m}$ according to the setup of the wind-tunnel experiment, as shown in Figure 6.2. Initially, it contains the solid phase and two fluid phases, the liquid water phase and the gaseous air phase, with a uniform water saturation of 98 Vol.-% and a hydrostatic pressure distribution. An initialization time of 864 s without coupling allows the water to distribute within the porous medium according to the prevailing forces (gravity, capillary and viscous forces). The porous medium has closed boundaries on all sides but the top, with a Dirichlet condition for the temperature at the bottom. As solid phase, a quartz sand is considered, of which the porous-medium properties are based on measured values from the drying experiment (see Table 3.1, also summarized as reference case in Table 6.1).

The reference case has been computed with the three combinations listed before: laminar free-flow model, laminar flow with boundary-layer approximation and algebraic turbulence model. In this section, the setup for the cases involving a laminar free-flow model is explained. For the simulations with a turbulent free flow, the free-flow domain has a larger extent and a different grid resolution, as will be shown in Chapter 6.3. Above the porous medium is the equally-sized free-flow compartment with air flowing in a parabolic shape from the inflow on the left to the outflow on the right with a maximum velocity of 3.5 m/s in the center of the air stream. The gas-phase pressure is fixed on the outflow boundary of the free flow. The overall temperature in the inflowing air and in the porous medium is chosen as $25\text{ }^\circ\text{C}$, the mass fraction of vapor in the free flow as $8 \times 10^{-3}\text{ kg/kg}$, which corresponds to a relative humidity of approximately 40%. The temperature and vapor mass fraction are set in a weak form as Neumann boundary condition as $\rho_g \mathbf{v}_g X_g^w$ and $\rho_g \mathbf{v}_g h_g$ with the given velocity and the density

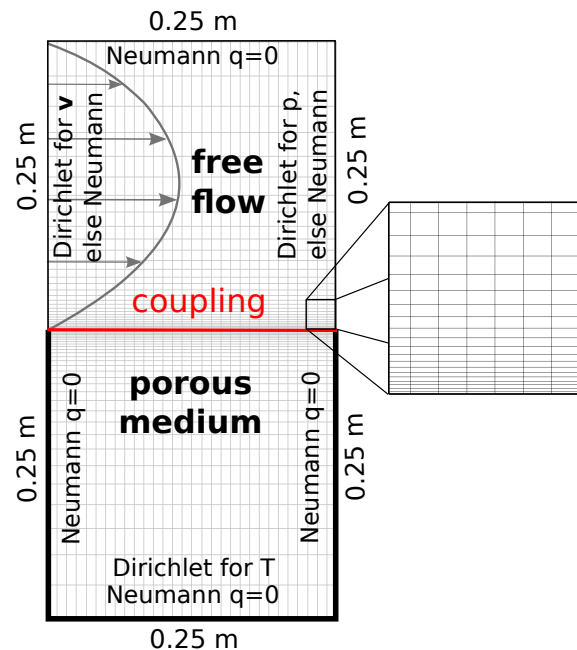
at the given conditions. Dirichlet conditions would create strong and grid-dependent gradients between the corner points where the external boundary meets the interface, resulting in unphysical fluxes.

The following lines summarize the setup of the reference case:

- two-dimensional setup with a total domain size of $0.25\text{ m} \times 0.5\text{ m}$,
- coupling interface at $y = 0.25\text{ m}$, lower part of the domain porous medium, upper part free flow,
- overall temperature of $T = 298.15\text{ K}$ ($= 25\text{ }^\circ\text{C}$),
- initial water saturation in the porous medium of $S_l = 98\%$,
- maximum wind velocity of $v_g = 3.5\text{ m/s}$,
- inflow mass fraction of vapor $X_g^w = 0.008$,
- atmospheric pressure of $P_g = 10^5\text{ Pa}$,
- soil parameters as described in Table 3.1.



(a)



(b)

Figure 6.2: (a) Setup of wind tunnel, insulated sand sample and measurement devices. (b) Model setup with grid and boundary conditions.

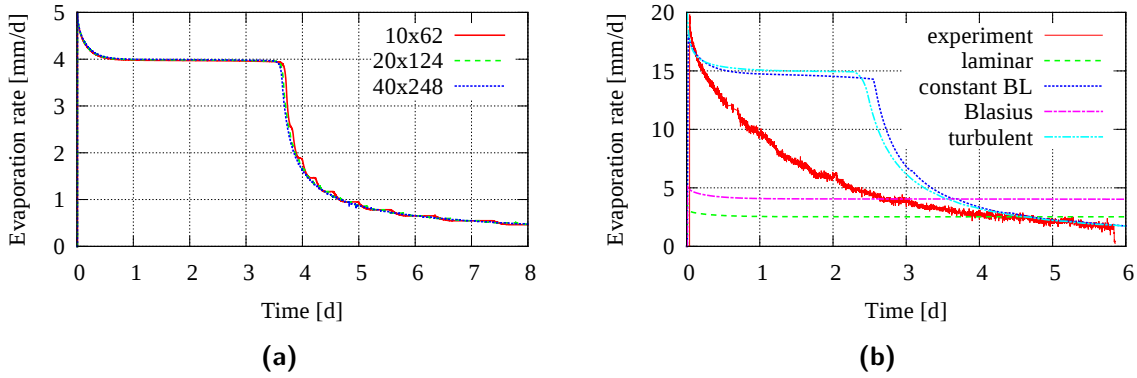


Figure 6.3: (a) Successive grid refinement using the laminar free-flow model coupled to the porous medium, starting with 10×62 cells. The grid is refined (each element is split into four equally-sized elements) twice to a grid with 40×248 cells. The drying curve of the coarsest grid shows small differences to the other two curves. The first and the second refinement level are almost on top of each other. (b) Comparison of a measured drying curve from a wind tunnel experiment with computed drying curves employing a laminar free-flow model, a laminar free flow in combination with a boundary layer approximation (constant boundary layer thickness and Blasius solution) and a turbulent free-flow model.

In the simulations involving the laminar free-flow model, the domain is discretized on a structured grid with 30×62 cells, which is bisected by the interface to two subdomains, the free-flow and the porous-medium domain. Figure 6.2 provides an overview of the employed grid (Figure 6.2b) and boundary conditions and the related experimental setup. The height of the grid cells is refined by a factor of 0.885 towards the coupling interface (see Figure 6.2), because the strongest changes happen there and the processes in the vicinity of the interface are of main interest. A grid convergence study with respect to the computed drying rates has been performed, as depicted in Figure 6.3a. For this purpose, the laminar coupled model without further modification has been employed. With ten cells, the horizontal resolution was lower as in the simulations for the process and parameter study in which thirty cells have been used, while the vertical resolution was the same. The grid was refined by splitting each cell into four equally-sized cells, leading to 40×248 cells, when the grid is refined twice. The chosen grid resolution leads only to minor changes in the computed drying rates after a grid refinement, as illustrated in Figure 6.3a, while keeping the computational efforts in a reasonable range. Even the coarser mesh with 10×62 cells, shows grid convergence and the differences between the computed drying rates at the respective refinement level are comparable to one another. This leads to the conclusion that grid convergence is also satisfied for a higher horizontal resolution of 30×62 cells, which has been employed for several simulations in the course of this study.

Figure 6.4 illustrates the simulated evaporation process in a series of figures where the upper part depicts the mass fraction of vapor in the free flow and the lower part shows the saturation distribution in the porous medium. The arrows in the free flow in Figure 6.4a depict the

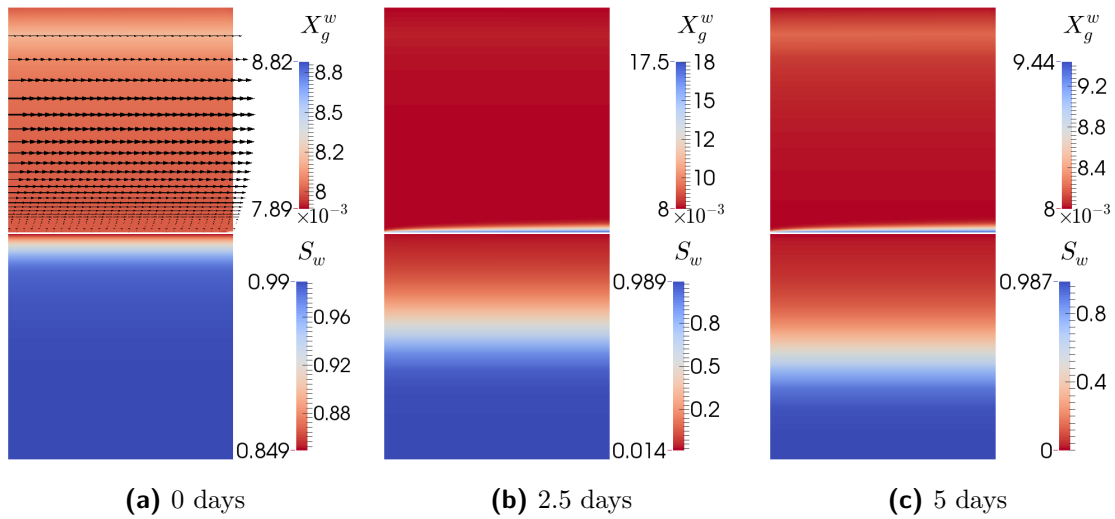


Figure 6.4: Evolution of the mass fraction of vapor in the free-flow domain (upper part of the figure) and of the water saturation in the porous medium (lower part).

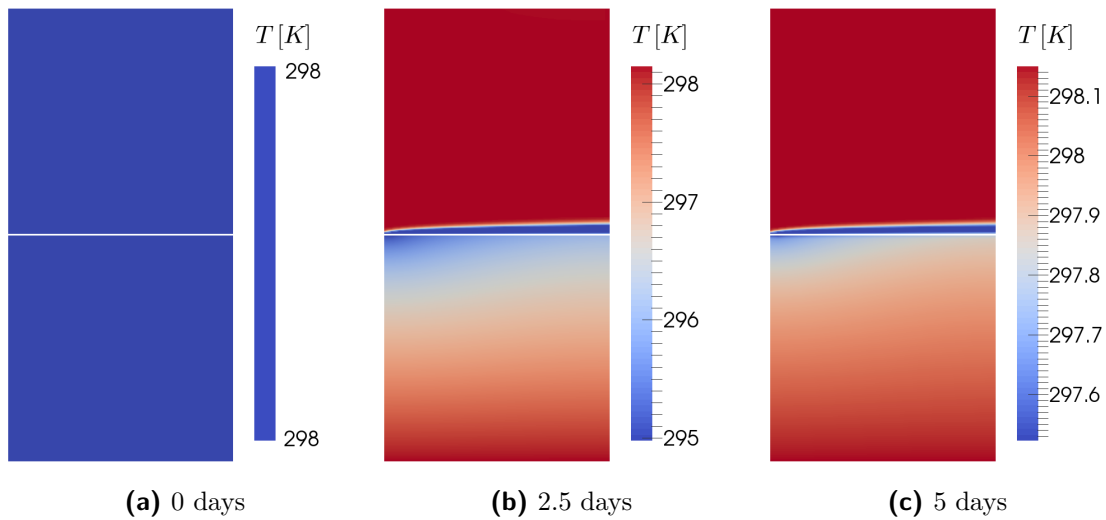


Figure 6.5: Evolution of the temperature in the free-flow domain (upper part of the figure) and in the porous medium (lower part).

velocity vectors of the laminar velocity field showing a parabolic shape. In the presented simulation example, a constant boundary layer was set to compute the diffusive vapor fluxes across the interface. This leads to a relatively even saturation distribution and a relatively uniform drying of the porous medium. Normally, the boundary layer thickness varies along the way, leading to a more non-uniform drying behavior.

The first image in Figure 6.4 shows the saturation distribution after the initialization time, which is lower at the top of the domain, because the water is distributed under the influence of gravity. In the second figure, the porous medium is almost about to dry out at the interface to the free flow. Until then, capillary forces have transported water from deeper regions of the porous medium to the evaporating surface. There, both fluid phases are still present (stage-1), leading to a relatively high vapor concentration. The last figure shows the system in stage-2, when the interface has already dried out and water is transferred exclusively in the gas phase to the free-flow domain. The vapor concentration at the surface of the porous medium is considerably lower then.

Figure 6.5 gives the respective temperature distribution in both domains, showing a uniform temperature at the beginning of the simulation. In stage-1 of the evaporation process, the temperature at the surface of the porous medium decreases approximately by 3 K due to the enthalpy of vaporization, as long as both fluid phases are present and evaporate. In stage-2, when the interface is dry (last figure), the temperature in both domains equilibrates again.

Figure 6.3b shows the computed drying curves for the reference case simulated with these different model combinations in the context of an experimentally determined evaporation curve. With the given air velocity of 3.5 m/s, turbulent conditions can be expected to develop within the free air stream. Assuming laminar flow conditions leads to an underestimation of the exchange fluxes, because the thickness of the boundary layers is overestimated, resulting in a larger concentration and temperature gradient at the interface. Hence, the use of a laminar free flow leads to considerably lower evaporation rates as observed in the drying experiment, as Figure 6.3b demonstrates. Two different boundary layer approximations have been tested: a boundary layer thickness computed with the analytical solution for laminar boundary layers, and a constant boundary layer thickness. As analytical solution, the boundary-layer thickness provided in Blasius (1908) for the growing thickness of a laminar velocity boundary layer above a smooth and flat plate has been employed:

$$\delta_v = \frac{4.91 x}{\sqrt{Re_x}}, \quad (6.1)$$

with the local Reynolds number Re_x which depends on the position x on the interface (characteristic length). Using the dimensionless Schmidt number as explained in Section 2.4.3,

the concentration boundary-layer thickness can be estimated based on the velocity boundary-layer thickness. The Blasius solution leads to a slightly higher drying rate than the laminar free flow model, mainly because the boundary layer with the Blasius approximation starts to evolve from the beginning of the porous sample on whereas in the laminar free-flow model a parabolic laminar velocity profile, as it occurs in a laminar pipe flow, has been set at the inflow. Still, the computed evaporation rate is lower than determined in the wind-tunnel experiment. The rates computed with the constant boundary-layer approximation and with the algebraic turbulence model resemble each other and both match the initial drying rate, but the further course deviates from the measured curve, which continuously decreases.

Indeed, at the beginning of the drying process, the computed drying rates show an initial decrease. This first decrease is mainly due to evaporative cooling of the porous-medium surface, which comes along with a reduction of the saturated vapor pressure and a lower equilibrium concentration of vapor in the gas phase. However, in contrast to the measured drying curve, the initial decrease is followed by a period with a relatively stable drying rate, which decreases only marginally in response to the diminishing water saturation. This period, also termed constant-rate period, could be observed in many experiments and can usually be found for low flow velocities, thick boundary layers and large-pored media (Shahraeeni et al., 2012).

However, several experiments have revealed continuously decreasing drying rates from the beginning of the drying process on without a distinct constant-rate period. According to the model concept presented so far, the water saturation at the surface has only little influence on the drying rate during stage-1. This small influence is mainly due to the effects of the saturation on the effective diffusivity and thermal conductivity. As long as both fluid phases are present, the air at the surface of the porous medium is assumed to be fully vapor-saturated (equilibrium vapor pressure). This results in a relatively constant concentration gradient across the boundary layer at the free-flow side of the interface and to a rather constant drying rate, if the diffusive fluxes at the interface dominate the exchange fluxes. Thus, the saturation-dependency of the drying rate cannot be captured with the model presented so far; this topic will be further addressed in Section 6.4.2.

The drying of the surface with zero water saturation marks the transition to stage-2 with a precipitous decrease in the evaporation rate. Then, the diffusive vapor transport through the tortuous pore space gradually decreases the evaporation rate as the thickness of the dry region, and thus the distance between secondary evaporation plane and porous-medium surface, increases. The computed drying curves show a rather step-wise decrease of the drying rate at the transition to stage-2, when the control volumes dry out. This is due to two counteracting mechanisms: When a cell dries out, there is no direct evaporation from the water phase anymore. Hence, the water is only transported via the gas phase through that cell, which

considerably reduces the amount of transported water. At the same time the temperature increases at that position, because the vaporization enthalpy is not required anymore, and with the temperature, the diffusivity of vapor increases. This starts over when the next cell dries out and the distance to the interface between free flow and porous medium increases further. For a finer grid, this mechanism is less pronounced.

In the following sections, single parameters are changed to shed a light on their effect on the computed drying rate, while keeping all other parameters equal to the reference case described above. The considered parameter ranges are shown in Table 6.1.

Table 6.1: Values of the reference case and considered parameter ranges.

Parameter	Reference	Parameter Range	Unit
<i>Porous medium</i>			
porosity	0.41	0.3 - 0.5	-
permeability	2.65×10^{-10}	$10^{-9} - 10^{-12}$	m^2
vertical layer permeability	2.65×10^{-10}	$10^{-9} - 10^{-11}$	m^2
van-Genuchten α	$1/1570$	$1/1000 - 1/2000$	$1/\text{Pa}$
van-Genuchten n	8	4 - 12	-
thermal conductivity solid	5.3	4.3 - 6.3	$\text{W}/(\text{m K})$
temperature	298.15	288.15 - 308.15	K
<i>Free flow & Interface</i>			
inflow vapor concentration	0.008	0.004 - 0.012	-
inflow temperature	298.15	288.15 - 308.15	K
atmospheric pressure	10^5	$10^5 \pm 3000$	Pa
flow velocity	3.5	0.75 - 3.5	m/s
Beavers-Joseph coefficient	1.0	0.05 - 5.0	-

6.2 Influence of the porous-medium system

In stage-1 of the evaporation process, the boundary layer has usually a dominant influence on the drying rate. Thus, the free flow provides the upper boundary condition for the porous medium and limits the vapor transfer across the interface. For the analysis of the influence of different porous-medium properties, the comparability and expressiveness is given with the approximation of a constant boundary-layer thickness, which simplifies the system. Therefore, the continuity of the vapor flux at the interface is modified to:

$$- \left[\varrho_g \mathbf{v}_g X_g^w \cdot \mathbf{n} + J^{\text{vap}} \right]^{\text{ff}} = \left[\left(\varrho_g \mathbf{v}_g X_g^w - D_{g,\text{pm}} \varrho_g \nabla x_g^w \frac{M^w}{M} + \varrho_l \mathbf{v}_l X_l^w - D_{l,\text{pm}} \varrho_l \nabla x_l^w \frac{M^w}{M} \right) \cdot \mathbf{n} \right]^{\text{pm}} \quad (6.2)$$

where J^{vap} are the diffusive vapor fluxes at the free-flow side of the interface. For the flux approximation across the boundary layer, an averaged concentration boundary-layer thickness is estimated. The estimate is based on the physical experiments using the measured evaporation rate, the vapor concentration in the center of the wind tunnel, the saturated vapor pressure at the interface and thus the concentration of the fully saturated air and the diffusion coefficient of vapor in air. For a free flow velocity of 3.5 m/s, this leads to an estimated average thickness of $\delta_m = 1.6$ mm. This value is slightly higher than the value stated in Shahraeeni et al. (2012), which was determined for a free water surface.

With that, the diffusive vapor flux across the boundary layer J^{vap} at the free-flow side of the interface in Equation (6.2) can be approximated as a function of the difference between the vapor mole fraction in the external free flow $x_{g,\infty}^w$ where well-mixed conditions are assumed due to a strong turbulent mixing, and the vapor mole fraction at the surface of the porous medium $x_{g,\infty}^w$

$$\left[J^{\text{vap}} = -D_g^w \varrho_g \frac{x_{g,\infty}^w - x_{g,\text{pm}}^w}{\delta_m} \frac{M^w}{M} \right]^{\text{ff}}. \quad (6.3)$$

Apart from that, the porous-medium model is coupled to a laminar free-flow model in the usual manner. The continuity of total mass and heat fluxes and the local thermodynamic equilibrium is enforced with the coupling conditions described before. Further implications of turbulent conditions in the free flow, like viscous energy dissipation, eddy dispersivity and eddy thermal conductivity, are not considered in this case and the focus is completely on the porous-medium constraints on the evaporation process.

6.2.1 Porosity

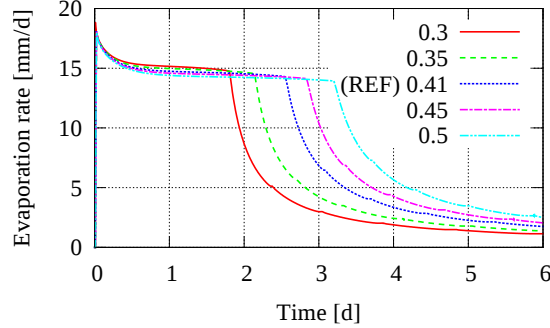


Figure 6.6: Influence of the porosity on the computed drying rates. The transition from stage-1 to stage-2 happens later for a higher porosity because more water is in place and can evaporate.

The computed drying rates for porosities between 30% and 50% are depicted in Figure 6.6. A medium with a higher porosity provides more space for the two fluids; with the same water saturation, more water is in place and can evaporate and the transition to stage-2 happens later. A high porosity comes usually along with large pores, which can be more easily penetrated by the free air stream. Hence, advective fluxes caused by the adjacent free air stream are more likely for a medium with a large porosity. Moreover, porosity affects the values of the effective thermal conductivity and the effective diffusivity. A higher porosity leads to a lower effective thermal conductivity, as dictated by Equations (4.9), (4.10). Thus, less energy is delivered to the evaporating surface, which cools down more, resulting in a lower evaporation rate in stage-1 and a later transition to stage-2. In contrast, the drying rate is higher in stage-2 for a higher porosity due to more pore space and a larger effective vapor diffusivity in the porous medium.

6.2.2 Intrinsic permeability

The intrinsic permeability is the proportionality factor between potential gradient and the averaged phase velocity (Darcy velocity). It is also a measure of the resistance, that the porous medium puts up against the water supply to the evaporating region. The effect of the permeability on the drying process is illustrated in Figure 6.7 with numerical simulations using different homogeneous intrinsic permeabilities in a range between 10^{-9} and 10^{-12} m². Here, the evaporation rate in stage-1 has the same level for all permeability values, but the transition from stage-1 to stage-2 happens later for a higher intrinsic permeability due to a delayed breakup of the liquid connections to the interface.

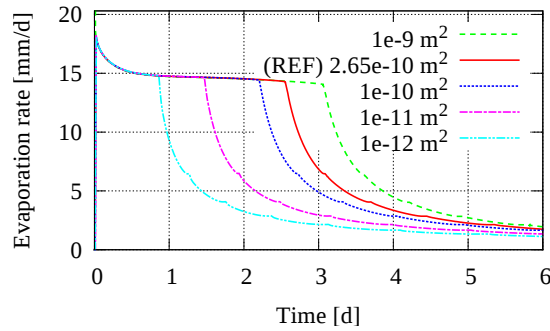


Figure 6.7: Influence of the intrinsic permeability on the computed drying rates. A lower permeability shortens the duration of stage-1 due to a higher resistance to flow.

6.2.3 Capillary pressure and relative permeability

A *van-Genuchten* parametrization has been chosen for the majority of the simulations, because measured parameters were readily available. The two *van-Genuchten* parameters n (shape parameter) and $\alpha_{v_{gN}}$, which are used therein to parametrize the nonlinear capillary pressure and the relative permeability as function of the water saturation, have been varied in the range between 4 and 12 for n , and between $5 \cdot 10^{-4}$ and 10^{-3} 1/Pa for $\alpha_{v_{gN}}$. The parameter n is related to the grain size distribution and has usually a small value for a relatively slim pore-size distribution. $\alpha_{v_{gN}}$ is related to the entry pressure of a medium, known from the *Brooks-Corey* model. Both parameters also influence the end-point value of the capillary pressure, as can be seen in Figures 6.8a and 6.9a. From the numerical simulations it becomes obvious that the maximum capillary pressure, or more precisely its gradient in the dry region close to residual water saturation, in combination with the relative permeability is critical for the transition from stage-1 to stage-2. Note that the capillary pressure should not exceed the gas phase pressure, or a negative water phase pressure is obtained which has no physical meaning and may lead to surprising values for the secondary variables from the material laws.

A high capillary pressure with a strong gradient close to the residual water saturation leads to a good supply of the evaporating surface with water from the interior of the porous medium. Thus, stronger capillary-pressure gradients can sustain the high evaporation rate in stage-1 much longer. As shown in Figure 6.8b, the curves with a higher value for the *van-Genuchten* $\alpha_{v_{gN}}$ (see Figure 6.8a) have less steep capillary-pressure gradients especially in the dry region of the curve. Thus, the transition to stage-2 happens earlier than for small values of $\alpha_{v_{gN}}$. The influence of the shape parameter n on the resulting capillary-pressure / saturation curve is relatively strong (see Figure 6.9a), because it affects the entire shape of the capillary-pressure curve and leads to much higher values of the end-point capillary pressure and to steeper gradients close to the residual saturation. Here, lower values of n lead to a prolonged stage-1,

as the curves in Figure 6.9b demonstrate.

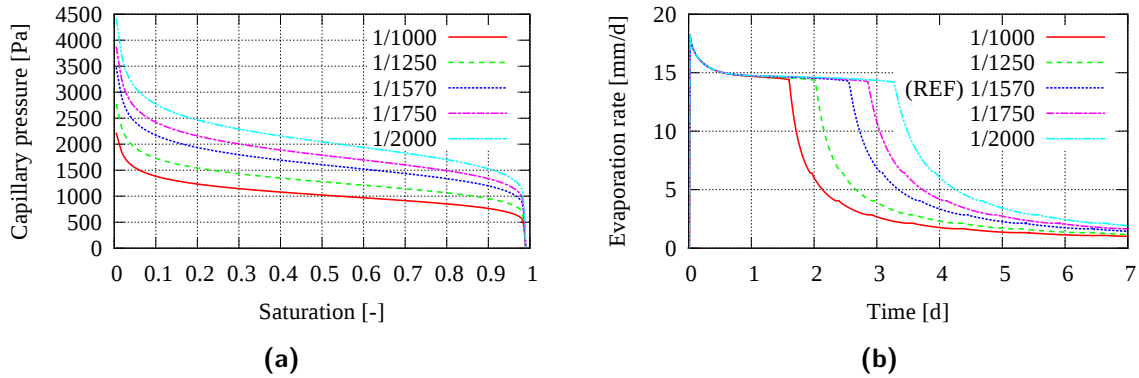


Figure 6.8: (a) Capillary-pressure curves for different *van-Genuchten* parameters α_{vGN} [1/Pa]. (b) Influence of the *van-Genuchten* parameter α_{vGN} [1/Pa] (related to the entry pressure) on the computed drying rates.

In most simulations, the *van-Genuchten* model has been employed, because measured values were readily available. To check, if the *Brooks-Corey* parametrization in combination with a relative permeability computed according to Burdine (1953) leads to a similar drying behavior, the parameter values have been converted to Brooks-Corey model. In context of evaporation processes, the main differences between the two parametrizations are the handling of the entry pressure and the end-point capillary pressure at the dry range of the curves. The *Brooks-Corey* parametrization has a non-zero entry pressure at full water saturation, which has to be overcome for the non-wetting phase to enter a control volume. Opposed to *van-Genuchten*, the curve using the *Brooks-Corey* formulation starts relatively flat at full water saturation. With the Brooks-Corey formulation, a uniform distribution of the initial saturation may lead to strong variations in the capillary pressure at heterogeneities because of differing entry pressures.

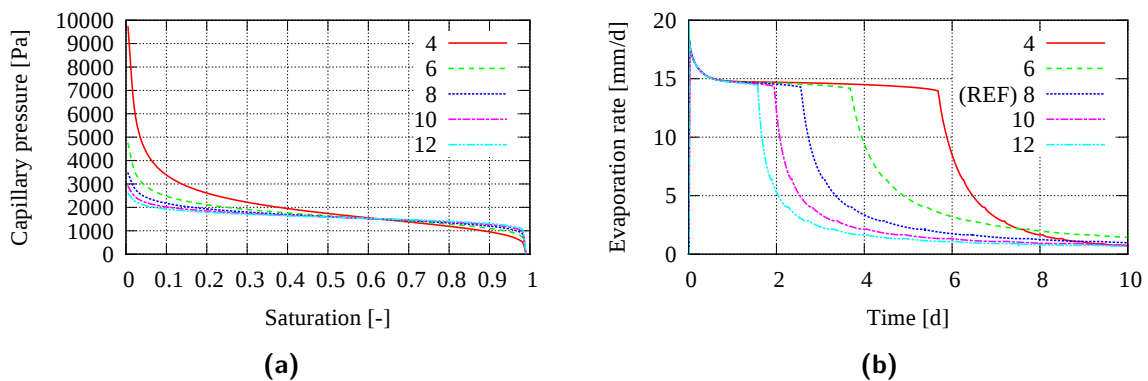


Figure 6.9: (a) Capillary-pressure curves for different *van-Genuchten* parameters n [-]. (b) Influence of the *van-Genuchten* shape parameter n [-] on the computed drying rates.

In contrast, the *van-Genuchten* model does not account for an entry pressure but has a smooth and continuous interpolation to a capillary pressure of zero at full water saturation. This formulation is especially numerically attractive because it is more stable at high liquid saturations, where it leads to a capillary pressure of 0 Pa and to steeper gradients of the capillary-pressure curve. Thus, it avoids strong discontinuities of the capillary pressure for high water saturations at the interface of soil heterogeneities.

A method to transform capillary-pressure curves parametrized with *van-Genuchten* to the *Brooks-Corey* formulation is provided in Lenhard et al. (1989):

$$\lambda = \frac{m}{1-m} \left(1 - S_{w,\text{eff}}^{1/m}\right), \quad (6.4a)$$

$$\overline{S}_x = 0.72 - 0.35e^{-n^4}, \quad (6.4b)$$

$$p_d = \frac{\overline{S}_x^{-1/\lambda}}{\alpha_{\text{VgN}}} \left(\overline{S}_x^{-1/m}\right)^{1-m}. \quad (6.4c)$$

For the determination of a saturation-independent λ which results in similar curves over a wide saturation range, $S_{w,\text{eff}}$ may be chosen as 0.5. Figure 6.10 shows an example where the *van-Genuchten* parameters have been converted to *Brooks-Corey* parameters using this method. The strong influence of the capillary pressure (gradient) close to residual saturation is crucial for the Lenhard-transformation: Independent of the choice of the parametrization, the capillary-pressure curve has to be regularized at some point, or it goes to infinity. If the regularization point is chosen in a way that the endpoint-capillary pressure is similar, the two parametrizations lead to comparable results.

Different simulation runs have shown that if the capillary-pressure curve is used in the entire saturation range with one of the two parametrizations described above in combination with the relative permeability determined according to Mualem (1976) or Burdine (1953), the

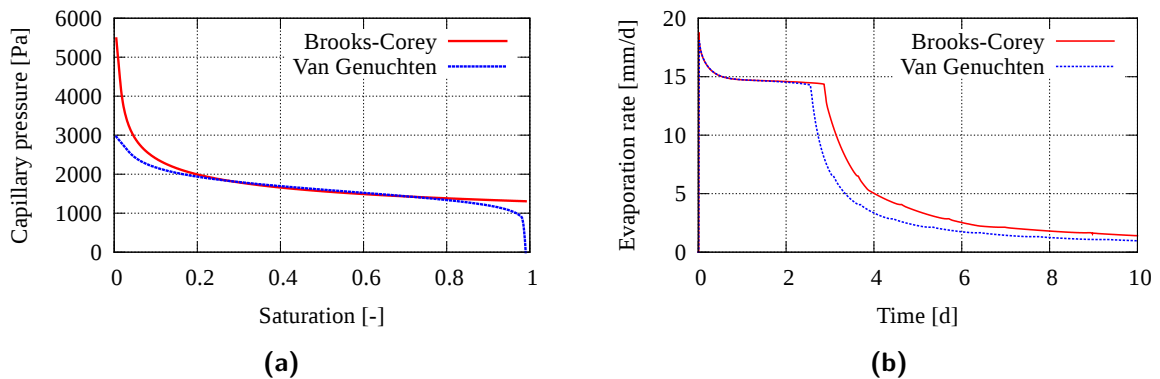


Figure 6.10: Computed drying rates with the *van-Genuchten* and the *Brooks-Corey* model with the respective capillary-pressure curves.

duration of stage-1 is overestimated. In Schneider and Goss (2012) it is argued, that the common capillary-pressure / saturation relationships are not valid in the dry range. The measurement quality in this region is usually relatively low and often different measurement techniques are used to determine the wet and the dry part of the curve. These measurements may partly include the effects of vapor diffusion through the porous medium, which is not conform with the employed model here. Anyway, some regularization has to be chosen, or the capillary pressure goes towards infinity at the residual water saturation. So far, there is no clear opinion, how the maximum capillary pressure should be defined. Approaches to mitigate that can be found in various papers (e.g. Zhang and van Genuchten, 1994; Webb, 2000; Tuller and Or, 2005). Usually, the capillary-pressure curve is extended at a critical saturation value with a logarithmic shape into the dry region without modifying the relative-permeability curve. Alternatively, a variable residual saturation may be defined (Zhang et al., 2010) affecting both, the capillary pressure and the relative-permeability curve.

In Lehmann et al. (2008), the capillary-pressure curve is linearized at the inflection point to determine a characteristic length for the evaporation process. In this way, the end-point capillary pressure at residual saturation is limited. The *van-Genuchten* model has been adapted according to this concept. The results of numerical simulations using the linearly regularized *van-Genuchten* curves (Figure 6.11a) are shown in Figure 6.11b.

Compared to the measured drying curve, the results indicate that the usual *van-Genuchten* curve leads to an overestimation of the capillary pressure in the dry region, when a two-phase two-component model is used. With the linear extrapolation, the transition from stage-1 to stage-2 due to insufficient water supply in linked capillaries can be captured better.

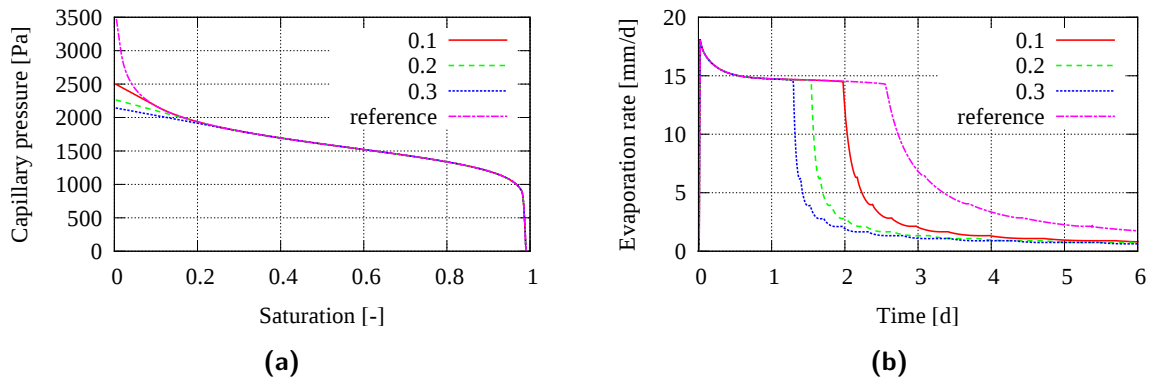


Figure 6.11: (a) Capillary-pressure curve with and without linear regularization at different effective water saturations (0.1, 0.2 and 0.3). This results in a lower gradient and a lower maximum capillary pressure when approaching the residual water saturation. (b) This figure demonstrates the earlier onset of stage-2, when the capillary-pressure curve is linearized in the dry region roughly at the inflection point. The linear interpolation is used at an effective water saturation of 0.1, 0.2 and 0.3.

6.2.4 Vertically textured porous medium

In environmental or technical applications, sharp discontinuities of material parameters can be often observed. The *Leverett-J* function (Leverett, 1941) is a possible means to scale the capillary pressure according to the permeability in the porous medium. The *Leverett-J* function is approximately constant for different porous materials at the same saturation level and can be utilized to compute the capillary pressure for an adjacent medium based on the given parameter values. It reads

$$J(S_l) = \frac{p_c(S_l) \sqrt{k/\phi}}{\sigma \cos \alpha}. \quad (6.5)$$

Then, the *Leverett-J* function is employed to compute the according capillary-pressure curve of the other media, generating heterogeneous structures where the permeability of one medium is varied. The contact angle is assumed to remain constant and changes of the porosity are not considered in this context. Figure 6.12a shows different capillary-pressure curves scaled with the Leverett-J function for different values of the intrinsic permeability.

For the simulations of the heterogeneous setup, a deeper simulation domain was chosen: $0.25 \text{ m} \times 1.0 \text{ m}$, with the interface between free flow and porous medium at $z = 0.75 \text{ m}$ and the material interface in the center of the porous-medium domain at $x = 0.25 \text{ m}$. This is to preclude an influence of the lower boundary condition on the processes. In the performed simulations, the soil parameters, such as permeability, diffusivity or thermal conductivity, are all defined on the control volumes. For the evaluation of the fluxes from one control volume to another one, these parameter values are harmonically averaged. In case of an element-wise definition of these parameter, an interface condition as proposed in Papafotiou et al. (2010) is

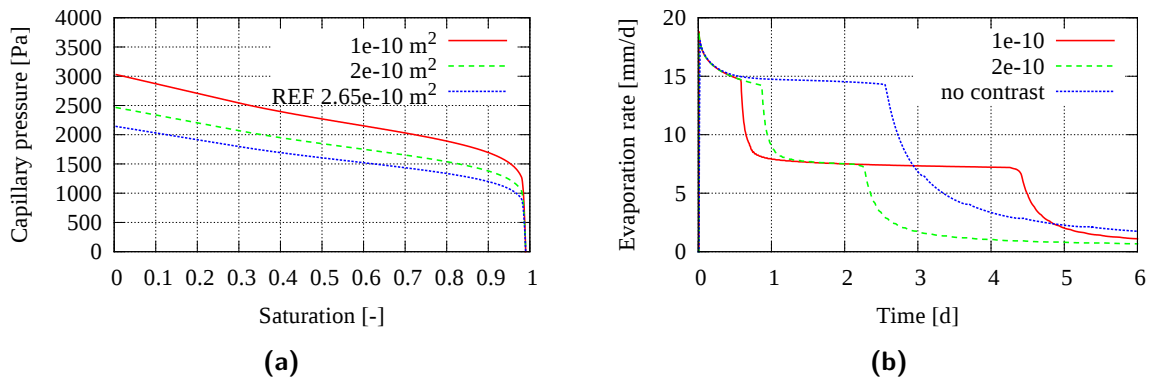


Figure 6.12: (a) The capillary-pressure curve of the reference case scaled with the Leverett-J function using different intrinsic permeabilities with a linearized capillary pressure at an effective water saturation of 0.3. (b) Computed drying rates with no contrast and with a lower permeability in the right half of the domain. Three stages can be observed.

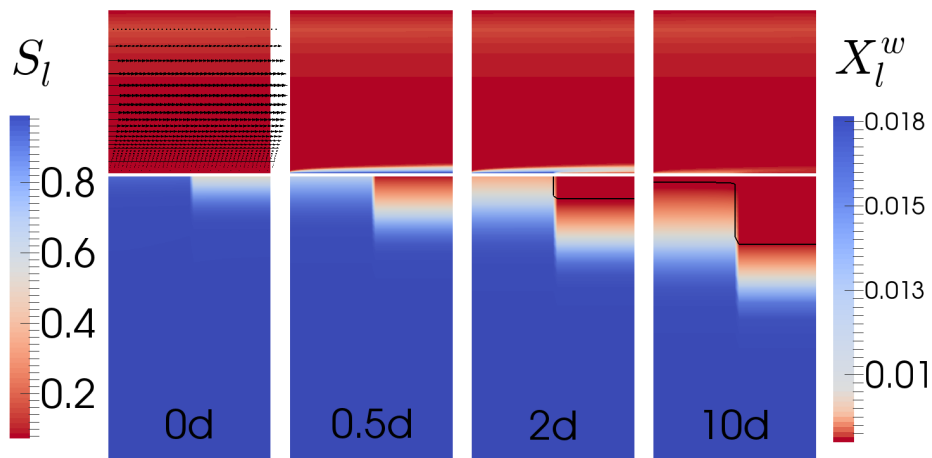


Figure 6.13: The mass fractions of vapor in the free flow (top) and the evolution of the water saturation (bottom) are shown after 0, 0.5, 2 and 10 days. The water saturation in the coarse material decreases faster. The black arrows indicate the flow field in the free air stream. The black line in the porous medium after two days (right two images) defines the region, that has already dried out. Only the upper part of the porous-medium domain is shown.

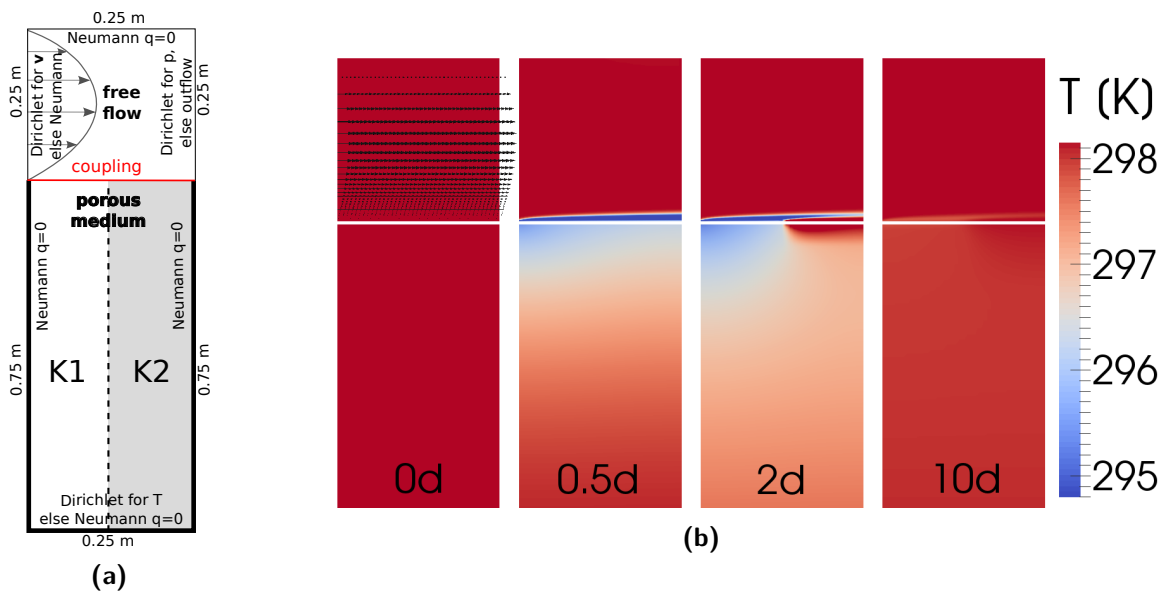


Figure 6.14: (a) Model setup and boundary conditions. (b) Evolution of temperature in the free flow and the porous medium. Only the upper part of the porous medium is shown.

required.

The drying of such medium with a vertical texture involving two different porous media has been studied in Lehmann and Or (2009). At the beginning of the evaporation process, both porous-medium compartments contribute similarly, as long as both fluid phases are present at the evaporating surface. With decreasing water saturation, the water is driven by capillary forces from the coarse into the fine material. The coarse material, or more precisely the material with the lower capillary pressure, dries out first. This continues until the drying front has receded into the coarse material and the capillary pressure gradient is too low to sustain the evaporative demand. Then, the two compartments detach and the finer one dries. The simulation results show the same behavior as observed in the experiments. Figures 6.14b and 6.13 depict the evolution of vapor concentration, saturation and temperature. Furthermore, the flow field of water after 0.3 days (Figure 6.15) illustrates the internal water redistribution from the coarse to the fine material during the drying process. The computed drying curves (Figure 6.12b) show three stages, one at the beginning of the evaporation process, one when the coarse material is dry out and the last one when the fine material has dried out as well.

When the coarse material is dry, the temperature increases at the coarse part of the interface, while the fine material remains cool as long as the water phase is still evaporating. Thus, temperature differences between the two materials can be observed at the porous-medium surface, as can be seen in the infrared images taken during the physical experiments (Figure 3.6 in Chapter 3).

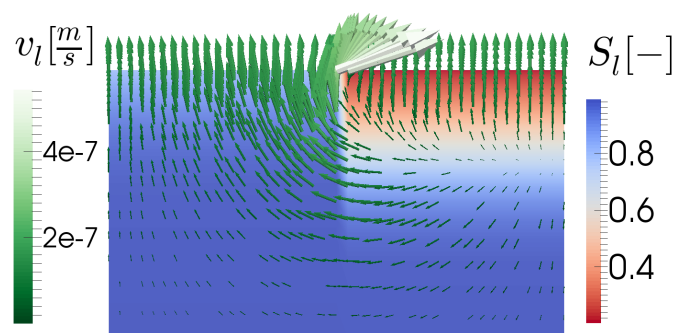


Figure 6.15: Upper part of the simulated porous-medium domain. The arrows indicate the flow field of the water phase after 0.3 days. Water flows due to capillary forces from the coarse (right) into the fine material (left). Thus, the water saturation in the coarse material decreases faster. The highest velocities can be found at the top of the domain at the interface between the two materials.

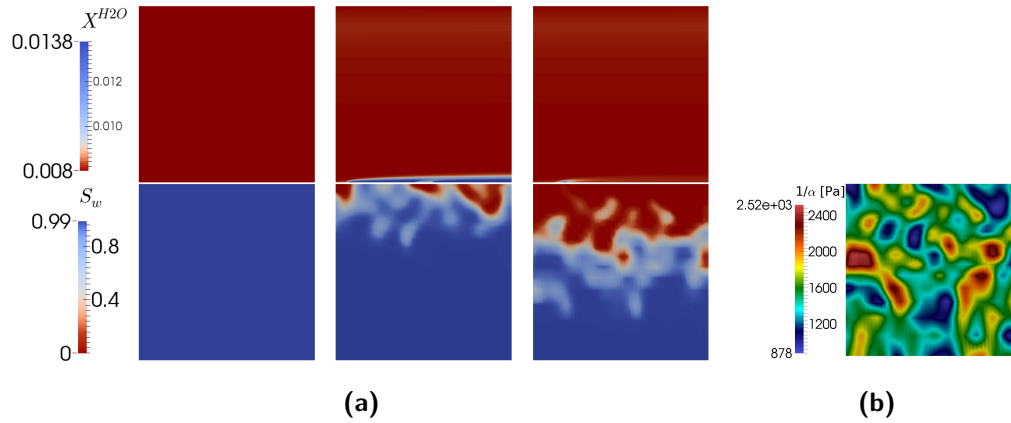


Figure 6.16: (a) Evolution of mass fractions of vapor (top) and water saturation (bottom). (b) Heterogeneous distribution of the van-Genuchten α .

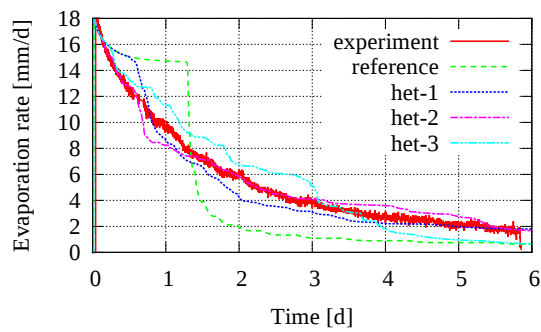


Figure 6.17: Comparison of a measured drying curve with a simulation with a heterogeneous distribution of the *van-Genuchten* parameter α . Three different realizations are chosen, which lead to slightly different drying rates. Compared to the results with a macroscopically homogeneous distribution, the computed drying curve matches the measured evaporation rates better.

6.2.5 Statistical distribution of the soil parameters

Porous-medium systems are in general not homogeneous but have local heterogeneities due to the shape of the grains and their configuration (packing). To show the influence of such a heterogeneous parameter distribution, the geostatistical tool *GStat* is employed to generate correlated fields (Pebesma and Wesseling, 1998). For a better resolution of the heterogeneous field, a grid with 50×62 cells (higher horizontal resolution) was employed. With that, a Gaussian distribution is set for the distribution of the *van-Genuchten* parameter α with a correlation length of 2 cm. One example of such distribution is depicted in Figure 6.16b. As a consequence, some cells at the interface dry out earlier mainly due to a lower capillary pressure and an insufficient water supply. This leads to an earlier and gradual drop in the evaporation rate and a shorter constant-rate period. The vapor distribution in the free flow shows a stronger evaporation at locations where the water phase is present leading to higher vapor concentrations there, as illustrated in Figure 6.16a. It is clear that each realization of a heterogeneous parameter distribution will lead to different results and several runs with the same distribution parameters would have to be run to improve the expressiveness. For this purpose, the choice of the variance and correlation length for the geostatistical field should be linked to the porous-medium properties. Here, the heterogeneous setup is used to demonstrate the possible influence on the computed drying rates (Figure 6.17).

With a uniform soil-parameter distribution, a relatively steep and abrupt transition from stage-1 to stage-2 is generally observed. A heterogeneous distribution of the *van-Genuchten* parameters leads to a slower and smoother transition. The difference in capillary pressures at different locations on the interface leads to an altered drying behavior. Volumes with a lower capillary pressure will dry out earlier, while volumes with a higher capillary pressure preserve the direct evaporation from the water phase locally for a longer time.

6.2.6 Temperature

A higher temperature in the porous medium leads to a higher equilibrium vapor pressure and thus higher vapor concentrations in the soil air. Further effects are an increased diffusion coefficient and a higher thermal conductivity in the gas phase. The computed drying rates are depicted in Figure 6.18. When the temperature of the porous medium is initially much lower than the free-flow temperature, the temperature at the surface of the porous-medium and thus the drying rate may increase at the beginning of the evaporation process.

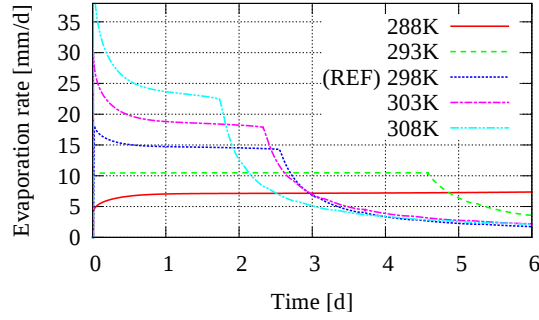


Figure 6.18: Influence of the temperature in the porous medium on the computed drying rates.

6.2.7 Thermal conductivity

At the beginning of the drying process, the porous medium and the two fluid phases have a uniform temperature throughout the porous medium. When water evaporates, the latent heat of vaporization cools the surface of the porous medium, leading to a decrease of the saturated vapor pressure at the surface and subsequently to a lowering of the drying rate. The surface temperature will decrease until an equilibrium between the latent heat of vaporization and the heat supply is established. The incoming heat fluxes are composed of the heat transfer from the free flow due to thermal conduction and convection in the ambient air, radiative heat input, and fluxes from the interior of the porous medium, such as thermal conduction through the porous medium (water, air and soil) and convective heat fluxes. Presumably, the heat of vaporization is withdrawn partly from the water phase, which is assumed to be in equilibrium with the solid material, and from the surrounding air. Radiative heat transfer within the porous medium is not considered here because it is usually accounted for in the effective thermal conduction.

The thermal conductivity of the gas phase is orders of magnitude lower than the thermal conductivity of water and a decrease of the water saturation results in a nonlinear reduction of the effective thermal conductivity (see Equations (4.9) and (4.10)), thereby reducing the energy supply from the porous medium to the evaporating surface. At the same time, the effective diffusion coefficient of vapor in the gas phase increases for a decreasing water saturation (Equation (4.4)), leading to stronger diffusive vapor fluxes in the porous medium. The equilibrium temperature at the surface will set depending on the cumulative heat demand and supply at the interface.

The general surface energy balance can be formulated as

$$R_n = L_e E + H + G, \quad (6.6)$$

with the net radiation R_n , the latent heat of vaporization $L_e E$, the sensible heat flux into the atmosphere H , and the ground heat flux G (Brutsaert, 1982). When the interface between free flow and atmosphere is considered, Equation (6.6) can be subdivided into fluxes from the porous medium, the free flow and the latent heat of vaporization. This leads to the following balance equation:

$$R_n = \left[\underbrace{\rho_g (h^w X_g^w + h^a X_g^a) \mathbf{v}_g - \lambda_g \nabla T}_H \right]^{\text{ff}} + \left[\underbrace{\rho_g (h^w X_g^w + h^a X_g^a) \mathbf{v}_g + \rho_w h_w \mathbf{v}_w - \lambda_{\text{pm}} \nabla T}_{L_e E + G} \right]^{\text{pm}} \quad (6.7)$$

The total internal energy is composed of the enthalpies of the different phases, because only one energy balance is used. The latent heat of vaporization $L_e E$ is inherently in Equation (6.7). When water vaporizes into the gas phase, the saturation of the water phase decreases while the vapor concentration in the gas phase increases, leading to an overall decrease of temperature. Furthermore, the gas phase enthalpy is composed of the enthalpy of the pseudo-component air and of the component vapor. Evaporation from the liquid phase or a diffusive component transport affecting the vapor concentration in the gas phase will lead to a change in the gas phase enthalpy. Due to the coupling of the heat fluxes at the interface, the latent heat of vaporization is properly accounted for. In the simulated cases, the decrease of temperature at the surface due to the cooling effect of evaporation was approximately 3 to 4 K. Similar values have been observed during stage-1 of the drying experiment.

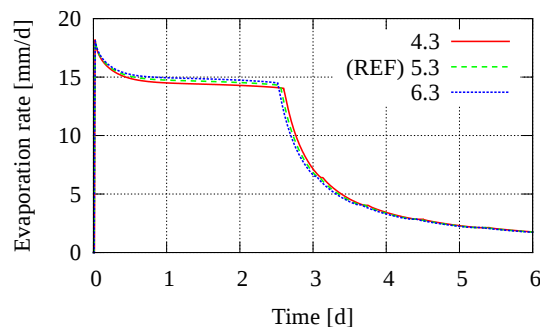


Figure 6.19: Influence of different values for the thermal conductivity of the solid phase on the computed drying rates. A higher thermal conductivity provides a better energy supply due to heat conduction within the porous medium. This counteracts the cooling effect of evaporation and leads to higher vapor concentrations at the surface during stage-1 evaporation.

An estimation of the heat supply from the porous medium to the surface is possible, if the heat input across the boundaries of the porous medium is quantifiable. To reduce the external heat input, the vessel for the sand sample in the drying experiment has been insulated with Styrofoam, which has a considerably lower thermal conductivity than the sand and the glass walls of the vessel. The external heat input requires special care when choosing the boundary conditions in the porous medium. No-flow boundaries are chosen at all sides but the bottom boundary where a constant temperature is set. The influence of the solid thermal conductivity has been examined with three simulation runs, varying the thermal conductivity of the solid material in the range of 4.3 to 6.3 W/m K. As can be seen in Figure 6.19, a lower thermal conductivity of the solid material leads to a weaker supply of conducted heat from the porous medium to the evaporating surface. Thus, the initial decrease of the drying rate is stronger for a lower thermal conductivity in stage-1. However, the overall effect of the thermal conductivity of the solid material on the drying rate is small compared to other soil properties.

6.2.8 Thermal non-equilibrium in the porous medium

The local thermodynamic equilibrium, which is assumed in the porous-medium domain, is composed of mechanical, thermal and chemical equilibrium. First analyses regarding the local thermal non-equilibrium within the porous medium have been made in the scope of a Diploma thesis (Geiges, 2009). Two models according to Crone et al. (2002), which consider a thermal non-equilibrium between the fluid phases and a heat exchange across the fluid-solid interfaces, have been employed to simulate several infiltration and evaporation examples using a porous-medium model without coupling to the free flow. Therefore, two energy-balance equations are solved, one combined equation for the two fluids and one for the solid phase. The energy exchange is managed via source and sink terms, which link the energy balance equations dependent on the specific interfacial areas of the fluids and the solid phase. The difference between the two considered approaches is the handling of thermal conduction: In one model, thermal conduction was still treated as effective heat flux within all phases, whereas the second approach considers thermal conduction separately for both fluid phases and the solid phase.

As crucial quantities, the flow velocity and the interfacial area between the fluids and the solid phase, which is strongly dependent on the grain diameter of the solid material, have been identified. Fine material has a high specific surface area where heat can be transferred. Thus, thermal non-equilibrium occurs more likely for coarse-grained media. Thermal non-equilibrium influences the temperature distribution within the fluids and the solid material, which affects the fluid properties and the properties of the solid material. This may lead to a different flow behavior. In the considered examples, the influence of thermal non-equilibrium on the

evolution of the saturation distribution was minor. Based on the findings, the local thermal equilibrium is regarded as a valid assumption within the porous medium for the considered system. However, the assumption may not hold at the interface to the free flow where the free-stream velocity may be high. As temperature significantly influences the evaporation process, an ill-founded assumption of local thermal equilibrium can lead to a wrong estimation of the evaporation rate. Moreover, in the context of evaporation processes with vapor exchange at the soil-atmosphere interface, the chemical equilibrium should also be scrutinized. A possible approach is presented in Nuske et al. (2013). The validity limits of thermal equilibrium and the development of suitable non-equilibrium approaches should be further addressed in future research.

6.2.9 Summary of the influence of the porous-medium system

The soil properties especially close to the surface of the porous medium revealed a strong impact on the evaporation behavior. All fluid-structure parameters (capillary pressure, relative permeability, effective thermal conductivity and diffusivity), are non-linear, and the representation on averaged volumes contains severe uncertainties considering their values at the porous-medium surface. Area-specific quantities would give a better representation of the processes happening at fluid-fluid and fluid-solid interfaces and would eliminate the grid dependency at the interface. This holds also for the surface water content, which is approximated by the volumetric quantities water saturation and porosity. Here, the influence of the grid was minimized by a successive grid refinement towards the interface. Single fluid and soil properties, such as the thermal conductivity of the solid material, had only little influence on the computed drying rates. However, the overall temperature in the porous medium has a significant influence, because it influences all fluid and solid parameters simultaneously.

6.3 Conditions and processes in the free-flow compartment

This section considers the conditions outside the porous medium in the ambient free flow and their effect on the computed drying rate, namely the influence of the vapor concentration, the atmospheric pressure, the temperature and the flow conditions. Using a laminar free-flow model would not allow to properly analyze the effects of the free flow on the drying rate. On the one hand, the boundary layer is underestimated and on the other hand the influence of turbulent diffusion and turbulent heat conduction would not be accounted for. Thus, the heat and vapor exchange would be badly approximated and a reasonable analysis of the influence of free-flow parameters would have a limited expressiveness. Hence, an algebraic turbulence model is selected and integrated for this part of the analysis.

In the scope of a Diploma thesis (Fetzer, 2012), several algebraic turbulence models have been analyzed for their accuracy and applicability. These models employ algebraic expressions for the computation of the turbulent viscosity, which arises from the *Reynolds*-averaging of the *Navier-Stokes* equations, as explained in Section 4.3.4. The turbulent viscosity accounts for the velocity fluctuations due to the eddying motion. The *Baldwin and Lomax* turbulence model (Baldwin and Lomax, 1978) was found to reproduce a measured turbulent velocity field presented in Laufer (1954) best (Fetzer, 2012). The *van Driest* model with the modification according to Hanna and Sandall (1972), called *modified van-Driest model* in the sequel, gives also a good approximation of the flow field, especially in the vicinity of a wall, while being numerically more stable. Figure 6.20 shows the evaluation of the different models for their ability to reproduce the measured profile. The velocity profile is scaled by the wall friction velocity $u_{\tau,*} = \sqrt{\tau_{xz,*}/\rho_*}$ where the wall shear stress is defined as $\tau_{xz,*} = \mu_* \left(\frac{\delta \bar{u}}{\delta z} \right)_*$. For more details on the tested model concepts, be referred to Fetzer (2012).

For the turbulent simulations, the free flow domain has been extended according to the geometry of the wind tunnel with an extent of $0.5 \text{ m} \times 0.5 \text{ m}$, as schematically shown in Figure 6.21. A run-up distance of 0.25 m without coupling to the porous medium allows a

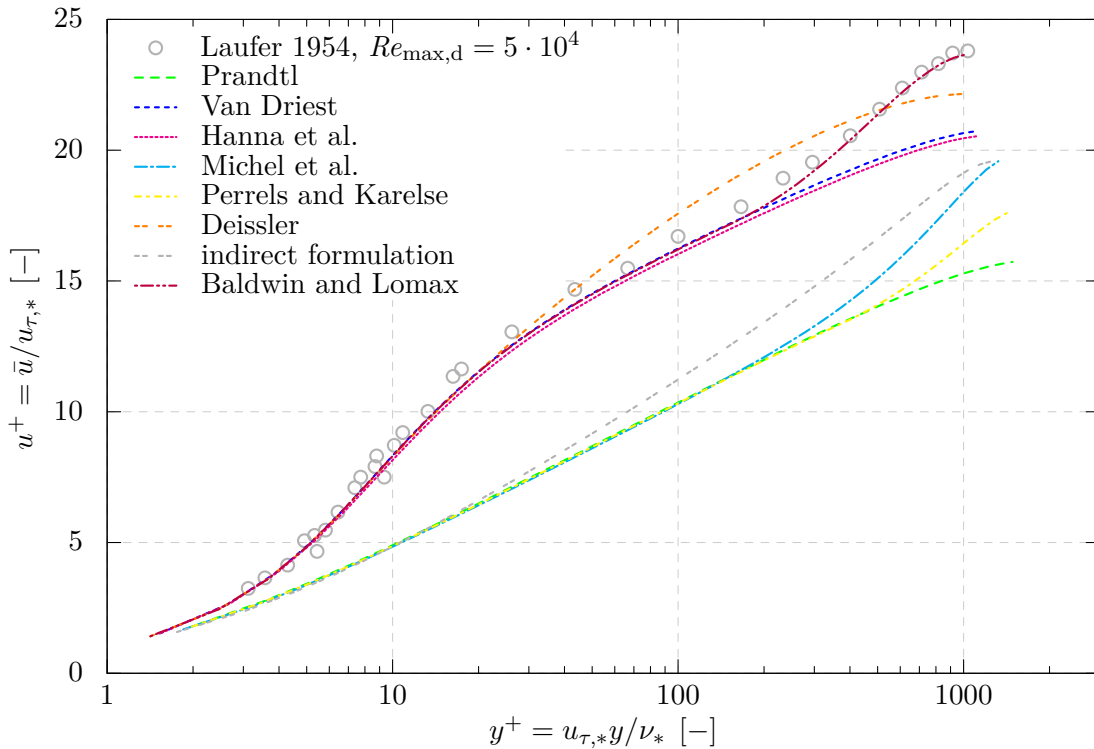


Figure 6.20: Semi-logarithmic velocity profile, scaled by the wall friction velocity $u_{\tau,*}$, for a fully developed pipe flow. (Courtesy of Fetzer, 2012).

development of the turbulent flow field. This is also justified by the setup of the experiment where a flow straightener was placed in the wind tunnel at this distance before the sand sample. The setup is shown in Figure 6.21. With 50×120 cells, the computational grid is much finer in this case in order to get a good resolution of the processes happening in the boundary layer and close to the interface. The grid is vertically refined using a grading factor of 0.86. With that, a minimum cell height of 10^{-4} m is obtained at the upper and lower boundary of the free-flow domain and the boundary layer is covered by several elements. As described in Chapter 5, due to the use of a collocated grid where pressure and velocity are evaluated at the vertices, and due to the employed discretization scheme (vertex-centered finite-volume scheme) pressure oscillations are observed in the free flow. These are strongest in the run-up region and are dampened towards the coupled part. The replacement of the discretization scheme by a more robust one, which uses, for example, a staggered grid, is subject to future work.

Comparisons of the *modified van-Driest* model with the *Baldwin and Lomax* approach coupled to the porous-medium model have revealed only small differences in the computed drying rates. The *modified van-Driest* model has been selected for the survey of the influence of free flow on the drying curves in this section. With a combination of the eddy-viscosity concept with a suitable eddy-diffusivity and eddy-thermal conductivity model, the initial drying rate of the evaporation experiment can be matched. The combination of the *modified van-Driest* model for the turbulent viscosity with the eddy-diffusivity and eddy-thermal-conductivity approach presented in Deissler (1963) is employed for the simulations presented in the further course of this section. A comparison of different eddy-diffusivity and eddy-thermal-conductivity models is presented in Figure 6.22. Note that the eddy-diffusivity was always identical to the employed eddy-thermal-conductivity model.

6.3.1 Inflow vapor concentration

The inflow vapor concentration in the main air stream determines the concentration gradients across the boundary layer at the interface. It has a strong impact on the evaporative demand at the surface and thus on the computed drying rate. A series of numerical simulations with mass fractions of vapor in the gas phase in the range between 0.004 and 0.012 kg/kg have been performed, corresponding to relative humidity of 30 %, 40 % and 50 %. As expected, lower vapor concentrations in the free flow lead to higher evaporation rates, see Figure 6.23a.

6.3.2 Atmospheric pressure variation

The atmospheric pressure shows daily cycles and may vary in a range of several thousand Pascal (Patterson and Davis, 2009). This may trigger advective vapor fluxes in the porous

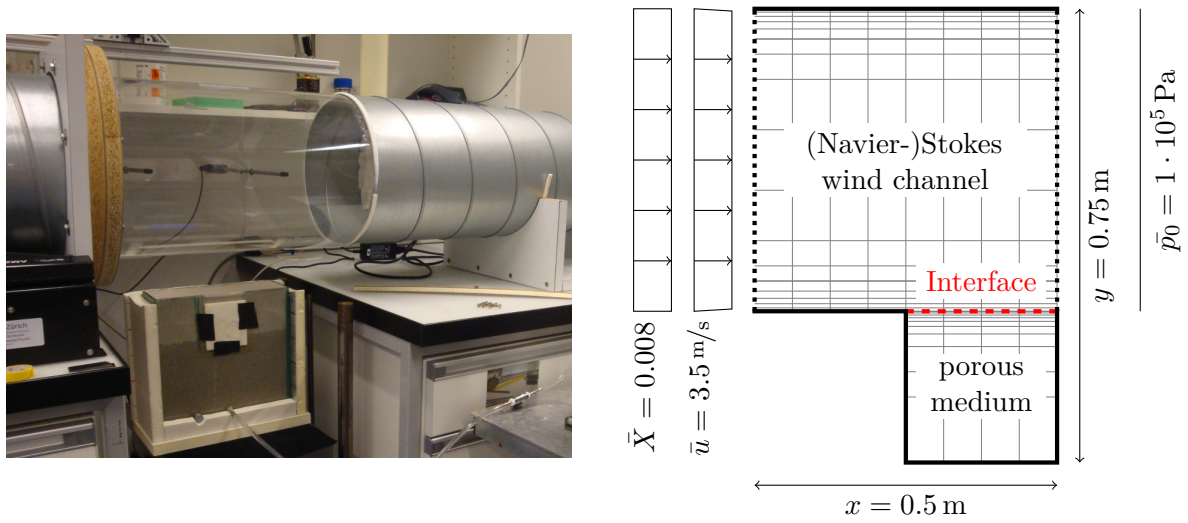


Figure 6.21: Foto of the experimental setup, the two domains are still decoupled. Two-dimensional model domain for the turbulent simulation (right). (Courtesy of Fetzer, 2012).

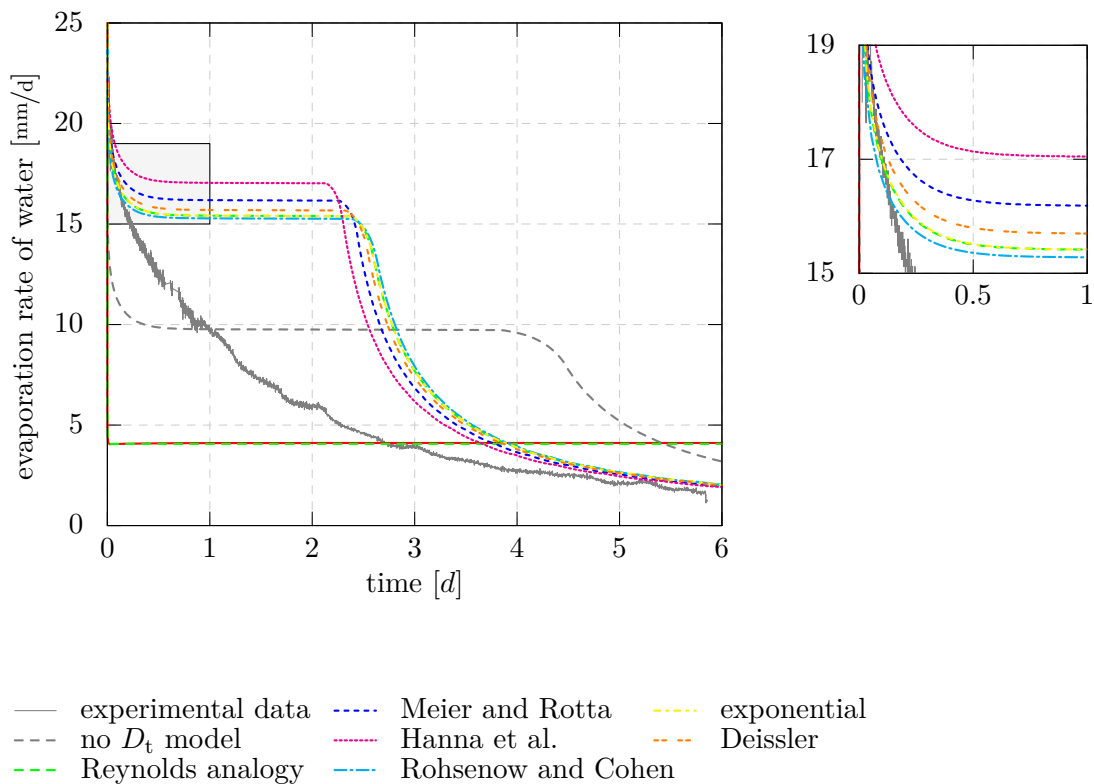


Figure 6.22: Evaporation rate over time for different eddy thermal conductivity models (left) in combination with the *Baldwin-Lomax* model for the eddy viscosity (left) with detailed view of the gray rectangle (right). The initial drying rate can be met. (Courtesy of Fetzer, 2012).

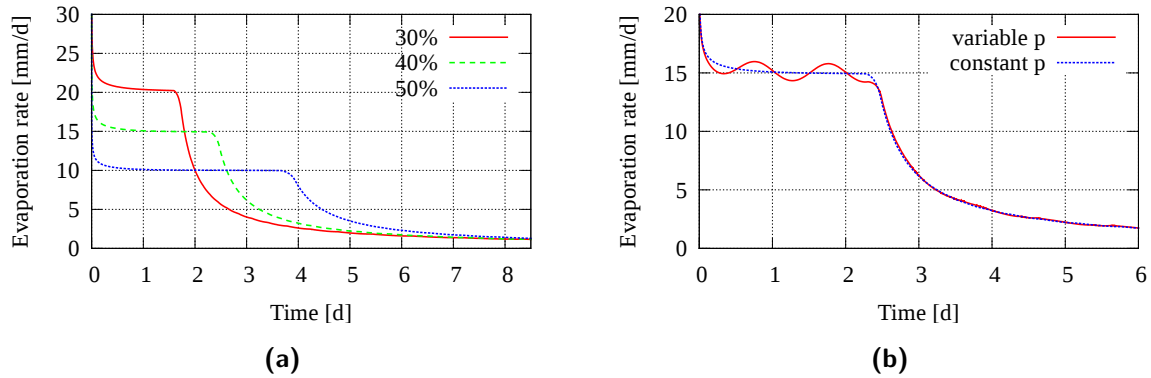


Figure 6.23: (a) Influence of the relative humidity at the inflow on the computed drying rates. (b) Influence of a sinusoidal variation of atmospheric pressure with ± 3000 Pa

medium. To examine this effect, first calculations with a sinusoidally varying pressure at the outflow boundary have been performed:

$$p_{\text{atm}} = p_{\text{mean}} \pm 3000 \sin\left(\frac{2\pi t}{86400}\right)$$

The results are presented in Figure 6.23. The computed drying rates reflect the variation of the atmospheric pressure. A lowering of the atmospheric pressure leads to stronger advective gas fluxes in the porous medium towards the interface. These change their direction, when the pressure increases again. However, the net effect of this atmospheric pumping on the drying rate was relatively small in the simulations, because the evaporation processes is still dominated by diffusive processes across the boundary layer.

6.3.3 Free-flow velocity

The flow velocity in the free air stream has a strong influence on the boundary-layer thickness and the mixing behavior. A higher flow velocity results in a thinner boundary layer. Thus, higher velocities lead to a stronger concentration gradient across the mass boundary layer, as depicted in Figure 6.24. Comparisons with a series of evaporation rates with flow velocities between 0.75 m/s and 3.5 m/s show a good agreement for the initial drying rates, see Figure 6.24. The further course of the drying rate deviates.

6.3.4 Temperature

The temperature of the porous surface often differs from the temperature of the main air stream caused, for example, by radiative heat input or evaporative cooling of the porous surface.

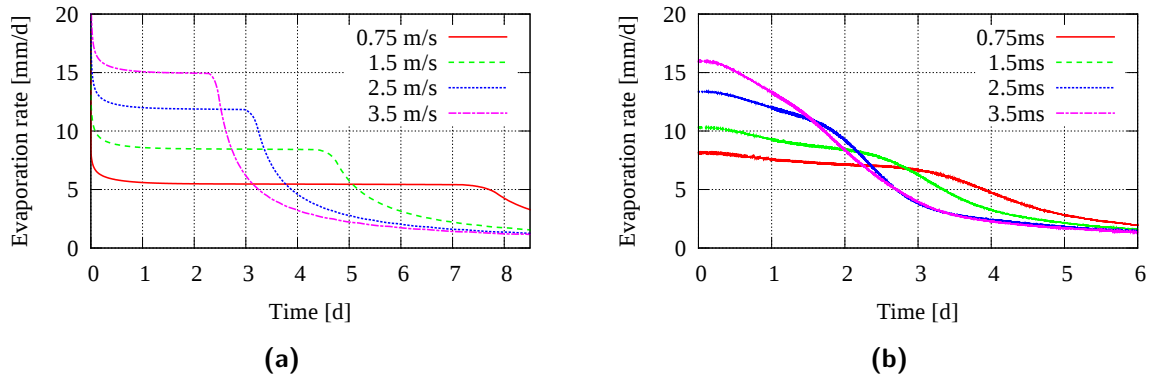


Figure 6.24: (a) Influence of the free air stream velocity on the computed drying rates. (b) Measured drying curves from a wind tunnel experiment at different flow velocities (Shahraeeni et al., 2012).

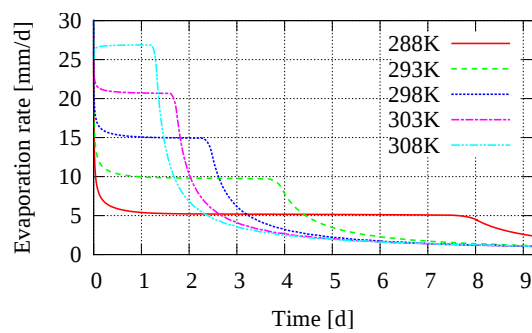


Figure 6.25: Influence of the inflow air temperature on the computed drying rates.

Then, the temperature difference leads to heat transfer from warmer to colder regions. If the air in the free flow is warmer than at the surface of the porous medium, heat is transferred into the porous medium, providing additional energy for the evaporation process and increasing the equilibrium vapor pressure. In contrast, a lower air temperature than the surface temperature of the porous medium leads to a further cooling of the porous-medium surface and lower drying rates. The respective drying curves are presented in Figure 6.25 and differ considerably for the different inflow temperatures.

6.3.5 Summary of the influence of the free-flow system

The conditions in the free flow, like temperature, vapor concentration and pressure, have a crucial influence on the exchange fluxes. Together with the flow field and the boundary layer, they govern the gradients and resulting fluxes across the interface.

6.4 Influence of interface processes

In the following section the influence of processes happening mainly at the interface between free flow and the porous medium are discussed. These are the influence of the surface water content on the drying rate, heat input by radiation and a short discussion of possible effects of the surface roughness on the drying rate.

6.4.1 Beavers-Joseph coefficient - slip velocity

In the coupled models, the Beavers-Joseph condition is employed involving a tangential velocity component at the free-flow side of the interface, as described in Section 4.3.1. A series of simulations with a wide range of *Beavers-Joseph* coefficients in using a laminar free-flow model has been analyzed. The analysis shows, that the influence of the *Beavers-Joseph* coefficient on the computed drying rate is relatively small for coefficients in the range between 0.05 and 5, which have been reported in the literature (Sahraoui and Kaviany, 1992; Goyeau et al., 2003). To avoid that this is only due to the limited extent of the simulation domain, the domain size has been chosen as $1 \text{ m} \times 0.5 \text{ m}$, providing a larger area where the slip velocity is active. Furthermore, the *Beavers-Joseph* coefficients have been varied beyond the values stated above, because these values for α_{BJ} showed no significant influence on the computed drying rate. For very small values for α_{BJ} , effects on the computed drying rate can be observed, as shown in Figure 6.26. Furthermore, only the interaction between the gaseous phase of the porous medium and the one in the free flow is considered. Here, a saturation-dependent condition

may be required, accounting for the influence of the surface water content on the slip velocity and the effects on the the boundary layer. Therefore, the coefficient α_{BJ} has to be determined for different saturation levels. This could be done experimentally supported by pore-scale modeling, like the lattice-*Boltzmann* method (He and Luo, 1997; Chen and Doolen, 1998; Lallemand and Luo, 2000).

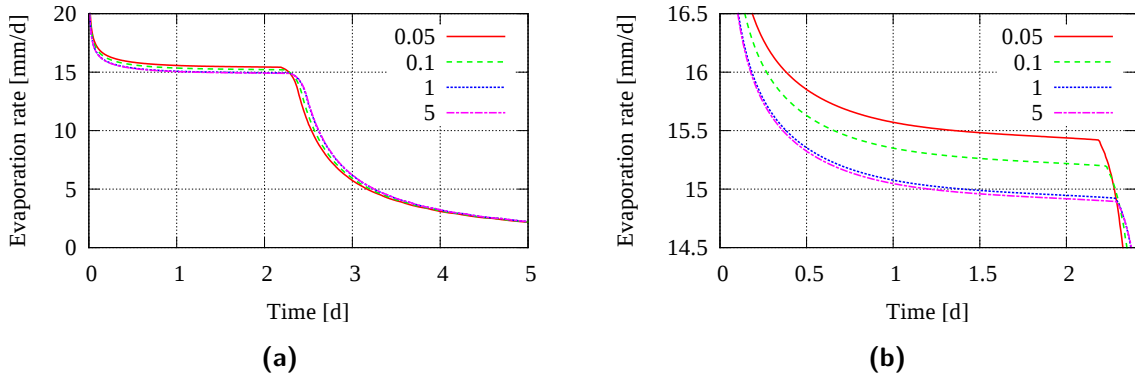


Figure 6.26: (6.26a) Comparison of the computed drying rates for different *Beavers-Joseph* coefficients. (6.26b) Zoom to stage-1 of the evaporation process.

6.4.2 Surface water content / saturation

The drying rates within stage-1 of the evaporation process may remain relatively constant over a wide range of the surface water content at the interface. In the analysis presented in Shahraeeni et al. (2012), they identify that the relative evaporation rate per individual pore may drastically increase during an evaporation process. This may even compensate the decreasing wet surface area which contributes to direct evaporation at the surface.

However, the evaporation rate may also depend in a nonlinear fashion on the surface water content during stage-1, as demonstrated before. For large pores and for a high free-stream velocity with thin boundary layers the drying rate may decrease already from the beginning of the evaporation process on without exhibiting a constant drying rate. The decreasing drying rate is readily observable in reported experiments (Lehmann et al., 2008; Shahraeeni et al., 2012) and in the experiments presented in Chapter 3. The efficiency of flux compensation postulated for increased spacing between pores (Shahraeeni et al., 2012) is greatly reduced for large pores and thin boundary layers.

A possible explanation is presented based on the consideration of equally sized and spaced evaporating pores in Suzuki and Maeda (1968); Schlünder (1988) and Haghighi et al. (2013). In a half-sphere directly above the evaporating pore, saturated vapor pressure is assumed, whereas a lower vapor pressure can be found outside this half-sphere. At a high water saturation, these

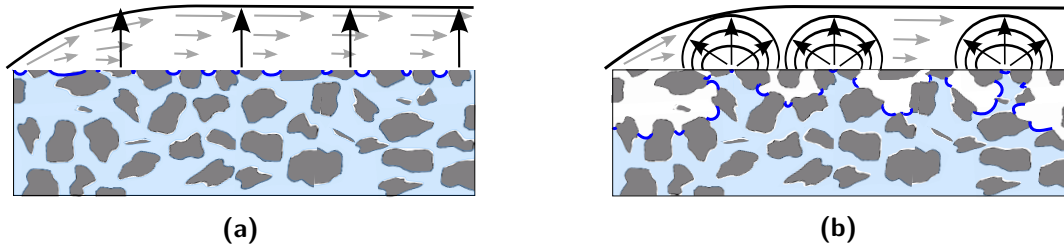


Figure 6.27: Pore-scale consideration of evaporation in the boundary layer with orderly flow parallel to the interface: A high surface water content and a short distance between evaporating pores leads to a quasi one-dimensional diffusion of the vapor normal to the boundary layer and relatively constant evaporation rates in stage-1. When the saturation decreases and the boundary layer is thin, the diffusion from evaporating pores lateral to the interface may become important. The evaporation rate can decrease already in stage-1, particularly if the diffusion length between these pores is large in relation to the mass boundary layer thickness (Suzuki and Maeda, 1968; Shahraeeni et al., 2012).

half-spheres overlay, leading to a rather one-dimensional concentration gradient across the boundary layer. When the interface becomes dryer, the air at the evaporating surface may no longer be fully saturated everywhere and a one-dimensional gradient cannot be established, if the mass boundary layer is relatively thin. Then, the lateral components of the vapor pressure gradient within the (mass) boundary layer lead to a gradual decrease of the drying rate during stage-1, as illustrated in Figure 6.27. In Haghghi et al. (2013) a formula is developed based on a geometric analysis as presented in Schlünder (1988), which allows to approximate the relative evaporation rate as a function of the surface water content. The concept is based on a known boundary-layer thickness and accounts especially for the interplay between the boundary layer and the water distribution at the surface.

On the REV scale, it is difficult to capture the influence of surface moisture content on the drying rate, because geometric information about the distribution of evaporating pores is lost due to the volume averaging. The spatial variability of the soil parameters is usually not resolved on this scale. If a homogeneous parameter distribution throughout the porous medium and especially at the surface is employed in REV-scale models, the cells at the interface have to dry out within a short time. This results generally in a period with a relatively constant drying rate and to an abrupt decrease to stage-2, if the water supply at the interface is not restricted by flow processes in the porous medium. On the REV scale, the influence of the surface moisture content has to be accounted for using averaged quantities, such as a function which depends on the surface area of water-filled pores, θ_l . A rough approximation thereof is provided by the volumetric information of the water saturation at the surface and the porosity,

$$\theta_l = \phi S_l. \quad (6.8)$$

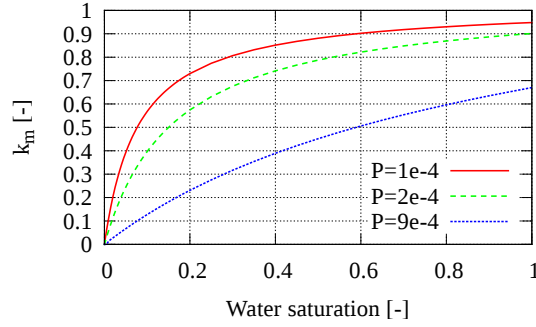


Figure 6.28: The relative evaporation rate k_m according to the Schlünder model with a constant boundary-layer thickness of 1.6 mm is depicted for different characteristic pore sizes.

In order to get integrate the possible saturation-dependency of the evaporation rate in the REV-scale models, a parametrization that depends on the surface moisture content as proposed in Suzuki and Maeda (1968); Schlünder (1988); Shahraeeni et al. (2012) and Haghghi et al. (2013) can be employed. This necessitates to scale the diffusive vapor fluxes in the coupling conditions ((6.2)) with a saturation-dependent mass transfer coefficient k_m as

$$J^{\text{vap}} = -k_m D_g^w \rho_g \frac{\Delta x_g^w}{\delta_m} \frac{M^\kappa}{\bar{M}}. \quad (6.9)$$

The mass-transfer coefficient may also be expressed as a resistance for the evaporative flux using the inverse (van de Griend and Owe, 1994; Haghghi et al., 2013). According to Schlünder (1988) the mass-transfer coefficient k_m as evaporation rate relative to the potential rate e_0 can be calculated on the pore scale as

$$k_m = \frac{\dot{e}}{e_0} = \left(1 + \frac{2}{\pi} \frac{r_{\text{char}}}{\delta_m} \sqrt{\frac{\pi}{4\theta_l}} \left(\sqrt{\frac{\pi}{4\theta_l}} - 1 \right) \right)^{-1}. \quad (6.10)$$

Here, θ_l is the relative wetted surface area, which is defined in Schlünder (1988) on the pore scale as $\theta_l = \frac{\pi r^2}{(2l)^2}$. On the REV scale, Equation (6.8) is used as approximation. This leads to an overestimation of the surface moisture content, because there is no uniform drying behavior within the cells at the interface, but they will dry out from top to bottom. To avoid a large influence, the cells at the interface have to be relatively thin. In contrast to the work presented in Haghghi et al. (2013), the resistance of the porous medium is already accounted for by the model concept.

The Schlünder approach was implemented and tested on the REV scale. The nonlinear interplay between relative evaporation rate and surface moisture content has to be parametrized with a suitable model, which may also account for a range of pore sizes. Current models lead to relative evaporation rates of zero for a dry surface, which does not represent reality properly and

does not allow to model stage-2. When the interface is dry, there is no direct evaporation from the water phase at the interface anymore, but vapor transfer via the gas phase still happens. Thus, a new parametrization with a proper scaling should be developed. To circumvent this, a blending has been included in the numerical model. As described before, a laminar free-flow model underestimates the boundary-layer thickness. To improve the quality of the computed diffusive fluxes across the air boundary layer, the computation has been modified as described in Equation (6.9).

It is further assumed that during stage-1 evaporation, the (vertical) transport of vapor through the boundary layer is limiting the evaporation rate and the porous medium provides a sufficient water supply due to water flow in capillaries, whereas stage-2 is mainly limited from the porous-medium side, because vapor transport happens via advective and diffusive transport in the void space of the porous medium. Thus, the water supply at the interface is much lower as in stage-1, and the transfer of vapor through the boundary layer is less important. The diffusive fluxes in the free flow are computed via the conventional coupling, which sustains the continuity of vapor fluxes and facilitates a continuation of the evaporation process after the transition to stage-2. This was realized by modifying the computation of the diffusive vapor fluxes to

$$\begin{aligned}
 & \left[\underbrace{-S_l k_m D_g \varrho_g \frac{\Delta x_g^w}{\delta_{BL}} M^w / \bar{M}}_{\text{direct evaporation through BL}} + \underbrace{S_g \left(\varrho_g \mathbf{v}_g X_g^w - D_g \varrho_g \nabla x_g^w M^w / \bar{M} \right) \cdot \mathbf{n}}_{\text{transport in gas phase}} \right]^{\text{ff}} = \\
 & - \left[\underbrace{\left(\varrho_g \mathbf{v}_g X_g^w + \varrho_l \mathbf{v}_l X_l^w \right)}_{\text{advective PM fluxes}} \underbrace{- D_{g,\text{pm}} \varrho_g \nabla x_g^w M^w - D_{l,\text{pm}} \varrho_l \nabla x_l^w M^w / \bar{M}}_{\text{diffusive PM fluxes}} \right]^{\text{pm}} \cdot \mathbf{n} .
 \end{aligned} \tag{6.11}$$

The direct evaporation from the water phase at the interface is weighted by the water saturation and computed with the mass-transfer concept presented in this chapter. For the vapor fluxes in the gas phase across the interface, the original coupling condition is employed and weighted by the gas phase saturation. In contrast to the evaporation from the water phase, this includes also advective gas fluxes across the interface.

For the proposed scaling of the direct evaporation from the water phase it is necessary to choose a characteristic pore radius, r_{char} . Different options have been tested:

- the radius of pores in the order of the largest grain diameter (0.9 mm),
- the smallest pore radius estimated from the capillary-pressure curve as 0.1 mm,
- the estimated mean pore diameter, which is roughly 0.2 mm,
- a variable pore radius delineated from the capillary-pressure curve.

The scaling of the evaporation rate according to Schlünder approach and the results are presented in Figures 6.28 and 6.29a. The most physical choice would be to delineate the characteristic pore radius with the help of the Young-Laplace equation from the capillary-pressure / saturation relationship as

$$r_{\text{char}} = 2\sigma/P_c(S_i) \quad (6.12)$$

where σ is the surface tension. With that, the pores that dry out (air entry at a contact angle of 0°) at the respective saturation are considered. However, compared to the measured drying curve, a constant pore radius of 0.9 mm leads to the closest results, as shown in Figure 6.29.

As already discussed in Section 6.2.3, with the van-Genuchten or Brooks-Corey curves employed in the entire saturation range, the transition to stage-2 is delayed in comparison to the measured drying rate. Thus, the capillary-pressure curve has been linearized roughly at the inflection point of the curve, as suggested in Lehmann et al. (2008) and as discussed before. This leads to a closer agreement of the rates and the transition time can be roughly met, as it is visible in Figure 6.29b.

The presented analysis was related to an evaporation experiment with 3.5 m/s air stream velocity and a relatively high atmospheric water demand. Thus, the drying curve decreased continuously. The same numerical setting is employed to compute drying rates for a lower air stream velocity of 1.5 m/s with a lower atmospheric demand. Figure 6.30 shows the comparison of the drying curve from an evaporation experiment with a free-stream velocity of 1.5 m/s ,

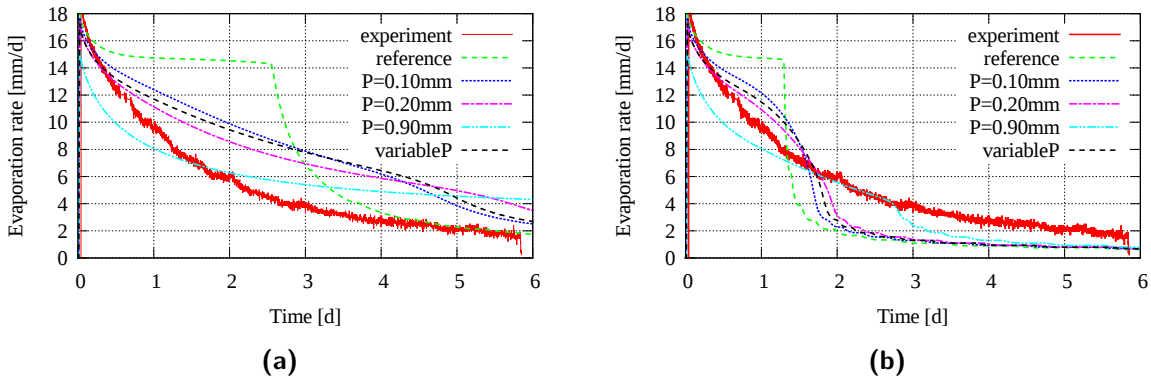


Figure 6.29: (a) Comparison of the measured evaporation rate with computed drying curves using the Schlünder concept. The figure shows drying rates using non-regularized capillary-pressure curves. The transition from stage-1 to stage-2 is not captured correctly. b) Comparison of the measured evaporation rate and the computed drying curves using capillary-pressure curves which are linearized roughly at an effective saturation of 0.3. The transition, which happened in the experiment roughly after two days, can be captured better with the linearization. The computations with the Schlünder concept indicate, that the use of the largest pore diameter leads to the best results.

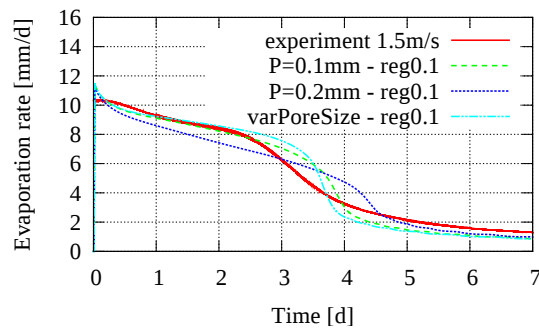


Figure 6.30: Comparison of a drying curve from a wind tunnel experiment (Shahraeeni et al., 2012) with a computed drying with a lower free air stream velocity of 1.5 m/s leading to a lower atmospheric demand. Compared to the curve with 3.5 m/s , the decrease in stage-1 is less.

which was published in Shahraeeni et al. (2012). The boundary-layer thickness was adapted to the flow velocity to a mean thickness of 2.5 mm to meet the initial drying rates. Although the physical setup of the evaporation experiment is the same, the packing of the sand may differ, leading to a slightly different pore size distribution especially at the interface and thus to a different relation between capillary pressure and water saturation. The capillary-pressure curve is linearized 0.1 before reaching the residual saturation in this case. Then, a good agreement between computed and measured drying rate can be obtained.

6.4.3 Surface roughness

The influence of surface roughness of bounding walls on the free air stream has been well-studied in the literature (see for example Acharya et al., 1986; Raupach et al., 1991; Antonia and Krogstad, 2001; Krogstad et al., 2005; Buschmann et al., 2009). Often, a displacement height is used to account for the effect of wall roughness on the boundary layer and flow field. Surface roughness may trigger the onset to a turbulent boundary layer and it affects the boundary layer thickness, where it decreases the flow velocity in vicinity of the surface, influencing the fluxes of vapor and energy across the boundary layer. However, the influence of a porous medium, where small eddies may perturb into the pores, is less clear. Turbulent fluctuations may be dampened by the porous medium and flow through the pores may occur.

For the algebraic turbulence models a simple approach using an equivalent sand roughness has been tested in Fetzer (2012). When the a characteristic roughness length (usually the grain diameter) of the surface is larger than the viscous sublayer thickness, the surface is considered as hydraulically rough. In Fetzer (2012), a hydraulically smooth wall was considered and only small effects of surface roughness on the drying rates were observed. However, the influence of the processes at the interface and in the boundary layer was already emphasized. A relatively

simple model was used for the analysis in Fetzer (2012), and more detailed studies considering the influence of the roughness of the porous-medium surface on the boundary layer and on the evaporation process is required. This can be done in conjunction with pore-scale modeling and measurements. Moreover, considering the influence of surface roughness on evaporation processes, the surface water content may also play a role.

6.4.4 Radiation

Solar radiation is one of the main driving forces of evaporation from natural soils. The sun emits high-energetic short-wave radiation, which is partly absorbed in the atmosphere, partly absorbed by the soil surface and partly reflected as long-wave radiation. In the scope of a Bachelor's thesis (Riesterer, 2013), possible ways to quantify and integrate radiation in the coupled model have been analyzed. Naturally, radiation is accounted for as surface term and can be integrated as Neumann boundary condition. However, due to the coupling of the energy balance at the interface, where the residuum is employed (see Chapter 5), it is advantageous to formulate radiation as volume term in the first volumes below the coupling interface. In order to convert the radiative heat input per volume in the source and sink term to radiation per surface area, it is divided by the respective cell height. Comparative simulations presented in Riesterer (2013) have shown only minor differences between the approach using a Neumann flux or specifying radiative heat input via the source and sink term. Furthermore, the implementation as volume term could be shown to be relatively independent of the grid resolution.

The performed simulations including solar radiation reveal a dominating influence of radiative energy input on the evaporation rate. Solar radiation may increase the evaporation rate drastically. In addition to the heat that is conducted from a heated surface, radiation from the porous medium may lead to a further cooling, if the atmospheric temperature is lower, as it may occur at night.

The net radiation, which acts at the soil surface, is strongly affected by the conditions in the atmosphere like albedo and temperature, and by the soil properties like surface emissivity. Note that only the lowest meters of the atmosphere are considered here. The equations which were most suitable for the computation of the solar radiation and its contribution to the energy balance are shown in the sequel. The net radiation at the soil surface can be approximated as suggested in Brutsaert (1982); Yamanaka et al. (1998) and Novak (2010) as

$$R_n = \underbrace{S_{\text{irr}}(1 - \alpha_s)}_{\text{short-wave radiation}} + \underbrace{\sigma_B \varepsilon_s (\varepsilon_a T_a^4 - T_s^4)}_{\text{long-wave radiation}} \quad (6.13)$$

where S denotes the solar irradiance, for which approximations of daily cycles exist (Bowers, 1978; Yamanaka et al., 1998) and which can be easily measured at the location of interest, α_s is the surface albedo, $\sigma_B = 5.67 \times 10^{-8} \text{ W/m}^2\text{K}^4$ is the Boltzmann constant, ε_s is the surface emissivity and ε_a is the atmospheric emissivity. In Riesterer (2013), all parameters appearing in Equation (6.13) have been varied and analyzed for their influence. Only the surface emissivity ε_s showed a negligible influence.

Furthermore, a long-term simulation was performed where diurnal cycles of irradiance, air temperature, etc. have been simulated over a period of ten days. A qualitative comparison to measured values (Novak, 2010) showed slightly higher values for the latent heat fluxes, which are also a measure of the evaporative vapor fluxes. The computed net radiation was comparable, and with regard to the complexity of the simulated system, the computed latent heat fluxes using the coupled model show a satisfying agreement, as depicted in Figure 6.31. Furthermore, the curve shows a memory effect for the temperature and the peaks of the evaporation rate increase in the first couple of days. This is due to heat stored in the deeper part of the porous medium during the nights, when the surface is cooled again. Simulations have shown a local heat maximum within the porous medium during nighttime.

6.4.5 Summary of the influence of the interface processes

The choice of the Beavers-Joseph coefficient used for the computation of the slip velocity at the interface showed to have only an influence on the drying rates for very small values of the coefficient. A surface-moisture dependency was not captured by the coupled model presented before. For this purpose, a concept to account for the surface water content has been implemented and tested. This integration lead to a better agreement between measured and computed drying rates. Furthermore, a concept for the integration of radiation into the coupled model was demonstrated.

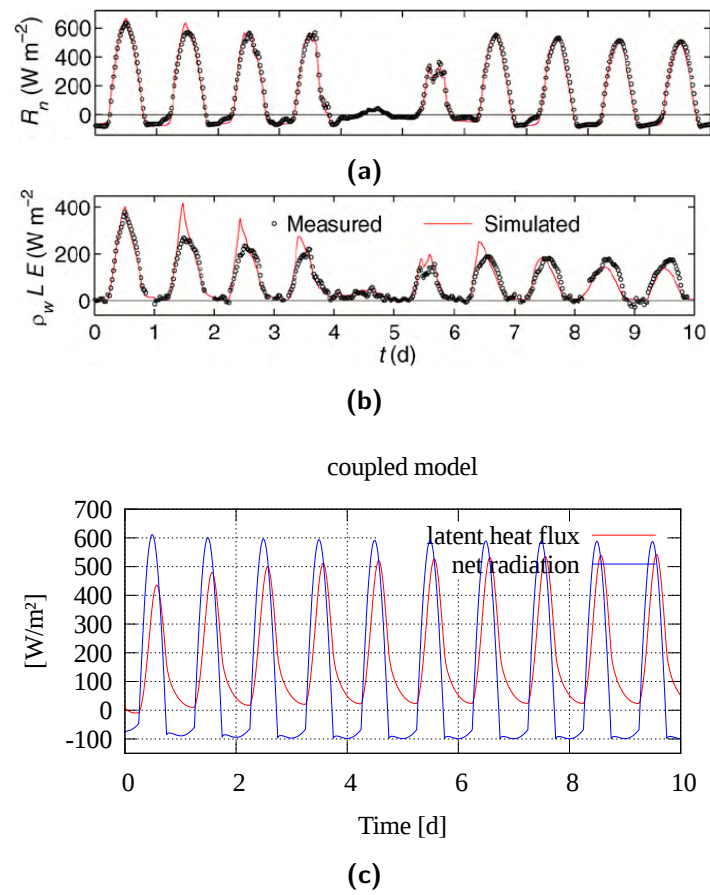


Figure 6.31: (a) Net radiation and latent heat flux (b) according to Novak (2010). (c) Computed net radiation and latent heat flux using the coupled model. Courtesy of Riesterer (2013).

6.5 Summary of this chapter and discussion

In the scope of this chapter, the influence of a wide array of parameters and processes in the porous medium, in the free flow and at the interface on the computed drying rate was investigated.

In the porous medium, the hydraulic parameters especially in the vicinity of the surface have a strong influence on the evaporation process. Especially the capillary-pressure curve at low saturations in conjunction with the relative permeability was shown to have a crucial impact on the drying rates in stage-1 and on the onset of stage-2. Heterogeneous structures (vertical textures, geostatistical distribution of parameter values) in the porous medium showed to critically influence the shape of the drying curve. Furthermore, the temperature in the porous medium affects various properties in the porous medium simultaneously and has a strong influence on the saturated vapor pressure at the interface. A less critical parameter in the considered cases was the solid thermal conductivity.

The conditions in the free flow, in particular the vapor concentration, temperature and flow velocities, shape the gradients across the boundary layer and on the drying rates. Together with the flow field and the boundary layer, they govern the gradients and resulting fluxes across the interface. Diurnal atmospheric pressure variations are reflected in the computed drying rates. The pressure influences fluid properties and may induce advective fluxes in the porous medium. A sinusoidal variation of the pressure showed temporal variations of the drying rate but has only a minor net effect, when the general course of the drying curves is considered. However, the variations in the atmosphere are usually highly complex involving simultaneous variations of several conditions which may lead to much stronger net effects. For the examination of the conditions and processes in the free flow, an algebraic turbulence model was employed. With that, the initial drying rates observed in wind-tunnel experiments at different air flow velocities could be reproduced using an algebraic turbulence model. However, the further course of the computed drying rates deviate from the measured ones.

The further course of the measured curve shows a saturation-dependency due to processes in the boundary layer in conjunction with geometric information of the evaporating pores and the interface area between water and air at the surface. The saturation-dependency of the evaporation rate was discussed and a concept based on a saturation-dependent mass-transfer coefficient was integrated and its effect shown. This coefficient scales the direct evaporation from the water phase at the interface between free flow and porous medium. With the inclusion of the saturation-dependency, the measured and the computed drying rates show a better agreement and decreasing drying rates during stage-1 were achieved. In the context of evaporation processes from natural porous media, solar radiation plays a crucial role and has

to be accounted for. Solar radiation may contribute a substantial amount of energy, which critically influences the conditions at the evaporating surface and enhances the drying rate. It was demonstrated, how radiation can be integrated in the coupled model. Simulations with a diurnal variation of the radiative heat input were conducted and the results presented. Similar results as in field experiment were obtained.

Discussion

In summary, evaporation processes are influenced by a great variety of parameters within both flow compartments which reveal a dynamical interplay. The boundary layer at the interface of the two compartments influences decisively the exchange of mass, momentum and energy. To capture this influence is quintessential for the modeling of evaporation processes from porous media.

All fluid-structure parameters (capillary pressure, relative permeability, effective thermal conductivity and diffusivity), are non-linear. Their representation on averaged volumes contains severe uncertainties considering their values at the porous-medium surface. This holds also for the surface water content, which is approximated by the volumetric quantities water saturation and porosity, and which is determining the transition from stage-1 to stage-2. The influence of the volumetric approximation of surface quantities can be reduced by a high grid vertical grid resolution in the vicinity of the interface. The interface processes are restricted to a relatively small region and do in general not scale, if a larger domain is considered. However, they crucially influence the evaporation behavior and have to be properly accounted for in REV-scale and field-scale models. Usually, area-specific quantities are not available, but would give a better representation of the processes happening at fluid-fluid and fluid-solid interfaces.

A good agreement between measured and computed drying curves was achieved on two different ways: with a statistical distribution of soil parameters and using a saturation-dependent transfer coefficient. The statistical distribution of the porous-medium parameters leads to a non-uniform drying behavior at the surface. However, information about small-scale heterogeneities is usually not available and, thus, the choice of the variance and correlation length is somehow arbitrary. Furthermore, the introduction of a heterogeneous distribution does not account for the processes happening in the boundary layer, and are further independent of the flow velocity. Hence, the scaling of the diffusive fluxes with a well-founded transfer coefficient that depends on the surface water content is the more promising approach.

7 Summary and outlook

7.1 Summary

The main focus of this study is on one hand on the development of a detailed coupled model which allows the simulation of a two-phase porous-medium system in conjunction with a single-phase free flow and on the other hand on a comprehensive analysis of the relevant processes for the mass, momentum and energy transfer. The objective is to advance the development of an elaborate model description of evaporation processes from porous media on the REV scale, taking the mutual influence of the two flow compartments and the processes occurring at the common interface into account and allowing for a detailed analysis of the influencing quantities. Theoretical and experimental evidence suggests that the interface between free flow and porous medium plays a crucial role for modeling evaporation processes on the REV scale.

Evaporation experiments in which a water-saturated porous medium (sand) was exposed to the air stream of a wind tunnel, were performed in cooperation with the Soil and Terrestrial Environmental Physics (STEP) research group of Professor Dani Or at the ETH Zürich. The experimental data are presented and used as a basis and anchor in reality for the model development, giving important insights into the dynamics of drying processes, with the aim of capturing relevant processes and characteristics with the developed model concept. The physical fundamentals in the two regions and their representation and conceptual model on the REV scale are explained. Then, a coupling concept for two-phase porous-medium flow exposed to an adjacent free flow under non-isothermal conditions allowing for compositional effects is developed. It considers two composite subdomains with different sets of equations which are coupled by appropriate coupling conditions at the lower-dimensional interface. The coupling conditions ensure flux continuity across the common interface and are based on local mechanical, thermal, and chemical equilibria. The numerical implementation of the sub-models and the coupling concept into the modeling framework *DuMu^x* in a monolithic fashion is elaborated and the employed discretization scheme described.

In a first step, the coupling concept is developed for laminar flow conditions in the free flow. Phenomenological explanations and model examples lend support to the developed concept,

but also show its limitations and issues requiring suitable extensions and adaptations. When air flow above a porous medium is considered, turbulent conditions are likely to develop. This has a crucial impact on the flow field and the boundary layers for mass, momentum and energy, which critically influence the exchange fluxes between porous medium and free flow. Comparisons of simulated data with experimental drying curves with high atmospheric demand demonstrate, that a laminar free-flow model leads to an overestimation of the relevant boundary-layer thickness and thus to drying rates below the ones observed in the experiments. The integration of a simple boundary-layer approximation and, alternatively, of an algebraic turbulence model help to improve the expressiveness of the model computations and the observed drying rates could be met.

A parameter and process analysis with the coupled model sheds light on the influence of several processes and properties of the porous medium, the fluids, the flow field and the interface. The influence of soil hydraulic properties, such as porosity and permeability, and parameters which quantify fluid-solid interactions, like the effective thermal conductivity and capillary pressure, on the evaporation dynamics is demonstrated. To this end, a reference case based on the wind-tunnel experiment is defined and single parameters are varied over a wide range. The capillary-pressure gradient close to residual saturation is identified as having a crucial influence on the transition from the high drying rate in the externally-controlled stage-1 to the diffusion-dominated stage-2 of an evaporation process. Further, the numerical investigations indicate that common parametrizations of the capillary-pressure / saturation relation, like the *Brooks-Corey* or the *van-Genuchten* model, overestimate the capillary pressure and relative permeability of water in the dry regime, resulting in a delayed transition from stage-1 to a lower rate in stage-2. Thus, the capillary-pressure curve is linearized and limited in the dry range. This adjustment results in an improved capture of the transition from stage-1 to stage-2, emphasizing the significance of the capillary pressure and relative permeability for the drying dynamics.

Drying experiments with relatively high evaporative demand have exhibited decreasing evaporation rates during stage-1, which is also known as the “constant rate period”. These are caused by the complex interplay of evaporating pores or pore clusters and the boundary layer. However, geometrical information about evaporating pores is not readily available on the REV scale, and this effect can only be integrated in an averaged fashion in dependency of the surface water content. The simulation runs demonstrate that the use of a homogeneous distribution of the soil parameters without a further modification of the coupling conditions in the numerical simulations leads to relatively constant drying rates in stage-1. To include a representation of the surface-water dependency on the exchange fluxes, the model is extended by a mass-transfer coefficient obtained from pore-scale considerations. This coefficient scales the diffusive vapor fluxes dependent on surface moisture content and boundary-layer thickness

based on the work presented in Haghighi et al. (2013) and Schlünder (1988). It is integrated and tested for its applicability in the REV-scale framework. Incorporation of this coefficient to scale the diffusive vapor fluxes at the interface improved the representation of experimentally measured evaporation rates at the transition to stage-2.

7.2 Outlook and suggestions for future work

The coupling concept presented in this thesis lays the cornerstone for modeling various applications involving the interplay of a single-phase free flow and a two-phase porous-medium flow under non-isothermal conditions with component transfer. The concept can be easily extended and adapted to a variety of other applications, like contaminant transport, salt deposition or drop formation at the surface of hydrophobic porous media (polymer-electrolyte-membrane fuel cells). Naturally, not all issues in such a complex system could be addressed and there is still a lot of space for further research and developments. In the following, suggestions are made considering future work deduced from this thesis, subdivided in concept development, numerical developments and experiments.

7.2.1 Concept development

The free flow is still represented with a relatively simple model and should be modeled with a more elaborate one. The influence of a possibly rough interface on the turbulent wind field and on the exchange fluxes and the further propagation of heat and vapor require a further analysis.

Moreover, the water saturation at the surface may influence the exchange fluxes critically and more attention should be paid to its impact. To capture this influence, the saturation-dependency and boundary-layer effects may be determined on the pore scale (numerically or experimentally) and integrated into the REV-scale model with suitable wall functions. The wall functions should incorporate sub-REV-scale processes as effective quantities and parametrizations obtained from detailed experiments or pore-scale simulations. For that purpose, the momentum, vapor and heat exchange at the boundary layer on the porous-medium and on the free-flow side of the common interface and the occurrence of penetrating turbulent eddies into the porous medium have to be analyzed in more detail.

Another issue which should receive attention is the assumption of a local thermodynamic equilibrium. Probably, the local thermal and chemical equilibrium at the interface may be violated for high free-stream velocities, leading to an overestimation of the heat and vapor

transfer. In which cases the equilibrium assumption holds and when the kinetic interfacial heat and mass transfer has to be accounted for remains a subject for further research.

In order to simulate realistic larger-scale scenarios with, for example, sequences of infiltration due to rainfall and evaporation under varying external conditions, hysteretic constitutive relations and dynamic capillary effects have to be considered. With the developed coupled model, simplified modeling approaches can be checked for the scope of their applicability. At the interface of the two flow compartments, strong gradients of velocity, concentration and temperature occur. The diffusion due to thermal gradients is not considered separately in this study. However, first calculations show that it may have a strong influence on the exchange fluxes. The same holds for radiative energy transfer between the porous-medium surface and the surroundings. It may also be beneficial to consider a non-simple interface that actually can store mass or energy.

7.2.2 Numerical developments

So far, the implemented model can only handle two-dimensional problems, although turbulence and the flow processes in the free flow and the porous medium clearly reveal three-dimensional features. This limitation can be mainly attributed to the high numerical effort of such complex simulations. The model could not yet be parallelized properly, because the employed *DUNE* module *DUNE-multidomain* has not been parallelized at the time of this research. Moreover, the coupled matrix is badly conditioned and requires the use of a direct numerical solver which has a high memory and computational demand that increases disproportionately with the degrees of freedom. Until now, only shared-memory solvers are available in conjunction with the *DUNE* framework and thus no suitable parallelized linear solver with a distributed-memory architecture could be integrated. A domain-decomposition and iterative subdomain scheme with a decoupled time-stepping would probably boost model efficiency and allow dedicated schemes and solvers to be employed for each subdomain.

Furthermore, the implemented model relies on the assumption of a flat surface. Due to the equal-order approximation of velocity and pressure, the free-flow model tends to produce pressure oscillations. Thus, it is desirable to exchange the free-flow discretization with a more robust and flexible one, using, for example, a staggered grid where pressure and velocity are evaluated at different positions. More elaborate turbulence models, like $k-\epsilon$ or $k-\omega$ models, should be integrated.

7.2.3 Experiments

Future experimental work should focus on the processes occurring at the interface between porous medium and free flow and within the boundary layer. Larger and standardized samples would minimize the influence of the sample filling, of the vessel walls and of small-scale heterogeneities on resulting drying curves and allow a systematic code verification. For this purpose, the soil properties have to be determined accurately. The combination of modern tomography methods and pore-scale modeling could provide an excellent tool for the determination of effective quantities for the REV-scale models.

Bibliography

- Acharya, M., Bornstein, J., and Escudier, M. Turbulent boundary layers on rough surfaces. *Experiments in Fluids*, 4:33–47, 1986.
- Ahrenholz, B., Niessner, J., Helmig, R., and Krafczyk, M. Pore-scale determination of parameters for macro-scale modeling of evaporation processes in porous media. *Water Resources Research*, 47:W07543, 2011.
- Alazmi, B. and Vafai, K. Analysis of fluid flow and heat transfer interfacial conditions between a porous medium and a fluid layer. *International Journal of Heat and Mass Transfer*, 44: 1735–1749, 2001.
- Angot, P. Analysis of singular perturbations on the Brinkman problem for fictitious domain models of viscous flows. *Mathematical Methods in the Applied Sciences*, 22:1395–1412, 1999.
- Antonia, R. and Krogstad, P.-A. Turbulence structure in boundary layers over different types of surface roughness. *Fluid Dynamics Research*, 28:139–157, 2001.
- Atkins, P. and De Paula, J. *Physical Chemistry*. W. H. Freeman, 2006.
- Aydin, M., Yang, S. L., Kurt, N., and Yano, T. Test of a simple model for estimating evaporation from bare soils in different environments. *Ecological Modelling*, 182:91–105, 2005.
- Baber, K., Mosthaf, K., Flemisch, B., Helmig, R., and Müthing, S. Numerical scheme for coupling two-phase compositional porous-media flow and one-phase compositional free flow. *IMA Journal of Applied Mathematics*, 77:887–909, 2012.
- Baehr, H. D. and Stephan, K. *Wärme- und Stoffübertragung*. Springer-Verlag, 2010.
- Baldwin, B. S. and Lomax, H. Thin layer approximation and algebraic model for separated turbulent flows. *American Institute of Aeronautics and Astronautics Journal*, pages 78–257, 1978.
- Bastian, P., Blatt, M., Dedner, A., Engwer, C., Klotzkorn, R., Kornhuber, R., Ohlberger, M., and Sander, O. A generic grid interface for parallel and adaptive scientific computing. part ii: Implementation and tests in DUNE. *Computing*, 82:121–138, 2008.

- Bastian, P., Heimann, F., and Marnach, S. Generic implementation of finite element methods in the Distributed and Unified Numerics Environment (DUNE). *Kybernetika*, 46:294–315, 2010.
- Bear, J. *Dynamics of fluids in porous media*. Elsevier, 1988.
- Beavers, G. S. and Joseph, D. D. Boundary conditions at a naturally permeable wall. *Journal of Fluid Mechanics*, 30:197–207, 1967.
- Bechtold, M., Haber-Pohlmeier, S., Vanderborght, J., Pohlmeier, A., Ferré, T. P. A., and Vereecken, H. Near-surface solute redistribution during evaporation. *Geophysical Research Letters*, 38:L17404, 2011.
- Bird, R. B., Stewart, W. E., and Lightfoot, E. N. *Transport phenomena*. John Wiley and Sons, 2007.
- Bittelli, M., Ventura, F., Campbell, G., Snyder, R. L., Gallegati, F., and Pisa, P. R. Coupling of heat, water vapor, and liquid water fluxes to compute evaporation in bare soils. *Journal of Hydrology*, 362:191–205, 2008.
- Blasius, H. The boundary layers in fluids with little friction. *Zeitschrift für Mathematik und Physik*, 56:1–57, 1908.
- Boussinesq, J. Essai sur la theorie des eaux courantes. *Memoires a l'Academie des Sciences*, 1, 1872.
- Bowers, J. Surface radiation and energy balances at a mid-latitude alpine tundra site during the summer. Master's thesis, University of Victoria, 1978.
- Brinkman, H. A calculation of the viscous force exerted by a flowing fluid on a dense swarm of particles. *Applied Scientific Research*, A1:27–34, 1947.
- Brooks, R. H. and Corey, A. T. *Hydraulic properties of porous media*. Colorado State University, 1964.
- Brutsaert, W. *Evaporation into the atmosphere: Theory, history and applications*. Kluwer Academic Publishers, 1982.
- Burdine, N. Relative permeability calculations from pore size distribution data. *Trans. AIME*, 198:71–77, 1953.
- Buschmann, M. H., Indinger, T., and Gad-el Hak, M. Near-wall behavior of turbulent wall-bounded flows. *International Journal of Heat and Fluid Flow*, 30:993–1006, 2009.
- Chandesris, M. and Jamet, D. Boundary conditions at a planar fluidporous interface for a Poiseuille flow. *International Journal of Heat and Mass Transfer*, 49:2137–2150, 2006.

-
- Chandesris, M. and Jamet, D. Boundary conditions at a fluid-porous interface: An a priori estimation of the stress jump coefficients. *International Journal of Heat and Mass Transfer*, 50:3422–3436, 2007.
- Chandesris, M. and Jamet, D. Jump conditions and surface-excess quantities at a fluid/porous interface: A multi-scale approach. *Transport in Porous Media*, 78:419–438, 2009.
- Chen, S. and Doolen, G. D. Lattice Boltzmann method for fluid flows. *Annual Review of Fluid Mechanics*, 30:329–364, 1998.
- Choudhury, B. and DiGirolamo, N. A biophysical process-based estimate of global land surface evaporation using satellite and ancillary data i. model description and comparison with observations. *Journal of Hydrology*, 205:164–185, 1998.
- Class, H. *Multiphase flow and transport in porous media theory and modeling*. PhD thesis, Universität Stuttgart, Institut für Wasserbau, 2009.
- Class, H., Helmig, R., and Bastian, P. Numerical simulation of non-isothermal multiphase multicomponent processes in porous media - 1. An efficient solution technique. *Advances in Water Resources*, 25:533–550, 2002.
- Class, H., Ebigbo, A., Helmig, R., Dahle, H. K., Nordbotten, J. M., and Celia, M. A. A benchmark study on problems related to co2 storage in geologic formations. *Computational Geosciences*, 13:409–434, 2009.
- Côté, J. and Konrad, J. A generalized thermal conductivity model for soils and construction materials. *Canadian Geotechnical Journal*, 42:443–458, 2005.
- Crone, S., Bergins, C., and Strauss, K. Multiphase flow in homogeneous porous media with phase change. part i: Numerical modeling. *Transport in Porous Media*, 49:291–312, 2002.
- Darcy, H. P. G. *Les fontaines publiques de la ville de Dijon*. Dalmont, 1856.
- Defraeye, T., Blocken, B., and Carmeliet, J. Analysis of convective heat and mass transfer coefficients for convective drying of a porous flat plate by conjugate modelling. *International Journal of Heat and Mass Transfer*, 55:112–124, 2012a.
- Defraeye, T., Houvenaghel, G., Carmeliet, J., and Derome, D. Numerical analysis of convective drying of gypsum boards. *International Journal of Heat and Mass Transfer*, 55:2590—2600, 2012b.
- Deissler, R. G. Analysis of turbulent heat transfer, mass transfer, and friction in smooth tubes at high Prandtl and Schmidt numbers. Technical report, Naca report, 1210, 1954.

- Deissler, R. G. Turbulent heat transfer and temperature fluctuations in a field with uniform velocity and temperature gradients. *International Journal of Heat and Mass Transfer*, 6: 257–270, 1963.
- Discacciati, M., Quarteroni, A., and Valli, A. Robin–Robin domain decomposition methods for the Stokes–Darcy coupling. *SIAM Journal on Numerical Analysis*, 45:1246–1268, 2007.
- Durlofsky, L. and Brady, J. Analysis of the Brinkman equation as a model for flow in porous media. *Physics of Fluids*, 30:3329–3341, 1987.
- Erbertseder, K., Reichold, J., Flemisch, B., Jenny, P., and Helmig, R. A coupled discrete/continuum model for describing cancer-therapeutic transport in the lung. *PLOS ONE*, 7(e31966), 2012.
- Ferziger, J. H. and Peric, M. *Computational methods for fluid dynamics*. Springer, 2002.
- Fetzer, T. Numerical analysis of the influence of turbulence on exchange processes between porous-medium and free flow. Master’s thesis, Department of Hydromechanics and Modeling of Hydrosystems, University of Stuttgart, 2012.
- Fick, A. Über Diffusion. *Annalen der Physik*, 170:59–86, 1855.
- Flemisch, B., Darcis, M., Erbertseder, K., Faigle, B., Lauser, A., Mosthaf, K., Müthing, S., Nuske, P., Tatomir, A., Wolff, M., and Helmig, R. Dumux: Dune for multi-{Phase, Component, Scale, Physics, ...} flow and transport in porous media. *Advances in Water Resources*, 34:1102–1112, 2011.
- Franca, L. P., Hughes, T. J. R., and Stenberg, R. Stabilized finite element methods for the Stokes problem. This is a preprint of Chapter 4 in *Incompressible Computational Fluid Dynamics*. M. Gunzburger and R.A. Nicolaides, Eds. Cambridge University Press 1993. pp. 87-107.
- Geiges, A. Examination of the assumption of thermal equilibrium on the fluid distribution and front stability. Master’s thesis, Department of Hydromechanics and Modeling of Hydrosystems, University of Stuttgart, 2009.
- Girault, V. and Rivière, B. DG approximation of coupled Navier-Stokes and Darcy equations by Beaver-Saffman interface condition. *SIAM Journal on Applied Mathematics*, 47:2052–2089, 2009.
- Goyeau, B., Lhuillier, D., Gobin, D., and Velarde, M. Momentum transport at a fluid-porous interface. *International Journal of Heat and Mass Transfer*, 46:4071–4081, 2003.

- Gray, W. and Miller, C. Thermodynamically constrained averaging theory approach for modeling flow and transport phenomena in porous media systems: 1. motivation and overview. *Advances in Water Resources*, 28:161–180, 2005.
- Gray, W., Leijnse, A., Randall, L., and Blain, C. *Mathematical tools for changing spatial scales in the analysis of physical systems*. CRC Press, 1993.
- Gupte, S. K. and Advani, S. G. Flow near the permeable boundary of a porous medium: An experimental investigation using LDA. *Experiments in Fluids*, 22:408–422, 1997.
- Gurau, V. and Mann, J. A. A critical overview of computational fluid dynamics multiphase models for proton exchange membrane fuel cells. *SIAM Journal on Applied Mathematics*, 70:410–454, 2009.
- Haghighi, E., Shahraeeni, E., Lehmann, P., and Or, D. Evaporation rates across a convective air boundary layer are dominated by diffusion. *Water Resources Research*, 49:1602–1610, 2013.
- Hahn, S., Je, J., and Choi, H. Direct numerical simulation of turbulent channel flow with permeable walls. *Journal of Fluid Mechanics*, 450:259–285, 2002.
- Hanna, O. T. and Sandall, O. C. Developed turbulent transport in ducts for large Prandtl or Schmidt numbers. *Aiche Journal*, 18:527–533, 1972.
- Hassanizadeh, S. Derivation of basic equations of mass transport in porous media, part 2: Generalized Darcy’s and Fick’s laws. *Advances in Water Resources*, 9:207–222, 1986.
- Hassanizadeh, S. M. and Gray, W. G. Derivation of conditions describing transport across zones of reduced dynamics within multiphase systems. *Water Resources Research*, 25: 529–539, 1989.
- Hassanizadeh, S. M. and Gray, W. G. Mechanics and thermodynamics of multiphase flow in porous media including interphase boundaries. *Advances in Water Resources*, 13:169–186, 1990.
- He, X. Y. and Luo, L. S. Lattice Boltzmann model for the incompressible Navier-Stokes equation. *Journal of Statistical Physics*, 88:927–944, 1997.
- Helmig, R. *Multiphase flow and transport processes in the subsurface*. Springer-Verlag, 1997.
- Heywood, J. G., Rannacher, R., and Turek, S. Artificial boundaries and flux and pressure conditions for the incompressible Navier-Stokes-equations. *International Journal for Numerical Methods in Fluids*, 22:325–352, 1996.
- Hillel, D. *Introduction to environmental soil physics*. Academic Press, 2004.

- Ho, C. K. *Vapor transport processes*, chapter 3, pages 27–46. Springer, 2006.
- Huber, R. and Helmig, R. Node-centered finite volume discretizations for the numerical simulation of multiphase flow in heterogeneous porous media. *Computational Geosciences*, 4:141–164, 2000.
- IAPWS. IAPWS, 2009. URL <http://www.iapws.org>. Revised release on the IAPWS formulation 1995 for the thermodynamic properties of ordinary water substance for general and scientific use.
- Incropera, F. P., Dewitt, D. P., Bergman, T. L., and Lavine, A. S. *Fundamentals of heat and mass transfer*. John Wiley and Sons, 2007a.
- Incropera, F. P., Dewitt, D. P., Bergman, T. L., and Lavine, A. S. *Introduction to heat transfer*. John Wiley and Sons, 2007b.
- Jackson, A. S., Rybak, I., Helmig, R., Gray, W. G., and Miller, C. T. Thermodynamically constrained averaging theory approach for modeling flow and transport phenomena in porous media systems: 9. Transition region models. *Advances in Water Resources*, 42:71–90, 2012.
- Jackson, A., Miller, C., and Gray, W. Thermodynamically constrained averaging theory approach for modeling flow and transport phenomena in porous medium systems: 6. two-fluid-phase flow. *Advances in Water Resources*, 32:779–795, 2009.
- Jäger, W. and Mikelić, A. On the interface boundary condition of Beavers, Joseph and Saffman. *SIAM Journal on Applied Mathematics*, 60:1111–1127, 2000.
- Jäger, W. and Mikelić, A. Modeling effective interface laws for transport phenomena between an unconfined fluid and a porous medium using homogenization. *Transport in Porous Media*, 78:489–508, 2009.
- Jamet, D., Chandesris, M., and Goyeau, B. On the equivalence of the discontinuous one- and two-domain approaches for the modeling of transport phenomena at a fluid/porous interface. *Transport in Porous Media*, 78:403–418, 2009.
- Johansen, O. Thermal conductivity of soils. Technical report, Cold Regions Research and Engineering Laboratory Hanover, New Hampshire, 1977.
- Jury, W. A. and Horton, R. *Soil physics*. John Wiley and Sons, 2004.
- Kolmogorov, A. N. The local structure of turbulence in incompressible viscous fluid for very large Reynolds numbers. *Doklady Akademiyi Nauk SSSR*, 30:9–13, 1941.
- Krogstad, P., Andersson, H., Bakken, O., and Ashrafian, A. An experimental and numerical study of channel flow with rough walls. *Journal of Fluid Mechanics*, 530:327–352, 2005.

-
- Lallemand, P. and Luo, L. S. Theory of the Lattice Boltzmann method: Dispersion, dissipation, isotropy, Galilean invariance, and stability. *Physical Review E*, 61:6546–6562, 2000.
- Laufer, J. The structure of turbulence in fully developed pipe flow. Technical Report 1174, National Advisory Committee for Aeronautics, 1954.
- Lauser, A., Hager, C., Helmig, R., and Wohlmuth, B. A new approach for phase transitions in miscible multi-phase flow in porous media. *Advances in Water Resources*, 34:957–966, 2011.
- Layton, W. J., Schieweck, F., and Yotov, I. Coupling fluid flow with porous media flow. *SIAM Journal on Numerical Analysis*, 40(6):2195–2218, 2002.
- Lehmann, P., Assouline, S., and Or, D. Characteristic lengths affecting evaporative drying of porous media. *Physical Review E*, 77:056309, 2008.
- Lehmann, P. and Or, D. Evaporation and capillary coupling across vertical textural contrasts in porous media. *Physical Review E*, 80:046318, 2009.
- Lenhard, R., Parker, J., and Mishra, S. On the correspondence between Brooks-Corey and van Genuchten models. *Journal of Irrigation and Drainage Engineering*, 115:744–751, 1989.
- Leverett, M. C. Capillary behavior in porous solids. *Transactions of the American Institute of Mining and Metallurgical Engineers*, 142:152–169, 1941.
- Levy, T. and Sanchez-Palencia, E. On boundary conditions for fluid flow in porous media. *International Journal of Engineering Science*, 13:923–940, 1975.
- Li, X. S. An overview of SuperLU: Algorithms, implementation, and user interface. *ACM Transactions on Mathematical Software*, 31:302–325, 2005.
- Liu, S., Graham, W. D., and Jacobs, J. M. Daily potential evapotranspiration and diurnal climate forcings: influence on the numerical modelling of soil water dynamics and evapotranspiration. *Journal of Hydrology*, 309:39–52, 2005.
- Lundgren, T. Slow flow through stationary random beds and suspensions of spheres. *Journal of Fluid Mechanics*, 51:273–299, 1972.
- Maroulis, Z. B., Kiranoudis, C. T., and Marinou-Kouris, D. Heat and mass transfer modeling in air drying of foods. *Journal of Food Engineering*, 26:113–130, 1995.
- Martys, N., Bentz, D. P., and Garboczi, E. J. Computer simulation study of the effective viscosity in Brinkman’s equation. *Physics of Fluids*, 6(4):1434–1439, 1994.
- Masson, C., Saabas, H. J., and Baliga, B. R. Co-located equal-order control-volume finite element method for two-dimensional axisymmetric incompressible fluid flow. *International Journal for Numerical Methods in Fluids*, 18:1–26, 1994.

- Millington, R. and Quirk, J. Permeability of porous solids. *Transactions of the Faraday Society*, 57:1200–1207, 1961.
- Mosthaf, K., Baber, K., Flemisch, B., Helmig, R., Leijnse, A., Rybak, I., and Wohlmuth, B. A coupling concept for two-phase compositional porous medium and single-phase compositional free flow. *Water Resources Research*, 47:W10522, 2011.
- Mosthaf, K., Helmig, R., and Or, D. Modeling and analysis of evaporation processes from porous media on the rev scale. *Submitted to Water Resources Research*, 2013.
- Mualem, Y. A new model predicting the hydraulic conductivity of unsaturated porous media. *Water Resources Research*, 12:513–522, 1976.
- Müthing, S. and Bastian, P. DUNE-Multidomaingrid: A metagrid approach to subdomain modelling. In Dedner, A., Flemisch, B., and Klöforn, R., editors, *Advances in DUNE. DUNE User Meeting 2010*, Stuttgart, 2012.
- Neumann, R., Bastian, P., and Ippisch, O. Modeling and simulation of two-phase two-component flow with disappearing nonwetting phase. *Computational Geosciences*, 17: 139–149, 2013.
- Nield, D. A. and Bejan, A. *Convection in porous media*. Springer, 2006.
- Novak, M. Dynamics of the near-surface evaporation zone and corresponding effects on the surface energy balance of a drying bare soil. *Agricultural and Forest Meteorology*, 150: 1358–1365, 2010.
- Nuske, P., Joekar-Niasar, V., and Helmig, R. Non-equilibrium in multiphase flow in porous media: An evaporation example. *Submitted to Water Resources Research*, 2013. submitted.
- Ochoa-Tapia, J. A. and Whitaker, S. Momentum transfer at the boundary between a porous medium and a homogeneous fluid – I. theoretical development. *International Journal of Heat and Mass Transfer*, 38(14):2635–2646, 1995.
- Ochs, S., Class, H., Färber, A., and Helmig, R. Methods for predicting the spreading of steam below the water table during subsurface remediation. *Water Resources Research*, 46: W05520, 2010.
- Oke, T. R. *Boundary Layer Climates*. Methuen & Co., 1978.
- Pan, C., Luo, L., and Miller, C. An evaluation of Lattice Boltzmann schemes for porous medium flow simulation. *Computers and Fluids*, 35:898–909, 2006.

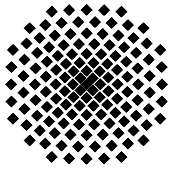
-
- Papafotiou, A., Sheta, H., and Helmig, R. Numerical modeling of two-phase hysteresis combined with an interface condition for heterogeneous porous media. *Computational Geosciences*, 14:273–287, 2010.
- Patterson, B. M. and Davis, G. B. Quantification of vapor intrusion pathways into a slab-on-ground building under varying environmental conditions. *Environmental Science and Technology*, 43:650–656, 2009.
- Pebesma, E. J. and Wesseling, C. G. Gstat: A program for geostatistical modelling, prediction and simulation. *Computers & Geosciences*, 24:17–31, 1998.
- Pope, S. B. *Turbulent flows*. Cambridge University Press, 2000.
- Prandtl, L. über Flüssigkeitsbewegung bei sehr kleiner Reibung. In *Verhandlungen des III. Internationalen Mathematiker-Kongresses Heidelberg*, 1904.
- Prat, M. Modelling of heat transfer by conduction in a transition region between a porous medium and an external fluid. *Transport in Porous Media*, 5:71–95, 1990.
- Raupach, M., Antonia, R., and Rajagopalan, S. Rough-wall turbulent boundary layers. *Applied Mechanics Reviews*, 44:1–25, 1991.
- Reid, R. C., Prausnitz, J. M., and Poling, B. E. *The properties of gases & liquids*. McGraw-Hill, Inc., 1987.
- Riesterer, D. Analysis of modeling concept for radiative heat exchange during evaporation processes from porous media. Master’s thesis, Department of Hydromechanics and Modeling of Hydrosystems, University of Stuttgart, 2013.
- Rosenzweig, R. and Shavit, U. The laminar flow field at the interface of a Sierpinski carpet configuration. *Water Resources Research*, 43(W10402):W10402, 2007.
- Saffman, P. On the boundary condition at the surface of a porous medium. *Studies in Applied Mathematics*, L:93–101, 1971.
- Sahraoui, M. and Kaviany, M. Slip and no-slip velocity boundary conditions at interface of porous, plain media. *International Journal of Heat and Mass Transfer*, 35(4):927–943, 1992.
- Saneinejad, S., Moonen, P., Defraeye, T., Derome, D., and Carmelie, J. Coupled cfd, radiation and porous media transport model for evaluating evaporative cooling in an urban environment. *Journal of Wind Engineering and Industrial Aerodynamics*, 104:455–463, 2012.
- Scheidegger, A. E. *The physics of flow through porous media*. University of Toronto Press, 1974.

- Schenk, O., Waechter, A., and Hagemann, M. Matching-based preprocessing algorithms to the solution of saddle-point problems in large-scale nonconvex interior-point optimization. *Computational Optimization and Application*, 36:321–341, 2007.
- Schenk, O., Bollhoefer, M., and Roemer, R. A. On large-scale diagonalization techniques for the Anderson model of localization. *SIAM Review*, 50:91–112, 2008.
- Schlichting, H. and Gersten, K. *Grenzschicht-Theorie*. Springer, 2006.
- Schlünder, E.-U. On the mechanism of the constant drying rate period and its relevance to diffusion controlled catalytic gas phase reactions. *Chemical Engineering Science*, 43 (10): 2685–2688, 1988.
- Schneider, M. and Goss, K.-U. Prediction of water retention curves for dry soils from an established pedotransfer function: Evaluation of the Webb model. *Water Resources Research*, 48(W06603), 2012.
- Shahraeeni, E. and Or, D. Pore-scale evaporation-condensation dynamics resolved by synchrotron x-ray tomography. *Physical Review E*, 85:016317, 2012.
- Shahraeeni, E., Lehmann, P., and Or, D. Coupling of evaporative fluxes from drying porous surfaces with air boundary layer: Characteristics of evaporation from discrete pores. *Water Resources Research*, 48:W09525, 2012.
- Shavit, U. Special issue: Transport phenomena at the interface between fluid and porous domains. *Transport in Porous Media*, 78:327–330, 2009.
- Shavit, U., Bar-Yosef, G., and Rosenzweig, R. Modified Brinkman equation for a free flow problem at the interface of porous surfaces: The Cantor-Taylor brush configuration case. *Water Resources Research*, 38(12):1320, 2002.
- Shavit, U., Rosenzweig, R., and Assouline, S. Free flow at the interface of porous surfaces: A generalization of the Taylor brush configuration. *Transport in Porous Media*, 54:345–360, 2004.
- Shokri, N. and Or. What determines drying rates at the onset of diffusion controlled stage-2 evaporation from porous media? *Water Resources Research*, 47:W09513, 2011.
- Shokri, N., Lehmann, P., Vontobel, P., and Or, D. Drying front and water content dynamics during evaporation from sand delineated by neutron radiography. *Water Resources Research*, 44:W06418, 2008.
- Shokri, N., Lehmann, P., and Or, D. Critical evaluation of enhancement factors for vapor transport through unsaturated porous media. *Water Resources Research*, 45:W10433, 2009.

-
- Smits, K. M., Ngo, V. V., Cihan, A., Sakaki, T., and Illangasekare, T. H. An evaluation of models of bare soil evaporation formulated with different land surface boundary conditions and assumptions. *Water Resources Research*, 48:W12526, 2012.
- Smits, K. M., Cihan, A., Sakaki, T., Howington, S., Peters, J. F., and Illangasekare, T. Soil moisture and thermal behavior in the vicinity of buried objects affecting remote sensing detection: Experiments and modeling investigation. *IEEE Transactions on Geoscience and Remote Sensing*, 51:2675–2688, 2013.
- Smits, K. M., Sakaki, T., Limsuwat, A., and Illangasekare, T. H. Thermal conductivity of sands under varying moisture and porosity in drainage-wetting cycles. *Vadose Zone Journal*, 9:172–180, 2010.
- Smits, K., Cihan, A., Sakaki, T., and Illangasekare, T. Evaporation from soils under thermal boundary conditions: Experimental and modeling investigation to compare equilibrium- and nonequilibrium-based approaches. *Water Resources Research*, 47:W05540, 2011.
- Soares, D. J., Rodrigues, G. G., and Gonçalves, K. A. An efficient multi-time-step implicit-explicit method to analyze solid-fluid coupled systems discretized by unconditionally stable time-domain finite element procedures. *Computers and Structures*, 88:387–394, 2010.
- Somerton, C. W. and Catton, I. On the thermal-instability of superposed porous and fluid layers. *Journal of Heat Transfer*, 104:160–165, 1982.
- Suzuki, S. and Maeda, S. On the mechanism of drying of granular bed – mass transfer from discontinuous source. *Journal of Chemical Engineering of Japan*, 1 (1):26–31, 1968.
- Szymkiewicz, A., Helmig, R., and Neuweiler, I. Upscaling unsaturated flow in binary porous media with air entry pressure effects. *Water Resources Research*, 48:W04522, 2012.
- Tölke, J., Freudiger, S., and Krafczyk, M. An adaptive scheme using hierarchical grids for Lattice Boltzmann multi-phase flow simulations. *Computers and Fluids*, 35:820–830, 2006.
- Truckenbrodt, E. *Fluidmechanik 1: Grundlagen und elementare Strömungsvorgänge dichtebeständiger Fluide*. Springer, 2. edition, 2008a.
- Truckenbrodt, E. *Fluidmechanik 2: Elementare Strömungsvorgänge dichteveränderlicher Fluide sowie Potential- und Grenzschichtströmungen*. Springer, 2008b.
- Tuller, M. and Or, D. Water films and scaling of soil characteristic curves at low water contents. *Water Resources Research*, 41(W09403), 2005.

- Valdes-Parada, F. J., Alvarez-Ramirez, J., Goyeau, B., and Ochoa-Tapia, J. A. Computation of jump coefficients for momentum transfer between a porous medium and a fluid using a closed generalized transport equation. *Transport in Porous Media*, 78(5):439–457, March 2009a.
- Valdés-Parada, F., Goyeau, B., and Ochoa-Tapia, A. Diffusive mass transfer between a microporous medium and an homogeneous fluid: Jump boundary conditions. *Chemical Engineering Science*, 61:1692–1704, 2006.
- Valdés-Parada, F., Ochoa-Tapia, J., and Alvarez-Ramirez, J. Diffusive mass transport in the fluid–porous medium inter-region: Closure problem solution for the one-domain approach. *Chemical Engineering Science*, 62:6054–6068, 2007.
- Valdes-Parada, F. J., Alvarez-Ramirez, J., Goyeau, B., and Ochoa-Tapia, J. A. Jump condition for diffusive and convective mass transfer between a porous medium and a fluid involving adsorption and chemical reaction. *Transport in Porous Media*, 78:459–476, 2009b.
- van Brakel, J. *Advances in drying*, volume 1, chapter 7: Mass transfer in convective drying, pages 217–267. Hemisphere Publishing Corporation, 1980.
- van Dam, J. C. and Feddes, R. A. Numerical simulation of infiltration, evaporation and shallow groundwater levels with the richards equation. *Journal of Hydrology*, 233:72–85, 2000.
- van de Griend, A. and Owe, M. Bare soil surface-resistance to evaporation by vapor diffusion under semiarid conditions. *Water Resources Research*, 30:181–188, 1994.
- van Driest, E. On turbulent flow near a wall. *American Institute of Aeronautics and Astronautics Journal*, 23, 1956.
- van Genuchten, M. T. A closed-form equation for predicting the hydraulic conductivity of unsaturated soils. *Soil Science Society of America Journal*, 44:892–898, 1980.
- Versteeg, H. and Malalasekera, W. *An introduction to computational fluid dynamics*. Pearson Education, 2. edition, 2007.
- Webb, S. W. A simple extension of two-phase characteristic curves to include the dry region. *Water Resources Research*, 36:1425–1430, 2000.
- Whitaker, S. *The method of volume averaging*. Kluwer Academic Publishers, 1999.
- Whitaker, S. Flow in porous media I: A theoretical derivation of Darcy’s law. *Transport in Porous Media*, 1:3–25, 1986a.

-
- Whitaker, S. Flow in porous media II : The governing equations for immiscible, two-phase flow. *Transport in Porous Media*, 1:105–125, 1986b.
- White, F. M. *Fluid mechanics*. McGraw-Hill, 2000.
- Wilcox, D. C. *Turbulence Modeling for CFD*. DCW Industries, 2006.
- Wildenschild, D. and Sheppard, A. P. X-ray imaging and analysis techniques for quantifying pore-scale structure and processes in subsurface porous medium systems. *Advances in Water Resources*, 51:217–246, 2013.
- Yamanaka, T., Takeda, A., and Shimada, J. Evaporation beneath the soil surface: Some observational evidence and numerical experiments. *Hydrological Processes*, 12:2193–2203, 1998.
- Yiotis, A. G., Tsimpanogiannis, I. N., Stubos, A. K., and Yortsos, Y. C. Coupling between external and internal mass transfer during drying of a porous medium. *Water Resources Research*, 43(W06403):1–12, 2007.
- Zeng, Y., Su, Z., Wan, L., and Wen, J. A simulation analysis of the advective effect on evaporation using a two-phase heat and mass flow model. *Water Resources Research*, 47 (W10529), 2011.
- Zhang, K., Burns, I., Greenwood, D., Hammond, J., and White, P. Developing a reliable strategy to infer the effective soil hydraulic properties from field evaporation experiments for agro-hydrological models. *Agricultural Water Management*, 97:399–409, 2010.
- Zhang, R. and van Genuchten, M. T. New models for unsaturated soil hydraulic properties. *Soil Science*, 158:77–85, 1994.



Institut für Wasser- und Umweltsystemmodellierung Universität Stuttgart

Pfaffenwaldring 61
70569 Stuttgart (Vaihingen)
Telefon (0711) 685 - 64717/64749/64752/64679
Telefax (0711) 685 - 67020 o. 64746 o. 64681
E-Mail: iws@iws.uni-stuttgart.de
<http://www.iws.uni-stuttgart.de>

Direktoren

Prof. Dr. rer. nat. Dr.-Ing. András Bárdossy
Prof. Dr.-Ing. Rainer Helmig
Prof. Dr.-Ing. Silke Wieprecht

Vorstand (Stand 19.08.2013)

Prof. Dr. rer. nat. Dr.-Ing. A. Bárdossy
Prof. Dr.-Ing. R. Helmig
Prof. Dr.-Ing. S. Wieprecht
Prof. Dr. J.A. Sander Huisman
Jürgen Braun, PhD
apl. Prof. Dr.-Ing. H. Class
Dr.-Ing. H.-P. Koschitzky
Dr.-Ing. M. Noack
Jun.-Prof. Dr.-Ing. W. Nowak, M.Sc.
Dr. rer. nat. J. Seidel
Dr.-Ing. K. Terheiden

Emeriti

Prof. Dr.-Ing. habil. Dr.-Ing. E.h. Jürgen Giesecke
Prof. Dr.h.c. Dr.-Ing. E.h. Helmut Kobus, PhD

Lehrstuhl für Wasserbau und Wassermengenwirtschaft

Leiter: Prof. Dr.-Ing. Silke Wieprecht
Stellv.: Dr.-Ing. Kristina Terheiden
Versuchsanstalt für Wasserbau
Leiter: Dr.-Ing. Markus Noack

Lehrstuhl für Hydromechanik und Hydrosystemmodellierung

Leiter: Prof. Dr.-Ing. Rainer Helmig
Stellv.: apl. Prof. Dr.-Ing. Holger Class
**Jungwissenschaftlergruppe: Stochastische
Modellierung von Hydrosystemen**
Leiter: Jun.-Prof. Dr.-Ing. Wolfgang Nowak, M.Sc.

Lehrstuhl für Hydrologie und Geohydrologie

Leiter: Prof. Dr. rer. nat. Dr.-Ing. András Bárdossy
Stellv.: Dr. rer. nat. Jochen Seidel
Hydrogeophysik der Vadosen Zone
(mit Forschungszentrum Jülich)
Leiter: Prof. Dr. J.A. Sander Huisman

VEGAS, Versuchseinrichtung zur Grundwasser- und Altlastensanierung

Leitung: Jürgen Braun, PhD, AD
Dr.-Ing. Hans-Peter Koschitzky, AD

Verzeichnis der Mitteilungshefte

- 1 Röhnisch, Arthur: *Die Bemühungen um eine Wasserbauliche Versuchsanstalt an der Technischen Hochschule Stuttgart*, und Fattah Abouleid, Abdel: *Beitrag zur Berechnung einer in lockeren Sand gerammten, zweifach verankerten Spundwand*, 1963
- 2 Marotz, Günter: *Beitrag zur Frage der Standfestigkeit von dichten Asphaltbelägen im Großwasserbau*, 1964
- 3 Gurr, Siegfried: *Beitrag zur Berechnung zusammengesetzter ebener Flächen-tragwerke unter besonderer Berücksichtigung ebener Stauwände, mit Hilfe von Randwert- und Lastwertmatrizen*, 1965
- 4 Plica, Peter: *Ein Beitrag zur Anwendung von Schalenkonstruktionen im Stahlwasserbau*, und Petrikat, Kurt: *Möglichkeiten und Grenzen des wasserbaulichen Versuchswesens*, 1966

- 5 Plate, Erich: *Beitrag zur Bestimmung der Windgeschwindigkeitsverteilung in der durch eine Wand gestörten bodennahen Luftschicht, und*
Röhnisch, Arthur; Marotz, Günter: *Neue Baustoffe und Bauausführungen für den Schutz der Böschungen und der Sohle von Kanälen, Flüssen und Häfen; Gesteigungskosten und jeweilige Vorteile, sowie Unny, T.E.: Schwingungsuntersuchungen am Kegelstrahlschieber, 1967*
- 6 Seiler, Erich: *Die Ermittlung des Anlagenwertes der bundeseigenen Binnenschiffahrtsstraßen und Talsperren und des Anteils der Binnenschifffahrt an diesem Wert, 1967*
- 7 *Sonderheft anlässlich des 65. Geburtstages von Prof. Arthur Röhnisch mit Beiträgen von* Benk, Dieter; Breitling, J.; Gurr, Siegfried; Haberhauer, Robert; Honekamp, Hermann; Kuz, Klaus Dieter; Marotz, Günter; Mayer-Vorfelder, Hans-Jörg; Miller, Rudolf; Plate, Erich J.; Radomski, Helge; Schwarz, Helmut; Vollmer, Ernst; Wildenhahn, Eberhard; 1967
- 8 Jumikis, Alfred: *Beitrag zur experimentellen Untersuchung des Wassernachschubs in einem gefrierenden Boden und die Beurteilung der Ergebnisse, 1968*
- 9 Marotz, Günter: *Technische Grundlagen einer Wasserspeicherung im natürlichen Untergrund, 1968*
- 10 Radomski, Helge: *Untersuchungen über den Einfluß der Querschnittsform wellenförmiger Spundwände auf die statischen und rammtechnischen Eigenschaften, 1968*
- 11 Schwarz, Helmut: *Die Grenztragfähigkeit des Baugrundes bei Einwirkung vertikal gezogener Ankerplatten als zweidimensionales Bruchproblem, 1969*
- 12 Erbel, Klaus: *Ein Beitrag zur Untersuchung der Metamorphose von Mittelgebirgsschneedecken unter besonderer Berücksichtigung eines Verfahrens zur Bestimmung der thermischen Schneequalität, 1969*
- 13 Westhaus, Karl-Heinz: *Der Strukturwandel in der Binnenschifffahrt und sein Einfluß auf den Ausbau der Binnenschiffskanäle, 1969*
- 14 Mayer-Vorfelder, Hans-Jörg: *Ein Beitrag zur Berechnung des Erdwiderstandes unter Ansatz der logarithmischen Spirale als Gleitflächenfunktion, 1970*
- 15 Schulz, Manfred: *Berechnung des räumlichen Erddruckes auf die Wandung kreiszylindrischer Körper, 1970*
- 16 Mobasseri, Manoutschehr: *Die Rippenstützmauer. Konstruktion und Grenzen ihrer Standsicherheit, 1970*
- 17 Benk, Dieter: *Ein Beitrag zum Betrieb und zur Bemessung von Hochwasserrückhaltebecken, 1970*

- 18 Gàl, Attila: *Bestimmung der mitschwingenden Wassermasse bei überströmten Fischbauchklappen mit kreiszylindrischem Staublech*, 1971, vergriffen
- 19 Kuz, Klaus Dieter: *Ein Beitrag zur Frage des Einsetzens von Kavitationserscheinungen in einer Düsenströmung bei Berücksichtigung der im Wasser gelösten Gase*, 1971, vergriffen
- 20 Schaak, Hartmut: *Verteilleitungen von Wasserkraftanlagen*, 1971
- 21 *Sonderheft zur Eröffnung der neuen Versuchsanstalt des Instituts für Wasserbau der Universität Stuttgart mit Beiträgen von* Brombach, Hansjörg; Dirksen, Wolfram; Gàl, Attila; Gerlach, Reinhard; Giesecke, Jürgen; Holthoff, Franz-Josef; Kuz, Klaus Dieter; Marotz, Günter; Minor, Hans-Erwin; Petrikat, Kurt; Röhnisch, Arthur; Rueff, Helge; Schwarz, Helmut; Vollmer, Ernst; Wildenhahn, Eberhard; 1972
- 22 Wang, Chung-su: *Ein Beitrag zur Berechnung der Schwingungen an Kegelstrahlschiebern*, 1972
- 23 Mayer-Vorfelder, Hans-Jörg: *Erdwiderstandsbeiwerte nach dem Ohde-Variationsverfahren*, 1972
- 24 Minor, Hans-Erwin: *Beitrag zur Bestimmung der Schwingungsanfachungsfunktionen überströmter Stauklappen*, 1972, vergriffen
- 25 Brombach, Hansjörg: *Untersuchung strömungsmechanischer Elemente (Fluidik) und die Möglichkeit der Anwendung von Wirbelkammerelementen im Wasserbau*, 1972, vergriffen
- 26 Wildenhahn, Eberhard: *Beitrag zur Berechnung von Horizontalfilterbrunnen*, 1972
- 27 Steinlein, Helmut: *Die Eliminierung der Schwebstoffe aus Flußwasser zum Zweck der unterirdischen Wasserspeicherung, gezeigt am Beispiel der Iller*, 1972
- 28 Holthoff, Franz Josef: *Die Überwindung großer Hubhöhen in der Binnenschifffahrt durch Schwimmerhebwerke*, 1973
- 29 Röder, Karl: *Einwirkungen aus Baugrundbewegungen auf trog- und kastenförmige Konstruktionen des Wasser- und Tunnelbaues*, 1973
- 30 Kretschmer, Heinz: *Die Bemessung von Bogenstaumauern in Abhängigkeit von der Talform*, 1973
- 31 Honekamp, Hermann: *Beitrag zur Berechnung der Montage von Unterwasserpipelines*, 1973
- 32 Giesecke, Jürgen: *Die Wirbelkammertriode als neuartiges Steuerorgan im Wasserbau*, und Brombach, Hansjörg: *Entwicklung, Bauformen, Wirkungsweise und Steuereigenschaften von Wirbelkammerverstärkern*, 1974

- 33 Rueff, Helge: *Untersuchung der schwingungserregenden Kräfte an zwei hintereinander angeordneten Tiefschützen unter besonderer Berücksichtigung von Kavitation*, 1974
- 34 Röhnisch, Arthur: *Einpreßversuche mit Zementmörtel für Spannbeton - Vergleich der Ergebnisse von Modellversuchen mit Ausführungen in Hüllwellrohren*, 1975
- 35 *Sonderheft anlässlich des 65. Geburtstages von Prof. Dr.-Ing. Kurt Petrikat mit Beiträgen von:* Brombach, Hansjörg; Erbel, Klaus; Flinspach, Dieter; Fischer jr., Richard; Gàl, Attila; Gerlach, Reinhard; Giesecke, Jürgen; Haberhauer, Robert; Hafner Edzard; Hausenblas, Bernhard; Horlacher, Hans-Burkhard; Hutarew, Andreas; Knoll, Manfred; Krummet, Ralph; Marotz, Günter; Merkle, Theodor; Miller, Christoph; Minor, Hans-Erwin; Neumayer, Hans; Rao, Syamala; Rath, Paul; Rueff, Helge; Ruppert, Jürgen; Schwarz, Wolfgang; Topal-Gökceli, Mehmet; Vollmer, Ernst; Wang, Chung-su; Weber, Hans-Georg; 1975
- 36 Berger, Jochum: *Beitrag zur Berechnung des Spannungszustandes in rotations-symmetrisch belasteten Kugelschalen veränderlicher Wandstärke unter Gas- und Flüssigkeitsdruck durch Integration schwach singulärer Differentialgleichungen*, 1975
- 37 Dirksen, Wolfram: *Berechnung instationärer Abflußvorgänge in gestauten Gerinnen mittels Differenzenverfahren und die Anwendung auf Hochwasserrückhaltebecken*, 1976
- 38 Horlacher, Hans-Burkhard: *Berechnung instationärer Temperatur- und Wärmespannungsfelder in langen mehrschichtigen Hohlzylindern*, 1976
- 39 Hafner, Edzard: *Untersuchung der hydrodynamischen Kräfte auf Baukörper im Tiefwasserbereich des Meeres*, 1977, ISBN 3-921694-39-6
- 40 Ruppert, Jürgen: *Über den Axialwirbelkammverstärker für den Einsatz im Wasserbau*, 1977, ISBN 3-921694-40-X
- 41 Hutarew, Andreas: *Beitrag zur Beeinflußbarkeit des Sauerstoffgehalts in Fließgewässern an Abstürzen und Wehren*, 1977, ISBN 3-921694-41-8, vergriffen
- 42 Miller, Christoph: *Ein Beitrag zur Bestimmung der schwingungserregenden Kräfte an unterströmten Wehren*, 1977, ISBN 3-921694-42-6
- 43 Schwarz, Wolfgang: *Druckstoßberechnung unter Berücksichtigung der Radial- und Längsverschiebungen der Rohrwandung*, 1978, ISBN 3-921694-43-4
- 44 Kinzelbach, Wolfgang: *Numerische Untersuchungen über den optimalen Einsatz variabler Kühlsysteme einer Kraftwerkskette am Beispiel Oberrhein*, 1978, ISBN 3-921694-44-2
- 45 Barczewski, Baldur: *Neue Meßmethoden für Wasser-Luftgemische und deren Anwendung auf zweiphasige Auftriebsstrahlen*, 1979, ISBN 3-921694-45-0

- 46 Neumayer, Hans: *Untersuchung der Strömungsvorgänge in radialen Wirbelkammerverstärkern*, 1979, ISBN 3-921694-46-9
- 47 Elalfy, Youssef-Elhassan: *Untersuchung der Strömungsvorgänge in Wirbelkammerdiolen und -drosseln*, 1979, ISBN 3-921694-47-7
- 48 Brombach, Hansjörg: *Automatisierung der Bewirtschaftung von Wasserspeichern*, 1981, ISBN 3-921694-48-5
- 49 Geldner, Peter: *Deterministische und stochastische Methoden zur Bestimmung der Selbstdichtung von Gewässern*, 1981, ISBN 3-921694-49-3, vergriffen
- 50 Mehlhorn, Hans: *Temperaturveränderungen im Grundwasser durch Brauchwasserleitungen*, 1982, ISBN 3-921694-50-7, vergriffen
- 51 Hafner, Edzard: *Rohrleitungen und Behälter im Meer*, 1983, ISBN 3-921694-51-5
- 52 Rinnert, Bernd: *Hydrodynamische Dispersion in porösen Medien: Einfluß von Dichteunterschieden auf die Vertikalvermischung in horizontaler Strömung*, 1983, ISBN 3-921694-52-3, vergriffen
- 53 Lindner, Wulf: *Steuerung von Grundwasserentnahmen unter Einhaltung ökologischer Kriterien*, 1983, ISBN 3-921694-53-1, vergriffen
- 54 Herr, Michael; Herzer, Jörg; Kinzelbach, Wolfgang; Kobus, Helmut; Rinnert, Bernd: *Methoden zur rechnerischen Erfassung und hydraulischen Sanierung von Grundwasserkontaminationen*, 1983, ISBN 3-921694-54-X
- 55 Schmitt, Paul: *Wege zur Automatisierung der Niederschlagsermittlung*, 1984, ISBN 3-921694-55-8, vergriffen
- 56 Müller, Peter: *Transport und selektive Sedimentation von Schwebstoffen bei gestautem Abfluß*, 1985, ISBN 3-921694-56-6
- 57 El-Qawasmeh, Fuad: *Möglichkeiten und Grenzen der Tropfbewässerung unter besonderer Berücksichtigung der Verstopfungsanfälligkeit der Tropfelemente*, 1985, ISBN 3-921694-57-4, vergriffen
- 58 Kirchenbaur, Klaus: *Mikroprozessorgesteuerte Erfassung instationärer Druckfelder am Beispiel seegangsbelasteter Baukörper*, 1985, ISBN 3-921694-58-2
- 59 Kobus, Helmut (Hrsg.): *Modellierung des großräumigen Wärme- und Schadstofftransports im Grundwasser*, Tätigkeitsbericht 1984/85 (DFG-Forschergruppe an den Universitäten Hohenheim, Karlsruhe und Stuttgart), 1985, ISBN 3-921694-59-0, vergriffen
- 60 Spitz, Karlheinz: *Dispersion in porösen Medien: Einfluß von Inhomogenitäten und Dichteunterschieden*, 1985, ISBN 3-921694-60-4, vergriffen
- 61 Kobus, Helmut: *An Introduction to Air-Water Flows in Hydraulics*, 1985, ISBN 3-921694-61-2

- 62 Kaleris, Vassilios: *Erfassung des Austausches von Oberflächen- und Grundwasser in horizontalebene Grundwassermodellen*, 1986, ISBN 3-921694-62-0
- 63 Herr, Michael: *Grundlagen der hydraulischen Sanierung verunreinigter Porengrundwasserleiter*, 1987, ISBN 3-921694-63-9
- 64 Marx, Walter: *Berechnung von Temperatur und Spannung in Massenbeton infolge Hydratation*, 1987, ISBN 3-921694-64-7
- 65 Koschitzky, Hans-Peter: *Dimensionierungskonzept für Sohlbelüfter in Schußrinnen zur Vermeidung von Kavitationsschäden*, 1987, ISBN 3-921694-65-5
- 66 Kobus, Helmut (Hrsg.): *Modellierung des großräumigen Wärme- und Schadstofftransports im Grundwasser*, Tätigkeitsbericht 1986/87 (DFG-Forschergruppe an den Universitäten Hohenheim, Karlsruhe und Stuttgart) 1987, ISBN 3-921694-66-3
- 67 Söll, Thomas: *Berechnungsverfahren zur Abschätzung anthropogener Temperaturanomalien im Grundwasser*, 1988, ISBN 3-921694-67-1
- 68 Dittrich, Andreas; Westrich, Bernd: *Bodenseeufererosion, Bestandsaufnahme und Bewertung*, 1988, ISBN 3-921694-68-X, vergriffen
- 69 Huwe, Bernd; van der Ploeg, Rienk R.: *Modelle zur Simulation des Stickstoffhaushaltes von Standorten mit unterschiedlicher landwirtschaftlicher Nutzung*, 1988, ISBN 3-921694-69-8, vergriffen
- 70 Stephan, Karl: *Integration elliptischer Funktionen*, 1988, ISBN 3-921694-70-1
- 71 Kobus, Helmut; Zilliox, Lothaire (Hrsg.): *Nitratbelastung des Grundwassers, Auswirkungen der Landwirtschaft auf die Grundwasser- und Rohwasserbeschaffenheit und Maßnahmen zum Schutz des Grundwassers*. Vorträge des deutsch-französischen Kolloquiums am 6. Oktober 1988, Universitäten Stuttgart und Louis Pasteur Strasbourg (Vorträge in deutsch oder französisch, Kurzfassungen zweisprachig), 1988, ISBN 3-921694-71-X
- 72 Soyeaux, Renald: *Unterströmung von Stauanlagen auf klüftigem Untergrund unter Berücksichtigung laminarer und turbulenter Fließzustände*, 1991, ISBN 3-921694-72-8
- 73 Kohane, Roberto: *Berechnungsmethoden für Hochwasserabfluß in Fließgewässern mit überströmten Vorländern*, 1991, ISBN 3-921694-73-6
- 74 Hassinger, Reinhard: *Beitrag zur Hydraulik und Bemessung von Blocksteinrampen in flexibler Bauweise*, 1991, ISBN 3-921694-74-4, vergriffen
- 75 Schäfer, Gerhard: *Einfluß von Schichtenstrukturen und lokalen Einlagerungen auf die Längsdispersion in Porengrundwasserleitern*, 1991, ISBN 3-921694-75-2
- 76 Giesecke, Jürgen: *Vorträge, Wasserwirtschaft in stark besiedelten Regionen; Umweltforschung mit Schwerpunkt Wasserwirtschaft*, 1991, ISBN 3-921694-76-0

- 77 Huwe, Bernd: *Deterministische und stochastische Ansätze zur Modellierung des Stickstoffhaushalts landwirtschaftlich genutzter Flächen auf unterschiedlichem Skalenniveau*, 1992, ISBN 3-921694-77-9, vergriffen
- 78 Rommel, Michael: *Verwendung von Kluftdaten zur realitätsnahen Generierung von Kluftnetzen mit anschließender laminar-turbulenter Strömungsberechnung*, 1993, ISBN 3-92 1694-78-7
- 79 Marschall, Paul: *Die Ermittlung lokaler Stofffrachten im Grundwasser mit Hilfe von Einbohrloch-Meßverfahren*, 1993, ISBN 3-921694-79-5, vergriffen
- 80 Ptak, Thomas: *Stofftransport in heterogenen Porenaquiferen: Felduntersuchungen und stochastische Modellierung*, 1993, ISBN 3-921694-80-9, vergriffen
- 81 Haakh, Frieder: *Transientes Strömungsverhalten in Wirbelkammern*, 1993, ISBN 3-921694-81-7
- 82 Kobus, Helmut; Cirpka, Olaf; Barczewski, Baldur; Koschitzky, Hans-Peter: *Versucheinrichtung zur Grundwasser und Altlastensanierung VEGAS, Konzeption und Programmrahmen*, 1993, ISBN 3-921694-82-5
- 83 Zang, Weidong: *Optimaler Echtzeit-Betrieb eines Speichers mit aktueller Abflußregenerierung*, 1994, ISBN 3-921694-83-3, vergriffen
- 84 Franke, Hans-Jörg: *Stochastische Modellierung eines flächenhaften Stoffeintrages und Transports in Grundwasser am Beispiel der Pflanzenschutzmittelproblematik*, 1995, ISBN 3-921694-84-1
- 85 Lang, Ulrich: *Simulation regionaler Strömungs- und Transportvorgänge in Karst-aquiferen mit Hilfe des Doppelkontinuum-Ansatzes: Methodenentwicklung und Parameteridentifikation*, 1995, ISBN 3-921694-85-X, vergriffen
- 86 Helmig, Rainer: *Einführung in die Numerischen Methoden der Hydromechanik*, 1996, ISBN 3-921694-86-8, vergriffen
- 87 Cirpka, Olaf: *CONTRACT: A Numerical Tool for Contaminant Transport and Chemical Transformations - Theory and Program Documentation -*, 1996, ISBN 3-921694-87-6
- 88 Haberlandt, Uwe: *Stochastische Synthese und Regionalisierung des Niederschlages für Schmutzfrachtberechnungen*, 1996, ISBN 3-921694-88-4
- 89 Croisé, Jean: *Extraktion von flüchtigen Chemikalien aus natürlichen Lockergesteinen mittels erzwungener Luftströmung*, 1996, ISBN 3-921694-89-2, vergriffen
- 90 Jorde, Klaus: *Ökologisch begründete, dynamische Mindestwasserregelungen bei Ausleitungskraftwerken*, 1997, ISBN 3-921694-90-6, vergriffen
- 91 Helmig, Rainer: *Gekoppelte Strömungs- und Transportprozesse im Untergrund - Ein Beitrag zur Hydrosystemmodellierung-*, 1998, ISBN 3-921694-91-4, vergriffen

- 92 Emmert, Martin: *Numerische Modellierung nichtisothermer Gas-Wasser Systeme in porösen Medien*, 1997, ISBN 3-921694-92-2
- 93 Kern, Ulrich: *Transport von Schweb- und Schadstoffen in staugeregelten Fließgewässern am Beispiel des Neckars*, 1997, ISBN 3-921694-93-0, vergriffen
- 94 Förster, Georg: *Druckstoßdämpfung durch große Luftblasen in Hochpunkten von Rohrleitungen* 1997, ISBN 3-921694-94-9
- 95 Cirpka, Olaf: *Numerische Methoden zur Simulation des reaktiven Mehrkomponententransports im Grundwasser*, 1997, ISBN 3-921694-95-7, vergriffen
- 96 Färber, Arne: *Wärmetransport in der ungesättigten Bodenzone: Entwicklung einer thermischen In-situ-Sanierungstechnologie*, 1997, ISBN 3-921694-96-5
- 97 Betz, Christoph: *Wasserdampfdestillation von Schadstoffen im porösen Medium: Entwicklung einer thermischen In-situ-Sanierungstechnologie*, 1998, ISBN 3-921694-97-3
- 98 Xu, Yichun: *Numerical Modeling of Suspended Sediment Transport in Rivers*, 1998, ISBN 3-921694-98-1, vergriffen
- 99 Wüst, Wolfgang: *Geochemische Untersuchungen zur Sanierung CKW-kontaminierter Aquifere mit Fe(0)-Reaktionswänden*, 2000, ISBN 3-933761-02-2
- 100 Sheta, Hussam: *Simulation von Mehrphasenvorgängen in porösen Medien unter Einbeziehung von Hysterese-Effekten*, 2000, ISBN 3-933761-03-4
- 101 Ayros, Edwin: *Regionalisierung extremer Abflüsse auf der Grundlage statistischer Verfahren*, 2000, ISBN 3-933761-04-2, vergriffen
- 102 Huber, Ralf: *Compositional Multiphase Flow and Transport in Heterogeneous Porous Media*, 2000, ISBN 3-933761-05-0
- 103 Braun, Christopherus: *Ein Upscaling-Verfahren für Mehrphasenströmungen in porösen Medien*, 2000, ISBN 3-933761-06-9
- 104 Hofmann, Bernd: *Entwicklung eines rechnergestützten Managementsystems zur Beurteilung von Grundwasserschadensfällen*, 2000, ISBN 3-933761-07-7
- 105 Class, Holger: *Theorie und numerische Modellierung nichtisothermer Mehrphasenprozesse in NAPL-kontaminierten porösen Medien*, 2001, ISBN 3-933761-08-5
- 106 Schmidt, Reinhard: *Wasserdampf- und Heißluftinjektion zur thermischen Sanierung kontaminierter Standorte*, 2001, ISBN 3-933761-09-3
- 107 Josef, Reinhold.: *Schadstoffextraktion mit hydraulischen Sanierungsverfahren unter Anwendung von grenzflächenaktiven Stoffen*, 2001, ISBN 3-933761-10-7

- 108 Schneider, Matthias: *Habitat- und Abflussmodellierung für Fließgewässer mit unscharfen Berechnungsansätzen*, 2001, ISBN 3-933761-11-5
- 109 Rathgeb, Andreas: *Hydrodynamische Bemessungsgrundlagen für Lockerdeckwerke an überströmbaren Erddämmen*, 2001, ISBN 3-933761-12-3
- 110 Lang, Stefan: *Parallele numerische Simulation instationärer Probleme mit adaptiven Methoden auf unstrukturierten Gittern*, 2001, ISBN 3-933761-13-1
- 111 Appt, Jochen; Stumpp Simone: *Die Bodensee-Messkampagne 2001, IWS/CWR Lake Constance Measurement Program 2001*, 2002, ISBN 3-933761-14-X
- 112 Heimerl, Stephan: *Systematische Beurteilung von Wasserkraftprojekten*, 2002, ISBN 3-933761-15-8, vergriffen
- 113 Iqbal, Amin: *On the Management and Salinity Control of Drip Irrigation*, 2002, ISBN 3-933761-16-6
- 114 Silberhorn-Hemming, Annette: *Modellierung von Kluftaquifersystemen: Geostatistische Analyse und deterministisch-stochastische Kluftgenerierung*, 2002, ISBN 3-933761-17-4
- 115 Winkler, Angela: *Prozesse des Wärme- und Stofftransports bei der In-situ-Sanierung mit festen Wärmequellen*, 2003, ISBN 3-933761-18-2
- 116 Marx, Walter: *Wasserkraft, Bewässerung, Umwelt - Planungs- und Bewertungsschwerpunkte der Wasserbewirtschaftung*, 2003, ISBN 3-933761-19-0
- 117 Hinkelmann, Reinhard: *Efficient Numerical Methods and Information-Processing Techniques in Environment Water*, 2003, ISBN 3-933761-20-4
- 118 Samaniego-Eguiguren, Luis Eduardo: *Hydrological Consequences of Land Use / Land Cover and Climatic Changes in Mesoscale Catchments*, 2003, ISBN 3-933761-21-2
- 119 Neunhäuserer, Lina: *Diskretisierungsansätze zur Modellierung von Strömungs- und Transportprozessen in geklüftet-porösen Medien*, 2003, ISBN 3-933761-22-0
- 120 Paul, Maren: *Simulation of Two-Phase Flow in Heterogeneous Poros Media with Adaptive Methods*, 2003, ISBN 3-933761-23-9
- 121 Ehret, Uwe: *Rainfall and Flood Nowcasting in Small Catchments using Weather Radar*, 2003, ISBN 3-933761-24-7
- 122 Haag, Ingo: *Der Sauerstoffhaushalt staugeregelter Flüsse am Beispiel des Neckars - Analysen, Experimente, Simulationen -*, 2003, ISBN 3-933761-25-5
- 123 Appt, Jochen: *Analysis of Basin-Scale Internal Waves in Upper Lake Constance*, 2003, ISBN 3-933761-26-3

- 124 Hrsg.: Schrenk, Volker; Batereau, Katrin; Barczewski, Baldur; Weber, Karolin und Koschitzky, Hans-Peter: *Symposium Ressource Fläche und VEGAS - Statuskolloquium 2003, 30. September und 1. Oktober 2003*, 2003, ISBN 3-933761-27-1
- 125 Omar Khalil Ouda: *Optimisation of Agricultural Water Use: A Decision Support System for the Gaza Strip*, 2003, ISBN 3-933761-28-0
- 126 Batereau, Katrin: *Sensorbasierte Bodenluftmessung zur Vor-Ort-Erkundung von Schadensherden im Untergrund*, 2004, ISBN 3-933761-29-8
- 127 Witt, Oliver: *Erosionsstabilität von Gewässersedimenten mit Auswirkung auf den Stofftransport bei Hochwasser am Beispiel ausgewählter Stauhaltungen des Oberrheins*, 2004, ISBN 3-933761-30-1
- 128 Jakobs, Hartmut: *Simulation nicht-isothermer Gas-Wasser-Prozesse in komplexen Kluft-Matrix-Systemen*, 2004, ISBN 3-933761-31-X
- 129 Li, Chen-Chien: *Deterministisch-stochastisches Berechnungskonzept zur Beurteilung der Auswirkungen erosiver Hochwasserereignisse in Flusstauhaltungen*, 2004, ISBN 3-933761-32-8
- 130 Reichenberger, Volker; Helmig, Rainer; Jakobs, Hartmut; Bastian, Peter; Niessner, Jennifer: *Complex Gas-Water Processes in Discrete Fracture-Matrix Systems: Upscaling, Mass-Conservative Discretization and Efficient Multilevel Solution*, 2004, ISBN 3-933761-33-6
- 131 Hrsg.: Barczewski, Baldur; Koschitzky, Hans-Peter; Weber, Karolin; Wege, Ralf: *VEGAS - Statuskolloquium 2004*, Tagungsband zur Veranstaltung am 05. Oktober 2004 an der Universität Stuttgart, Campus Stuttgart-Vaihingen, 2004, ISBN 3-933761-34-4
- 132 Asie, Kemal Jabir: *Finite Volume Models for Multiphase Multicomponent Flow through Porous Media*. 2005, ISBN 3-933761-35-2
- 133 Jacoub, George: *Development of a 2-D Numerical Module for Particulate Contaminant Transport in Flood Retention Reservoirs and Impounded Rivers*, 2004, ISBN 3-933761-36-0
- 134 Nowak, Wolfgang: *Geostatistical Methods for the Identification of Flow and Transport Parameters in the Subsurface*, 2005, ISBN 3-933761-37-9
- 135 Süß, Mia: *Analysis of the influence of structures and boundaries on flow and transport processes in fractured porous media*, 2005, ISBN 3-933761-38-7
- 136 Jose, Surabhin Chackiath: *Experimental Investigations on Longitudinal Dispersive Mixing in Heterogeneous Aquifers*, 2005, ISBN: 3-933761-39-5
- 137 Filiz, Fulya: *Linking Large-Scale Meteorological Conditions to Floods in Mesoscale Catchments*, 2005, ISBN 3-933761-40-9

- 138 Qin, Minghao: *Wirklichkeitsnahe und recheneffiziente Ermittlung von Temperatur und Spannungen bei großen RCC-Staumauern*, 2005, ISBN 3-933761-41-7
- 139 Kobayashi, Kenichiro: *Optimization Methods for Multiphase Systems in the Sub-surface - Application to Methane Migration in Coal Mining Areas*, 2005, ISBN 3-933761-42-5
- 140 Rahman, Md. Arifur: *Experimental Investigations on Transverse Dispersive Mixing in Heterogeneous Porous Media*, 2005, ISBN 3-933761-43-3
- 141 Schrenk, Volker: *Ökobilanzen zur Bewertung von Altlastensanierungsmaßnahmen*, 2005, ISBN 3-933761-44-1
- 142 Hundecha, Hirpa Yeshewatersfa: *Regionalization of Parameters of a Conceptual Rainfall-Runoff Model*, 2005, ISBN: 3-933761-45-X
- 143 Wege, Ralf: *Untersuchungs- und Überwachungsmethoden für die Beurteilung natürlicher Selbstreinigungsprozesse im Grundwasser*, 2005, ISBN 3-933761-46-8
- 144 Breiting, Thomas: *Techniken und Methoden der Hydroinformatik - Modellierung von komplexen Hydrosystemen im Untergrund*, 2006, 3-933761-47-6
- 145 Hrsg.: Braun, Jürgen; Koschitzky, Hans-Peter; Müller, Martin: *Ressource Untergrund: 10 Jahre VEGAS: Forschung und Technologieentwicklung zum Schutz von Grundwasser und Boden*, Tagungsband zur Veranstaltung am 28. und 29. September 2005 an der Universität Stuttgart, Campus Stuttgart-Vaihingen, 2005, ISBN 3-933761-48-4
- 146 Rojanschi, Vlad: *Abflusskonzentration in mesoskaligen Einzugsgebieten unter Berücksichtigung des Sickerraumes*, 2006, ISBN 3-933761-49-2
- 147 Winkler, Nina Simone: *Optimierung der Steuerung von Hochwasserrückhaltebecken-systemen*, 2006, ISBN 3-933761-50-6
- 148 Wolf, Jens: *Räumlich differenzierte Modellierung der Grundwasserströmung alluvialer Aquifere für mesoskalige Einzugsgebiete*, 2006, ISBN: 3-933761-51-4
- 149 Kohler, Beate: *Externe Effekte der Laufwasserkraftnutzung*, 2006, ISBN 3-933761-52-2
- 150 Hrsg.: Braun, Jürgen; Koschitzky, Hans-Peter; Stuhmann, Matthias: *VEGAS-Statuskolloquium 2006*, Tagungsband zur Veranstaltung am 28. September 2006 an der Universität Stuttgart, Campus Stuttgart-Vaihingen, 2006, ISBN 3-933761-53-0
- 151 Niessner, Jennifer: *Multi-Scale Modeling of Multi-Phase - Multi-Component Processes in Heterogeneous Porous Media*, 2006, ISBN 3-933761-54-9
- 152 Fischer, Markus: *Beanspruchung eingeeerdeter Rohrleitungen infolge Austrocknung bindiger Böden*, 2006, ISBN 3-933761-55-7

- 153 Schneck, Alexander: *Optimierung der Grundwasserbewirtschaftung unter Berücksichtigung der Belange der Wasserversorgung, der Landwirtschaft und des Naturschutzes*, 2006, ISBN 3-933761-56-5
- 154 Das, Tapash: *The Impact of Spatial Variability of Precipitation on the Predictive Uncertainty of Hydrological Models*, 2006, ISBN 3-933761-57-3
- 155 Bielinski, Andreas: *Numerical Simulation of CO₂ sequestration in geological formations*, 2007, ISBN 3-933761-58-1
- 156 Mödinger, Jens: *Entwicklung eines Bewertungs- und Entscheidungsunterstützungssystems für eine nachhaltige regionale Grundwasserbewirtschaftung*, 2006, ISBN 3-933761-60-3
- 157 Manthey, Sabine: *Two-phase flow processes with dynamic effects in porous media - parameter estimation and simulation*, 2007, ISBN 3-933761-61-1
- 158 Pozos Estrada, Oscar: *Investigation on the Effects of Entrained Air in Pipelines*, 2007, ISBN 3-933761-62-X
- 159 Ochs, Steffen Oliver: *Steam injection into saturated porous media – process analysis including experimental and numerical investigations*, 2007, ISBN 3-933761-63-8
- 160 Marx, Andreas: *Einsatz gekoppelter Modelle und Wetterradar zur Abschätzung von Niederschlagsintensitäten und zur Abflussvorhersage*, 2007, ISBN 3-933761-64-6
- 161 Hartmann, Gabriele Maria: *Investigation of Evapotranspiration Concepts in Hydrological Modelling for Climate Change Impact Assessment*, 2007, ISBN 3-933761-65-4
- 162 Kebede Gurmessa, Tesfaye: *Numerical Investigation on Flow and Transport Characteristics to Improve Long-Term Simulation of Reservoir Sedimentation*, 2007, ISBN 3-933761-66-2
- 163 Trifković, Aleksandar: *Multi-objective and Risk-based Modelling Methodology for Planning, Design and Operation of Water Supply Systems*, 2007, ISBN 3-933761-67-0
- 164 Götzing, Jens: *Distributed Conceptual Hydrological Modelling - Simulation of Climate, Land Use Change Impact and Uncertainty Analysis*, 2007, ISBN 3-933761-68-9
- 165 Hrsg.: Braun, Jürgen; Koschitzky, Hans-Peter; Stuhmann, Matthias: *VEGAS – Kolloquium 2007*, Tagungsband zur Veranstaltung am 26. September 2007 an der Universität Stuttgart, Campus Stuttgart-Vaihingen, 2007, ISBN 3-933761-69-7
- 166 Freeman, Beau: *Modernization Criteria Assessment for Water Resources Planning; Klamath Irrigation Project, U.S.*, 2008, ISBN 3-933761-70-0

- 167 Dreher, Thomas: *Selektive Sedimentation von Feinstschwebstoffen in Wechselwirkung mit wandnahen turbulenten Strömungsbedingungen*, 2008, ISBN 3-933761-71-9
- 168 Yang, Wei: *Discrete-Continuous Downscaling Model for Generating Daily Precipitation Time Series*, 2008, ISBN 3-933761-72-7
- 169 Kopecki, Ianina: *Calculational Approach to FST-Hemispheres for Multiparametrical Benthos Habitat Modelling*, 2008, ISBN 3-933761-73-5
- 170 Brommundt, Jürgen: *Stochastische Generierung räumlich zusammenhängender Niederschlagszeitreihen*, 2008, ISBN 3-933761-74-3
- 171 Papafotiou, Alexandros: *Numerical Investigations of the Role of Hysteresis in Heterogeneous Two-Phase Flow Systems*, 2008, ISBN 3-933761-75-1
- 172 He, Yi: *Application of a Non-Parametric Classification Scheme to Catchment Hydrology*, 2008, ISBN 978-3-933761-76-7
- 173 Wagner, Sven: *Water Balance in a Poorly Gauged Basin in West Africa Using Atmospheric Modelling and Remote Sensing Information*, 2008, ISBN 978-3-933761-77-4
- 174 Hrsg.: Braun, Jürgen; Koschitzky, Hans-Peter; Stuhmann, Matthias; Schrenk, Volker: *VEGAS-Kolloquium 2008 Ressource Fläche III*, Tagungsband zur Veranstaltung am 01. Oktober 2008 an der Universität Stuttgart, Campus Stuttgart-Vaihingen, 2008, ISBN 978-3-933761-78-1
- 175 Patil, Sachin: *Regionalization of an Event Based Nash Cascade Model for Flood Predictions in Ungauged Basins*, 2008, ISBN 978-3-933761-79-8
- 176 Assteerawatt, Anongnart: *Flow and Transport Modelling of Fractured Aquifers based on a Geostatistical Approach*, 2008, ISBN 978-3-933761-80-4
- 177 Karnahl, Joachim Alexander: *2D numerische Modellierung von multifraktionalem Schwebstoff- und Schadstofftransport in Flüssen*, 2008, ISBN 978-3-933761-81-1
- 178 Hiester, Uwe: *Technologieentwicklung zur In-situ-Sanierung der ungesättigten Bodenzone mit festen Wärmequellen*, 2009, ISBN 978-3-933761-82-8
- 179 Laux, Patrick: *Statistical Modeling of Precipitation for Agricultural Planning in the Volta Basin of West Africa*, 2009, ISBN 978-3-933761-83-5
- 180 Ehsan, Saqib: *Evaluation of Life Safety Risks Related to Severe Flooding*, 2009, ISBN 978-3-933761-84-2
- 181 Prohaska, Sandra: *Development and Application of a 1D Multi-Strip Fine Sediment Transport Model for Regulated Rivers*, 2009, ISBN 978-3-933761-85-9

- 182 Kopp, Andreas: *Evaluation of CO₂ Injection Processes in Geological Formations for Site Screening*, 2009, ISBN 978-3-933761-86-6
- 183 Ebigbo, Anozie: *Modelling of biofilm growth and its influence on CO₂ and water (two-phase) flow in porous media*, 2009, ISBN 978-3-933761-87-3
- 184 Freiboth, Sandra: *A phenomenological model for the numerical simulation of multiphase multicomponent processes considering structural alterations of porous media*, 2009, ISBN 978-3-933761-88-0
- 185 Zöllner, Frank: *Implementierung und Anwendung netzfreier Methoden im Konstruktiven Wasserbau und in der Hydromechanik*, 2009, ISBN 978-3-933761-89-7
- 186 Vasin, Milos: *Influence of the soil structure and property contrast on flow and transport in the unsaturated zone*, 2010, ISBN 978-3-933761-90-3
- 187 Li, Jing: *Application of Copulas as a New Geostatistical Tool*, 2010, ISBN 978-3-933761-91-0
- 188 AghaKouchak, Amir: *Simulation of Remotely Sensed Rainfall Fields Using Copulas*, 2010, ISBN 978-3-933761-92-7
- 189 Thapa, Pawan Kumar: *Physically-based spatially distributed rainfall runoff modeling for soil erosion estimation*, 2010, ISBN 978-3-933761-93-4
- 190 Wurms, Sven: *Numerische Modellierung der Sedimentationsprozesse in Retentionsanlagen zur Steuerung von Stoffströmen bei extremen Hochwasserabflussereignissen*, 2011, ISBN 978-3-933761-94-1
- 191 Merkel, Uwe: *Unsicherheitsanalyse hydraulischer Einwirkungen auf Hochwasserschutzdeiche und Steigerung der Leistungsfähigkeit durch adaptive Strömungsmodellierung*, 2011, ISBN 978-3-933761-95-8
- 192 Fritz, Jochen: *A Decoupled Model for Compositional Non-Isothermal Multiphase Flow in Porous Media and Multiphysics Approaches for Two-Phase Flow*, 2010, ISBN 978-3-933761-96-5
- 193 Weber, Karolin (Hrsg.): *12. Treffen junger WissenschaftlerInnen an Wasserbauinstituten*, 2010, ISBN 978-3-933761-97-2
- 194 Bliedernicht, Jan-Geert: *Probability Forecasts of Daily Areal Precipitation for Small River Basins*, 2011, ISBN 978-3-933761-98-9
- 195 Hrsg.: Koschitzky, Hans-Peter; Braun, Jürgen: *VEGAS-Kolloquium 2010 In-situ-Sanierung - Stand und Entwicklung Nano und ISCO -*, Tagungsband zur Veranstaltung am 07. Oktober 2010 an der Universität Stuttgart, Campus Stuttgart-Vaihingen, 2010, ISBN 978-3-933761-99-6

- 196 Gafurov, Abror: *Water Balance Modeling Using Remote Sensing Information - Focus on Central Asia*, 2010, ISBN 978-3-942036-00-9
- 197 Mackenberg, Sylvia: *Die Quellstärke in der Sickerwasserprognose: Möglichkeiten und Grenzen von Labor- und Freilanduntersuchungen*, 2010, ISBN 978-3-942036-01-6
- 198 Singh, Shailesh Kumar: *Robust Parameter Estimation in Gauged and Ungauged Basins*, 2010, ISBN 978-3-942036-02-3
- 199 Doğan, Mehmet Onur: *Coupling of porous media flow with pipe flow*, 2011, ISBN 978-3-942036-03-0
- 200 Liu, Min: *Study of Topographic Effects on Hydrological Patterns and the Implication on Hydrological Modeling and Data Interpolation*, 2011, ISBN 978-3-942036-04-7
- 201 Geleta, Habtamu Itefa: *Watershed Sediment Yield Modeling for Data Scarce Areas*, 2011, ISBN 978-3-942036-05-4
- 202 Franke, Jörg: *Einfluss der Überwachung auf die Versagenswahrscheinlichkeit von Staustufen*, 2011, ISBN 978-3-942036-06-1
- 203 Bakimchandra, Oinam: *Integrated Fuzzy-GIS approach for assessing regional soil erosion risks*, 2011, ISBN 978-3-942036-07-8
- 204 Alam, Muhammad Mahboob: *Statistical Downscaling of Extremes of Precipitation in Mesoscale Catchments from Different RCMs and Their Effects on Local Hydrology*, 2011, ISBN 978-3-942036-08-5
- 205 Hrsg.: Koschitzky, Hans-Peter; Braun, Jürgen: *VEGAS-Kolloquium 2011 Flache Geothermie - Perspektiven und Risiken*, Tagungsband zur Veranstaltung am 06. Oktober 2011 an der Universität Stuttgart, Campus Stuttgart-Vaihingen, 2011, ISBN 978-3-933761-09-2
- 206 Haslauer, Claus: *Analysis of Real-World Spatial Dependence of Subsurface Hydraulic Properties Using Copulas with a Focus on Solute Transport Behaviour*, 2011, ISBN 978-3-942036-10-8
- 207 Dung, Nguyen Viet: *Multi-objective automatic calibration of hydrodynamic models – development of the concept and an application in the Mekong Delta*, 2011, ISBN 978-3-942036-11-5
- 208 Hung, Nguyen Nghia: *Sediment dynamics in the floodplain of the Mekong Delta, Vietnam*, 2011, ISBN 978-3-942036-12-2
- 209 Kuhlmann, Anna: *Influence of soil structure and root water uptake on flow in the unsaturated zone*, 2012, ISBN 978-3-942036-13-9

- 210 Tuhtan, Jeffrey Andrew: *Including the Second Law Inequality in Aquatic Ecodynamics: A Modeling Approach for Alpine Rivers Impacted by Hydropeaking*, 2012, ISBN 978-3-942036-14-6
- 211 Tolossa, Habtamu: *Sediment Transport Computation Using a Data-Driven Adaptive Neuro-Fuzzy Modelling Approach*, 2012, ISBN 978-3-942036-15-3
- 212 Tatomir, Alexandru-Bodgan: *From Discrete to Continuum Concepts of Flow in Fractured Porous Media*, 2012, ISBN 978-3-942036-16-0
- 213 Erbertseder, Karin: *A Multi-Scale Model for Describing Cancer-Therapeutic Transport in the Human Lung*, 2012, ISBN 978-3-942036-17-7
- 214 Noack, Markus: *Modelling Approach for Interstitial Sediment Dynamics and Reproduction of Gravel Spawning Fish*, 2012, ISBN 978-3-942036-18-4
- 215 De Boer, Cjstmir Volkert: *Transport of Nano Sized Zero Valent Iron Colloids during Injection into the Subsurface*, 2012, ISBN 978-3-942036-19-1
- 216 Pfaff, Thomas: *Processing and Analysis of Weather Radar Data for Use in Hydrology*, 2013, ISBN 978-3-942036-20-7
- 217 Lebreuz, Hans-Henning: *Addressing the Input Uncertainty for Hydrological Modeling by a New Geostatistical Method*, 2013, ISBN 978-3-942036-21-4
- 218 Darcis, Melanie Yvonne: *Coupling Models of Different Complexity for the Simulation of CO₂ Storage in Deep Saline Aquifers*, 2013, ISBN 978-3-942036-22-1
- 219 Beck, Ferdinand: *Generation of Spatially Correlated Synthetic Rainfall Time Series in High Temporal Resolution - A Data Driven Approach*, 2013, ISBN 978-3-942036-23-8
- 220 Guthke, Philipp: *Non-multi-Gaussian spatial structures: Process-driven natural genesis, manifestation, modeling approaches, and influences on dependent processes*, 2013, ISBN 978-3-942036-24-5
- 221 Walter, Lena: *Uncertainty studies and risk assessment for CO₂ storage in geological formations*, 2013, ISBN 978-3-942036-25-2
- 222 Wolff, Markus: *Multi-scale modeling of two-phase flow in porous media including capillary pressure effects*, 2013, ISBN 978-3-942036-26-9
- 223 Mosthaf, Klaus Roland: *Modeling and analysis of coupled porous-medium and free flow with application to evaporation processes*, 2014, ISBN 978-3-942036-27-6

Die Mitteilungshefte ab der Nr. 134 (Jg. 2005) stehen als pdf-Datei über die Homepage des Instituts: www.iws.uni-stuttgart.de zur Verfügung.